PERFORMANCE INVESTIGATION OF SWITCHED RELUCTANCE MOTOR DRIVE

Ph.D. THESIS

by

JIGNESH ASHOKBHAI MAKWANA

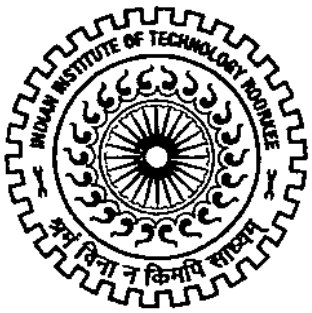

DEPARTMENT OF ELECTRICAL ENGINEERING
INDIAN INSTITUTE OF TECHNOLOGY ROORKEE
ROORKEE – 247 667 (INDIA)
JUNE, 2013

PERFORMANCE INVESTIGATION OF SWITCHED RELUCTANCE MOTOR DRIVE

A THESIS

Submitted in partial fulfilment of the requirements for the award of the degree of

DOCTOR OF PHILOSOPHY
in
ELECTRICAL ENGINEERING

by

JIGNESH ASHOKBHAI MAKWANA

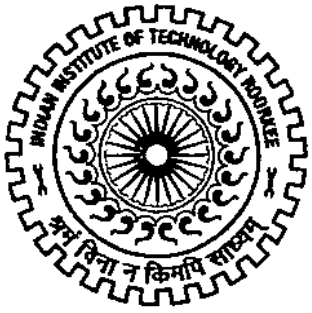

DEPARTMENT OF ELECTRICAL ENGINEERING
INDIAN INSTITUTE OF TECHNOLOGY ROORKEE
ROORKEE – 247 667 (INDIA)
June, 2013

INDIAN INSTITUTE OF TECHNOLOGY ROORKEE
ROORKEE

CANDIDATE'S DECLARATION

I hereby certify that the work which is being presented in this thesis entitled "**PERFORMANCE INVESTIGATION OF SWITCHED RELUCTANCE MOTOR DRIVE"** in partial fulfilment of the requirements for the award of *the Degree of Doctor of Philosophy* and submitted in the Department of Electrical Engineering of Indian Institute of Technology Roorkee, Roorkee is an authentic record of my own work carried out during a period from July, 2009 to June, 2013 under the supervision of Dr. Pramod Agarwal and Dr. S.P Srivastava, Professor, Department of Electrical Engineering, Indian Institute of Technology Roorkee, Roorkee.

The matter presented in this thesis has not been submitted by me for the award of any other degree of this or any other Institution.

(JIGNESH ASHOKBHAI MAKWANA)

This is to certify that the above statement made by the candidate is correct to the best of our knowledge.

(Pramod Agarwal)
Supervisor

(S. P. Srivastava)
Supervisor

Date:

The Ph.D. Viva-Voce Examination of ***Mr. Jignesh Ashokbhai Makwana***, Research Scholar, has been held on…….

Signature of Supervisors Chairman, SRC Signature of External Examiner

Head of the Deptt./Chairman, ODC

ABSTRACT

The Switched Reluctance Motor (SRM) offers significant benefits over conventional AC and DC motors which include higher efficiency over wide speed range operation and under partial loading. Even though it exhibits high starting torque, high power density, high torque to weight ratio, smaller size and weight, low material cost and maintenance free operation, its acceptance for industrial as well as domestic applications is limited. It is due to higher torque ripple for which SRM is known. It also produces acoustic noise as well as it requires costly position sensing arrangement to be attached with the motor for control. However, the recent quest of the energy efficiency has promoted the research and development of the cost effective efficient SRM drive.

In the present work the performance of the SRM drive and the suitability of the same for the various applications are investigated. Extensive simulation is carried out to evaluate the performance of the SRM drive and experimentally verified with the help of prototype model.

The magnetic non-linearity of the SRM increases the complexity of modelling and controller design. Different effective modelling techniques for the SRM have been proposed by the researchers in the past. In the present work few vital non-linear modelling techniques have been exemplified and compared. The embedded control function is designed in MATLAB simulink environment to model a SRM based on analytical modelling technique.

The concept of the physical modelling technique of the system is introduced which offers many advantages over conventional modelling techniques. The main advantage of the physical modelling is its ability to consider the effect of change in physical parameters of the system. In the present work the physical modelling technique is proposed to model the non-linearity of the switched reluctance motor. The variable reluctance characteristic of the motor is utilized to derive the non-linear model of the switched reluctance motor. The mathematical relation amongst the phase reluctance, angular rotor position and geometrical parameters of the motor is derived. The results show that the proposed modelling technique which considers magnetic non-linearity of the motor offers acceptable solution. It also requires only few geometrical parameters of the motor and information of the winding turns per phase. Furthermore, the 3-Dimensional (3D) visualization effect is added to the physical model of the motor with the help of virtual reality tool box of the MATLAB which extends the capabilities of the simulink software into the world of virtual reality graphics.

The high grade real-time simulation of the complete SRM drive is developed with the help of Opal's RT-Lab technology, which eliminates the issue of model latency present in CPU based simulation due to complex model and current overshoot. The drive is comprised

of asymmetric bridge converter, hysteresis current controller and a proportional and integral (PI) speed controller. The effect of commutation angle on the torque-speed characteristics of the switched reluctance motor drive is investigated with the help of real-time experimental studies.

There are applications where the issue of torque ripples of the switched reluctance motor is a major concern e.g. robotic actuators and electric power steering. Efforts are being made into both the motor design and control strategy to reduce the ripples in the torque. The fundamental electronic approach of torque ripple minimization is the current profiling which stores the non-linear relation of torque-current-angle as a lookup table. Then the rotor angle is being used as an index to generate the reference current. Accordingly, the phase current is being controlled by means of hysteresis current controller to maintain the torque to the reference value. Effort have been made by the researchers in the past to replace the lookup table by the mathematical relation for representing non-linear relation of the torque, current and angle. It employs the fuzzy logic controllers, artificial neural networks or the Fourier series based methods. Another vital approach of the torque ripple minimization is the use of torque-sharing-function (TSF) in which the phase current applied is controlled such that, the overall torque becomes constant. More or less all the torque ripple reduction techniques increase the complexity and cost of the drive. However the simplest solution to the torque ripple issue is to use of motor having higher number of phases or the higher stator/rotor pole configuration.

The low-cost switched reluctance motor drive is developed in the present work. In the developed model multi-phase excitation scheme is used to reduce the torque ripples. The proposed switched reluctance motor drive includes 8/6 pole four phase motor, one-switch per phase type converter and low-cost position sensing arrangement. The low-frequency PWM controller has been proposed and proven to be effective in noise reduction compared to hysteresis current controller. It also reduces the converter losses and makes the drive immune to electromagnetic interference. The conventional proportional and integral (PI) speed controller can be used for the switched reluctance motor drive, if transfer function of the non-linear switched reluctance motor is known. Due to non-linearity of SRM, it is difficult to derive the transfer function and hence, the design a controller with proper gains to achieve the desired stability. The ac small signal modelling technique is proposed for linearization of the SRM model. Accordingly, the closed-loop speed PI controller is designed for PWM current controlled SRM drive. Performance of the proposed SRM drive is investigated with the development of prototype SRM, converter and controller. The proposed SRM drive shows lower cost-versus-performance ratio and ensures higher efficiency of the drive even at partial loading. The torque ripple performance of the drive is investigated for the varying speed, load torque and PWM frequency. The investigation shows that the torque ripples are

quite low for the higher speed application as well as for the applications having heavy load inertia. It also shows that the selection of higher PWM frequency is advantageous in reduction of torque ripples for the light load applications; however it increases the converter losses.

The requirement of position feedback necessitates the mechanical position sensors to be attached with the motor which increases the overall cost and reduces the reliability of the operation. Many sensorless control techniques are reported in literature to eliminate the requirement of mechanical position sensors, but none of them is found suitable for the wide speed control range without having any constraint on the performance of the drive. It includes the waveform monitoring, state observer, active probing, modulated signal injection and flux-linkages based rotor position estimation techniques. In the present work a technique based on flux-linkage characteristics is investigated in detail with the help of simulation studies.

In the present work the fixed turn-off method of rotor position estimation is proposed and investigated for speed control which is low-cost and simple solution for the general purpose drive. The commutation instant of the phase is estimated by monitoring the phase voltage and current, while it is not intended to derive continuous rotor position estimation. The method is suitable where the fixed angle control is sufficient but the harsh environmental condition restricts the use of mechanical sensors for reliability issue.

To get rid of rotor position sensing, an ANN based sensorless rotor position estimation technique is proposed where the ANN is used to map the magnetic non-linearity of the motor. The neural network is designed to approximate the continuous rotor position form the flux-linkage and current. The feed-forward neural network structure is used to design a network while the Levenberg-Marquardt technique is used as training algorithm. The proposed method employs only one hidden layer and the training process is accomplished offline. The performance of the ANN is investigated to approximate the non-linear magnetic characteristics as well as the performance of the ANN based sensorless drive is investigated which shows the higher accuracy of the estimation. However the implementation of the ANN based method is computation intensive, time consuming and also pre-requires information of the motor magnetic characteristic.

An analytical sensorless method is proposed which reduces the computation burden and requirement of the storage space. It requires the information of the motor's magnetic characteristics at only two rotor positions that are aligned position and mid position. The simple mathematical expression is derived to estimate the continuous rotor position estimation form the phase voltage and phase current. The performance of the proposed sensorless scheme is investigated which shows the good accuracy of estimation.

The sensorless techniques based on magnetic characteristics require prior knowledge about motor magnetic characteristics which not only increase the time and cost of implementation, but also restrict the operation of the drive to the particular motor. Even the magnetic properties of the two motors from the same manufacturer and having same specifications could not be identical.

The sensorless rotor position estimation techniques that do not require any prior knowledge of the motor magnetic characteristics includes chopping current waveform method, regenerative current method and current gradient sensorless method (CGSM). The design and performance issues of the CGSM are investigated to incorporate with the low-frequency PWM controlled SRM drive. Result shows that the use of phase-lock-loop (PLL) and non-synchronized PWM increases the complexity of implementation and reduces the reliability of the CGSM. It is also observed that the response of the system is unstable to the step change in load-torque. A Modified-CGSM (MCGSM) technique is proposed which eliminates the requirement of the PLL and improves the stability of the system. Prototype setup of the sensorless SRM drive is developed in the laboratory and its performance is investigated under open-loop as well as closed-loop condition.

The study is carried out to exemplify the features and advantages of the SRM drive for a specific application. The switched reluctance motor is found favourable in the application of battery operated vehicle system because of higher efficiency, high starting torque, light weight, low maintenance and capability of electric braking. Furthermore the issue of the torque ripple is also not predominant due to the higher inertia loading. The performance of the low-frequency PWM controlled SRM drive in a low power in-wheel electric vehicle is investigated in detail. The feasibility of the electric braking with the fixed angle controller is explored.

The investigation summarized that, the SRM offers an energy efficient solution for the wide range of applications. However, the complete success of the SRM drive needs proper choice of application, converter, control scheme and position sensing arrangement.

ACKNOWLEDGEMENTS

This thesis is the end of my journey in obtaining my Ph.D. At the end of my thesis I would like to thank all those people who made this thesis possible. It is a pleasant task to express my thanks to all those who contributed in many ways to the success of this study and made it an unforgettable experience for me.

Foremost, I would like to express my sincere gratitude to my one of the supervisor Prof. Pramod Agarwal for the continuous support of my Ph.D study and research, for his patience, motivation, enthusiasm, and immense knowledge. His guidance helped me in all the time of research and writing of this thesis. I could not have imagined having a better advisor and mentor for my Ph.D study. I want to express my sincere acknowledgement with gratitude to my supervisor Prof. S.P. Srivastava. I can't say thank you enough for his tremendous support and help. I feel motivated and encouraged every time I met him. Without his encouragement and guidance this project would not have materialized.

Beside my supervisors, I would like to thank the rest of my thesis committee: Prof. S.P. Gupta, Prof. R.C. Mittal and Dr. S.P. Singh, for their encouragement, insightful comments and questions.

I express my deep sense of gratitude to the Head, Department of Electrical Engineering, Indian Institute of Technology Roorkee, for providing the excellent laboratory and computing facilities of department for the research work. I acknowledge my sincere gratitude to the Ministry of Human Resources Development (MHRD), Government of India for providing financial support for the PhD work. The research work has been carried out under this scheme.

I am thankful to the technical staff of the Electric Drives Lab, especially Mr. Gautam Singh, and Mr. Ameer Ahmad of Fabrication and Assembling Lab, and storekeeper of the department for their timely cooperation and needful help.

I would also like to thank some people from early days of my research tenure, Dr. Rajesh Patel, Dr. Kalpesh Bhalodi, Dr. Madhukar wavre, and Dr. Subhash dube, who kept me going at the beginning.

I am indebted to my friends, Dr. Subhash Joshi, who squeeze time from their busy schedule to help me finish my thesis. I have to offer my special thanks to my friends Ambarish, Amit, Bhargavsir and Giribabu. All they are busy with their own thesis and work, but they are willing to give their helping hands as soon as I am in need. I cannot finish my thesis so soon without their assistant and encouragement. My special thanks go to all the fellow research scholars for their cooperation and moral support during my stay.

I am also grateful to all my teachers from school to university education.

These acknowledgments would not be complete without thanking my parents for their sincere prayers, constant support and care. Even though they have missed me a lot during my work, they waited patiently for the completion of work. Today I feel that my parent's hard work and dreams have been blossomed. I thank my father Ashokbhai, my mother Rasilaben, and my sister Janki. I also wish to extend my thanks to my father-in-law, Abhubhai and my mother-in-law, Kalpnaben for their kind support. Finally, I would like to mention the person who is very important in my life; My wife, Hemagni. The emotional and moral support provided by my wife is unforgettable. I appreciate them for the kind of support extended to me during the entire period of stay at IIT Roorkee. No words can adequately express my gratitude to them. I thank Hemagni for everything.

I am proud to humbly dedicate this research work to my parents and wife.

(Jignesh A. Makwana)

CONTENTS

LIST OF FIGURES

LIST OF TABLES

LIST OF SYMBOLS

ψ	Flux-linkage (V-sec)
ψ_{ph}	Flux linked by the phase winding (v-sec)
ψ_{ref}	Reference flux-linkage
ψ_{cal}	Calculated flux-linkage
ψ_{diff}	Flux-linkage difference
ω_m	Rotor speed (rad/sec)
ω_{ref}	Reference speed
ω_n	Natural frequency
ω_0	Initial frequency
ω_{in}	Frequency of input
ω_{out}	Frequency of output
θ	Rotor angle (mech deg)
θ_a, θ_b, θ_c, θ_d	Rotor position of respective phase
θ_{ON}	Turn-ON angle
θ_{OFF}	Turn-OFF angle
θ_{dwell}	Dwell angle
θ_{estd}	Estimated rotor angle
θ_{pdp}	Rotor angle at which stator and rotor pole just begin to aligned
θ_r	Rotor pole arc (deg)
θ_s	Stator pole arc (deg)
ε	Stroke angle
φ_{in}	Phase delay of input
φ_{out}	Phase delay of output
ξ	Damping factor
τ_{ph}	Electric time constant (sec)
A_g	Cross section area of pole
B	Friction constant
CV	Count value
d_u	Duty cycle of PWM pulse
d	Width of rotor pole (m)
E_{ph}	Back emf (V)
f_{com}	Frequency of commutation pulse (Hz)
f_{pdp}	Frequency of peak detection pulse

f_{pwm}	Frequency of PWM pulse
f_{coff}	Cut-off frequency
F	Force (N)
G	Active length of rotor
i_{ph}	Phase current (Amp)
i_a, i_b, i_b, i_d	Current of respective phase
i_{ref}	Reference current
i_{Ts}	Average current over one switching period
J	Inertia
K	Spring constant
K_b	Back emf constant
K_p	Proportional gain
K_i	Integral gain
K_v	Proportional constant (rad/s/V)
K_{pdp}	Delay factor of peak detection pulse
K_0	Initial constant
l_g	Length of airgap (m)
L	Phase inductance (H)
L_A	Average inductance over one switching period
L_a	Inductance at aligned rotor position
L_m	Inductance at midway rotor position
L_u	Inductance at unaligned rotor position
M_f	Frequency multiplier
m	Number of phase
M	Mass
N_s	Motor speed (rpm)
n_{cr}	Number of cycle of peak detection pulse per revolution
R_s	Phase resistance (Ohm)
R_a, R_b, R_c, R_d	Resistance of respective phase winding (Ohm)
S	Reluctance
S_s	Stator reluctance
S_r	Rotor reluctance
S_g	Reluctance of sirgap
T	Torque developed (N-m)
T_s	Switching period of PWM pules
t_c	Time interval of PWM pulse (sec)
t_{com}	Time interval of commutation pulse (sec)

t_{on}	On time of PWM pulse (sec)
t_{off}	Off time of PWM pulse (sec)
T_{ripple}	Torque ripple
T_{max}	Maximum torque
T_{min}	Minimum torque
T_{avg}	Average torque
V_{rms}	AC input voltage (V)
V_{ph}	Phase voltage (V)
V_a, V_b, V_c, V_d	Phase voltage of respective phase
V_c	Control voltage (V)
V_m	Maximum voltage of comparator signal
W_c	Co-energy (w-sec)
W_f	Stored field energy (w-sec)
W_m	Mechanical energy

LIST OF ABBRIVIATIONS

3D	Three Dimensional
ADC	Analog to Digital Converter
ANN	Artificial Neural Network
BLDC	Brushless DC
CGSM	Current Gradient Sensorless Method
CMOS	Complementary Metal–Oxide–Semiconductor
CSC	Current Source Converter
DAC	Digital to Analog Converter
DIP	Dual In-line Package
DSO	Digital Signal Oscilloscope
DSP	Digital Signal Processor
DTC	Direct Torque Control
EC	Electronically Commutated
EI	Electromagnetic Interference
EMDS	Electrical Motor Driven Systems
FEA	Finite Element Analysis
FPGA	Field Programmable Gate Array
HIL	Hardware-In-Loop
IC	Integrated Circuit
IEC	International Electrotechnical Commission
IEEE	Institute of Electrical and Electronics Engineers
IGBT	Insulated Gate Bipolar Transistor
IM	Induction Motor
LPF	Low Pass Filter
MCGSM	Modified Current Gradient Sensorless Method
MEPS	Minimum Energy Performance Standard
MOSFET	Metal Oxide Semiconductor Field Effect Transistor
NN	Neural Network
OECD	Organization for Economic Cooperation and Development
Op-amp	Operational Amplifier
PD	Phase Detector
PDP	Peak Detection Pulse
pf	power factor
PFD	Phase Frequency Detector

PI	Proportional-Integral
PID	Proportional-Integral-Derivative
PLL	Phase Locked Loop
PMSM	Permanent Magnet Synchronous Motor
PWM	Pulse Width Modulation
RFI	Radio Frequency Interference
SRD	Switched Reluctance Drive
SRM	Switched Reluctance Motor
TDF	Torque Distribution Function
THD	Total Harmonic Distortion
TSF	Torque Sharing Function
TTL	Transistor-Transistor Logic
VCO	Voltage Controlled Oscillator
VFD	Variable Frequency Drive
VR	Virtual Reality
VRML	Virtual Reality Modeling Language
VSC	Voltage Source Converter
VSI	Voltage Source Inverter
ZCS	Zero Crossing Detector

Chapter 1: INTRODUCTION AND OVERVIEW

1.1 INTRODUCTION

There has been an enormous increase in the global demand for energy in recent years as a result of industrial development and population growth. Supply of energy is, therefore, far less than the actual demand in many developing countries and fast-growing economies like India. This leads to energy crisis which is apparent in frequent load shedding, power failure, closure of factories, man-hour loss and decrease in production. As per OECD (Organization for Economic Cooperation and Development) statistic global energy demand will be about 30 percent higher in 2040 compared to 2010. On the other hand, the economic growth and advancement in living standard demand more energy. Besides coal, oil and natural gas are major sources of primary energy which increase the level of carbon dioxide (CO2) emissions every year. Thus energy should be used more efficiently to expand new technologies and emerging sources.

EMDS (Electrical Motor Driven Systems) are the single largest electrical end-use, consuming more than twice as well as lighting, the next largest end-use. As per the IEA (International Energy Agency) statistic, EMDS share 46% of total global energy consumption. The largest proportion of motor electricity consumption is attributable to mid-size motors with output power of 0.75 kW to 375 kW. Motors in the mid-size range are most commonly found in industrial applications, but they are also widely used in commercial applications, infrastructure systems and, less often, in the residential sector. In general, their main applications are mechanical movement, compressors, pumps and fans.

Many different motor technologies and design types are available, but asynchronous induction motors (IMs) are most frequently used and consume the most energy. It makes necessary to pay attention on efficiency of the induction motor drive. At present, most OECD (Organization for Economic Cooperation and Development) and many non-OECD economies impose MEPS (Minimum energy performance standard) on asynchronous mid-size AC motors. Several countries have passed laws which have set deadlines by which date all motors sold in that country should comply with a specific IE class. According to IEC (International Electrotechnical Commission) efficiency standard IE1, IE2 and IE3, minimum efficiency required for 1.5KW AC motor are 77.2%, 82.8% and 85.3% respectively. The efficiency target a motor has to reach is dependent on the motor size and larger motors need to meet higher efficiency standards. It enforces the requirement of inverter fed complex control system (VFD and field oriented control, DTC etc.) to be incorporated with induction motor to meet the efficiency standards. Consequently it increases the cost and complexity of

the EMDS that is why all countries have not imposed the laws for efficiency standards of EMDS.

The present scenario obligates the research and development of new alternate technology for the electric motor drive. EC (Electronically commutated) motors technology offers a very high efficiency performance compared to asynchronous AC motors. These types of motor ensure the efficiency higher than the class IE3 (Premium efficiency standard) and further improvement is also possible with the new design and control techniques. Motors in this category cannot run direct on AC or DC supply as it always require synchronized switching of phase current with respect to rotor angle. Thus cost of motor and drive (converter plus controller) both should take under consideration while comparing with asynchronous AC motor.

Major types of EC motors employ costly rare-earth-magnet mounted on their rotor or stator. It increases manufacturing cost and complexity which results in cost of EMDS becomes more than twice of that of conventional motor drive which prevents use of such motor technology as a solution for energy efficient drive. Situation seems that the best alternative to the asynchronous AC motor which can provide energy efficient solution in a cost-effective manner is nothing but a SRM (Switched Reluctance Motor) as it does not required rare-earth-magnet unlike other EC motors.

Likewise, a quest for energy efficiency has promoted development of SRM drive. Major attractive features of SRM are simple mechanical structure, low manufacturing cost, flexibility in control, adjustable torque speed characteristics, higher efficiency, high torque weight ratio and constant power output capability over wide speed range. The switched reluctance motor has been used in many commercially adjustable speed applications. However, the SRM suffers from the problem of torque ripples and audible noise which prevents its use in high performance application. Main aim of this thesis is to provide distinctive contribution in the development of SRM technology by the exercise of independent critical power of knowledge, investigation and logical coherence.

1.2 APPLICATIONS OF SRM DRIVE

The SRM is suitable for the industrial and domestic fans, blowers, compressors, pumps, textile spinning, vacuum cleaner, washing machines, automotive application like power steering and wiper and electric vehicle propulsion system.

The web based survey has been carried out to explore the existing acceptance and importance of the SRM drive for the industrial and domestic applications [13, 14]. Emerson Motor Technology, Rocky Mountain Technology (RMT), Emorton, Ametek, Nidec SR Drive (NSRD), Marvik Motors and Radio Energie are the providers of the SRM technology.

The Maytang Neptune used the SRM developed by the Emerson Motor Technology for the washing machine. The single motor is used for spin, dry and wash cycle, which forced the competitors to rethink their inverter-driven induction motor based design. The Emerson Motor Technology also develops motors up to 100 to 200 hp. The SRMs are utilized in high-power (45, 75, and 120-kW) variable-speed screw compressors from CompAir UK Ltd and in off-road equipment such as the LeTourneau L1350 loader which uses an Emerson B40 300-kW SRM to drive each of its four wheels.

RMT is designing range(100KW to 10MW) of SRMs since 1994. The 7.5KW SR generator has been utilized in smaller wind turbines, where minimal drag and non-cogging performance of a generator (with proper current control) becomes advantageous, enabling operation in low winds. It has been reported that the efficiency of the SR generator reaches 95.5%, or higher, at low speeds. The company has built and tested SR machines up to 300 kW and speeds to 120,000 rpm.

The CG Drives & Automation (former Emotron) utilized the SRM technology for Mining machinery where extreme motor speeds are needed or acoustic noise of uncompensated SR motors is tolerable. The company is reputed market leader in Europe for rotary heat exchangers, for which SR technology provides a solution at 400 rpm nominal speed without the need for a gearbox.

Ametek Commercial Motor utilized the SRM for blower unit with integral controls and cooling fan in an unusually compact package. Size reduction was a basic design goal versus a prior brush dc motor-based system.

Nidec SR Drives Ltd (NSRD) is developing range of product utilizing SRM drive. The area of application includes aerospace, automotive, consumer appliance, mining, pumps and compressor and traction. The product includes washing machines, vacuum cleaner, ash-grab crane, screw air compressor, high pressure pump, train air conditioning, powered wheel-chair, sliding door operator, rail locomotive, streetcar tram, battery powered vehicle and other.

Mavrik Motors produces 2 and 3-phase SRM, as well as higher phase designs. It includes blowers for heating appliances and commercial floor-cleaning equipment. Combining soft start with variable-speed SRM enables one floor-care unit to do the job of separate scrubbing, polishing, and burnishing machines.

Radio-Energie (Marcoussis, France) manufactures SRMs (0.7 to 2kW) and digital controllers for low-voltage (24 V dc) forklift trucks, light vehicles, etc. The motor and drive provide 4-quadrant operation with regeneration available during braking. The efficiency is reported up to 80% at 3000rpm.

The SRM based electronic throttle controller is used in the Jaguar S V-6 and V-8 automobile engines.

1.3 LITERATURE REVIEW

The first reference to the term Switched Reluctance Motor was introduced by the Nasar in IEE proceeding of 1969. Even so the first recognizable SRM were built over 175 years ago by Davidson, which used it as traction drive for an electric locomotive in 1838. Lawrenson et al [84], Dawson et al [36], Ray et al [123] and Davis et al [35] explored the potential of SRM drive and explained the fundamentals of machine's nonlinearity and torque producing mechanism during 1980's. As the SRM is a nonlinear, multivariable and complex coupling system, the development of the SRM drive is a difficult task without using the modern numerical calculation technology, power electronics technology, numerical control technology and computer aided design.

Simulation of the system is an important tool and state-of-the-art in design, testing and experimental realization however, mathematic modelling of SRM seems to be complex because of non-linear motor magnetic characteristics. Several modelling techniques have been proposed by the researchers in the past which include both linear and non-linear modelling of the motor [82, 85, 104, 105, 144, 146]. The look-up table based approach is an outcome as very accurate non-linear modelling technique [79, 85, 100]. However it requires large amount of data to store and to conduct experimental workout for collecting the magnetic data prior to modelling. On the other hand, the accuracy of the modelling depends on the method used for obtaining the magnetic data and accuracy of the measuring instruments. The efforts have been made by the researchers to represent a magnetic non-linearity of the motor in term of mathematical equation with the help of exponential or trigonometric functions [104, 105, 144, 146]. These methods require huge calculation to determine number of unknown parameters from the geometrical parameters of the motor and numbers of turns per phase. The inductance based modelling technique is proposed in the literature which considers non-linear relation of inductance-current-angle to represent a magnetic non-linearity of the SRM, instead of flux-current-angle relation [48, 94]. This method requires less magnetic data to model a motor and gives reasonable accuracy even in saturation region. However the simulation of the inductance based model is somewhat slower than other modelling techniques because it involves larger derivative terms.

Many kinds of converter topologies are available for the SRM [32, 35, 55, 79, 81, 99, 100, 123, 155] which include asymmetric bridge converter, one-switch per phase type converters, one sharing switch type converters and bifilar converter. The selection of the converter depends on the cost, control scheme and performance requirement. The comparative evaluation of various converter topologies has been done [79, 155].

The converter for SRM needs to provide the unidirectional current to the phases which must be synchronized with the rotor position rotor position. The magnitude and the wave

shape of the current are regulated in order to meet the torque and speed requirements. Furthermore, the circuit needs to supply negative or zero voltage for freewheeling operation. Because of unidirectional current requirement, only one switch per phase is needed to fulfill the requirement of the converter for SRM. Figure 1.1 shows different types of converter topologies based on single switch per phase. The difference between them is a voltage that appears across phase during freewheeling period.

One switch and one diode is associated with each phase in the converter topology shown in Figure 1.1(a). The positive voltage V_{dc} is applied across the phase winding when the switch is ON. When switch is turned off, the phase current freewheels through the diode and the diode forward voltage drop appears across the phase. The time required for the freewheeling is too long as the diode forward voltage drop is too small. This will reduce the phase conducting angle. The main advantages of this configuration are low cost and simple structure.

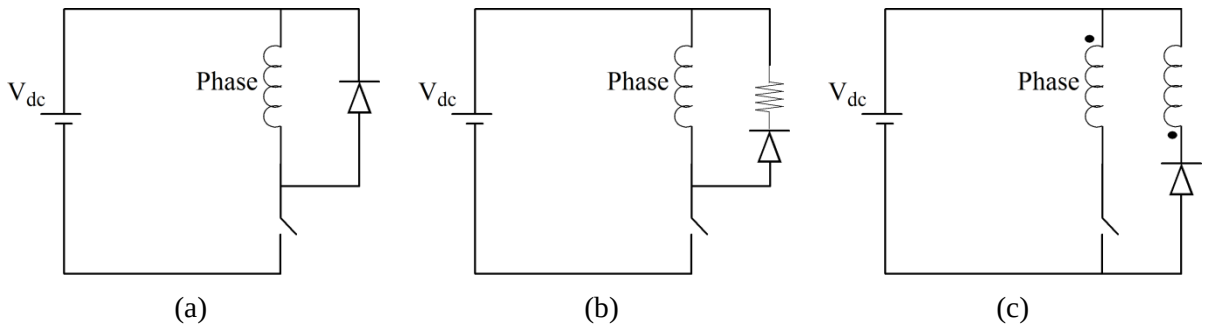

Figure 1.1 One switch per phase type converters

An extra resistance is added in series with the diode in the circuit shown in Figure 1.1(b). The purpose is to reduce the freewheeling period by increasing the negative voltage applied to the motor phase. However, the reverse voltage decreases with the current which reduces the effectiveness of the method to fulfill the purpose. Furthermore, conduction loss in the resistance reduces the system efficiency.

In the circuit configuration shown in the Figure 1.1(c), bifilar winding is used. When the switch is turned off, the current in the primary winding is transferred to the secondary winding and freewheels through the diode. Therefore, there is a negative voltage Vdc applied across the winding during freewheeling period. This circuit can achieve low loss and small freewheeling period however, the switch having higher voltage rating is required because double input voltage is applied when switch is off.

In order to increase the reliability and realize certain control strategies, more than one switch per phase type converters are used. The asymmetrical bridge converter topology, as shown in Figure 1.2, employs two switches and two diodes per phase. This converter is similar to the conventional dc-ac converter except that the phase winding is in series with the

phase switches. This converter provides high efficiency, reliability and control flexibility. The upper and lower switches can be controlled independently to realize different control schemes like soft chopping and hard chopping. In addition, this converter can provide maximum regenerative braking capability and equal performance in forward and reverse directions. Also, there is no protection circuit needed to prevent shoot-through faults because the switches on each phase conduct simultaneously. All these advantages make the asymmetrical bridge converter popular in SRM application.

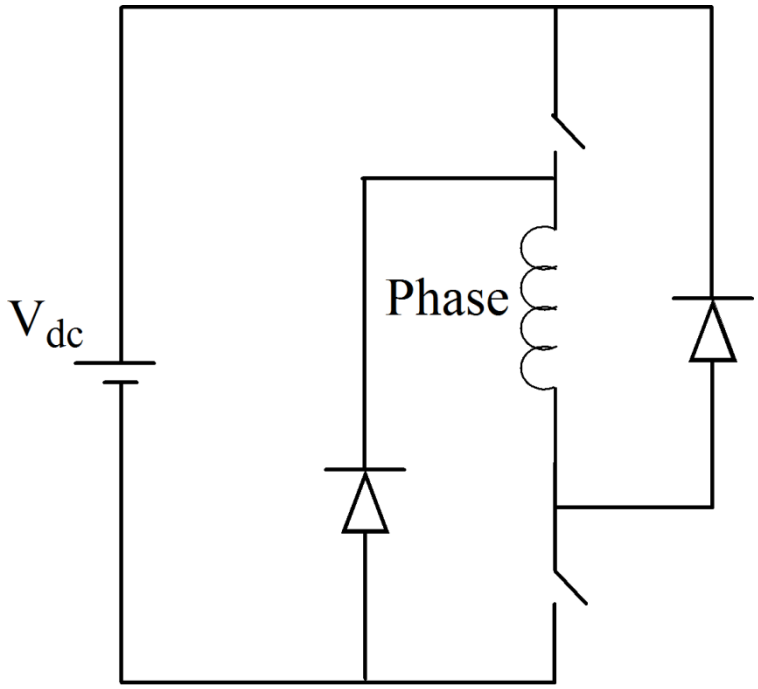

Figure 1.2 Asymmetric bridge converter

With the asymmetrical bridge converter, total of six switches and six diodes are required for three phase SRM. However the requirement of the semiconductor components can be reduced with the converter with shared components. The arrangement of converter with shared component is shown in Figure 1.3, which shows that only four diode and four switches are required for three phase motor. The common (upper) switch and diode operate all the time, while the other lower switches commutate the phase current in sequence. This circuit can realize the current control scheme with using only one current sensor as the main switch carries the current flowing through phase winding all the time. This circuit can save components, but, it lost the fault-tolerance characteristics as of the bridge converter.

Furthermore, high switching frequency brings the problem of Electromagnetic Interference (EI) and overheating of the semiconductor devices. Several soft-switching techniques have been reported in literature to achieve the zero voltage-turn-on condition of the main switch; however employing these techniques increases the cost and number of components. Likewise, many of converter topologies are available and more sophisticated combinations of components is possible to suite the specific application.

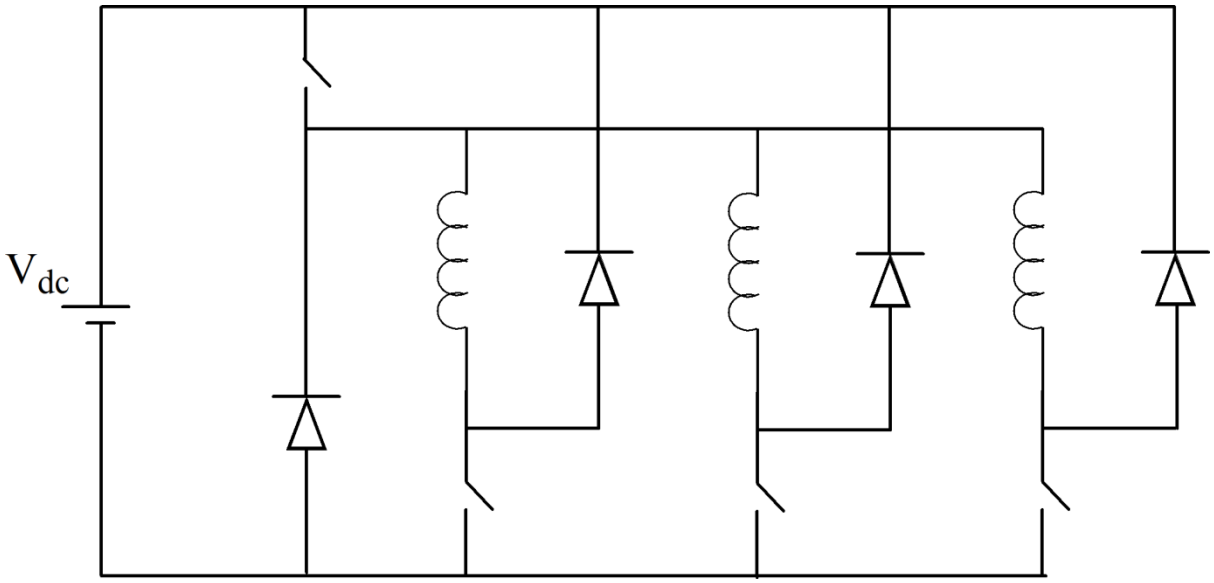

Figure 1.3 Converter with shared component

To control the speed and torque of the SRM, conventional speed PI controller can be used [20, 100]; however the process of designing the controller is complex compared to the conventional motor due to non-linear magnetic characteristics of the SRM. The phase current control can be achieved by the simple hysteresis current control or PWM control but, even for the constant current the torque of the motor is not constant. The torque of the SRM is a function of the phase current as well as the rotor angle. Thus for high performance application of the SRM drive, sophisticated speed controller needs to be developed rather that the conventional PI controller. The goal of the controller is not only to adjust the magnitude and shape of the current, but it should also control the commutation angles (turn-ON and turn OFF angle). The problem of high-performance SRM drive is investigated in [67]**.** A state feedback control algorithm is proposed which compensate for all non linearity and decouples the effect of stator phase current in the torque production. Commutation angle also affects the efficiency and average torque production. The optimum efficiency can be achieved by adjusting the commutation angle such that the phase current reach at the sufficient level at the unaligned position and it decays to zero at the aligned position. The angle control scheme is proposed in [145] to obtain optimal efficiency for the constant speed drive. However, to smoothen the torque transfer and to increase the average torque, it is required to increase the dwell angle. Thus angle control scheme designed to produce optimum torque output cannot achieve optimum efficiency. Even so the efficiency of the SRM is comparatively higher than the conventional DC and AC machines. Pollock et al [116], Husain [63,64], Rahman et al [119, 120] Panda et al [113], Changhwan Choi et al [34], Barrass et al [12] and Cheok et al [33] proposed new techniques to optimize control & torque ripple reduction for high performance SRM drive. Mir S at al [106], Rahman et al [119],

Henriques et al [61] and Panda S K et al [114] used the fuzzy and artificial neural networks (ANN) which also improves the control system of SRM drive. The problem of performance optimization is investigated in [93]. The online commutation control scheme is proposed to achieve the balance between energy efficiency and torque ripple criteria.

The major issue of the SRM is high torque ripples which tend to produce higher audible noise. The simplest way to reduce the torque ripples is to choose higher numbers of stator/rotor pole configuration. But it increases the cost of switching devices as number of phase increases. The magnetic non-linearity of the motor is responsible for the pulsating nature of the motor torque [36, 84]. In conventional motor (DC) the torque is directly proportional to the current or its transformed component (q-axis in AC motors). However, the three dimensional non-linear relation of flux-linkage, phase current and rotor angle exists in the SRM. Thus the torque is a non-linear function of the phase current as well as rotor angle. Even for the constant current, torque is varying with the rotor angle.

The most effective electronic approach of torque ripple minimization is to store torque-current-angle relation as three-dimensional lookup table, and thus optimum current can be derived for the rotor angle and required torque. The torque-ripple-minimizing technique is proposed in [124] and is applicable for the wide-speed-range. The commutation algorithm is speed dependent and does not require pre-calculated stored data. The method requires large amount of static data which can be derived experimentally. The Neural-network based torque ripple minimization techniques appeared in [97, 119, 127]. These techniques generate appropriate phase currents using neural networks in response to a desired torque. The adaptive fuzzy control scheme for torque ripple minimization is proposed in [106]. The controller is robust to the error in position information which allows in-expensive low resolution position sensing arrangement. Review of the torque ripple minimizing techniques has appeared in [63]. The approach of optimized shaping of the phase current waveform has been reported in [30, 138]. The torque sharing function (TSF) base methods is discussed in [34]. The TSF defines the phase torque produced in each phase so that the overall torque becomes the desired constant torque by applying appropriate phase current. The TSF method provides a simple computation procedure and it is also capable to consider other control objectives such as efficiency optimization and voltage requirement. The efforts have been made to apply the philosophy of Direct-torque-control (DTC) technique of the conventional AC motor to control the torque and speed of the SRM [33]. DTC is a well established control principle in which stator voltage vector is selected according to the difference between reference torque and stator flux linkage and actual value. However AC motors have a linear characteristics and three-phase balance sinusoidal excitation in contrast to SRM having non-linear characteristics and non-linear excitation. Furthermore the phases are independently excited. Thus the DTC of the conventional AC motors cannot

apply to the SRM as usual. The DTC method for the SRM is derived from the analysis of non-uniform torque characteristics. In the scheme, torque is directly controlled through the control of the magnitude of the flux linkage and the rate of change of the stator flux vector. The scheme directly regulates the torque output of the motor within a hysteresis band and thus provides the ripple free torque. The method is simple and easy to implement as it does not require a mathematical model or knowledge of motor parameters.

Another, area of research which is in current attention is to eliminate the mechanical position sensors from the SRM drive by means of sensorless control. The idea is to improve the reliability to operate in harsh environment and reduce the overall envelope of the SRM drive. Many types of the sensorless control techniques have been developed in the past which includes state observer [43, 91], active probing [4, 58], modulated signal injection [40, 100] and current waveform monitoring [50, 111] and flux-linkage based [92] method. But none of them is suitable for the wide speed range without putting limits on the performance of the drive.

1.4 SCOPE OF WORK AND AUTHOR'S CONTRIBUTION

The objective of this thesis is to investigate the performance of the Switched Reluctance Motor (SRM) drive for the variable speed application. It also covers the analysis of modelling techniques, control algorithm and sensorless control schemes.

Literature review shows that there are many linear as well as non-linear modelling techniques for the design and control of the SRM having some advantages and disadvantages. Several vital non-linear techniques have been exemplified in the present work which includes flux-linkage based method, the method based on analytical reasoning and inductance based modelling technique. All three techniques have been analysed and compared in this investigation. The MATLAB simulation tool is used in this work for the modeling and simulation of the SRM. The embedded function is designed in this work to model the non-linearity of the SRM.

Furthermore, the flux-linkages based modeling technique is found most accurate amongst all, which is designed and investigated in detail in this work with the help of MATLAB 'simulink' and "simpowersystem" library. The physical modelling technique is proposed in this work where the variable reluctance characteristic of the motor is utilized to derive the non-linear model of the switched reluctance motor. This method needs only few geometrical parameters and turns per phase information of the motor. Furthermore, the 3-Dimensional (3D) visualization effect is added to the physical model of the motor with the help of virtual reality tool box of the MATLAB, which extends the capabilities of the simulink software into the world of virtual reality graphics. In addition the high grade real-time

simulation of the complete SRM drive is developed with the help of Opal's RT-Lab technology, which eliminates the issue of model latency present in CPU based simulation.

The past investigation and development of the torque-ripple-minimization techniques made a significant achievement in performance improvement of the SRM drive and efforts are also made to reduce the complexity and cost of the implementation. Although, to produce the ripple-free torque through the firing-angle control scheme, require to compromise with the efficiency and/or average torque production. On the other hand, in many industrial applications, higher phases SRM and/or phase overlap switching can provide efficient performance where the small amount of ripple in torque is tolerable. The scope of this thesis is to investigate the performance of the SRM drive to serve the new industrial as well domestic application or to replace the excising one, for the quest of energy efficiency.

The low-cost switched reluctance motor drive is developed and investigated in the present work which employs multi-phase excitation to reduce the torque ripple and low-frequency PWM controller for higher converter efficiency. A literature survey shows that one switch per phase solution is suitable for the low cost application but it prolong the freewheeling period. The split DC converter is developed in the proposed work which offers one switch per phase configuration as well as speed up the freewheeling process by applying negative voltage. The ac small signal modelling technique is proposed for linearization of the SRM model and accordingly speed PI controller is designed. The performance of the proposed drive is investigated for the efficiency, noise and torque ripple, for which the prototype model of SRM drive is developed in the laboratory. The performance of the SRM drive is investigated using the developed simulation model and compared with experimental result. Furthermore, the effect of speed, load torque and PWM frequency on the torque ripple of the SRM is investigated.

An extensive review of the sensorless control schemes is carried out in this work. The flux-linkage based sensorless method is investigated and analysed in detail in the present work with the simulation and experimental studies. The fixed turn-off method, based on the flux-linkage characteristics of the motor, is proposed which offers simple and low-cost solution for the general purpose drive. The performance of the ANN technique is investigated to estimate the continuous rotor position form the flux and current. An analytical sensorless method is proposed in the present work which reduces the computation burden as well the requirement of the storage space and produces the reasonable accuracy of the estimation.

The performance of the current gradient sensorless method (CGSM), that does not require any prior knowledge of the motor magnetic characteristics, is investigated in detail in this work. The modified CGSM is proposed, which eliminates the requirement of the PLL and

improves the stability of the system. Prototype setup of the sensorless SRM drive is developed in the laboratory and its performance is investigated under the open-loop as well as closed-loop condition.

Further, the performance of the SRM is investigated for the low power in-wheel electric vehicle system. Also the feasibility of the electric braking with the fixed angle controller is explored.

1.5 THESIS ORGANIZATION

The rest of thesis is organized as follow:

The theory and operation of SRM is described in Chapter 2. Different schemes of current and speed control are discussed.

The non-linear modelling techniques of the SRM are compared in Chapter 3. The physical modelling technique is explained and run-time 3D-visulization model is developed. The real-time simulation of the complete SRM drive based the hysteresis current controller and speed PI controller is presented at the end.

The low-cost SRM drive based on one-switch per phase type converter and low-frequency PWM control is implemented and analysed in Chapter 4. The performance characteristic of the proposed SRM drive is derived from the experimental and simulation results. The merits and drawbacks of the SRM drive are summarized at the end.

Different sensorless control techniques of the SRM drive are investigated in Chapter 5. The flux-linkage based scheme of rotor position estimation is described in detail. The flux-linkage based sensorless control techniques are proposed which includes fixed-turn-off angle scheme, artificial neural network (ANN) based scheme and analytical rotor position estimation.

The sensorless techniques which do not required any prior knowledge of the motor magnetic characteristics are explained in Chapter 6. The chapter covers the investigation of CGSM for low-cost SRM drive and development of the modified CGSM with the simulation and experimental studies.

The performance of low-frequency PWM controlled SRM drive is investigated to serve the battery operated low-power electrical vehicle system in the Chapter 7.

Finally Chapter 8 draws the conclusion from the work done in this thesis and discusses further research possible in the future.

Chapter 2: FUNDAMENTAL OF SRM DRIVE

Fundamental theory and operation of the SRM is described in this chapter. An equivalent circuit of the SRM is obtained from the phase equation. The simplified torque equation is derived by neglecting the mutual inductance of the phase. The basic closed-loop control structure of the SRM drive is discussed in this chapter which includes fundamentals of asymmetric bridge converter, current control schemes, methods of speed/torque control and angle control schemes.

2.1 CHARACTERISTICS OF THE SRM

The structure of the SRM is simple to manufacture which consists of laminated yoke, stator and rotor. Both the stator and rotor have salient pole structure having different number of poles. A typical geometry of the motor having 6 stator pole, 4 rotor pole normally termed as 6/4 pole SRM is shown in Figure 2.1. The stator winding is a wound field coil as in DC motor which forms the phase per pole-pair. However, the rotor has neither coils nor permanent magnet attached to it.

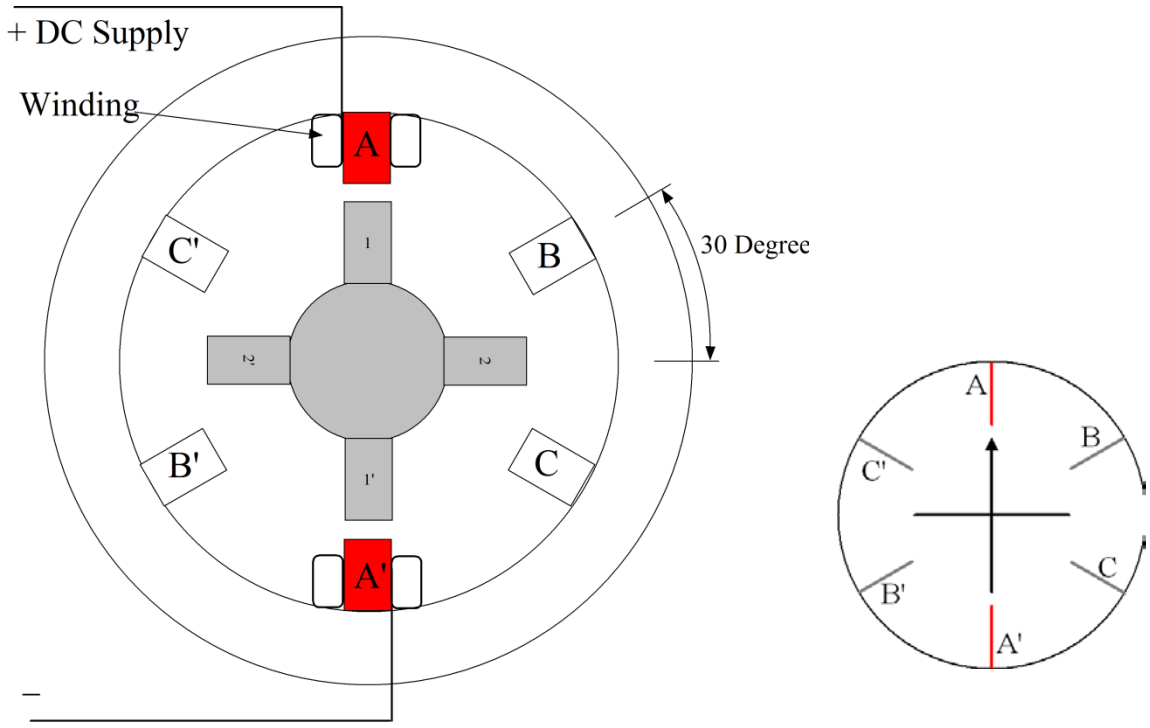

(a) (b)

Figure 2.1 Geometry of 6/4 pole three phase SRM

The torque production mechanism of the SRM is similar to that of stepper motor because the energized stator coil serves as electromagnet that attracts the nearest rotor pole. The main difference between the SRM and stepper motor is that the phase excitation of the SRM is always in synchronism with the rotor position which results in continuous

rotation at all speed. It requires the continuous rotor position monitoring and control of the switching of the phase. The SRM is generally designed for the desired power and efficiency rather than step accuracy as in case of stepper motor. The motor torque and thus direction of rotation are independent of direction of phase current, but the sequence of phase excitation governs the direction of speed. The developed motor torque depends on the magnitude of current and angular rotor position.

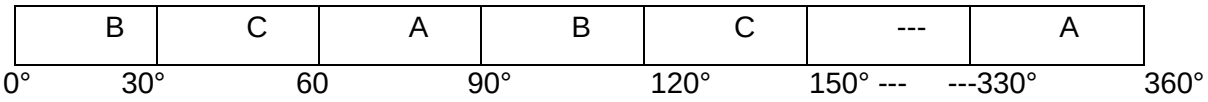

Figure 2.2 Phase energization sequence

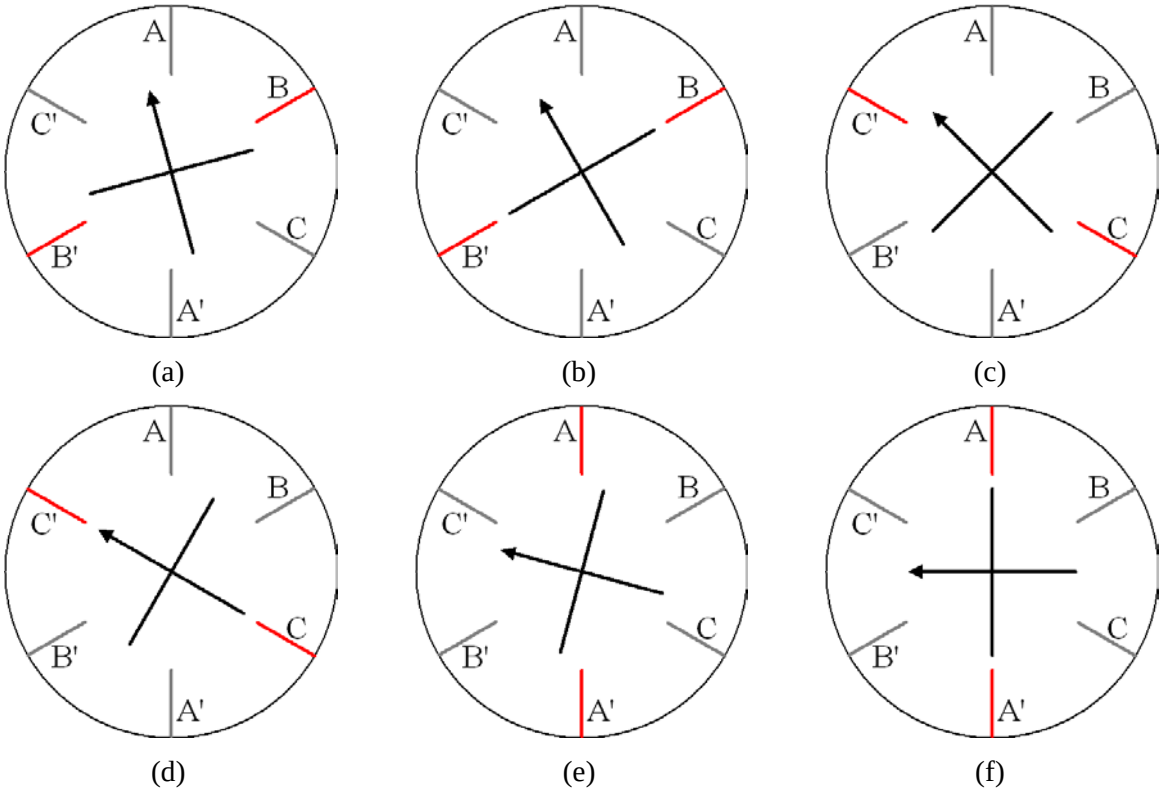

Figure 2.3 Demonstration of operation with sequence of phase excitation at an angle (a) 15° (b) 30° (c) 45° (d) 60° (e) 75° (f) 90°

The position of the rotor shows in Figure 2.1 is considered as reference where rotor poles are aligned with the stator pole pair A-A'. Figure 2.1(b) shows the line-view of the SRM which represents rotor-stator poles and phase excitation. The sequence of phase excitation with respect to rotor angle can be represented as shown in Figure 2.2 which produces torque for anti-clock wise rotation. The synchronized operation of the motor is shown in Figure 2.3. It is to be noted that 90° of rotation represents a complete electric cycle. The mid position, that is 45° treated as unaligned position respect to pole pair AA' (Phase-A). Each phase remains ON for the period of 30° which represents dwell angle and can be expressed as "$\theta_{dwell} = \theta_{OFF} - \theta_{ON}$", where θ_{ON} and θ_{OFF} represents the turn-ON and turn-OFF instant of

the phase excitation. The total number of stator-rotor poles and number of phases decide the minimum dwell angle of the motor.

Considering one cycle of operation, the condition for the phase excitation can be expressed as-

Phase-A ON $60° > \theta > 90°$

Phase-B ON $30° > \theta > 60°$ and

Phase-C ON $0° > \theta > 30°$

where 'θ' is the rotor position in mechanical degree. Considering the individual reference rotor position for the each phase, i.e when rotor pole is aligned with their respective phase (pole pair), the condition of the phase excitation becomes,

Phase ON $60° > \theta_K > 90°$

where θ_K is the rotor angle for the respective phase and accordingly K=A,B or C. There is phase difference of 30° amongst reference rotor position of each successive phase and can be expressed as-

$\theta_B = \theta_C + 30°$

$\theta_C = \theta_A + 30°$

$\theta_A = \theta_B + 30°$

The performance of the SRM is altered with the degree of phase commutation, therefore the following commutation parameters of the motor are specified to get the desired performance.

Turn-On angle = θ_{ON}

Turn-OFF angle = θ_{OFF} and

Dwell angle = θ_{dwell}

Furthermore, the inductance profile of the SRM gives the better understanding to select the commutation parameters. Figure 2.4 shows the variation of phase inductance with respect to the rotor angle, for the entire cycle of operation. Phase inductance increases as rotor moves toward aligned position from the unaligned position, and it reduces as rotor moves from aligned to unaligned position. The tip at the aligned position reflects that both the rotor and stator pole arcs are same, while for the unequal pole arcs, the inductance profile will became flat near aligned position. The flat area near unaligned rotor position is due to large airgap which is generally not present in the motor with the higher pole configuration for example 8/6 pole. The motor develops the positive torque during rising inductance profile only, while it develops the negative torque during the falling inductance period. However, it does not signify that the electromagnetic force produce is zero during the aligned and unaligned rotor position. The torque developed by the Phase-A, as a function of rotor angle is shown in Figure 2.4 considering constant current throughout the cycle. It shows that the torque produced during rising inductance period is such that it tends to move

the rotor in the positive (anti-clockwise) direction, while the negative torque forces the rotor to rotate in reverse direction. At the fully aligned and unaligned rotor position, tangential component of the electromagnetic force is zero while vertical component of the force produced holding torque.

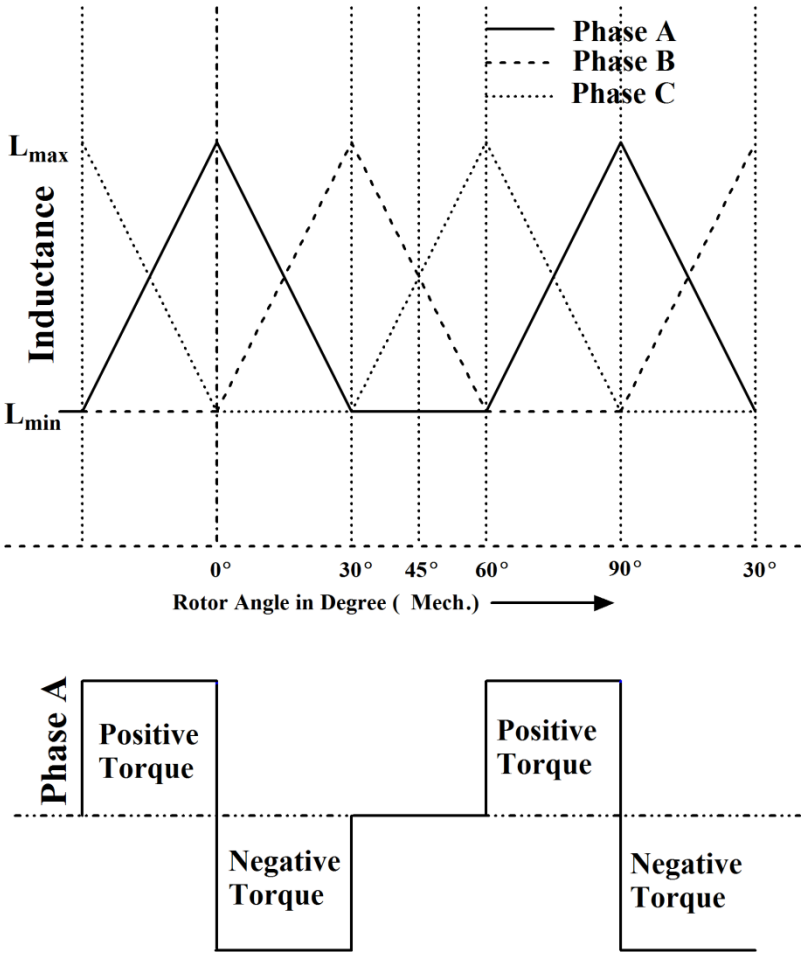

Figure 2.4 Inductance profile of 6/4 pole SRM

The phase current cannot rise or fall instantaneously due to phase inductance which necessitates advance excitation and commutation of the phase prior to the starting of rising inductance period. The advance phase excitation ensures the required magnitude of current to produce the desired torque, while advance commutation prevents the production of negative torque.

2.1.1 Topology of Switched Reluctance Motor

The SRM offers wide variety of aspect ratios and salient pole topologies. Some of the well known topologies are shown in Figure 2.5. Each topology has different advantages and disadvantages, thus selection of the SRM configuration depends on the application and requirement.

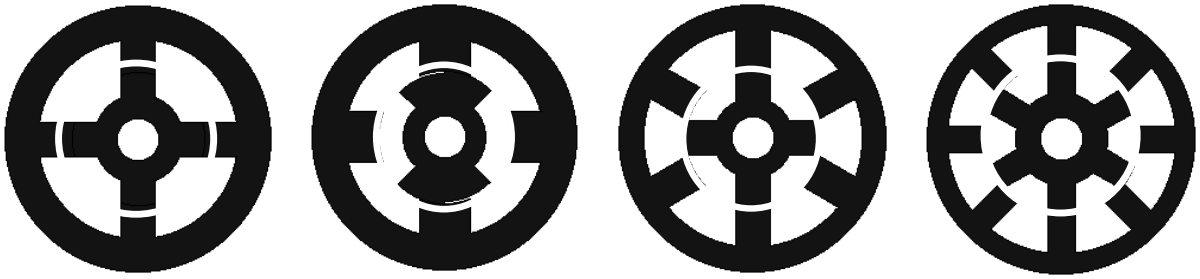

(a) (b) (c) (d)

Figure 2.5 SRM topologies (a) Single Phase (b) Two phase (c) Three phase (d) Four phase

Figure 2.5(a) shows the simplest SRM structure having 4/4 pole and single phase winding which offers advantage of fewest connections between machine and electronics. The high torque ripple and inability to starts at all rotor position are the main drawbacks. This topology is suitable for high speed application, but starting problem prevents its use.

Figure 2.5(b) shows the two phase SRM having 4/2 pole. The problems of starting can be overcome by stepping the air-gap, or providing asymmetry in the rotor poles. This topology may be attractive where the cost of winding connections is important. However, it also suffers from the problem of high torque ripple.

The SRM topology shown in Figure 2.5(c) offers simplest solution to starting and torque ripple with the 6/4 pole, three phase configuration.

The 8/6 pole four phase topology, shown in Figure 2.5(d), can be used for reducing torque ripple further. Five- and six-phase motors offer better torque ripple reduction compared with four-phase and three-phase. However the large number of power devices and connections limit the application of higher phase SRM.

2.1.2 Equivalent circuit of SRM and torque equation

The linear analytical model of the SRM can be represented by differential equations which includes voltage equation, motion equation and electromagnetic torque equation. The equivalent circuit of the motor represents voltage balance equation of the phase which consists resistance and inductance. The effect of leakage flux and mutual coupling of phases are neglected in the developed model as they are negligible in SRM.

The applied voltage to a phase is equal to the sum of the resistive voltage drop and the rate of change of flux linkages and is given as;

$$V_{ph} = R_s i + \frac{d\psi(\theta, i)}{dt} \tag{2.1}$$

where R_s is the resistance per phase, and ψ is the flux linkage per phase. Flux linkage is a product of inductance of the phase and phase current as mutual inductance is neglected.

$$\psi = L(\theta, i) \cdot i \tag{2.2}$$

where L is the inductance of the winding and depends on the rotor position and phase current. The phase equation can be modified as-

$$V_{ph} = R_s i + \frac{d\{L(\theta,i)\cdot i\}}{dt} = R_s i + L(\theta,i)\frac{di}{dt} + i\frac{d\theta}{dt}\cdot\frac{dL(\theta,i)}{dt} = R_s i + L(\theta,i)\frac{di}{dt} + e_b \tag{2.3}$$

It shows that, the applied phase voltage is balanced by the resistive voltage drop, inductive voltage drop, and induced emf. The induced emf in phase winding can be expressed as-

$$e = K_b \omega_m i \tag{2.4}$$

$$\omega_m = \frac{d\theta}{dt} \tag{2.5}$$

$$K_b = \frac{dL(\theta,i)}{d\theta} \tag{2.6}$$

where ω_m is angular velocity and 'K_b' is the emf constant.

Using equations (2.1) to (2.6), the equivalent circuit of the SRM can be derived shown in Figure 2.6.

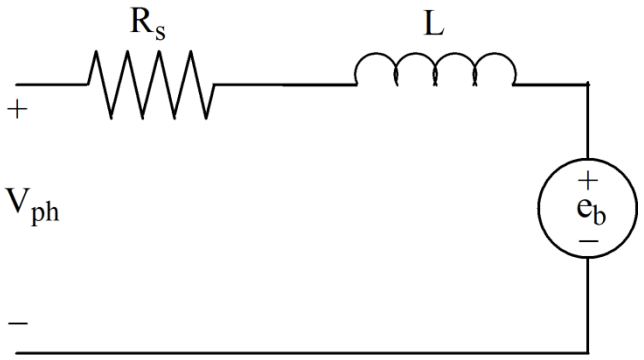

Figure 2.6 Equivalent circuit of SRM

Multiplying the voltage balance equation with the current results in instantaneous input power expressed as-

$$P_i = R_s i^2 + i \cdot \frac{d\psi(\theta,i)}{dt} \tag{2.7}$$

where first term on the right-hand side represents copper loss in the winding. Thus second term on the right-hand side should represent the sum of mechanical power output and power stored in the magnetic field. Therefore,

$$i \cdot \frac{d\psi(\theta,i)}{dt} = \frac{dW_m}{dt} + \frac{dW_f}{dt} \tag{2.8}$$

where dW_m/dt is the instantaneous mechanical power and dW_f/dt is the power stored in the magnetic field. The W_m is the mechanical energy and W_f is the field energy as the

power is defined as rate of change of energy. The mechanical power is a product of torque and speed, therefore,

$$\frac{dW_m}{dt} = T\omega_m = T\frac{d\theta}{dt} \tag{2.9}$$

Equation (2.8) can be re-arranged as below:

$$i \cdot \frac{d\psi(\theta,i)}{dt} = T\frac{d\theta}{dt} + \frac{dW_f}{dt} \tag{2.10}$$

Simplifying equation (2.10) for the torque developed by the motor,

$$T(\theta,\psi) = i(\theta,\psi) \cdot \frac{d\psi}{d\theta} - \frac{dW_f(\theta,\psi)}{d\theta} \tag{2.11}$$

For the constant flux, the torque developed can be expressed as,

$$T = -\frac{dW_f}{d\theta} \tag{2.12}$$

It is desirable to express the torque in term of current rather than energy. The torque equation is first represented as the co-energy Wc instead of field energy Wf, and then expression for torque is derived in term of current. Figure 2.7 shows graphical interpretation of the magnetic field energy and co-energy. The magnetization curve defines current as a function of flux for the constant rotor angle as shown by the shaded area in Figure 2.7(a). The field energy expression can be derived by integrating (2.10) at constant speed, which gives-

$$Wf = \int_0^{\psi} i(\theta,\psi)d\psi \tag{2.13}$$

To define the magnetic field co-energy, let the magnetization curve define flux as a function of current as shown by shaded area in Figure 2.7(b). Mathematically it can be represented as-

$$Wc = \int_0^{i} \psi(\theta,i)di \tag{2.14}$$

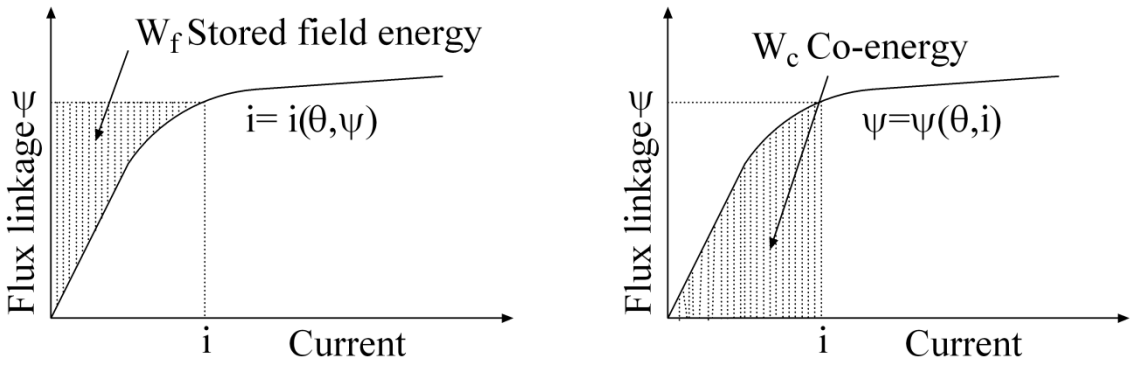

(a) (b)

Figure 2.7 Graphical interpretation of (a) magnetic field energy (b) co-energy

Sum of W_f and W_c represent a total area, and thus,

$$W_f + W_c = i \cdot \psi \tag{2.15}$$

Differentiating both side gives-

$$dW_f + dW_c = id\psi + \psi di \tag{2.16}$$

which simplified for W_f as-

$$dW_f = id\psi + \psi di - dW_c \tag{2.17}$$

where the differential co-energy can be written in term of its as partial derivative as-

$$dWc(\theta, i) = \frac{\partial Wc}{\partial \theta} d\theta + \frac{\partial Wc}{\partial i} di \tag{2.18}$$

From (2.11), (2.17) and (2.18) and assuming constant current, the torque can be derived as-

$$T = \frac{dW_c}{d\theta} \tag{2.19}$$

Neglecting the magnetic saturation, flux can be derived as-

$$\psi = L(\theta) \cdot i \tag{2.20}$$

where the motor inductance is a function of rotor angle. The magnetic co-energy can be derived by integrating flux as-

$$Wc = \frac{i^2}{2} L(\theta) \tag{2.21}$$

Thus simplified relation of torque and current is given by-

$$T = \frac{i^2}{2} \frac{dL}{d\theta} \tag{2.22}$$

2.2 SRM DRIVE SYSTEM

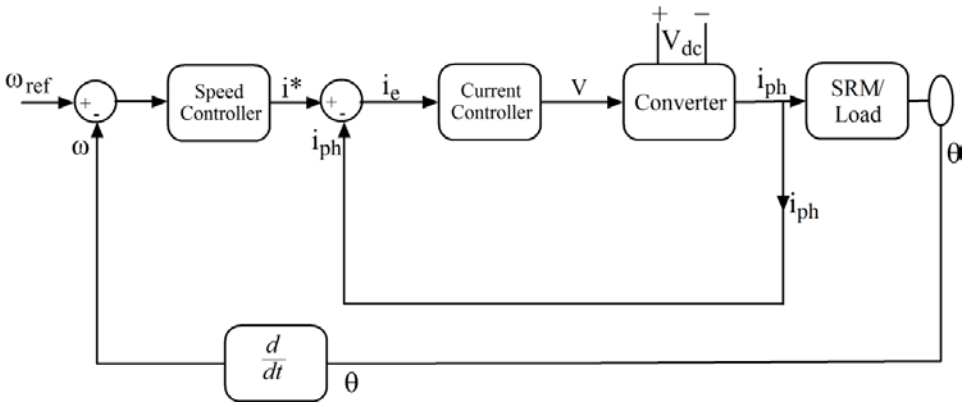

Figure 2.8 Block diagram of the SRM drive

The basic block diagram of the SRM drive with the current and speed feedback loop is shown in Figure 2.8. In general, the speed feedback is derived from the position information

as the SRM is always equipped with the position sensing arrangement. The speed error is processed through the speed PI controller which generates reference current. The current controller maintains phase current to the reference value by switching the phases ON and OFF. Thus speed of the SRM drive is maintained by the controller in varying load condition.

2.2.1 Converter topologies

Several converter topologies are reported in literature for the SRM [32, 35, 55, 79, 81, 99, 100, 123, 155]. The selection of converter depends on the cost, control scheme and performance required. The basic asymmetrical bridge converter is shown in the Figure 2.9, where the anti-parallel diodes across switches are not shown for the simplicity. This converter employs two switches and two diodes per phase which offers high reliability and control flexibility. To supply the voltage V_{dc} to the phase, both the switches of the converter leg are turned ON. Turning OFF both the switches simultaneously provide regeneration by applying reverse voltage to the phase as both the diode of the phase come to conduction. It's called hard chopping scheme. While turning off only single switch of the phase, say M_2 of the phase-1 freewheels the current through the diode D_2, switch M_1 and Phase-1. It's called soft-chopping scheme. During freewheeling, voltage across commutated phase is zero which reduces the rate of current reduction as compare to the hard-chopping.

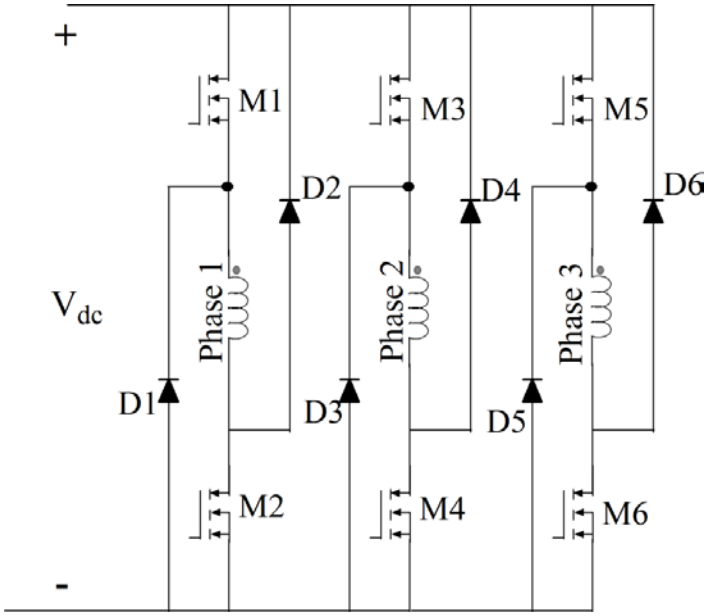

Figure 2.9 Asymmetric bridge converter

2.2.2 Current control scheme

The simplest way to maintain the constant current is to switch ON or OFF the phase accordingly whether the current is lower or higher than reference value. It's called hysteresis current controller. Fixed frequency PWM controller with the speed PI controller can also be used to adjust the current by controlling the PWM duty cycle.

2.2.3 Speed/Torque control scheme

B.K bose and Miller achieved the speed and torque control of SRM with the traditional proportional and integration (PI) controller [20, 100]. The conventional control scheme shown in Figure 2.8 does not taken into account the effect of the rotor angle on the torque production, whereas the SRM torque is not constant even for the constant current. It was found more difficult for the SRM drive to achieve optimal control performance as compared to conventional motor drive. The optimization process is complex and difficult to realize due to multivariable control, complex motor model and large calculation quantity. The problem of high-performance SRM drive is investigated [67] in which a state feedback control algorithm has been proposed. It compensates for all non linearity of the magnetic circuit and decouples the effect of stator phase current in the torque production. However, the selection of the commutation angle affects the efficiency as well as average torque production.

Generally, the firing angle θ_{on} and θ_{off} are selected to avoid the current overlap. However, in order to reduce the torque ripple, overlapping the phase current is beneficial. The minimum dwell angle gives maximum efficiency as it utilizes the entire rotor angle effectively to produce the torque. The increase in dwell angle increases the average torque. Thus selection of the θ_{on} and θ_{off} depends on the required performance parameter of the drive including speed, efficiency, torque and torque-ripple. The firing angle control scheme can be incorporated with the conventional speed control scheme to satisfy one or more performance characteristics.

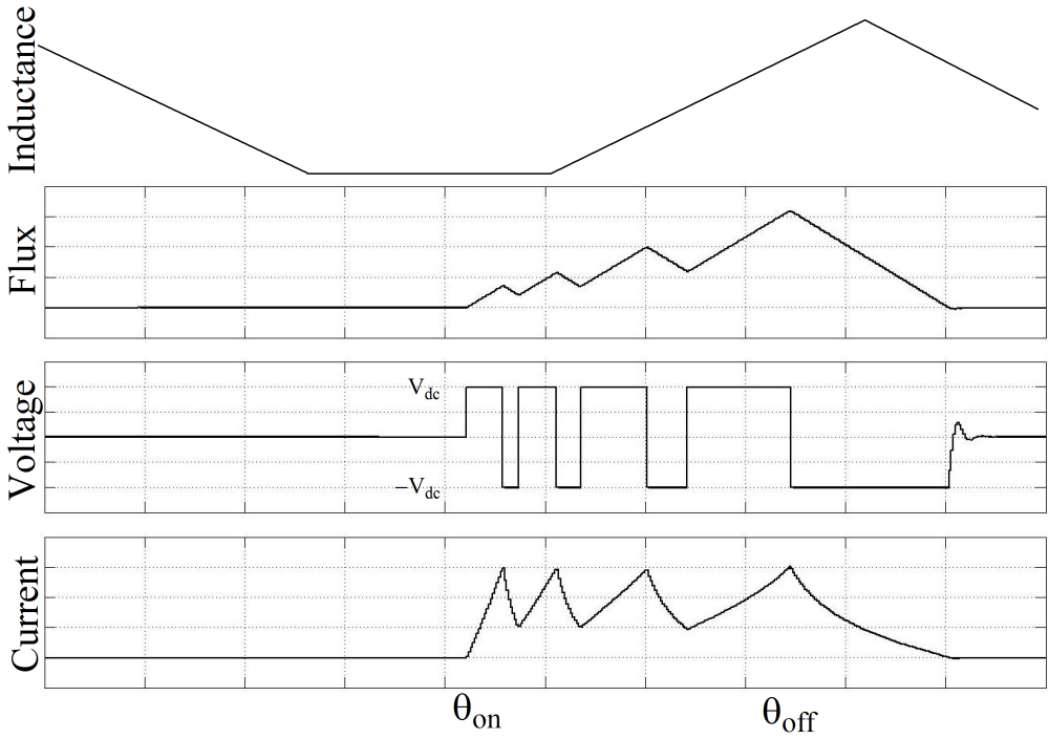

Figure 2.10 Normal speed operation

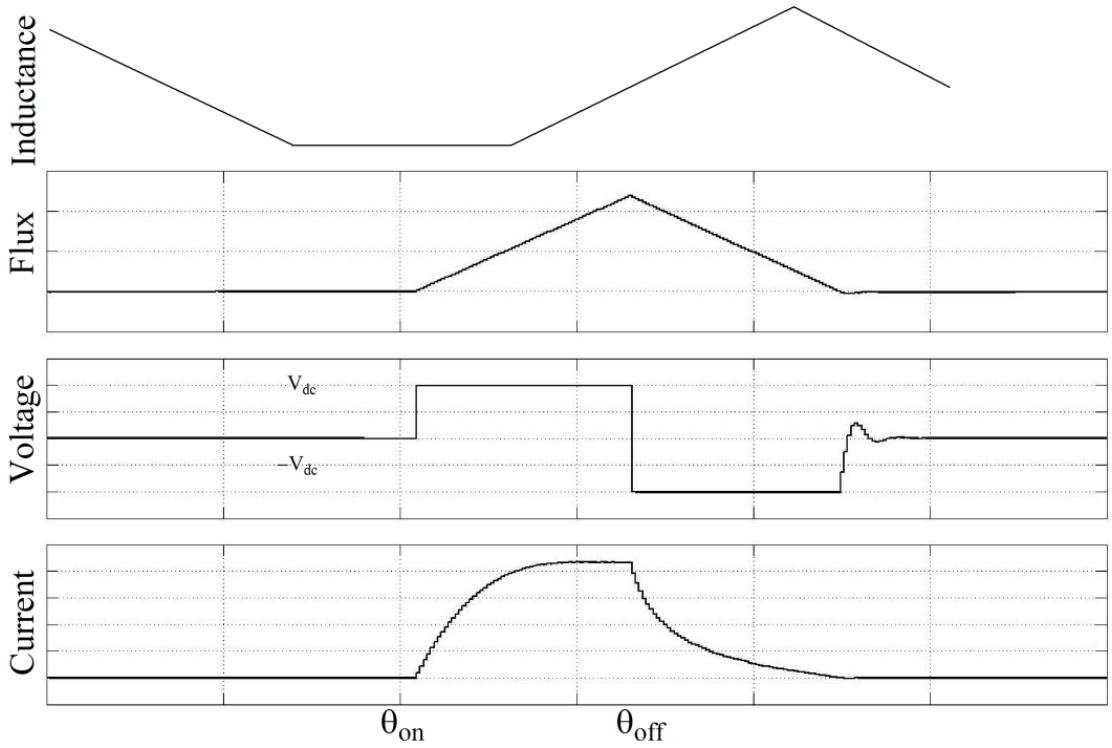

Figure 2.11 High speed operation

The turn-ON angle θ_{on} should be more advanced at higher speed to achieve the adequate level of current, as the back emf increases with speed. It may even come in the previous zone of falling inductance at very high speed. The turn-OFF angle θ_{off} should be advanced to the aligned position, which provides the time to decay the current before falling inductance zone. After the commutation angle θ_{off}, the current decreases rapidly as the reverse voltage is applied, however at the same time inductance increases. After the aligned position, the rate of change of current becomes small as back emf is negative. Thus, the θ_{off} should be advanced with increase in speed. Figure 2.10 and Figure 2.11 shows the normal speed and high speed operation of the SRM drive. It can be concluded that, both the θ_{on} and θ_{off} should be advanced with increase in speed. If speed is exceeding the reference value, then θ_{on} and θ_{off} can be increased to have the phase conduction in to the falling inductance zone. It improves the speed response of the drive by applying brakes as speed increases beyond reference value. However, design of an angle controller is a complex task as the commutation angles are not only function of rotor speed but load torque and phase inductance also influence the performance.

2.3 CONCLUSION

The SRM offers many advantages over conventional ac as well as dc motors. However the performance of the SRM drive and cost of the implementation varies with the applications. The position feedback system is must with the SRM drive for phase switching.

The PWM controller or hysteresis controller can be used to control the phase current of the motor. The conventional PI controller can be incorporated to control the speed of the motor, however, designing the PI speed controller of the SRM is the complex task as compared to conventional motor. To reduce the torque ripples, the angle control scheme must be incorporated with the speed control system of the SRM drive. To obtain the high level of performance from the SRM drive requires proper selection of the motor geometry, converter topology, control scheme and even position sensors.

Chapter 3: MODELING AND SIMULATION OF SRM DRIVE

Three imperative non-linear modeling techniques of the SRM are investigated and compared in this chapter. These techniques are based on lookup table, analytical modeling and inductance profile. Complete simulation model of the current controlled SRM drive is developed using real-time simulation approach and accordingly torque-speed characteristic of the motor is derived. A new modeling technique based on variable reluctance characteristics is proposed in this chapter which offers more flexible and realistic solution for the simulation of SRM. Virtual reality (VR) tool is embedded with the MATLAB based simulation model of the SRM to produce three dimensional visualization of the motor model while running a simulation.

3.1 MATHEMATICAL MODEL OF SRM

Simulation of the system is an important and state-of-the-art in the view of design and experimental realization [20] and for simulation mathematical model of the SRM is required. Mathematical modelling of SRM seems to be complex because of non-linear motor magnetic characteristics [84]. Earlier studies of system simulation involve programming languages like C, FORTRAN or even complex languages [84, 115]. Software design to simulate electric network have been also used in the past studies but it lacked in flexibility. Use of circuit based simulation techniques like SPICE has gained an importance in the late 19's and adopted for simulation of electronic circuits [48, 66].

Lately, there has been considerable progress in simulation software such as Matlab/Simulink, which allows flexible modeling environment to a wide range of electrical, mechanical and pneumatic system including electrical machinery. MATLAB is a simulation tool adopted worldwide for the modeling and simulation of electric system, converter and controllers. Choice of MATLAB for dynamic simulation of system offers advantages viz. gain of time for the simulation development, choice of several techniques for numerical resolution, several libraries are available for different domains, which includes simpowersystem, simulink, fuzzylogic, neuralnetwork, control, signal processing and many more. MATLAB simulation tool is used to examine elaborate simulation of the motor, converter and control techniques.

Main objective of motor modeling is to derive a non-linear function to relate the mechanical output (torque, speed) of the motor to the electrical input (voltage, current). In conventional motors torque can be represented as a function of motor current or its component. As against it, motor torque is non-linear function of phase current and angular position of rotor. The phase current is also a function of both flux linkage and rotor angle.

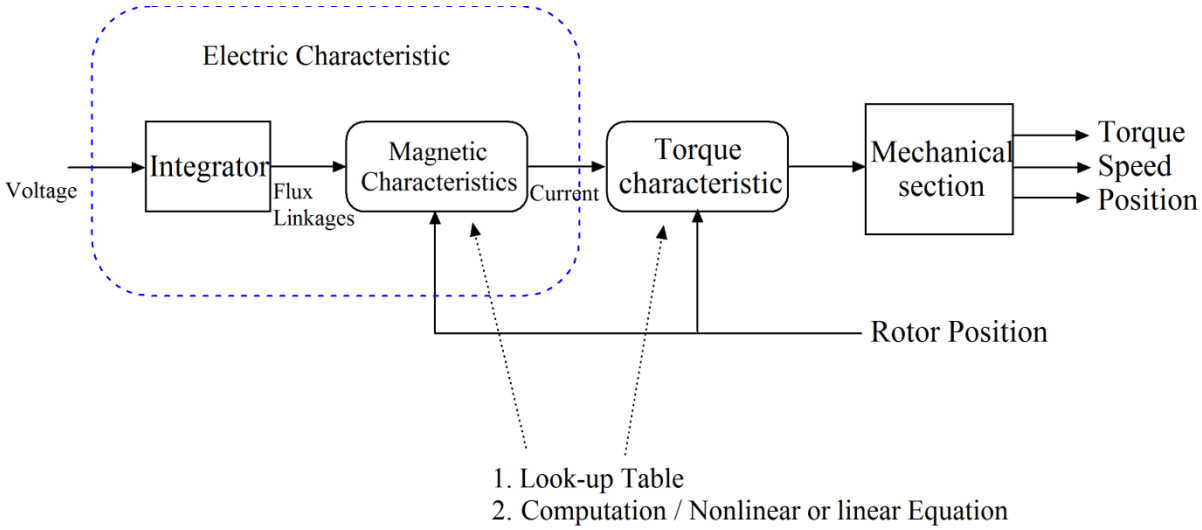

Figure 3.1 Block diagram of SRM model

Figure 3.1 represents simplified model of the SRM. SRM have only single source of magnetic field production, i.e. stator winding, and there is no winding on the rotor. Magnetic material (rotor) placed in between this magnetic field experience a force of attraction. Voltage balance equation for the phase can be written as (3.1) as applied phase voltage is equal to summation of the voltage drop across phase resistance and rate of change of flux-linkage. Flux-linkage equation (3.2) is derived using integration. Electrical characteristics of the SRM obtained from the equation (3.1) and (3.2), are shown in Figure 3.2 where black box i(ψ, θ) represents three dimensional nonlinear relation among phase current, flux-linkage and rotor angle. In the simplified model, torque characteristic represents non-linear relation among motor torque, phase current and rotor angle. The dynamics of the mechanical system as represented by equation (3.3) is shown in Figure 3.3. Therefore, to model the SRM, magnetic non-linearity is the only challenging task of the modeling process.

$$V_a = i_a R_a + \frac{d\psi_a}{dt} \tag{3.1}$$

$$\psi_a(t) = \int_0^t (V_a - i_a R_a)dt \tag{3.2}$$

$$T_e - T_L = J\frac{d\omega}{dt} + B\omega_m \tag{3.3}$$

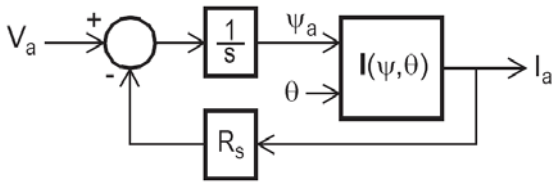

Figure 3.2 Simulink model of electric characteristics of the SRM

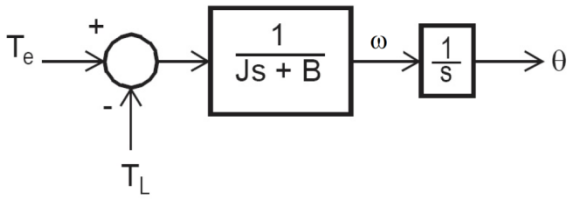

Figure 3.3 Simulink model of basic mechanical loading

Linear model of the SRM can be derived by neglecting the magnetic saturation and utilizing idealized inductance profile. Phase voltage equation of the SRM can be represented as shown in Figure 3.2 where the current i(ψ,θ) can be derived from the idealized inductance profile and phase flux ψ (2.20). The torque developed by the individual phases of the motor can be derived by simplified torque equation (2.22). The total instantaneous torque of the motor is given by the summation of the all phases. Linear model of the SRM is sufficient for the implementation of the controller; however the non-linear model is required for the realization of complete SRM drive and to investigate the dynamic behavior of the entire system.

Many practices have been in use to model the magnetic non-linearity of the SRM, out of which, several methods are covered in the following sections.

3.1.1 Method 1: Look-up Table Based Approach

The look-up table based approach [79, 85, 100] is very accurate method to represent the magnetic non-linearity of the SRM. The model of SRM discussed here is designed in [82, 147] for the electric vehicle propulsion, where the goal is optimal efficient operation of the drive. Magnetic characteristics of the SRM is shown in Figure 3.4, which represents number of magnetic curves at the different rotor angle [85]. Look-up table is used to store the magnetic characteristics as a three dimensional data. The flux-linkage, calculated from the equation (3.2) and the rotor angle are used as an index to select the phase current. One more Look-up table is used to represent torque characteristics of the motor. The torque characteristic of the SRM is shown in the Figure 3.5, which represents non-linear relation amongst torque, phase current and rotor angle. The look-up table based approach to map non-linear characteristics of the SRM, reduces involvement of the dynamics equations, and thus reduces the process time. This method is the most accurate method to model a physical SRM, if precise data of the magnetic as well as torque characteristics are available.

However, it requires a large amount of experimental workout to obtain the motor characteristics. The accuracy of the model depends on the experimental technique used to obtain the precise motor parameter as well as on the accuracy of the measuring instruments. This method is time consuming and costly but, is an accurate modeling technique of the

SRM. The experimental procedure required to obtain the motor magnetic characteristics is well explained in [100].

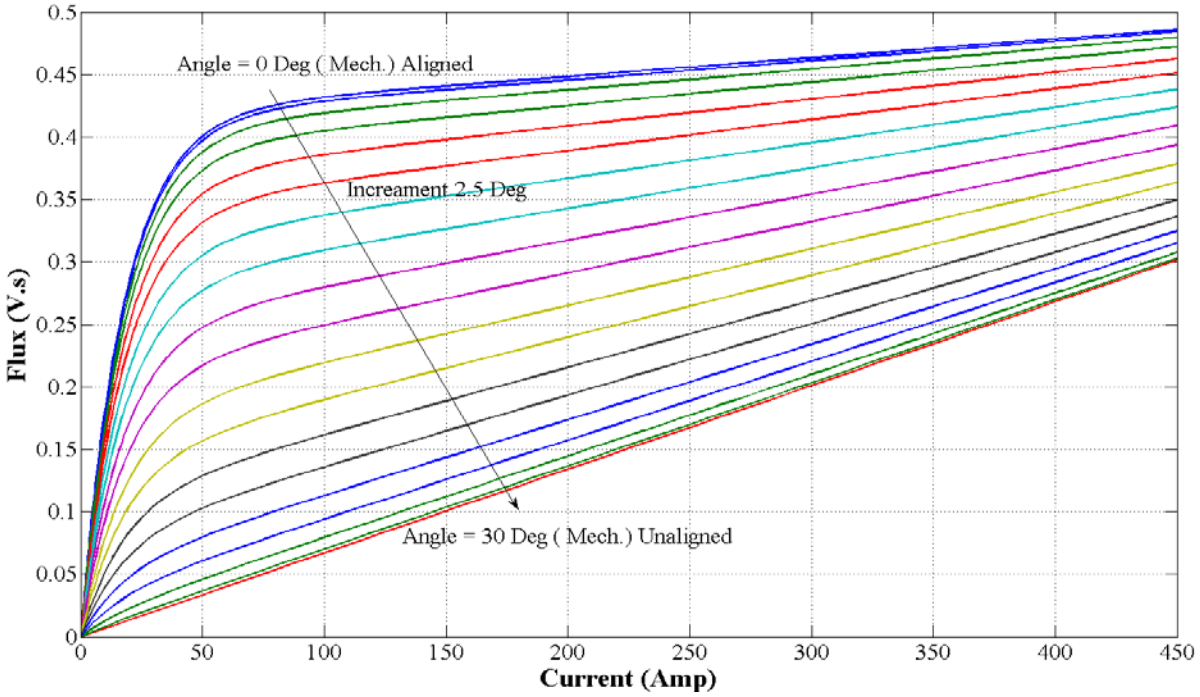

Figure 3.4 Magnetic characteristics of SRM

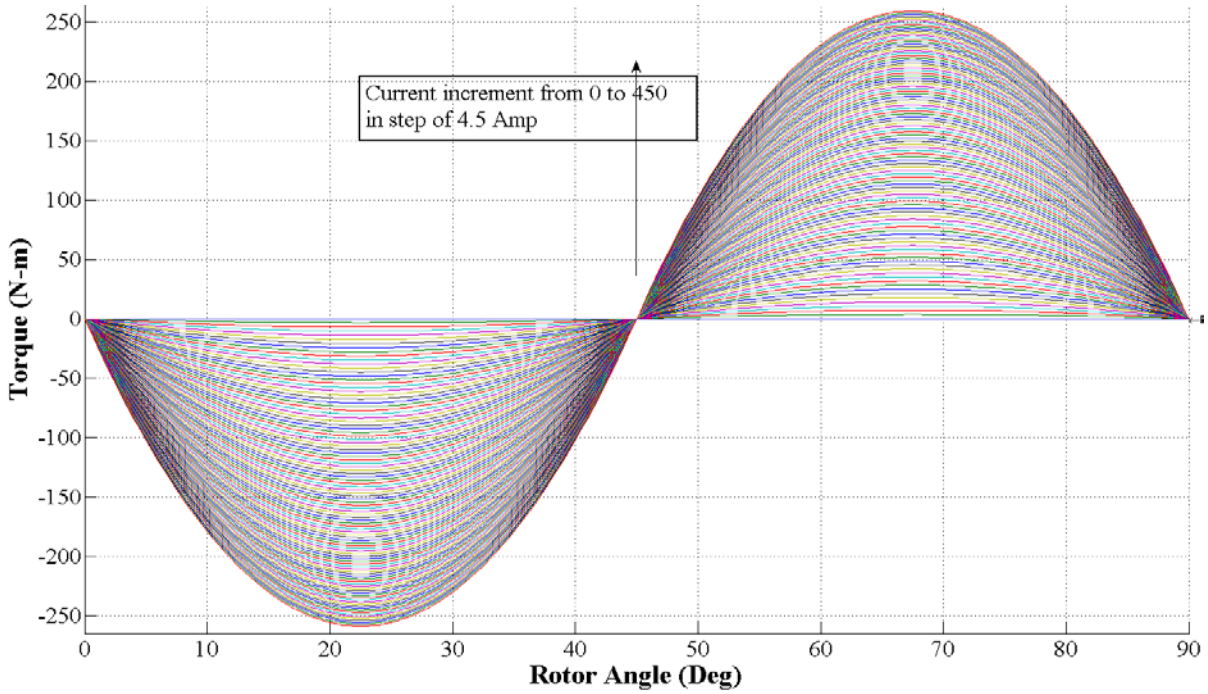

Figure 3.5 Torque characteristics of SRM

This method is suitable to model an existing SRM, where it is required to study the entire motor performance with high grade of accuracy along with the different types of converter and control techniques. PC based design and FEA software packages like PC-SRD and PC-FEA are available, which makes it possible to derive the magnetic parameters

of the motor from the dimensional detail and winding parameters of the motor. It saves the time to model a SRM based on look-up table, however it requires a skill to deal with an available software package.

3.1.2 Method 2: Analytical Modeling Technique

It is possible to develop a mathematical expression to represent the magnetic non-linearity of the motor with the help of exponential or trigonometric functions. Many modeling techniques have been published in the literatures to map the magnetic non-linearity in the form of mathematical equation, where the goal is to determine number of unknown parameters from the motor parameters with calculations and analytical reasoning [104, 105, 144, 146]. The piece-wise analysis is covered in [146] to connect the fundamental geometry and turns per phase of the motor with an analytical terminal description.

$$\psi(i,\theta) = a_1(\theta)[1 - e^{[a_2(\theta)i]}] + a_3(\theta)i \tag{3.4}$$

Equation (3.4) summarizes the magnetic characteristics of the SRM over all the rotor position and current, where, $a_1(\theta)$, $a_2(\theta)$ and $a_3(\theta)$ are the unknown coefficient needs to be determined. The derivative of flux represents an incremental inductance as a function of unknown coefficient as-

$$l(i,\theta) = \frac{\partial\psi(i,\theta)}{\partial i} = -a_1(\theta)\cdot a_2(\theta)\cdot e^{[a_2(\theta)i]} + a_3(\theta) \tag{3.5}$$

Unsaturated phase inductance 'L' can be represented as a function of rotor angle as given below:

$$L(\theta) = -a_1(\theta)\cdot a_2(\theta) + a_3(\theta) \tag{3.6}$$

Equation (3.6) is simplified as,

$$a_2(\theta) = \frac{a_3(\theta) - L(\theta)}{a_1(\theta)} \tag{3.7}$$

It is required to determine three unknown coefficients $a_1(\theta)$, $a_3(\theta)$ and $L(\theta)$, which depend on rotor angle. The piece-wise linear models assumed for the coefficients are shown in Figure 3.6. The angle θ_a and θ_u refer to aligned and unaligned position of the rotor respectively. The stator/rotor pole arc is fully covered by the rotor/stator pole arc, from the rotor angle θ_a to the angle θ_1, and just after θ_1 pole arcs start uncovering. The angle θ_2 represents a position, where both the pole arcs just become fully uncovered. The process of the determination involves determining all eleven parameters listed in Table 3.1. Seven parameters are found based on simple calculation, two are based on values from tables and two are found iteratively. Angular breakpoints are found directly from the motor design parameter. Inductive constant L_{max} is found from the equation, while determination of L_{corner} and L_{min} require dimensional detail of the rotor and stator pole, to find out the constant from the table [146]. The magnetization coefficient $a_1(\theta_a)$ and $a_3(\theta_a)$ are found iteratively. The

values for $a_1(\theta_u)$ and $a_3(\theta_u)$ are then taken as constant fraction of $a_1(\theta_a)$ and L_{min}, respectively. Step by step procedure of finding each parameter is covered in [146].

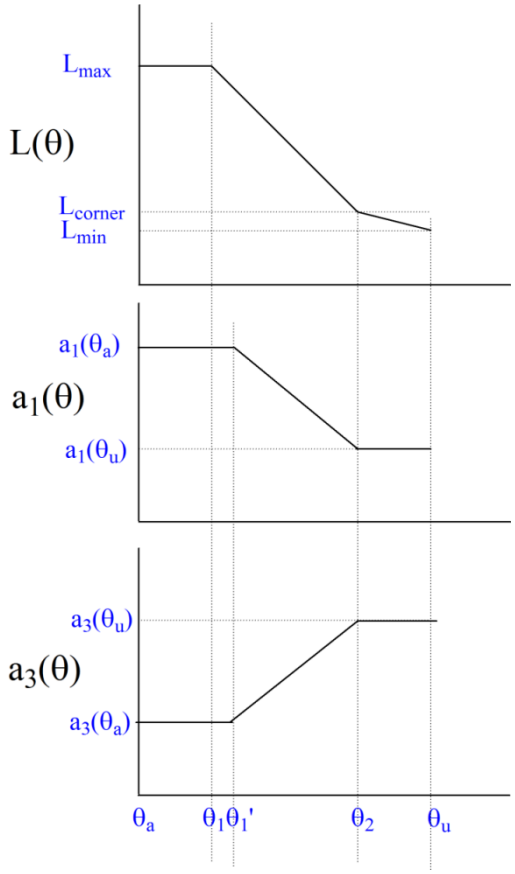

Figure 3.6 Piece-wise linear model assumed for unsaturated phase inductance, magnetization coefficient a1 and a3, as a function of rotor angle

If all the eleven parameters are known, then coefficients $a_3(\theta)$, $L(\theta)$ and $a_1(\theta)$ can be found from the simple equations. The MATLAB embedded function is designed to represent a non-linear relation amongst flux-linkage, phase current and rotor angle approaching analytical modeling technique. Flowchart of the embedded function design is shown in Figure 3.7 where it is assumed that, all the eleven parameters are known. The embedded function provides the value of the flux-linkage for the given phase current and rotor angle. The design parameters of the motor are listed in the Table 3.2. The magnetization coefficient, inductance constant and angular breakpoints are derived from the design parameter of the SRM, as summarized in Table 3.3.

Table 3.1 Eleven parameters needs to be determine

Magnetization coefficient	Inductive constant	Angular breakpoints
$a_1(\theta_a)$	L_{max}	θ_1
$a_3(\theta_a)$	L_{corner}	θ_1'
$a_1(\theta_u)$	L_{min}	θ_2
$a_3(\theta_u)$		θ_u

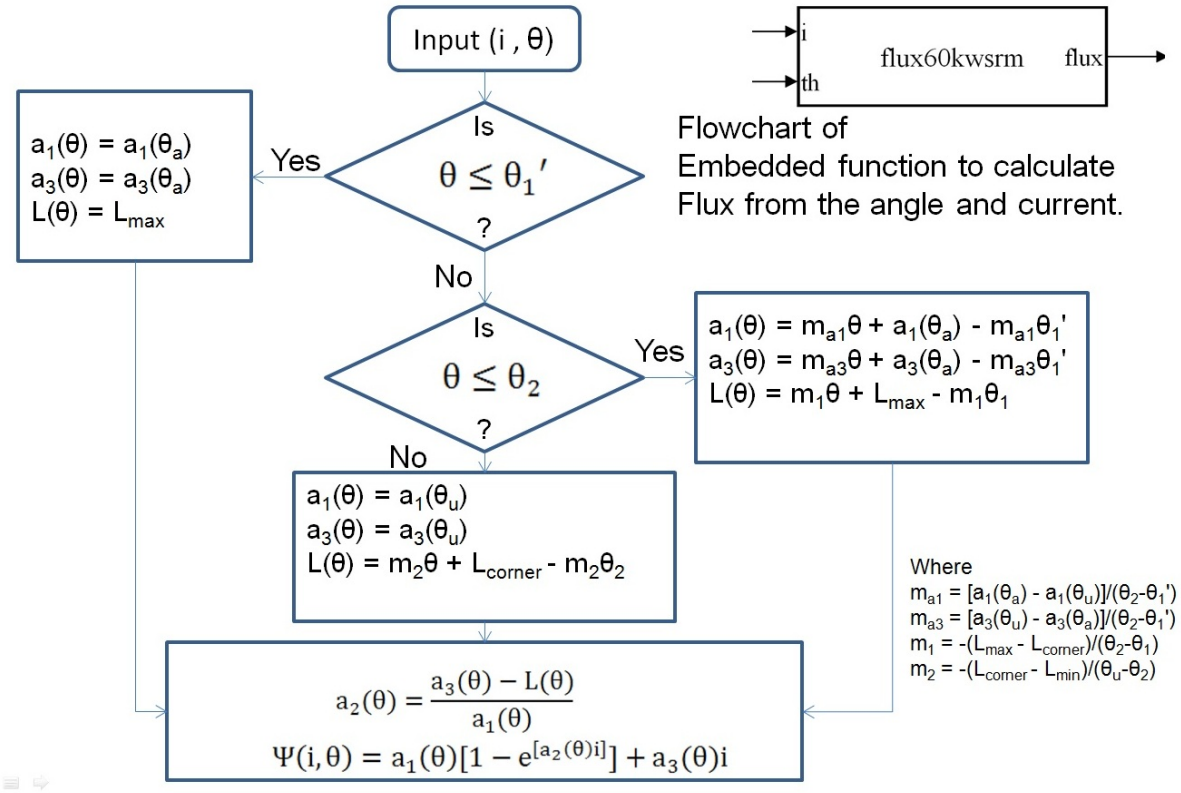

Figure 3.7 Flowchart of the embedded function design to represent a magnetic non-linearity

Table 3.2 Design parameter of 60KW SRM

Motor parameters	Value
Shaft radius (R_{sft})	0.0143 m
Rotor Back iron radius (R_{rbi})	0.034 m
Radius behind rotor pole (R_{rph})	0.041 m
Width of rotor pole base (W_{rpb})	0.032 m
Rotor radius at airgap (R_r)	0.055 m
Radial airgap (l_g)	0.0002 m
Stator radius at airgap (R_{sa})	0.0552 m
Radius at top of stator pole (R_{sbi})	0.082 m
Outside radius (R_o)	0.1 m
Active length (G)	0.3 m
Rotor pole arc (θ_r)	45°
Stator pole arc (θ_s)	32°
Number of rotor pole (N_r)	4
Turn per phase (N)	13

Table 3.3 Eleven parameters of the three phase SRM

Magnetization coefficient	Inductive constant	Angular breakpoints
$a_1(\theta_a)$ = 439.6 mWb	L_{max} = 23.68 mH	θ_1 = 6.5 deg
$a_3(\theta_a)$ = 177.7µH	L_{corner} = 1.19 mH	θ_1' = 12.83 deg
$a_1(\theta_u)$ = 43.96 mwb	L_{min} = 0.67 mH	θ_2= 38.5 deg
$a_3(\theta_u)$ = 636.5 µH		θ_u = 45 deg

The magnetic characteristics derived using embedded function is compared with the actual magnetic characteristics of method-1 in Figure 3.8. The accuracy of the non-linear function mapping is quite reasonable for the low phase current value. The phenomena of pole corner saturation and saturation of yoke reduces the accuracy of the mapping, at the higher current level. The details about motor geometry and winding turns are sufficient for the analytical modeling technique, however several pre-calculations are required. This method reduces the time and cost of the modeling technique compared to Method-1, where it was required to collect a large number of data from experimental setup. The method also eliminates requirement of experimental skill, which was needed in Method-1. The analytical modeling method is suitable for the performance evaluation of the power electronics converter and different control techniques as well as to predict the performance of the motor.

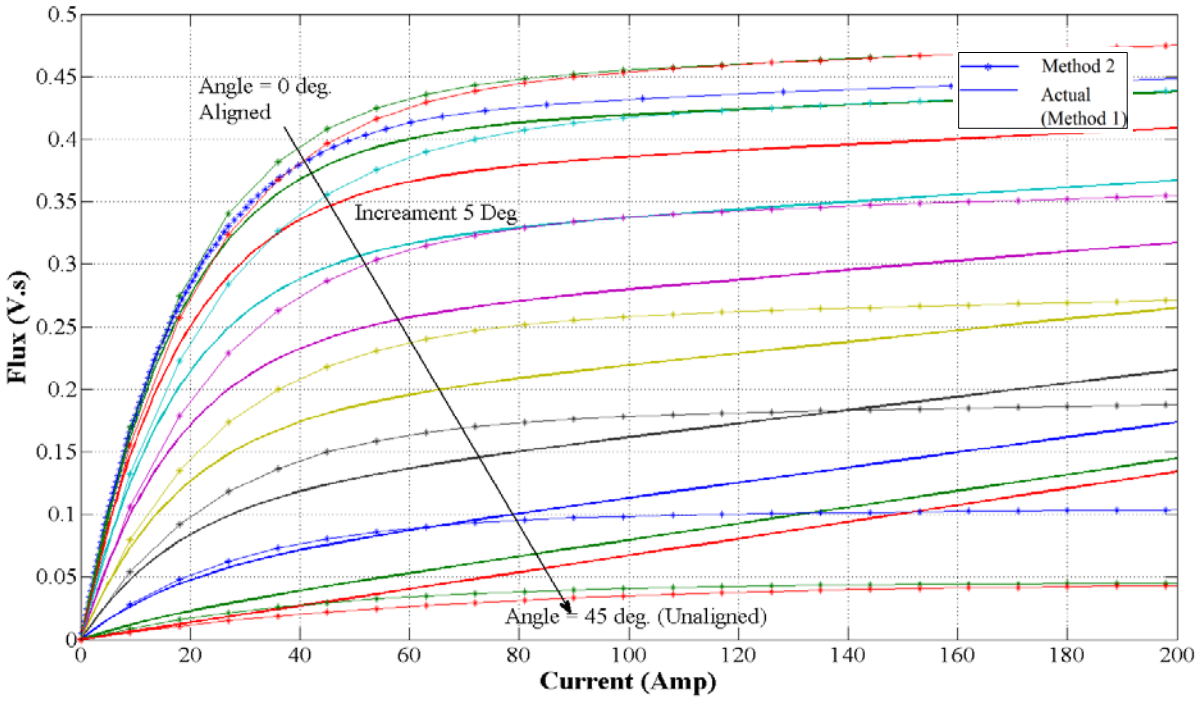

Figure 3.8 Magnetic characteristics of the SRM represented by the MATLAB embedded function

The electromagnetic torque is a non-linear function of the phase current and rotor angle, which is due to non-linear magnetic characteristics of the motor. The torque produced

by the phase of the SRM can be calculated as the derivative of the machine co-energy [85] as-

$$Te(i,\theta) = \frac{\partial}{\partial\theta} W_c(i,\theta) \tag{3.8}$$

where, 'W_c' is the co-energy. The co-energy can be obtained from the flux linkage as-

$$W_c = \int \psi(i,\theta) \cdot di \tag{3.9}$$

Figure 3.9 shows the torque characteristics of the SRM, calculated from the magnetic characteristics. The electromagnetic torque can be obtained using equation (3.8) and (3.9).

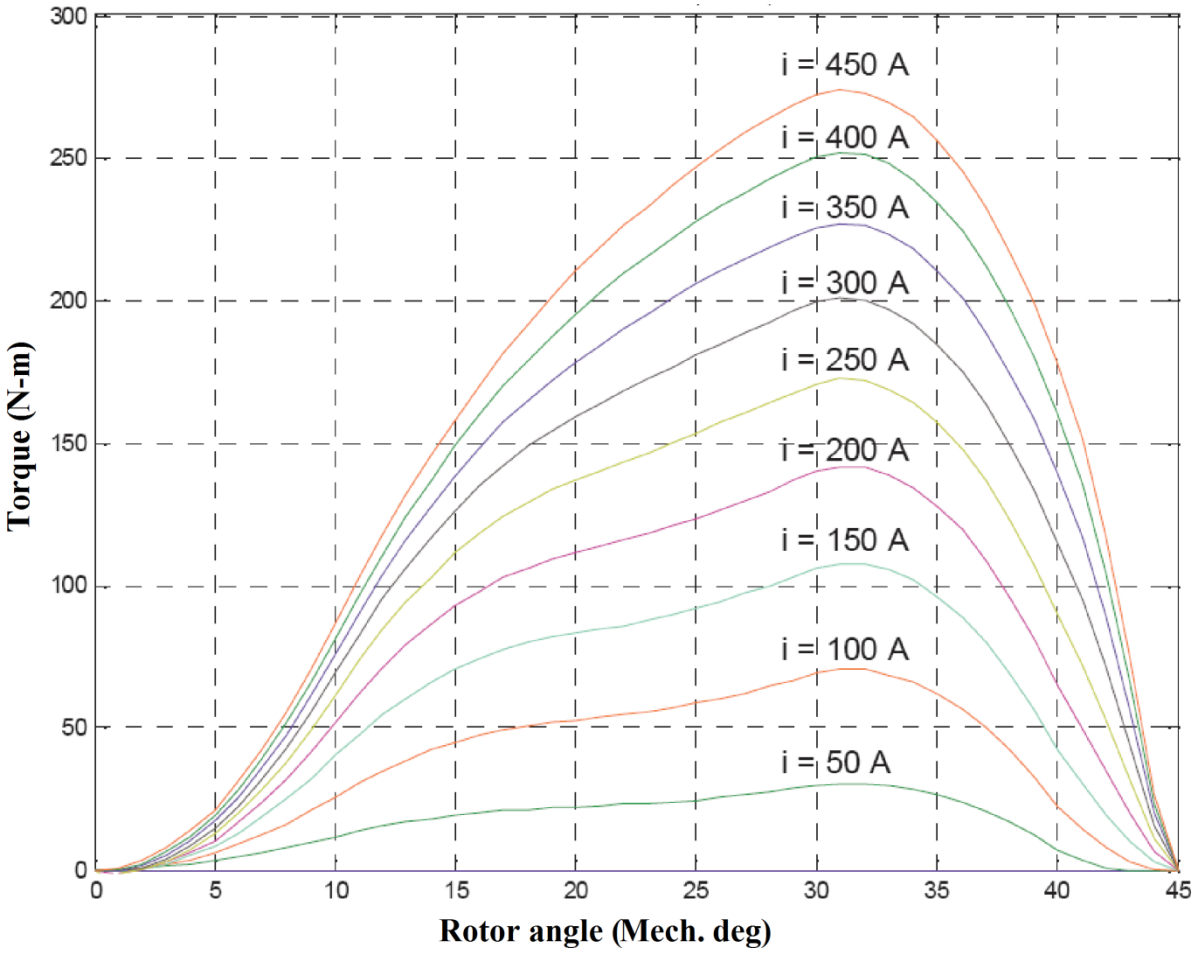

Figure 3.9 Torque characteristics of the SRM, calculated from the equation (3.8)

3.1.3 Method-3: Inductance Based Modelling

The inductance based modelling technique considers non-linear relation of inductance-current-angle relation to represent a magnetic non-linearity of the SRM, instead of flux-current-angle relation [48, 94]. The phase winding inductance is a non-linear function of rotor angle and phase current. The variation of the phase inductance with the rotor position is expressed by a limited number of Fourier series terms. The coefficients of the Fourier series are determined by the values of the inductance at the aligned position, unaligned position and midway position. The non-linear relation between the phase inductance and the current

is represented by the polynomial functions. The coefficients of the polynomial are derived by static characteristics obtained from experimental results or finite element analysis. The dynamic phase equation can be represented as a function of phase inductance as-

$$V_{ph} = R_s i + \frac{d[L(\theta,i)i]}{dt} = R_s i + L(\theta,i)\frac{di}{dt} + i\frac{d\theta}{dt}\frac{dL(\theta,i)}{dt} = R_s i + L(\theta,i)\frac{di}{dt} + \frac{dL(\theta,i)}{dt}\omega_m i \qquad (3.10)$$

where 'ω_m' is the motor speed in rad/sec, 'i' is the phase current and 'L(θ,i)' is the equivalent inductance of the phase. The leakage inductance and the mutual inductance of the winding are neglected. The phase equation can be simplyfied further as-

$$V_{ph} = R_s i + L(\theta,i)\frac{di}{dt} + e(\theta,i) \qquad (3.11)$$

where, e(θ,i) is the back EMF = $\frac{dL(\theta,i)}{dt}\omega_m i$

The equivalent inductance of the phase is represented as a three terms of the fourier series as-

$$L(\theta,i) = L_0(i) + L_1(i)\cos(\theta) + L_2(i)\cos(2\theta) \qquad (3.12)$$

and thus the back EMF can be represented by the derivative as-

$$e(\theta,i) = -\omega_m(L_1(i)\sin(\theta) + 2L_2(i)\sin(2\theta)\cdot i \qquad (3.13)$$

The current dependent coefficients $L_0(i)$, $L_1(i)$ and $L_2(i)$ are expressed by the three-order polynomials as-

$$L_0(i) = \frac{1}{2}[\frac{1}{2}(La + Lu) + Lm]$$

$$L_1(i) = \frac{1}{2}(La - Lu) \qquad (3.14)$$

$$L_2(i) = \frac{1}{2}[\frac{1}{2}(La + Lu) - Lm]$$

where 'L_a' is the aligned position inductance, 'L_m' is the midway position inductance and 'L_u' is the unaligned position inductance. The aligned and midway position inductance are function of the phase current, while the inductance at the unaligned position can be assumed as the independent of the phase current. The inductances L_a,L_m and L_u are represented as-

$$L_a = L(\theta = 0, i) = \sum_{m=0}^{k} a_m i^m$$

$$L_m = L(\theta = \frac{\pi}{2}, i) = \sum_{m=0}^{k} b_m i^m \qquad (3.15)$$

$$L_u = L(\theta = \pi, i)$$

where 'k' is the degree of approximation. The coefficients, a_m and b_m are determined by curve fitting methods such that, the inductance profile obtained using equation (3.12), would best fit into the profile obtained experimentally.

3.1.4 Comparision of the modelling techniques

Both the method-2 and method-3 provide analytical solution to account for the magnetic non-linearity of the SRM. Method-3 requires experimental data of inductance profile L(θ,i) of the SRM to obtain co-efficient of Fourier series. It provides reasonable accuracy compared to the method-2, however it requires experimental setup which increases the cost and time of implementation. Also the computation time of the simulation model is comparatively high as it involves derivative calculations. This method is suitable to analyse the performance of the converter as well as to obtain the dynamic performance of the SRM drive. The method-2 does not require experimental data, however it involves extensive calculations to derive polynomial coefficients. Even though the coefficients are computed with good precision, accuracy of method-2 is somewhat less due to error in flux derivative calculation. The details about motor geometry and winding turn parameters are required initially. This method takes minimum time and cost to derive the simulation model as compared to other methods. It gives high accuracy for low current level, while effect of magnetic saturation reduces the accuracy of the model at the higher current level. The method can be used to investigate the performance of various converter topologies and control techniques, which helps in its performance and design optimization. The method-1 accounts for the non-linearity of the SRM magnetic characteristics while it minimizes the simulation time. This is because it avoids all partial derivatives and utilize a look-up table which approximates the relation flux-current-position and torque-current-position. However it requires large number of experimental data, and thus it takes maximum time to derive simulation model of the SRM. Nevertheless, the method provides highest efficiency among all other methods, and it also has advantage of minimum computation time which results in faster simulation.

Thus the look-up table based approach is used in further investigation to develop the model of the 60KW, 6/4 pole, three phase SRM and also for development of the prototype SRM of 500W, 8/6 pole, four phase SRM.

3.1.5 MATLAB simulink model of the SRM

The non-linear model of the SRM is derived using method-1. The lookup tables are used to represent the magnetic characteristics (Figure 3.4) as well as the torque characteristics (Figure 3.5) of the 60KW SRM. The simulink model of the SRM is shown is Figure 3.10 where lookup tables 'ITBL' and 'TTBL' store the flux-angle-current and current-angle-torque relation respectively. The motor model produces the torque and speed for the voltage applied to the phase. The model of the converter is developed using 'simpowersystem' library components. It is also possible to model various converters and

control techniques using the simulink library. However, 'simpowersystem' library of the MALTAB offers flexibility and easy to model a power electronic and power system components using the node based circuit simulation approach. The main advantage of using a 'simpowersystem' library to develop the model of converter is that actual devices used in the drive system can be modelled quickly because of readily available modules of the power electronics switches. It offers a great flexibility to study the different converter topologies and certain practical issues can be clearly understood.

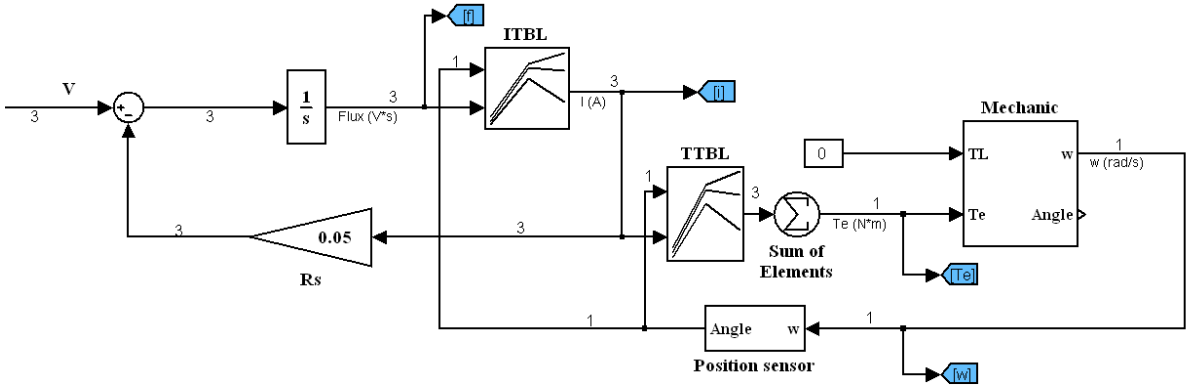

Figure 3.10 The simulink model of the SRM

Two methods are developed to incorporate the model of converter, designed with 'simpowersystem' library, and the model of the motor, designed with 'simulink' library. The first method uses the resistive element and the dependent current source from the 'simpowersystem' library to represent a phase of the motor as shown in Figure 3.11 [85, 107]. The switching device in series with the motor phase is not shown for the simplicity. The node voltage across the motor phase is converted in to the single line signal using the voltage measurement block of the 'simpowersystem' library, and it is applied to the simulink model of the motor. The motor model produces current, torque and speed according to the applied phase voltage. The phase current in the 'simpowersystem' based phase model depends upon the phase current of the 'simulink' model. Thus, phase voltage applied to the phase of the 'simpowersystem' model, results in the production of torque and speed in the 'simulink' model, while at the same time, the phase current of the 'simulink' model reflects to the phase of 'simpowersystem' model.

The second method is applicable where the flux-linkage is to be estimated from the phase current and rotor angle, as in method-2. The resistive element and dependent voltage source from the 'simpowersystem' library form a motor phase. The phase current is transformed to the single line signal using ampere meter. The voltage source depends on the rate of change of flux linkage generated from the embedded function, and thus phase current is governed by the equation (3.11).

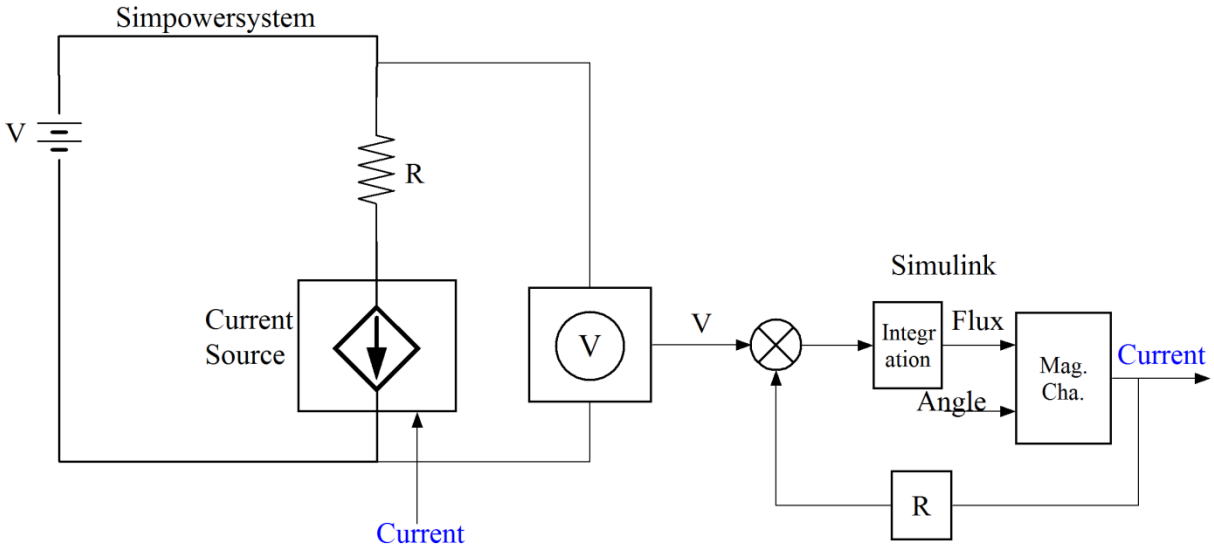

Figure 3.11 Transformation of the SRM model to be compatible with the 'simpowersystem' model using controlled current source

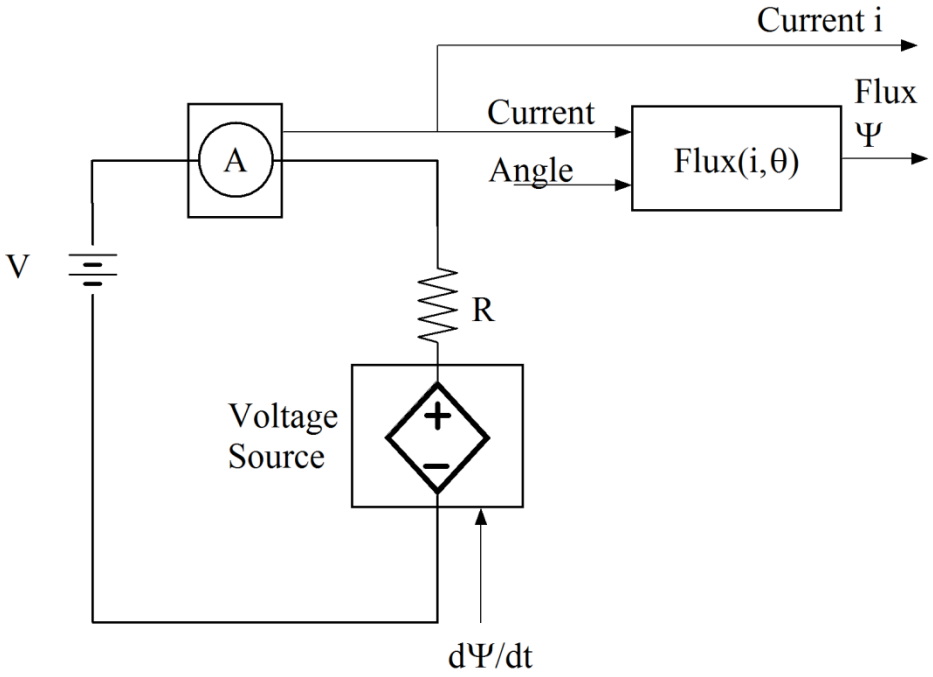

Figure 3.12 Transformation of the SRM model to be compatible with the 'simpowersystem' model using controlled voltage source

Simulation model of complete SRM drive including motor, converter and speed controller is developed in the following section using the 'simulink' and 'simpowersystem' library components.

3.2 REAL-TIME SIMULATION OF SRM DRIVE

The simulation of the SRM drive is conducted with the RT-lab which is a FPGA based real-time simulator. The goal is to derive torque-speed characteristic of the SRM drive. An FPGA based implementation of SRM drive offers advantage of very low computational time

(250 ns) and minimal hardware-in-loop latency just above 1 µs [93]. Thus there is no dispute that RT-Lab based real-time simulation of SRM drive eliminates the problem of model latency presence in CPU based approach, and have higher accuracy [26, 93, 152].

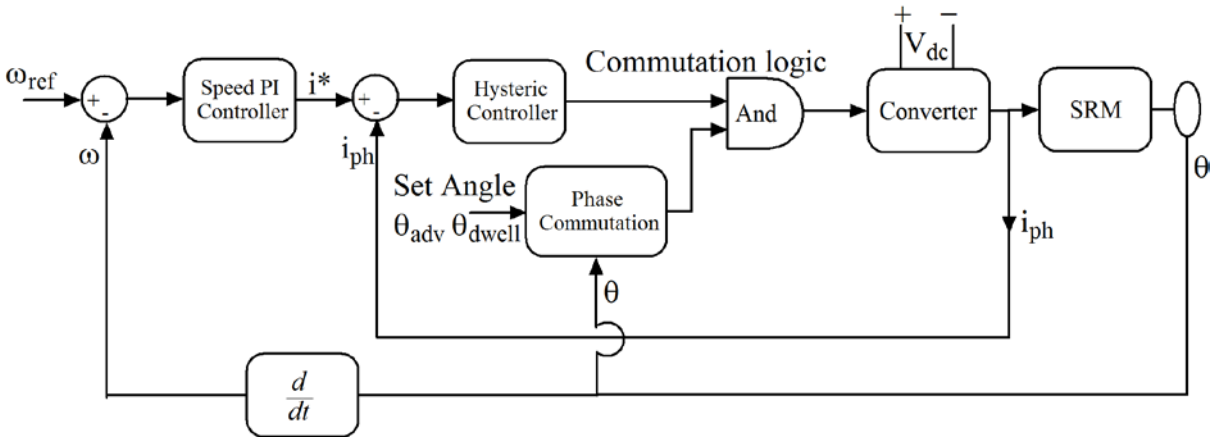

Figure 3.13 Block diagram of closed-loop speed controlled SRM drive

The block diagram of the closed loop speed control system is shown in Figure 3.13. The conventional converter (two IGBTs and two diodes per phase) supply the three phase SRM where hysteresis current controller limits the current. The model has a flexibility to adjust the advance angle and dwell angle along with the speed control system. The error in speed is processed through the speed PI controller which generates the reference current. The reference current is limited to maximum value and is decided by the phase winding current carrying capability. The difference in current is processed through the hysteresis current controller which limits the phase current within band of $\pm\Delta i_h$. It is required to derive maximum possible torque of the SRM drive which is a function of speed, advance angle and dwell angle. The complete drive is simulated using SRM model and simulink/simpowersystem library components along with the required RT-Lab block-sets.

The RT-Lab supports automatic code generation and FAPGA implementation of MATLAB simulation. It uses signal-wire interface which provides high speed real-time communication between FPGA and dual-core CPU. It identifies the separate simulink model by the suffix used with the name of the subsystem. The complete system of the simulation is shown in Figure 3.14. The main subsystem 'SM_srm' contains complete model of SRM drive while subsystem 'SC_user' provides the user interface to control and monitor the parameters in real-time via dual-core CPU. Figure 3.15 is simulink model of the main subsystem where 'OpComm' block is required to communicate with each incoming signals to the subsystem and 'Analog Output' block accomplishes digital to analog conversion to provide real-time analog signal. The 'OpCtrl' block configures the analog input/output card. It is configured to provide the real-time analog output of the current and gate pulse of the phase.

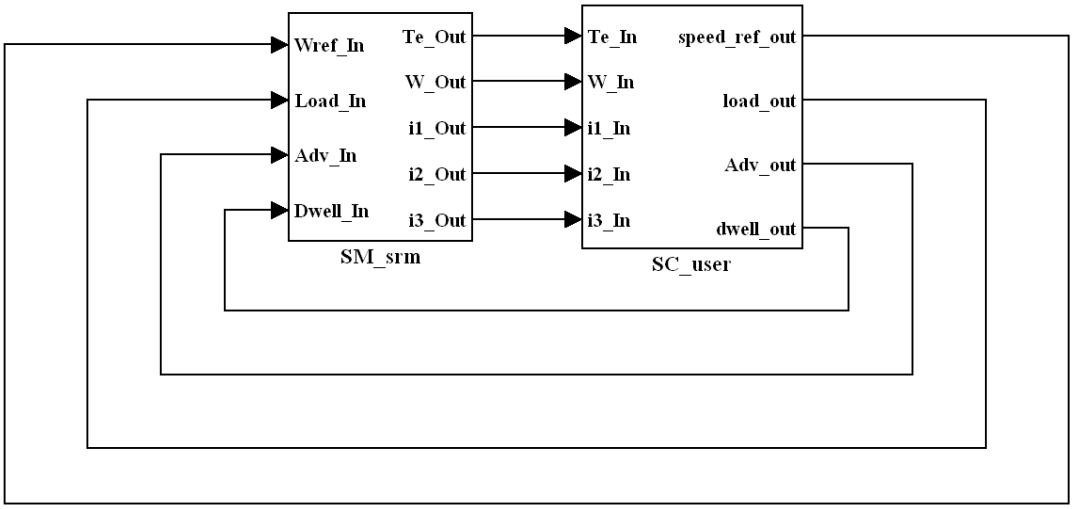

Figure 3.14 Simulation model of SRM drive

Figure 3.16 shows the complete model of three phase SRM which is derived using look-up table based approach. It is converted for compatibility with the 'simpowersystem' library components using current source, as explained. The nodes A1-A2, B1-B2 and C1-C2 represent the six terminals of the three phase SRM which input the voltage from the converter model. Accordingly it outputs the torque and speed signals. Simulation model of the asymmetric bridge converter is shown in Figure 3.17 which employs two IGBTs and two diodes to form a lag of a phase. Constant dc voltage of 200V is supplied across the nodes V+ and V- while controlled voltage will appear across the node A1-A2. The gate terminal 'g' of the IGBT controls the ON/OFF state of the switch accordingly whether the signal 'g' is high ('1') or low ('0'). Both the switches of the lag are turned ON or OFF simultaneously to employ the hard-chopping scheme. Figure 3.18 shows the simulation model of the position synchronization which generates phase commutation pulses. A signal of rotor angle coming from the motor model is first converted from radian to the degree. Then the rotor angle is transformed so that it is modulo $2\pi/N_r$ as each phase inductance has a periodicity of $2\pi/N_r$ degree. Where N_r is the number of rotor pole. The logic block process the rotor angle which generates phase commutation pulse for each phase as shown in Figure 3.18. It is also made possible to adjust the advance angle and dwell angle which in turn adjust the turn-On and turn-OFF angle of the phase. Simulation model of the PI speed controller is shown in the Figure 3.19 which processes the speed error and generates the reference current. Figure 3.20 shows the simulation model of the hysteresis current controller where G1in, G2in and G3in are phase commutation pulses coming from position synchronization block, while G1, G2 and G3 are gate pulses of the IGBTs. The controller switches ON or switches OFF the phase accordingly whether the phase current is lower or higher than the reference value by 5 A.

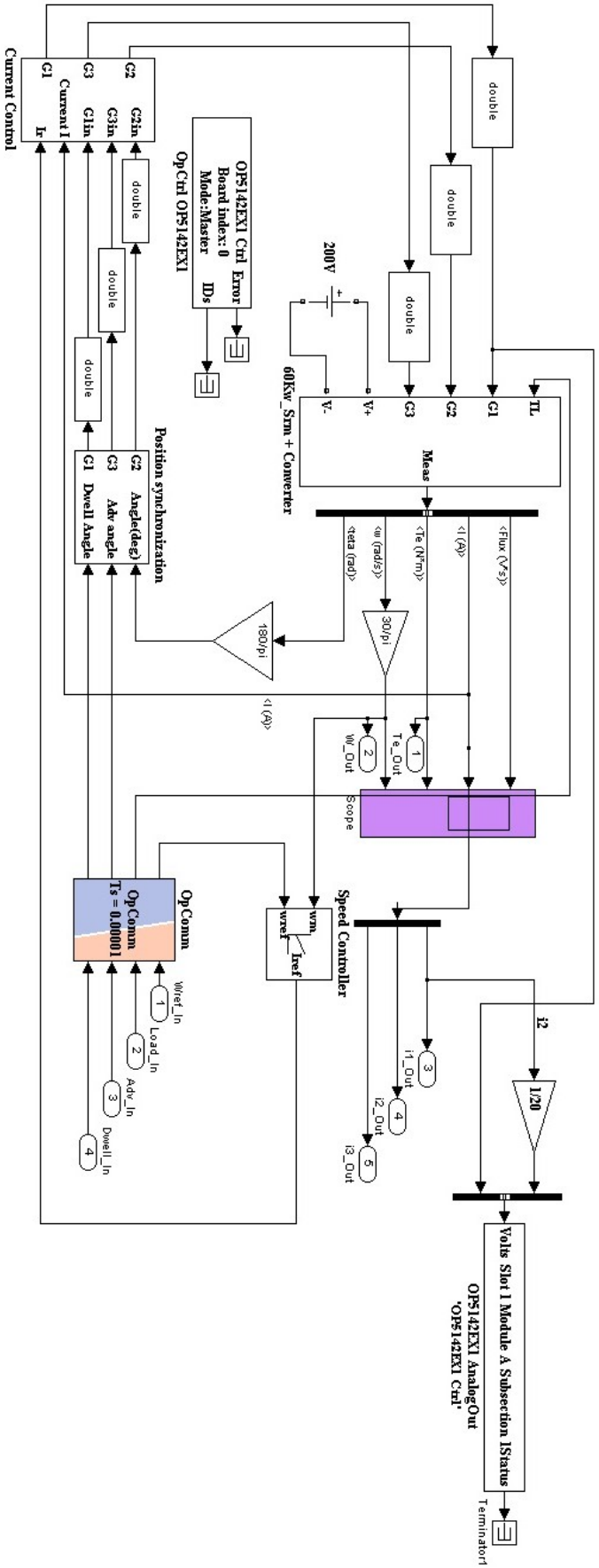

Figure 3.15 Main subsystem which contains model of SRM drive

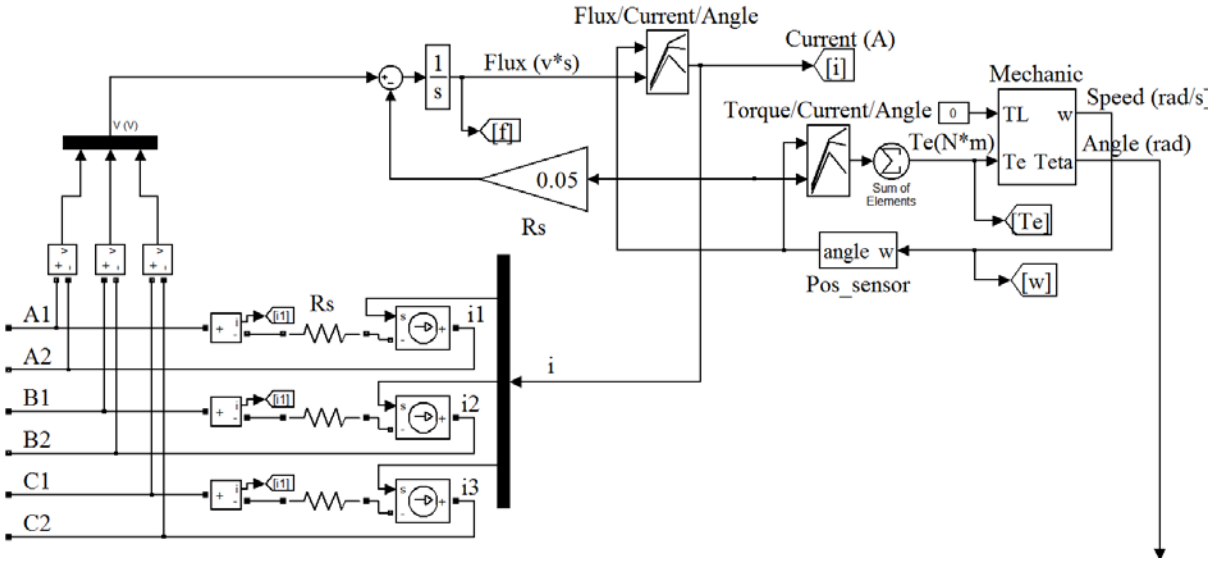

Figure 3.16 Simulation model of the three phase SRM

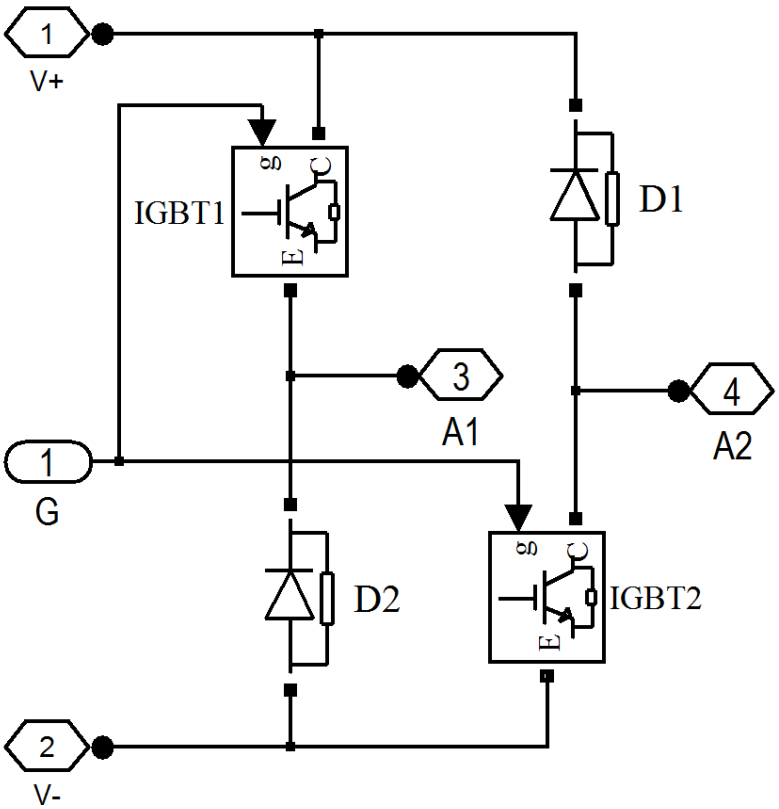

Figure 3.17 Simulation model of the asymmetric bridge converter

The simulation waveform of the phase voltage and phase current are shown in Figure 3.21 at the speed of 1500 rpm. Figure 3.22 and Figure 3.23 show the speed and torque response at the speed of 1500 rpm with no-load and with the load torque of 10 N-m.

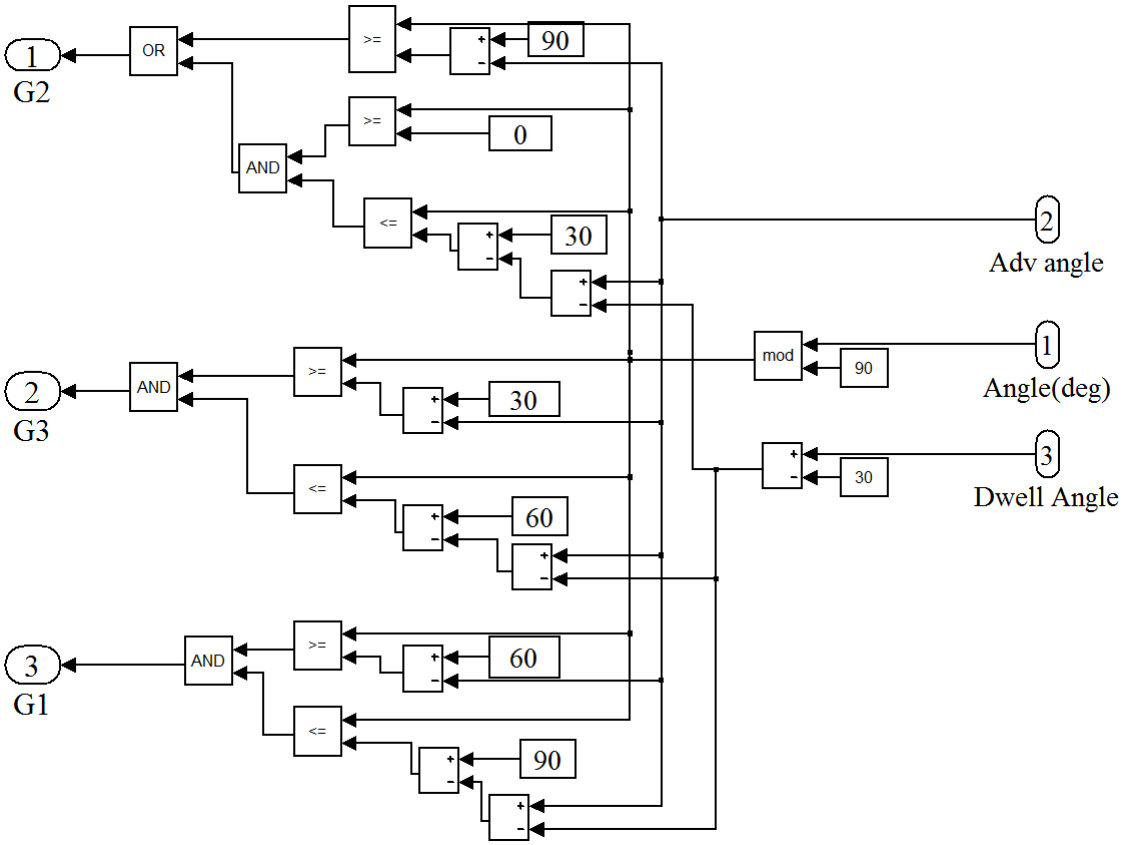

Figure 3.18 Simulation model of the position synchronization arrangement

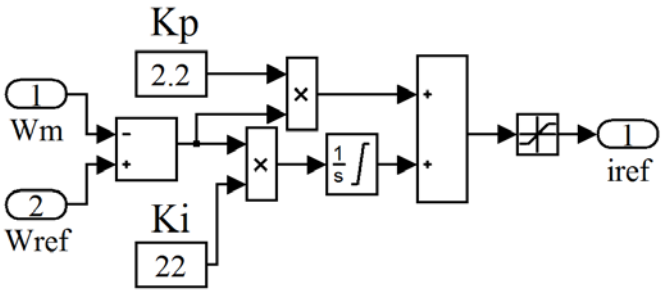

Figure 3.19 Simulation model of proportional and integral speed controller

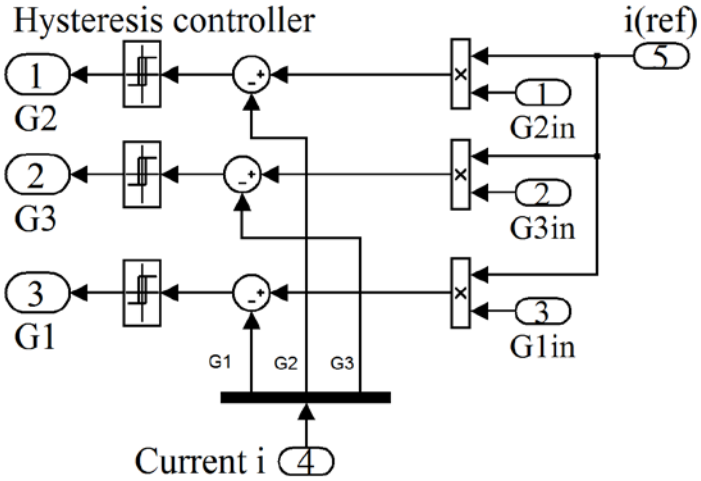

Figure 3.20 Simulation model of the hysteresis current controller

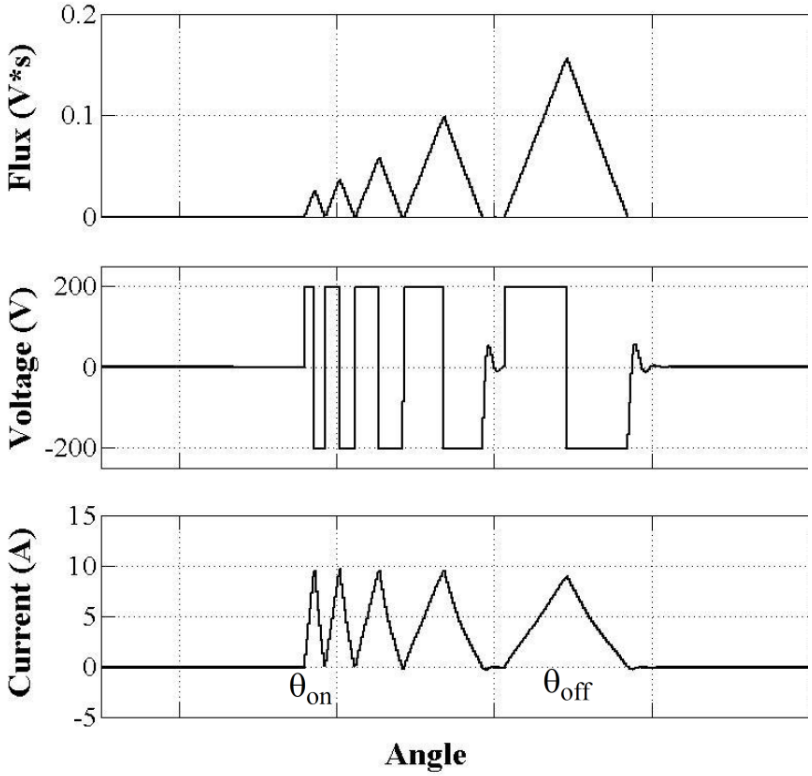

(a)

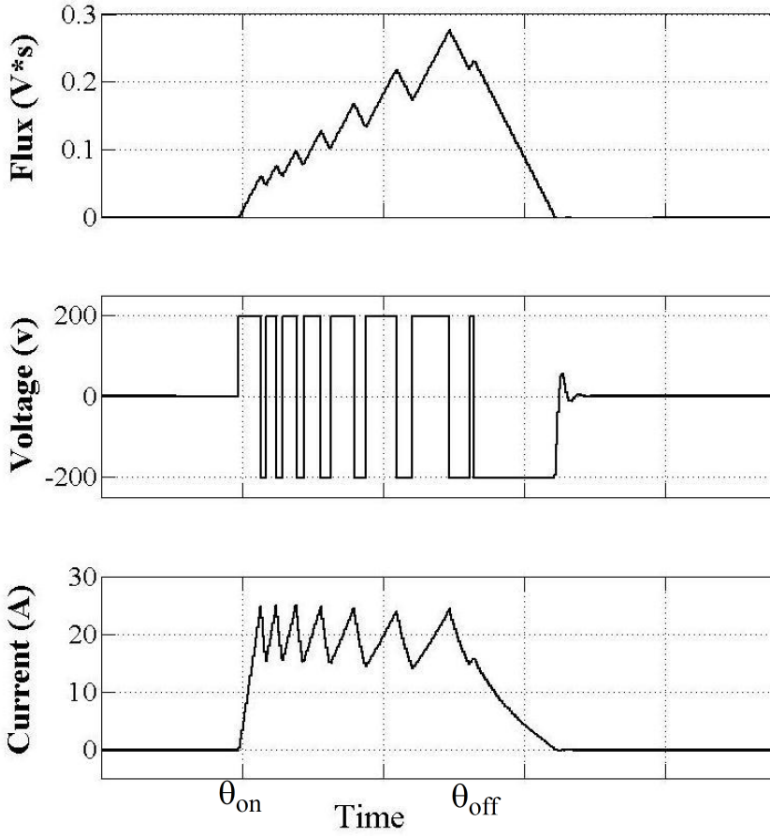

(b)

Figure 3.21 Phase voltage and phase current at 1500 rpm with (a) no-load and (b) load torque of 10 N-m

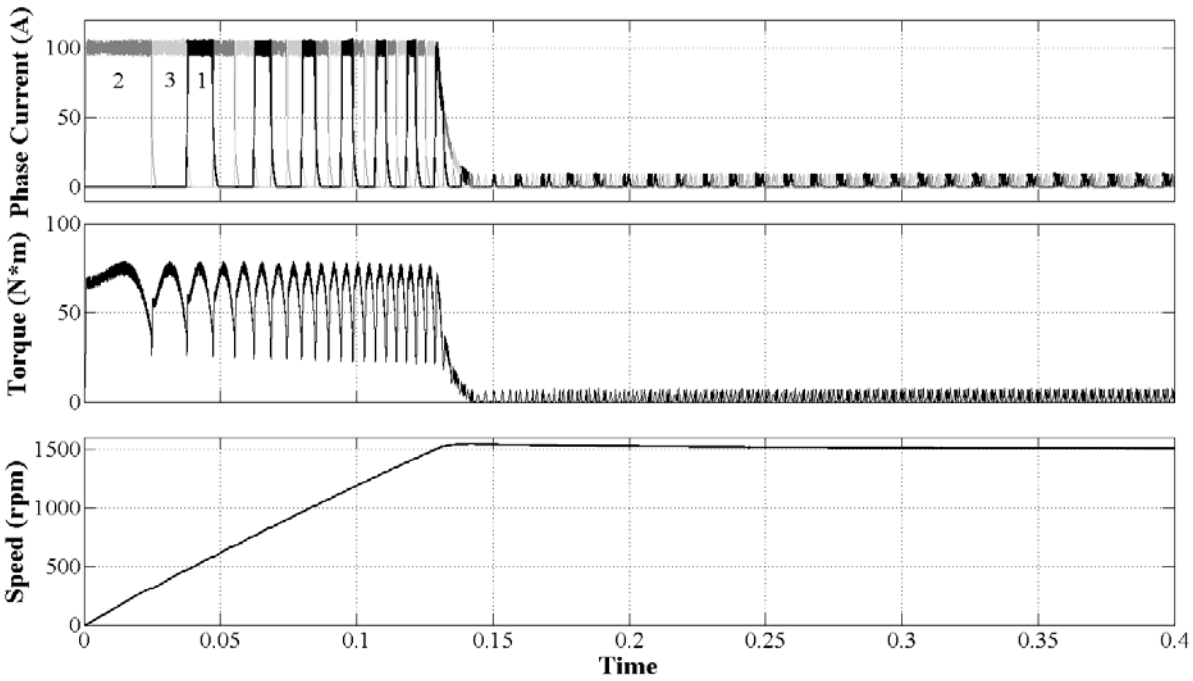

Figure 3.22 Speed and torque response at the speed of 1500 rpm with no-load

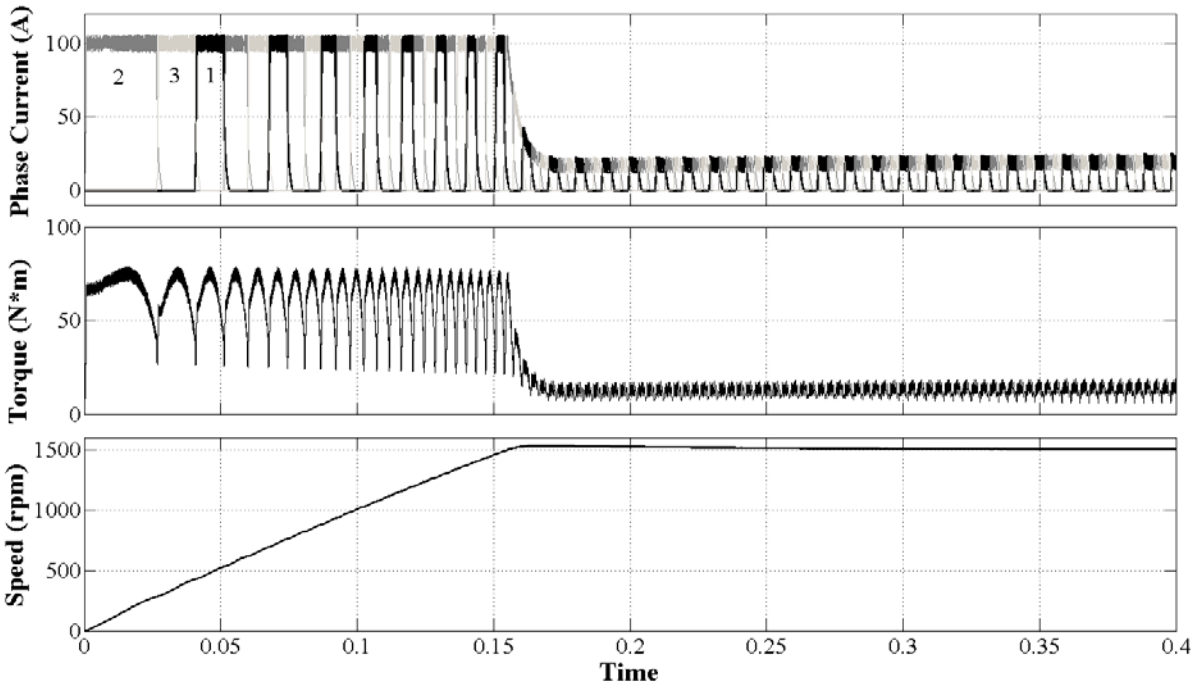

Figure 3.23 Speed and torque response at the speed of 1500 rpm with load torque of 10 N-m

Figure 3.24 shows the simuink model of the subsystem 'SC_User' which provides real time monitoring and control of the parameters. It provides flexibility to control the speed, load-torque, advance angle and dwell angle in real-time. The real-time simulation of the SRM drive is carried out with the model latency of 10µs.

The experiment is conducted to derive the torque-speed characteristics of the SRM drive. The actual speed of the motor is measured with increase in load torque while

reference speed, advance angle and dwell angle are maintained constant throughout. The speed PI controller compensates the effect of increase in torque by increasing the reference current. The speed remains equal to the reference speed as far as the current control is possible. Any further increase in torque results in reduction of motor speed, thus the torque limit is considered as maximum possible torque. The experiment is conducted for several speed and advance/dwell angle conditions, which results in torque-speed characteristics shown in Figure 3.25 and Figure 3.26. It shows that the modification in torque-speed characteristics is possible to meet the load requirement, via angle control scheme.

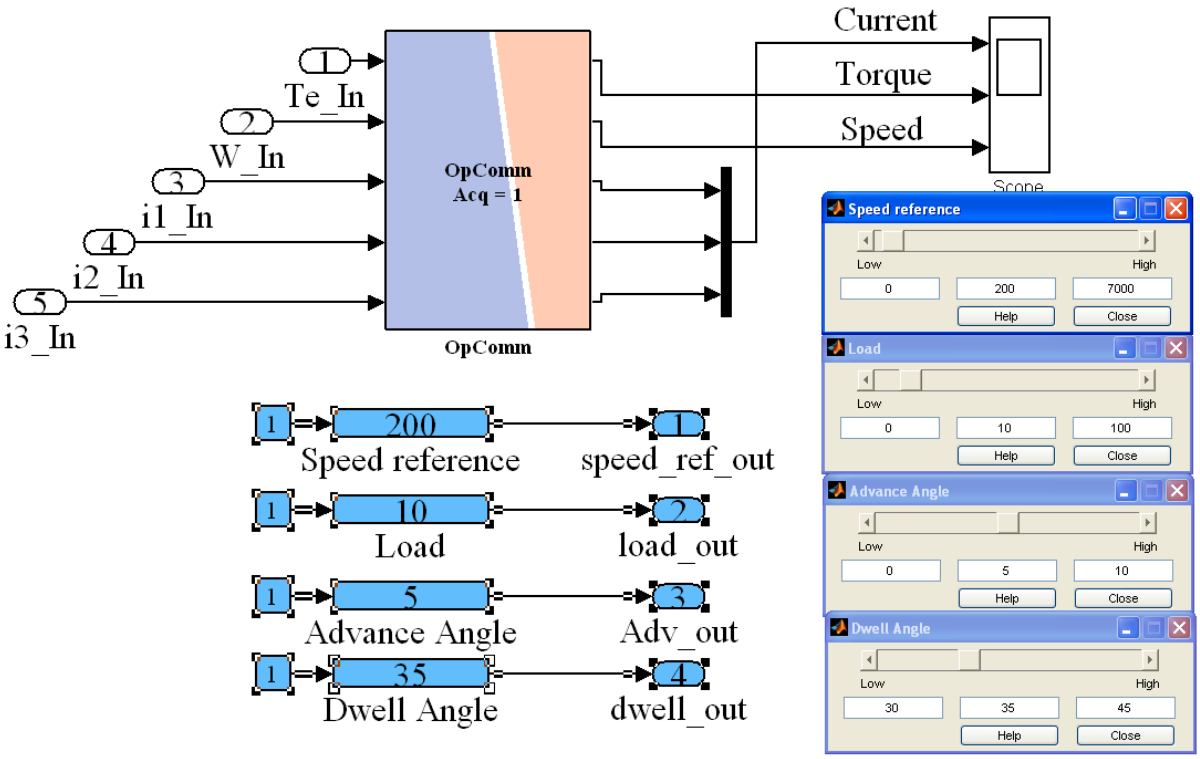

Figure 3.24 Real-time user interface to control and monitor variables

Figure 3.25 shows that the speed range can be increased by increasing the advance angle, even with constant dwell angle of 35°. But it reduces the maximum torque for the lower speed. Thus, to provide the wide range of speed and torque with the constant (fixed at low value to maximize the efficiency) dwell angle scheme, angle control scheme must be incorporated with the speed controller. Figure 3.26 shows that the increase in advance angle increases the range of speed without reducing the lower-speed torque, for the constant turn-OFF angle scheme. It reveals that higher range of torque and speed is possible even with the fixed angle control scheme by selecting the higher values of advance angle and dwell angle. The coarse rotor position sensors are enough where the angle control scheme is not required. Thus, fixed angle control scheme also reduces the implementation cost. However, efficiency of the SRM gets reduced at some extent, for higher dwell angle. Also, advance

angle and dwell angel can be fixed to suit the load demand, for the narrow-speed-band applications.

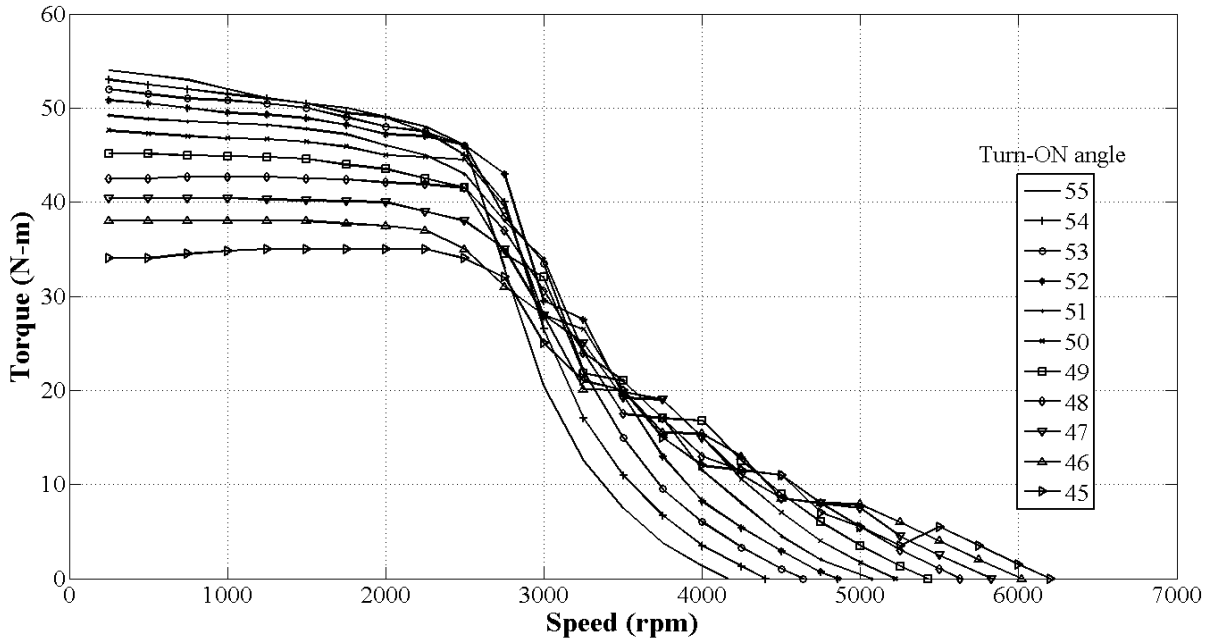

Figure 3.25 Measured torque-speed characteristics of the SRM with fixed dwell angle

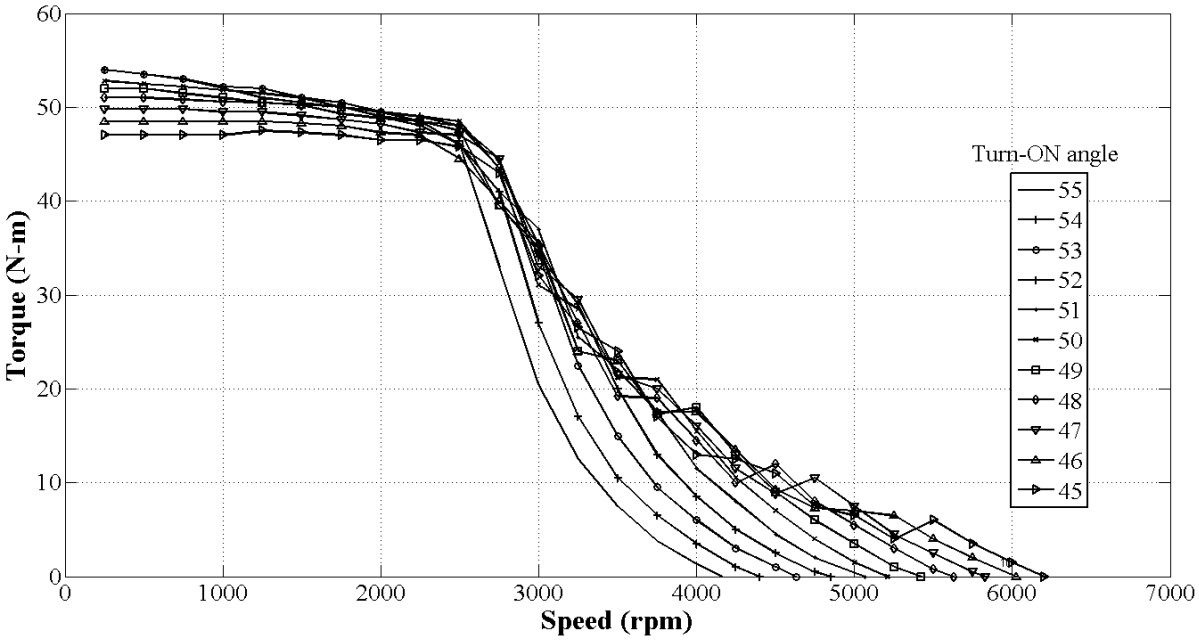

Figure 3.26 Measured torque-speed characteristics of the SRM with the constant turn-OFF angle

The real-time analog current and commutation pulse measured using DSO, are shown in Figure 3.27. It shows the current and commutation pulse of a phase at several speed and load conditions. Effect of speed and load torque on the shape of the current can be observed. It is to be noted that the rate of change of current is reduced with increase in phase inductance, which results in longer width of commutation pulse.

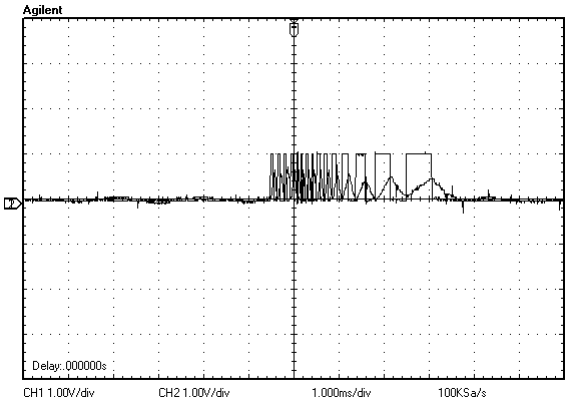

(a) at 1500 rpm with no-load

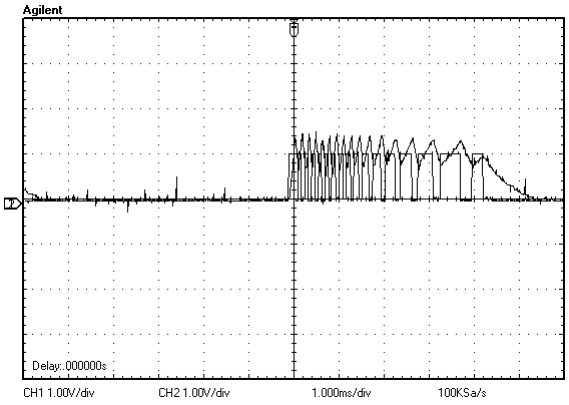

(b) at 1500 rpm with 10 N-m load

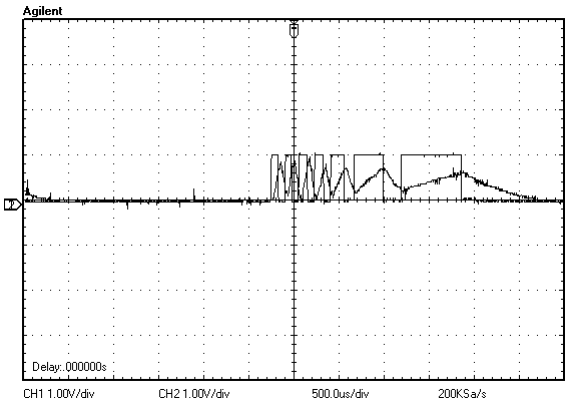

(c) at 3000 rpm with no-load

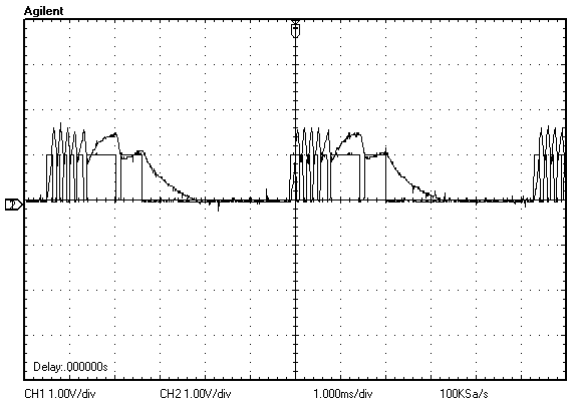

(d) at 3000 rpm with 10 N-m load

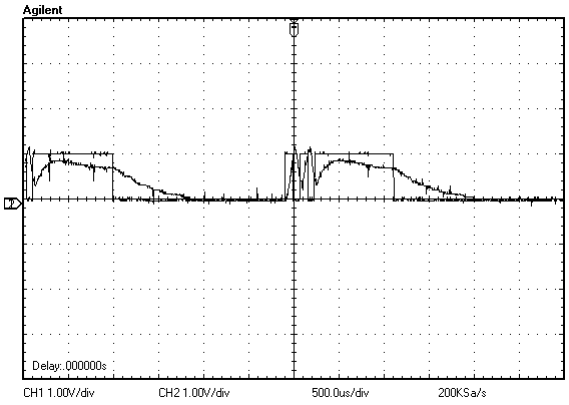

(e) at 5000 rpm with no-load

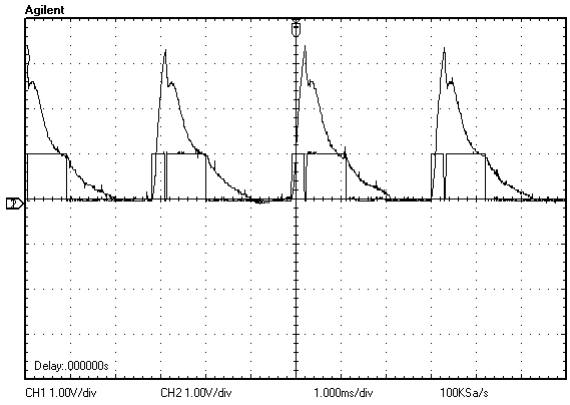

(f) at 5000 rpm with 10 N-m load

Figure 3.27 Waveform of real-time phase current and commutation pulse at the several speed and load conditions (Current scale is 20 ampere per division)

3.3 PHYSICAL MODELING OF SRM

It is beneficial if the simulation model allows variation of physical parameters of the motor and considers its effect with the minimum changes in the model. This will help in the performance investigation and design optimization of the SRM. Look-up table based method requires the experiment to be re-conducted to obtain the new magnetic characteristics for

any change in the physical parameter of the motor, which is time consuming and costly. The inductance based method also requires re-conduct the experiment to obtain the new inductance profile of the motor with the change in parameters. It also requires re-calculate the co-efficient of the Fourier series. An analytical method involves extensive calculation to find the new co-efficient with change in parameters. Likewise, none of the modelling method allows parameter variation of the motor, and each one is applicable to the specific motor model only.

A new modelling technique is proposed based on physical model of the system, which offers many advantages over conventional modelling techniques. The main advantage of the physical modelling of the system is that, it is able to consider the effect of change in physical parameters of the system and relations amongst them are clearly understood. The variable reluctance characteristic of the SRM is utilized to model a non-linearity of the SRM.

3.3.1 Physical modeling of the system

The modeling of the system involves representing a mechanical, electrical and magnetic system or even a complex interrelation in the form of differential equations or Laplace transformation. The physical modeling technique is an approach of representing a system model in the more realistic way, rather than representing a model in the form of only mathematical equations (input-output relation). The basic concept is to use electrical elements (resistor, inductor and capacitor) and electrical source from the 'simpowersystem' library to represent not only an electrical system, but also to represent a mechanical as well as magnetic system and their interrelation.

As a simple example, the basic mechanical system having mass, damping and spring is being considered. The system can be represented in the form of differential equation as-

$$F = M\frac{d^2x}{dt^2} + B\frac{dx}{dt} + Kx \tag{3.16}$$

Where 'M' is mass, 'B' is friction constant and 'K' is spring constant. The mechanical system can be represent in a transfer function form as-

$$\frac{x(s)}{F(s)} = \frac{1}{Ms^2 + Bs + K} \tag{3.17}$$

The mechanical system of (3.16) is compared with the following electrical system,

$$V = L\frac{di}{dt} + Ri + e_b \tag{3.18}$$

Each term of the equation (3.18) represent a voltage, while each term of the equation (3.16) represents a force. The comparison shows that, rate of change of displacement (velocity) is equivalent to the electrical current, mass of the system is equivalent to the inductor and friction constant of the system is equivalent to the electrical resistor, while term

'Kx' represents a opposing force of the spring which is equivalent to the back 'emf' of the electrical system. The physical model of the mechanical system is derived in the MATLAB simulink environment using 'simpowersystem' and 'simulink' library as shown in Figure 3.28. The transfer function model of the system is also shown in the figure where M=1000 Kg, B=50 N-sec/m and K=2. The physical model and transfer function model both represent the same mechanical system, and also produce-same input-output response as shown in Figure 3.29. The transfer function based model can represent an effect of input (force) on the output (displacement), while it is not able to give clear view about entire parameters of the system. The physical model of the system gives clear understanding about effect of entire parameters as well as feedback effect.

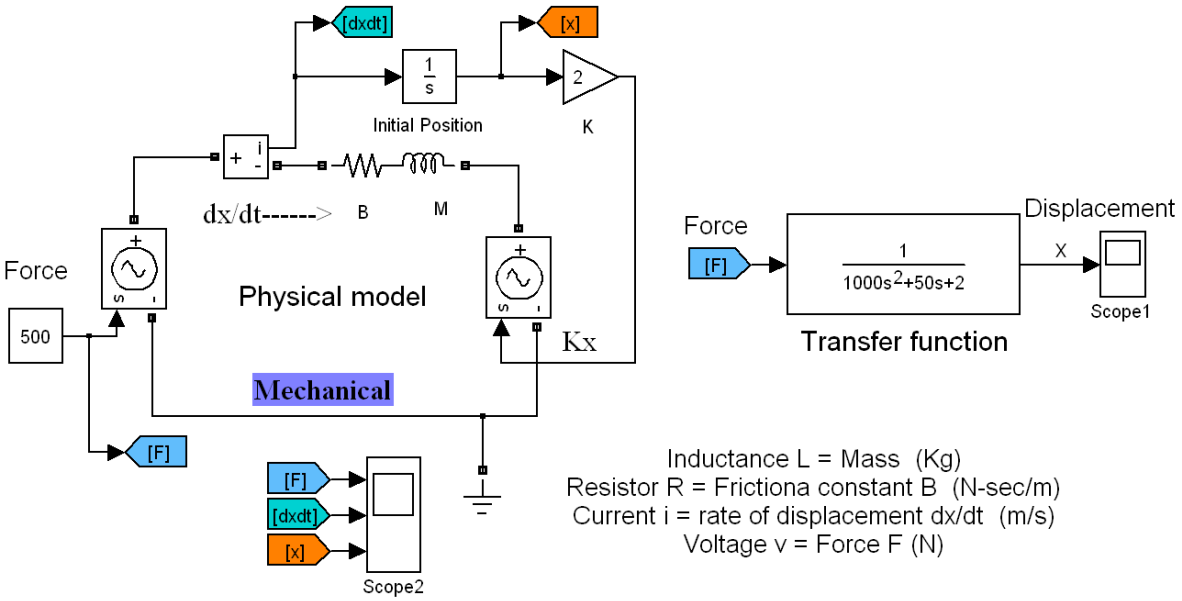

Figure 3.28 Physical model of the simple mechanical system

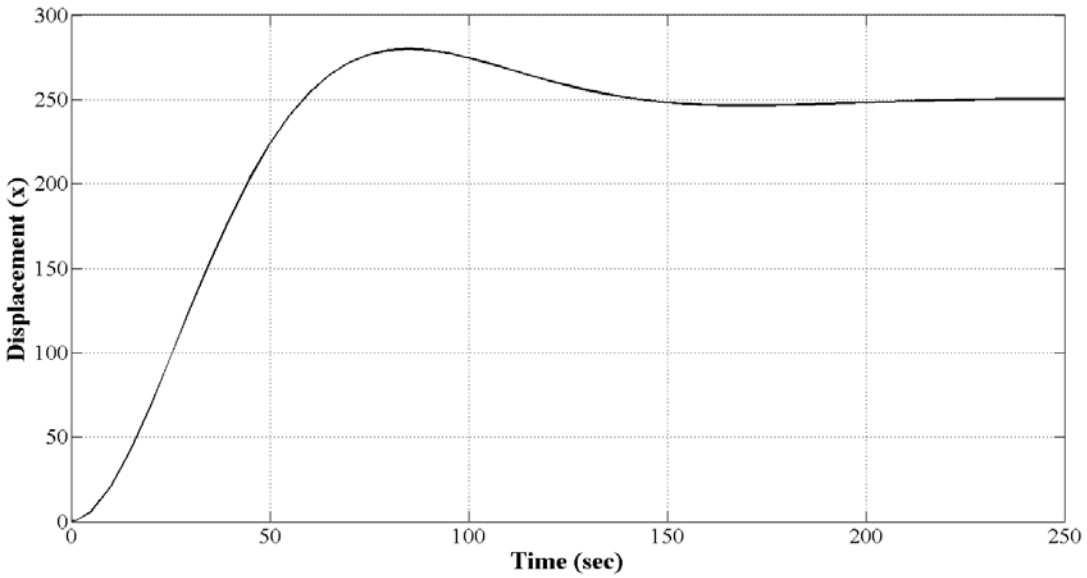

Figure 3.29 Transient response of the mechanical system shown in Figure 3.13 to the step change of 500 N-m

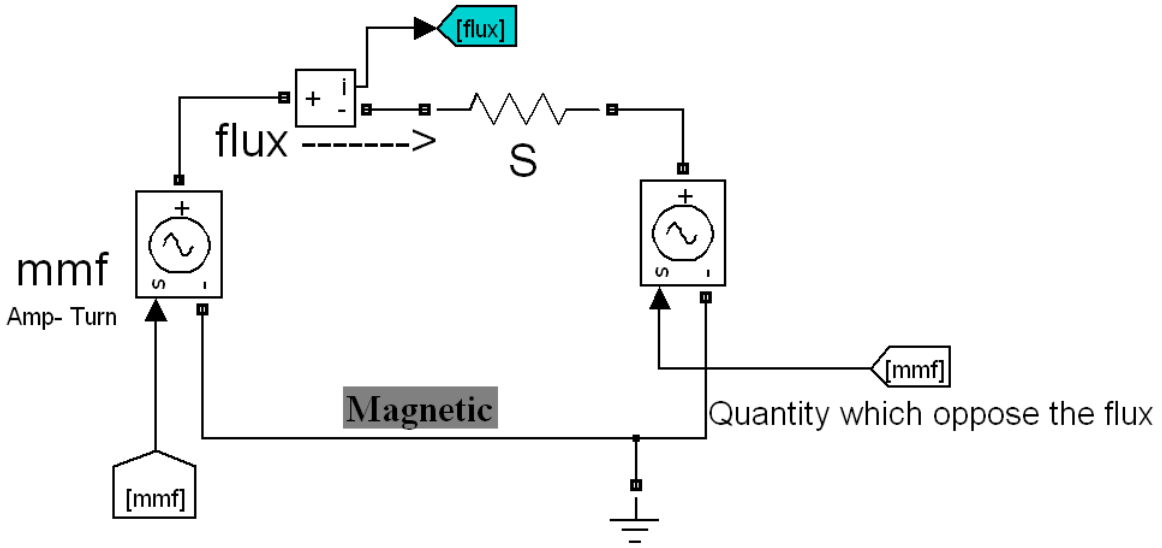

Figure 3.30 The physical model of the magnetic circuit

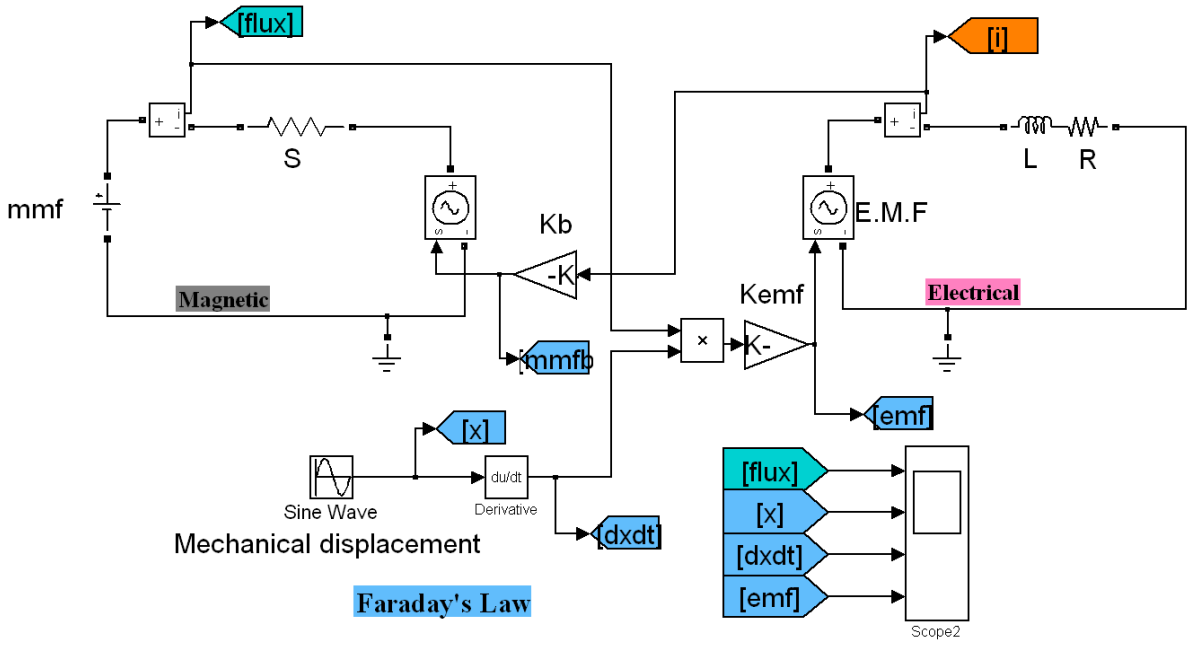

Figure 3.31 The model of the faraday's experiment of electromagnetic induction

The physical model of the magnetic circuit can be derived by comparing emf with the magneto motive force (mmf) as shown in Figure 3.30. The flux is equivalent to the electric current, while reluctance of the magnetic circuit is equivalent to the resistor. In the electromagnetic and electromechanical systems, magnetic flux or its change is responsible for the production of electric current (or emf) or mechanical force (or torque). Any energy conversion process must involve feed-back effect to endorse the 'law of energy conversion', which can be fulfilled by using controlled voltage source. Faraday's experiment of electromagnetic induction is considered as an example to represent the model of energy conversation process from the magnetic system to the electric system. It is assumed that the

constant source of mmf (Amp-turn) is available to feed the magnetic energy, and the piece of wired coil is moving (sinusoidal displacement) in the constant magnetic field. Accordingly, an emf will be induced in the coil. The model of the Faraday's experiment is shown in Figure 3.31. The rate of change of displacement, amount of magnetic flux and number of coil turns decides the amount of induced emf. The sinusoidal displacement of the coil is represented by the 'sine wave generator', while the feedback effect of the induced electric current on the magnetic flux is represented with the help of controlled voltage source. Thus the physical model of the system can represent the electro-mechanic-electrical system in the more clear way, so that the process of energy transfer and effect of each parameter can be analyzed and understood more conveniently.

The DC motor is an example of interrelation of the electrical, mechanical and magnetic system. However, field flux is assumed to be constant and thus developed torque becomes a function of armature current. The physical model of the DC motor is shown in Figure 3.32. The model gives more clear representation of various effects viz. mechanical (motor) speed on the electrical (back) emf, electrical current on the developed mechanical torque, load torque and about all the electrical as well as mechanical parameters. The physical model helps to understand the interrelation and cause-effect amongst all the variables, rather than representing a system as only input-output relation. The physical model of the SRM is derived by modeling the non-linear reluctance.

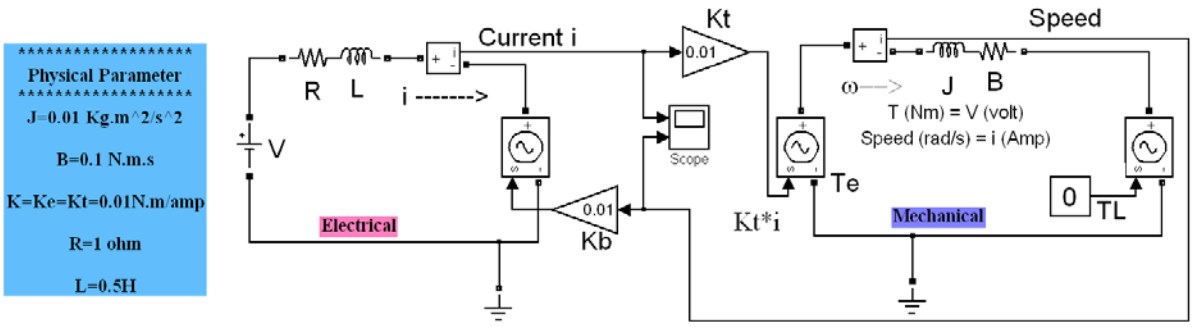

Figure 3.32 The physical model of DC motor

3.3.2 Physical Modelling of SRM

The principle of operation of the SRM is based on the varying reluctance characteristics, for which the motor is named as "Switched Reluctance Motor". The variable reluctance characteristic of the motor is utilized to model the non-linearity of the SRM. The block diagram of the SRM physical model is shown in Figure 3.33, where main aim is to derive non-linear flux-current-angle relation from the few design parameters. The SRM has an independent phase windings wound only on the stator, while rotor has no winding. The reluctance of the motor depends on the angular position of the rotor unlike the conventional

motors. The main cause of the reluctance variation is the variation in the airgap with the

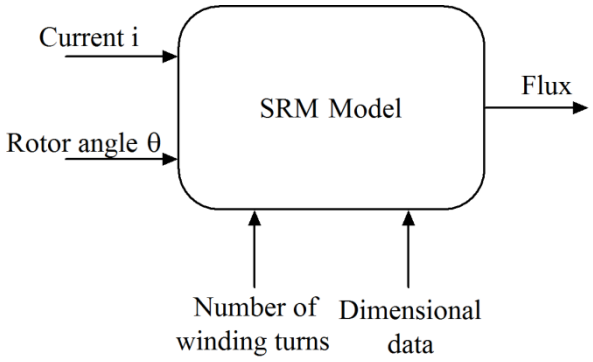

Figure 3.33 Block diagram of SRM physical model

change in rotor angle. The SRM is represented as an electromagnetic system consisting of winding, core and airgap in the magnetic path as shown in Figure 3.34, where only one

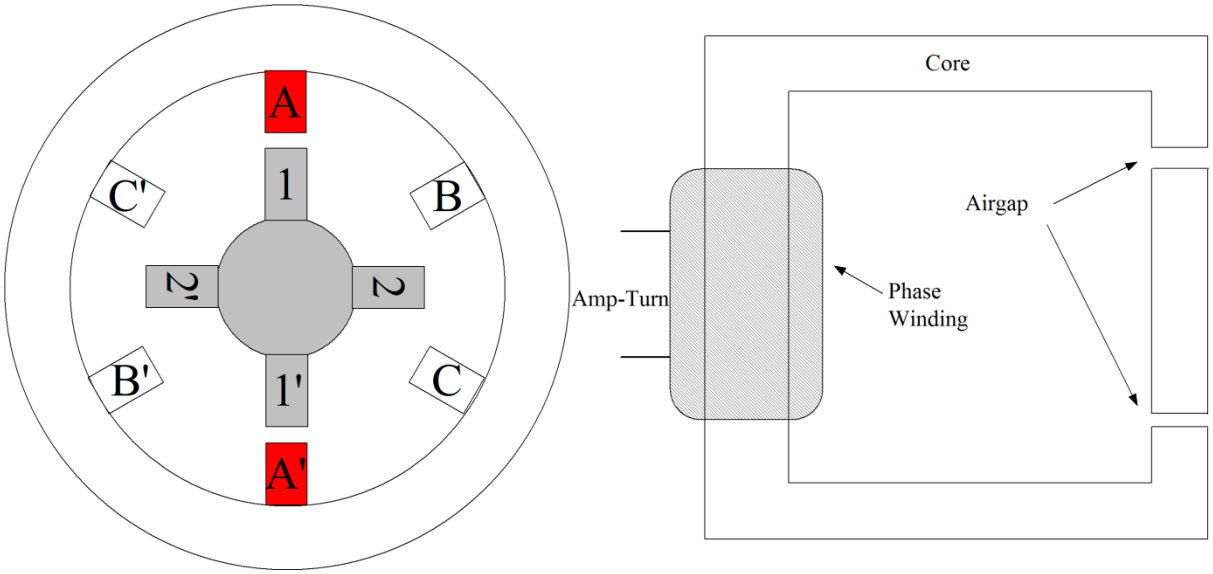

Figure 3.34 Magnetic circuit of the SRM

phase is being considered. The phase current produces an MMF (ampere-turn) in the magnetic core of the SRM. The magnetic circuit of the SRM can be expressed as-

$$MMF = \psi \cdot S \tag{3.19}$$

where, 'Ψ' is the total flux and 'S' is the total reluctance of the magnetic path. The total reluctance of the magnetic circuit can be represented as-

$$S = S_s + S_r + S_g \tag{3.20}$$

where, 'S_s', 'S_r' and 'S_g' are the reluctances of stator, rotor and airgap respectively. The reluctance of the stator and rotor are constant and also much small as compared to the reluctance of the airgap. The reluctance of the airgap depends on the rotor angle, which can be expressed as-

$$S_g = \frac{2 * l_g}{\mu_0 \cdot A_g} \tag{3.21}$$

where 'l_g' is the radial airgap, 'A_g' is the cross-section area and 'μ_0' is the permeability of the air. It seems that the variation in the reluctance, with rotor position, is an effect of variation of cross-section area only, because the radial length l_g and permeability of the air μ_0 both are constant. The cross-section area can be expressed as-

$$Ag = d \cdot G \tag{3.22}$$

where 'd' is the width of the rotor pole and 'G' is the active length of the rotor (stator). The variation of the cross-section area with the rotor position is shown in Figure 3.35 and expressed as-

$$Ag = [x + y \cdot d(1 - \cos(\theta_e)] \cdot G \tag{3.23}$$

where 'x' and 'y' are constant and needs to be determined and 'θ_e' is electric rotor angle in radian. The variation of the mechanical rotor position from θ=0 to θ=45, represent a

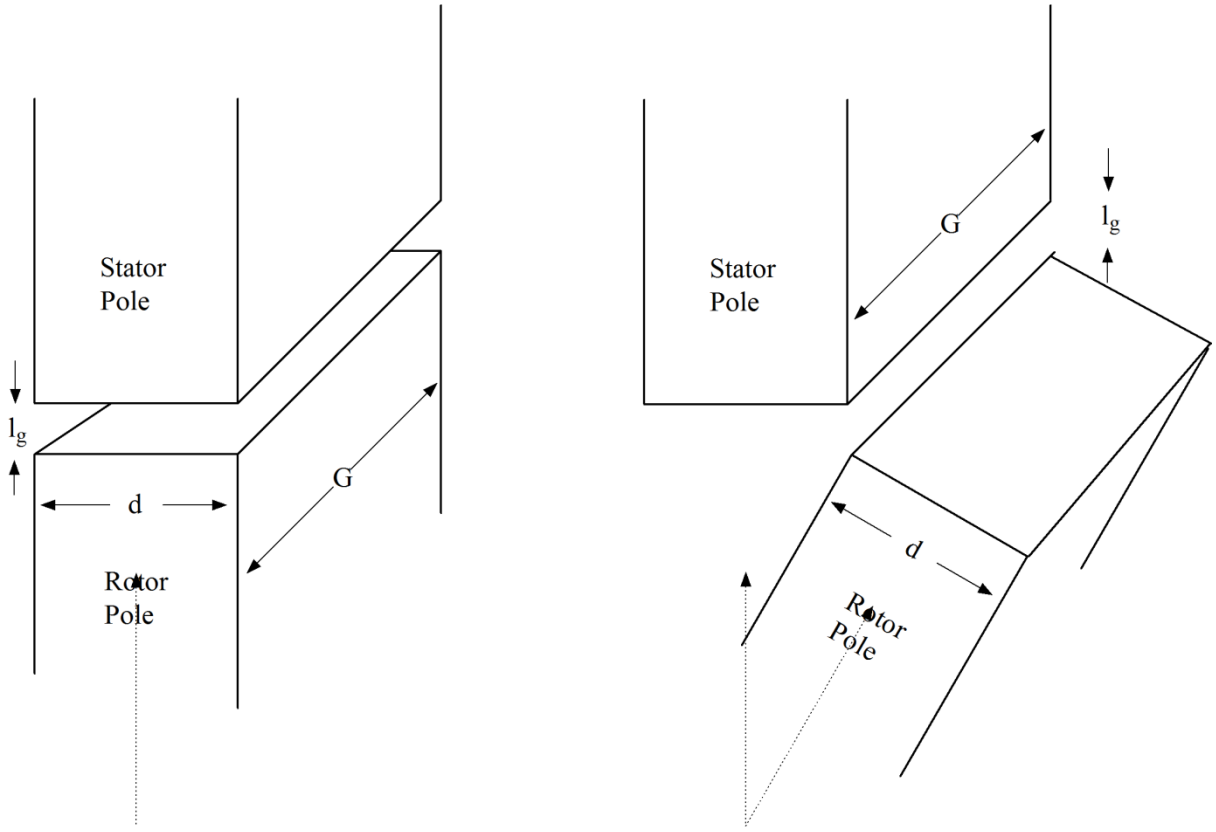

Figure 3.35 Variation of effective cross-section area

variation in the electrical rotor angle form θ_e=π to θ_e= 2π (for the 6/4 pole machine). The effective cross-section area A_g is a function of rotor angle and its value is maximum at the aligned rotor position (θ=0°). The effective cross-section area A_g reduces with increase in the rotor angle, and it becomes minimum at the unaligned rotor position (θ=45°). In contrast, the airgap reluctance S_g is minimum for the maximum cross-section area and vice-versa. The total reluctance of the motor is expressed as a function of rotor angle as-

$$S = \frac{2 * l_g}{\mu_0[x + y \cdot d(1 - \cos(\theta_e))] \cdot G} \quad (3.24)$$

where, reluctance of the magnetic core is neglected. The minimum and maximum reluctance of the motor are calculated from the value of flux at the aligned and unaligned rotor position respectively. The value of 20 ampere is considered for the current which is lower than the high-saturation current. The minimum and maximum values of the reluctance come out to S_{min} = 909 Amp-turn/Wb and S_{max} = 26000 Amp-turn/Wb, respectively. The value of the constant 'x' and 'y' are derived from the maximum and minimum reluctance of the motor respectively. The reluctance of the SRM is expressed as a function of rotor angle as-

$$S = \frac{2 * l_g}{\mu_0[0.04 + 18 \cdot d(1 - \cos(\theta_e))] \cdot G} \quad (3.25)$$

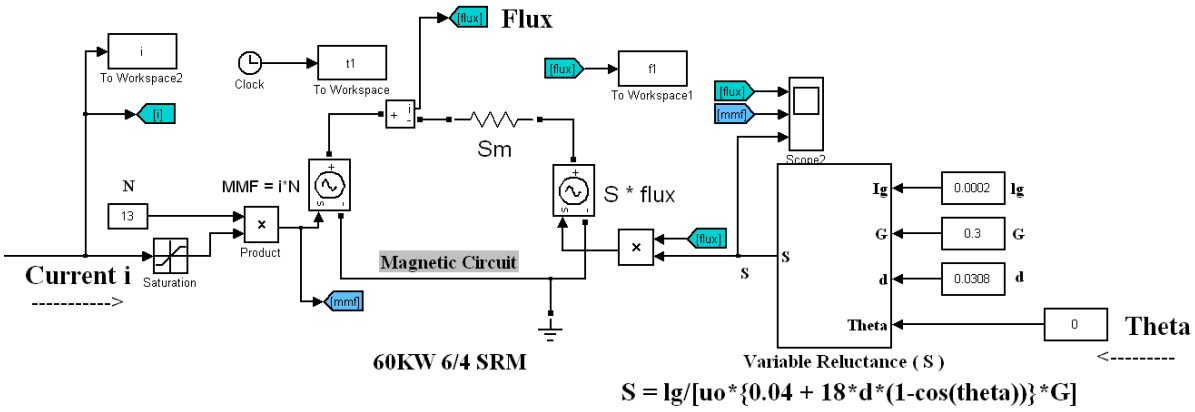

Figure 3.36 Physical model of the SRM

The physical model of the SRM is derived using equation (3.25) as shown in Figure 3.36, which represents a variable reluctance and magnetic model of the SRM. The model has phase current and rotor angle as input to generate a flux as an output. The rotor angle and motor dimensions decide the value of reluctance of the motor, while phase current decides ampere-turns of the magnetic source. The effect of the saturation is added by limiting the current at the 25 ampere, which does not affect an actual phase current of the motor. The magnetic characteristics derived from the physical model of the SRM are shown in Figure 3.37. The magnetic characteristic of the physical model shows a close approximation to the actual magnetic characteristics for the unsaturated region. However, in this model, the flux is saturated even at the unaligned rotor position, because the maximum current is limited to 25 ampere. Instead of limiting the current, a method is used where flux saturation effect is transposed to the current saturation using look-up table as shown in the Figure 3.38. The Figure 3.39 shows the magnetic characteristics represented by the physical model of the motor. It shows the close approximation of the motor magnetic characteristics

even at the higher current; however the effect of variation in flux-density with the rotor angle is not considered.

The results and comparison validate the proposed physical modeling technique of the SRM. The proposed method of the physical modeling is also applicable for the SRM having different pole geometry and rating. The summary of the physical modeling is covered in brief as-

- The simulation of the physical modeling method is fast compared to all three methods of the simulations.
- It involves least calculation and required a minimum data of the motor geometry.
- The modelling technique is more flexible, which reduces the time in case of changing design parameters or even motor geometry.
- It gives more clear understanding of energy transformation from one form to other, as well as the effect of the parameters.

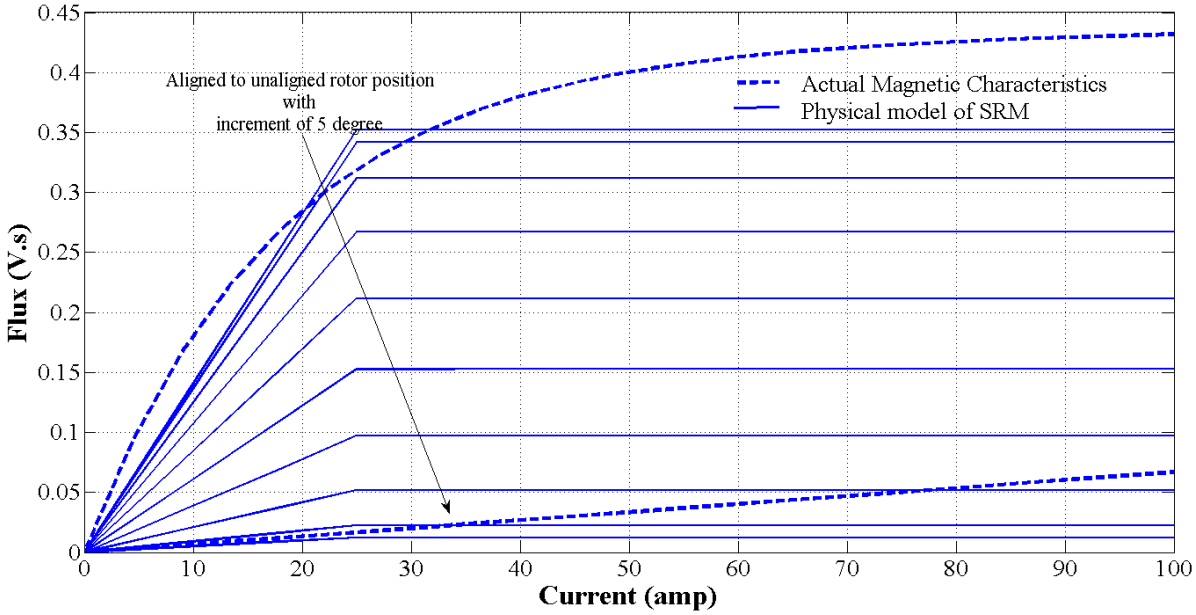

Figure 3.37 The magnetic characteristics derived from the physical model of the SRM

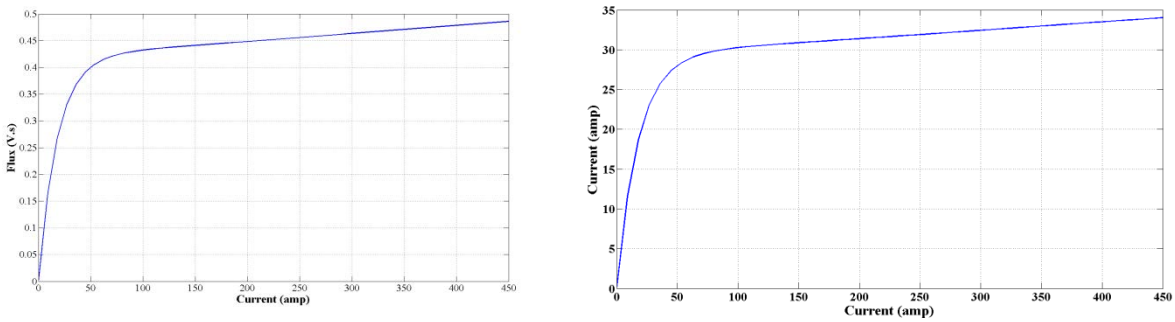

(a) Magnetic saturation (b) Current saturation

Figure 3.38 The transpose effect of the magnetic saturation to the current saturation

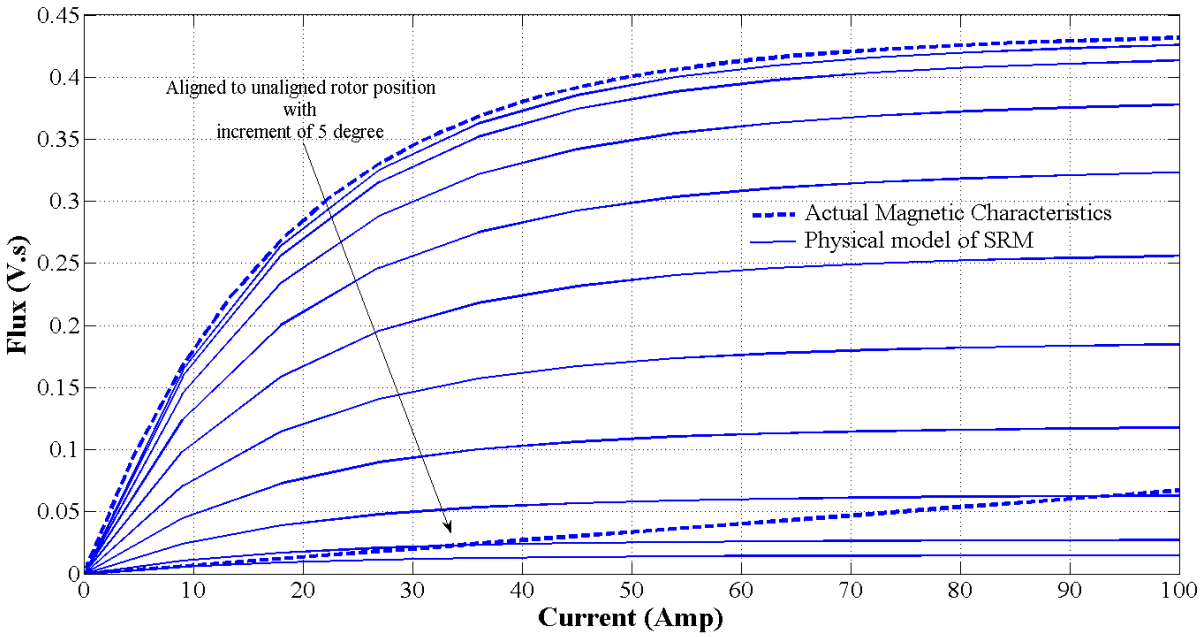

Figure 3.39 The magnetic characteristics of SRM represented by the physical model

3.3.3 Physical model with virtual realization

The physical model is derived from the geometrical data of the SRM; at the same time it is also possible to produce the three-dimensional (3D) moving visualization of the motor with the original aspect ratio. The virtual reality toolbox is introduced in brief which can add a visualization effect to the simulink model.

The MATLAB offers a 3D animation simulink product, which is a solution for interacting with virtual reality models of dynamic systems over time. It extends the capabilities of the simulink software into the world of virtual reality graphics. Complete working environment in the simulink 3D animation product provided with the additional components. The standard Virtual Reality Modeling Language (VRML) is being used to create virtual world (3D scenes). The V-Realm Builder software is used to create and edit VRML code with the MATLAB software. The Virtual Reality (VR) tool box of the MATLAB can create and define dynamic system with the simulink model. It is possible to view the moving 3D scenes using the VRML viewer of the MATLAB. The 3D animation is driven by the signals from the MATLAB simulink software, and it is possible to change the positions and properties of the objects in a virtual world while running a simulation.

The 3D animation model of rotor of the SRM is developed, which can run with the simulation model of the motor. The simulation model is shown in Figure 3.40 while the VRML editor and viewer are shown in Figure 3.41. The 3D model of the rotor is designed using two 'box' elements and one 'cylinder' element using the VRML editor. The 'VR sink' tool box provides the interaction to the MATLAB simulink environment with the VRML editor and viewer. The active length of the motor decides the length of the both boxes and length of the

cylinder. Two boxes form the four rotor poles, thus width of the boxes is decided by the rotor pole arcs, while the rotor diameter decides the height of the boxes. The synchronized rotation of both box simulate the visual effect of the moving rotor. The rotor angle of the motor from the simulation model decides the rotation of the boxes and thus rotation of the rotor. This animation gives the 3D visualization of the rotor which is driven by the simulation software in run time. It is also possible to view the 3D animation of the rotor at any viewing angle and distance while simulation is running.

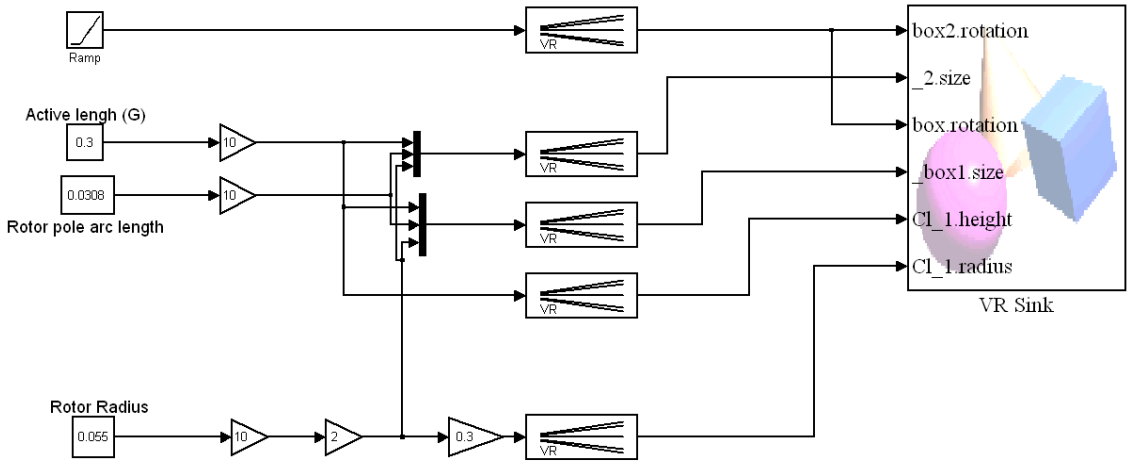

Figure 3.40 Virtual realization simulink model of the SRM

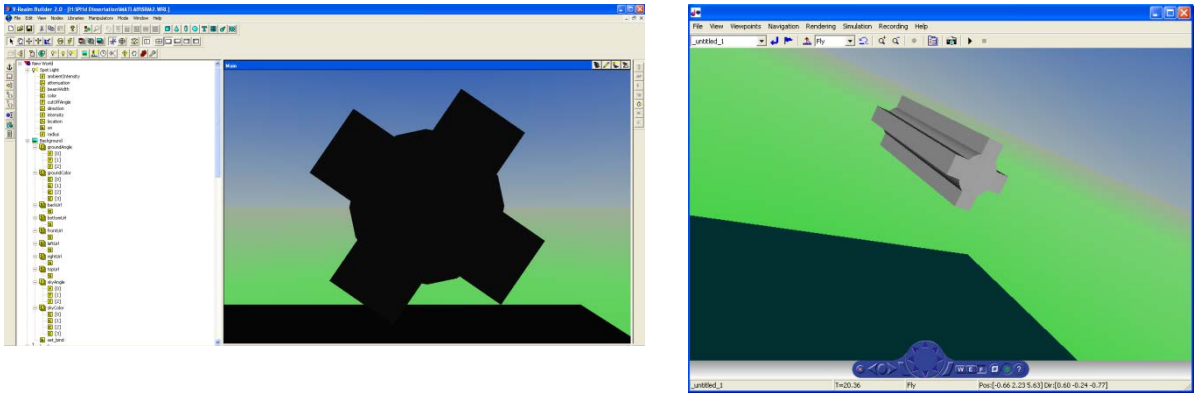

(a) (b)

Figure 3.41 (a) V-Realm Builder and (b) VRML viewer

3.4 CONCLUSION

With the advancement in simulation and software packages it becomes more practical to model a non-linearity of the SRM with accuracy, ease and time-saving. Implementation of the standard methods like look-up table based approach and analytical approach, becomes more convenient. Users have a choice to select a modeling technique based on accuracy, cost, time and applications. The concept of physical modeling and 3D visualization adds a new height to the simulation and modeling of the physical system. Modeling of the power electronics becomes more easy, realistic and practical with the 'simpowersystem' library.

Real-time simulation and FPGA base implementation increase the limit of model latency which provides an accuracy of simulation for even more complex model and current overshoot. It also reduces the significant time of simulation. Overall, an approximation of the physical system comes closer to the real one and thus, to investigate the performance of the SRM and drive becomes more accurate and ease.

Chapter 4: DEVELOPMENT OF LOW COST SRM DRIVE

The low-cost SRM drive is designed and developed in the present work. The ac small signal modelling technique is proposed for linearization of the SRM model and accordingly speed PI controller is designed. The performance of the drive is investigated under the open-loop and closed-loop condition in this chapter. A prototype experimental setup is also developed with the four-phase, 500W, 8/6-pole SRM to validate the simulation results.

4.1 INTRODUCTION

The main objective of this work was to explore the potential of the SRM for the variable speed drive and constant speed drive applications. The SRM was developed in 1800s but apart from the few drive applications they have not been widely applied. The SRM is found most suitable candidate for the electric bicycle [31] and electric vehicle propulsion applications [74]. Now, with emphasis on energy efficiency, it is felt by the researchers that the SRM is ready to take more potential role in applications viz. industrial equipments and domestic devices. Present scenario is that number of converter and controller modules are readily available for the medium size (1-75KW) Induction motors and Brushless DC motors, which reduces the overall cost of the drive. Thus the cost of the SRM drive must be competitive with a conventional motor drive system. It makes necessary for the SRM drive to provide the low-cost control solution, nevertheless SRM must require rotor position sensing and precise phase excitation in addition.

The low-cost SRM drive is developed in the present work which employs one switch per phase type converter and low frequency PWM controller. The low cost controller, that provides all the necessary functions of the variable speed drive, is developed for the four phase SRM drive. The ac small signal modelling technique is proposed for linearization of the SRM model and accordingly speed PI controller is designed. The performance of the drive is investigated under the open-loop and closed-loop condition. Both the simulation and experimental investigations are conducted for the proposed SRM drive. The prototype drive is developed with the four phase SRM of 500W having 8 stator pole and 6 rotor pole for the experimental validation. The RT-Lab is used as hardware-in-loop (HIL) controller to implement the controller for the ease of implementation; however this implementation is also possible with the fully analog electronics. The position sensing arrangement is developed using only two optical sensors for the four-phase SRM.

4.1.1 Prototype four phase SRM

The prototype SRM used is shown in Figure 4.1(b) where the single phase induction motor is also shown to compare its size with SRM. The power/weight ratio of the SRM is quite higher than that of the compared IM. The inertia of the rotor is also comparatively lower than the IM, which is due to their salient pole winding-free structure. The geometry of the four phase SRM is shown in the Figure 4.1(a). The detail parameters of the prototype SRM are listed in the Table 4.1.

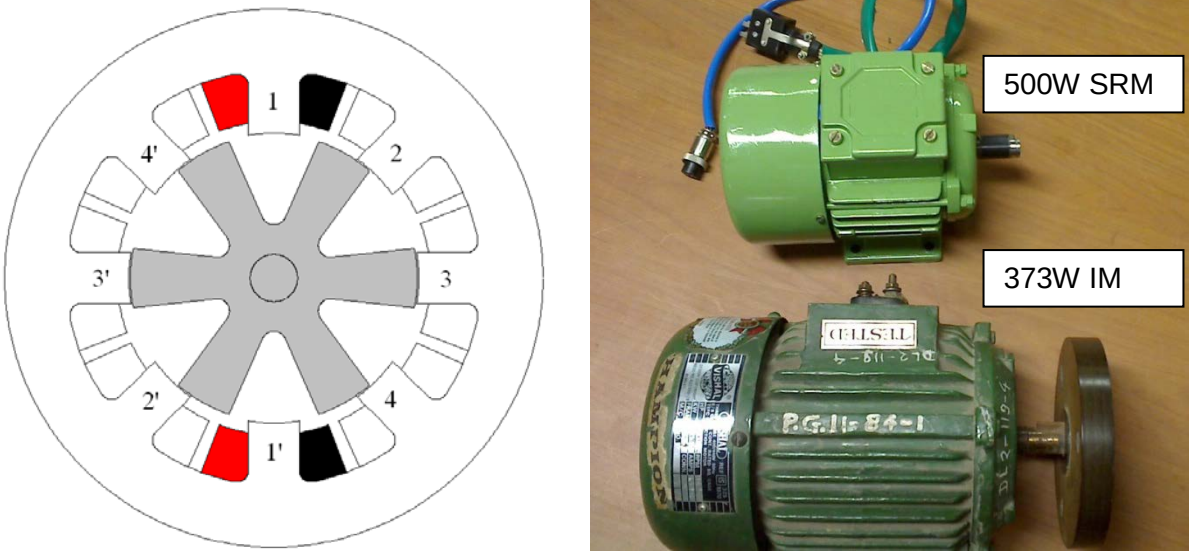

(a) (b)

Figure 4.1 (a) Cross section of the prototype 500W, 8/6 pole, four phase SRM (b) Photograph of the prototype SRM to compared it in size with the 370W single phase IM

Table 4.1 Details of the prototype SRM

Motor parameters	**Value**
Rating	500W, 150 V (Phase voltage), 3.5A
Number of phase	4
Number of stator pole	8
Number of rotor pole	6
Winding resistance	4.5 Ω/phase
Outer diameter of the stator	90.8mm
Inner diameter of the stator	48.6mm
Outer diameter of the rotor	48.4mm
Inner diameter of the rotor	18.0mm

4.1.2 Low-cost position sensing arrangement

It is true that precise synchronization of the phase pulse with the angular rotor position is must for the SRM, but it does not necessitate the use of costly high resolution encoders. The resolution of the position sensor required is relatively coarse as compared to the transducer used on a motion control applications. In fact, it needs to have only the same number of pulses per revolution as the number of rotor poles, because the position sensor feedback serves only to switch the phases ON and OFF. The high resolution encoder is required only with the high performance drive applications, where the current profiling, direct-torque-control (DTC) or torque sharing function (TSF) technique is adopted for the torque ripple minimization. Further, the high resolution encoder is required if the efficiency optimization algorithm is utilized for the wide speed and torque range. Simple low-cost method is used to fulfill the requirement of the position feedback, which employs optical interrupter on the stator and shutter on the rotor. The physical appearance of the position sensing arrangement with the schematic diagram is shown in the Figure 4.2. Slotted disk having teeth symmetrical to the rotor pole is attached on shaft and is in perfect synchronization with the rotor pole. Two optical light-sources are attached on the stator assembly, apart from each other at the same angular distance as the dwell angle (30°) of the motor. Slotted disk allows or blokes the transmission of light emitted by the source which generates two digital pulses 'L' and 'R', to decide commutation period of the two sequential phases 'Phase-3' and 'Phase-4' respectively. The commutation pulses of the ‘Phase-1’ and ‘Phase-2’ are derived from the commutation pulses of ‘Phase-3’ and ‘Phase4’ respectively using high speed TTL logic gates as shown in Figure 4.3. Likewise, the low-cost optical sensing arrangement requires only two sensors to produces the synchronized position pulses for the all four phases of the SRM. The pulses C_1 to C_4 decide the commutation period of the four phases. The position of the optical light-sources on the stator assembly and separation between them decide the value of the advance angle and dwell angle. The desired torque speed characteristics can be achieved by selecting the advance angle and dwell angle. Figure 4.4 shows the possibility of modifications in the torque-speed characteristics of the motor by adjusting the position of the optical sensors. The advance angle is set to the 7.5° while the dwell angle is set to 30° (minimum) by arranging the optical interrupter, which keeps the turn ON and turn OFF angles to the 22.5° and 52.5°, respectively. The advancement in turn ON angle ensures the level of current to produce the required torque at the instant of increasing inductance, particularly at the higher speed, while advancement in turn OFF angle reduces the chances of negative torque production during commutation period. The dwell angle can also be set to the higher value to meet the requirement of higher torque, but it is fixed to the minimum to have the higher efficiency.

However, more numbers of position sensors may be used to have flexibility in the torque-speed characteristics, so that shifting amongst the normal, high speed and high torque mode of operation is possible.

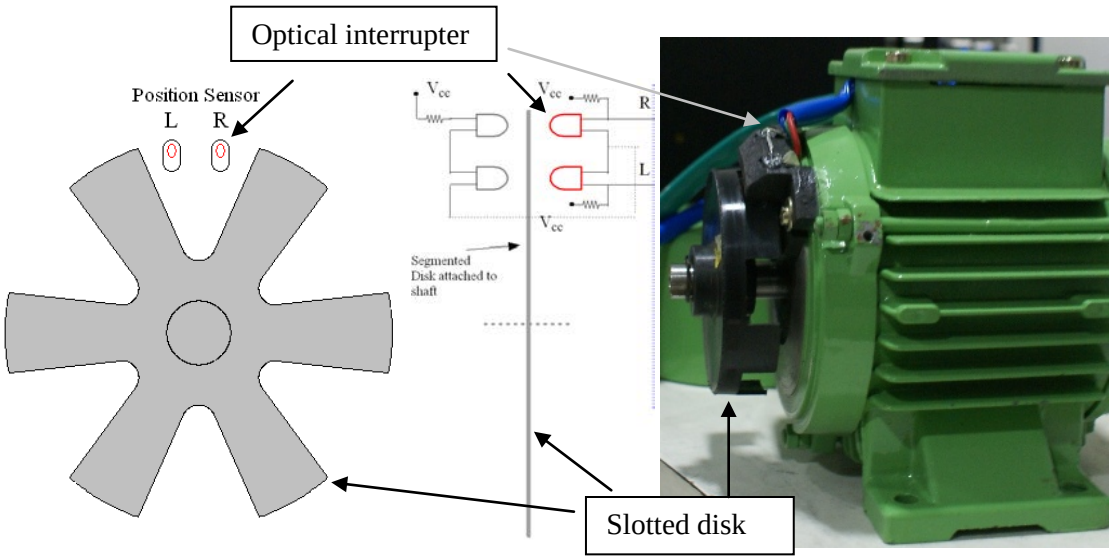

Figure 4.2 Position sensing arrangement using optical interrupter

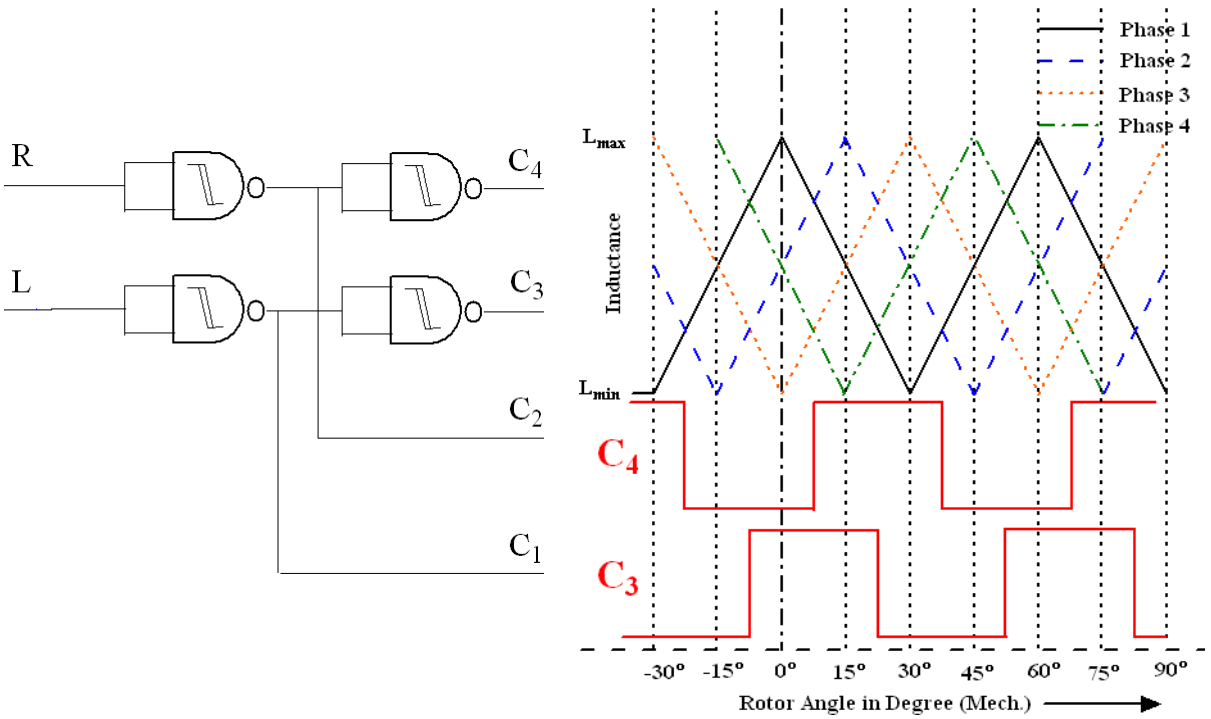

(a) (b)

Figure 4.3 (a) Logic used to derive phase commutation pulses from the optical interrupter's signals (b) Waveform of synchronized phase commutation pulses

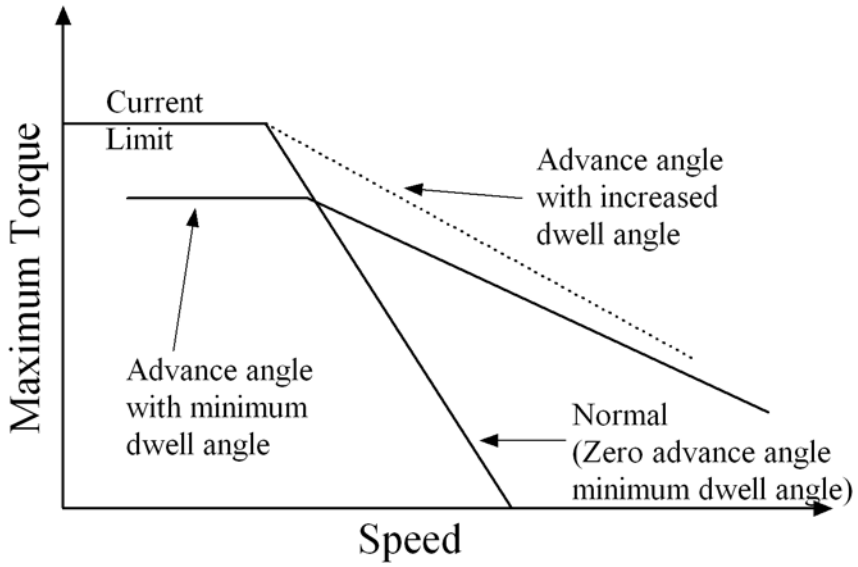

Figure 4.4 Torque-speed characteristics

4.1.3 Low-frequency PWM control

The fixed frequency PWM pulse is combined with each phase commutation pulse using logic gates as shown in Figure 4.5, where 'G1' is the GATE pulse of the phase-1. The duty cycle of the PWM pulse controls the phase current and thus torque of the motor. The frequency of the PWM pulse decides the switching rate of the converter switches. The PWM frequency can be set to very low value as compared to VFD drives that uses relatively higher switching frequency to synthesize sinusoidal AC waveform and keep down the harmonic content. The minimum frequency of the PWM pulse is decided by the maximum speed of the motor. It is because of the fact that the frequency of the PWM pulse must be higher than that of the phase commutation pulse for entire speed range. The maximum possible speed of the motor is the no-load speed with the full voltage. The frequency of the phase commutation pulse becomes 1.4 KHz at the maximum speed (14000 rpm) as the number of pulses per revolution is 6. Thus, PWM frequency is set to the 1.67 KHz, that is 1.2 time higher than maximum frequency of the phase commutation pulse. The switching frequency per phase is about 8 to 10 times lower than for the equivalent inverter (12 or 18-switched VFDs) that is why the term "Low-frequency" is used with PWM control. Switching losses are also 10 times lower which allows use of the power semiconductors having power rating lower than that in an equivalent AC drive. On the other hands, inverter of the VFDs tends to run hotter than that of the proposed low frequency PWM controlled drive, because of appreciable switching losses.

The RT-Lab is used as hardware-in-loop controller to generate PWM pulses as well as control part of the SRM drive for the ease of implementation and measurement. However, many low-cost integrated circuits (IC) have been developed which includes the control circuit necessary for a pulse width modulating regulator [103]. Thus benefits derived from the low-

cost PWM scheme include lower RFI, reduced switching losses, less electronics heating and better system efficiency and cost.

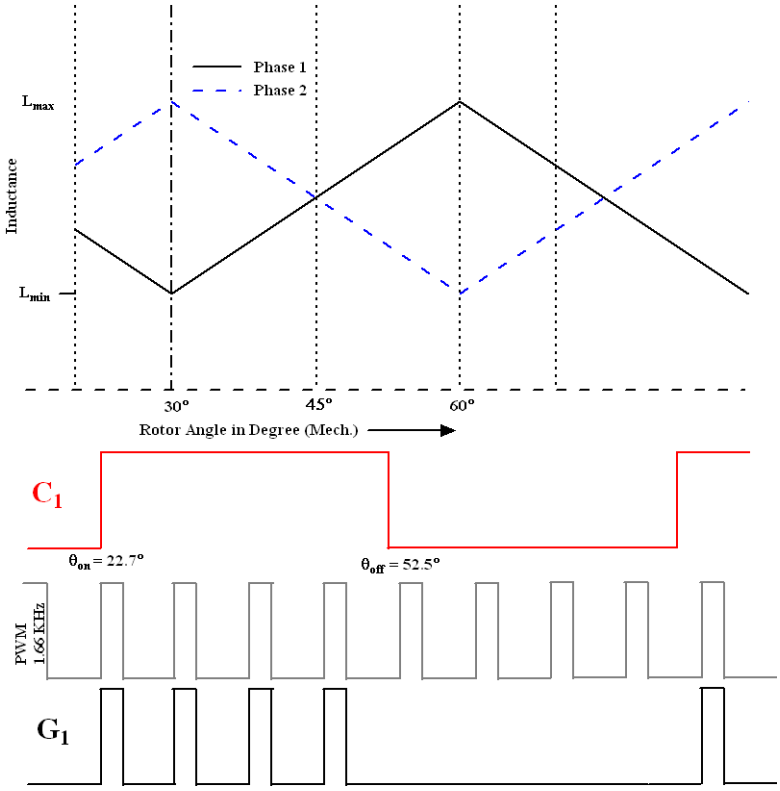

Figure 4.5 PWM current control strategy

4.1.4 Split DC Converter

The possibility of the one-switch per phase type converter adds benefits in the cost and efficiency of the SRM drive, since phase-to-phase currents need not be bipolar (or reversed). The Split DC converter topology preserve one-switch per phase [79], as shown in Figure 4.6, is used to control the power input to the SRM, and it is more justifiable with the 220V AC supply. The converter configuration also eliminates the risk of shoot-through faults that can happen in AC inverters, because they have power switches wired in series. Another benefit of the converter configuration is that motor is able to run continuously with reduced torque output after loss of a phase. Motor is able to run even with the short-circuited switching device with the reduced efficiency. The operation of the converter is as under.

One switch and one diode are associated with each phase. The Phase-1 is energized when switch M_1 is ON, and current will flow through capacitor C1, switch M_1 and Phase-1. When M_1 is turned OFF, current will continue to flow through Phase-1, capacitor C2 and diode D_1. In that process, stored magnetic energy of the phase-1 is depleted quickly by charging the capacitor C2, thus regeneration takes place. Multiphase excitation scheme is adapted to maximize the torque. At any instant two phases are ON which also minimizes the torque ripple. In general, alternative phases (1,3 and 2,4) never conduct simultaneously,

which also helps in balancing the voltage across capacitor C1 and C2. At any instant either of the two switches or two diodes are ON for regeneration of current. In the phase energized condition, voltage across particular phase becomes $+V_{dc}/2$, while it is $-V_{dc}/2$ during regeneration. Figure 4.7 explains the four possible modes of operations of the converter for the two phase excitation scheme. Mode 1 is an energized mode where switch M1 and M2 both are ON to supply the current to the phase. Mode 3 is a regenerating mode where D1 and D2 both are ON to charge up capacitor C2 and C1 respectively. The Mode-2 and Mode-4 are the effect of previously conducting phase, which is in regenerating mode before completion of their commutation period. Mode-2 and Mode-4 are energized and regenerating mode respectively, when phase-4 is at their last regeneration mode of the commutation interval. During these modes, three devices are ON at a time. Figure 4.8 explains the mode of operations using waveforms of phase current, while Table 4.2 summarizes the voltage across phase during modes of operation. Similar operation follows for all phase.

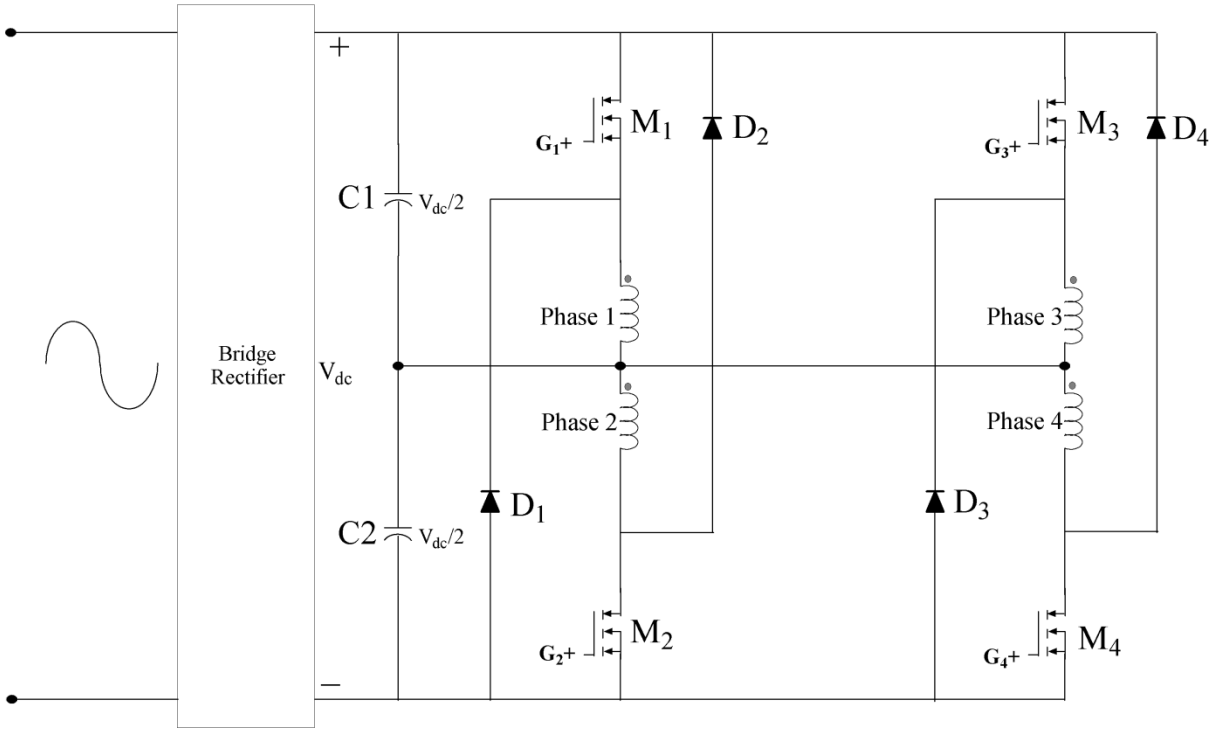

Figure 4.6 Split DC converter topology

Table 4.2 Phase voltage during mode of operation

Sr.No	Mode of operation	Phase-1	Phase-2	Phase-3	Phase-4
1	Mode 1 (M_1, M_2)	+Vdc/2	+Vdc/2	0	0
2	Mode 2 (M_1,M_2, D_4)	+Vdc/2	+Vdc/2	0	-Vdc/2
3	Mode 3 (D_1, D_2)	-Vdc/2	-Vdc/2	0	0
4	Mode 4 (D_1, D_2, D_4)	-Vdc/2	-Vdc/2	0	-Vdc/2

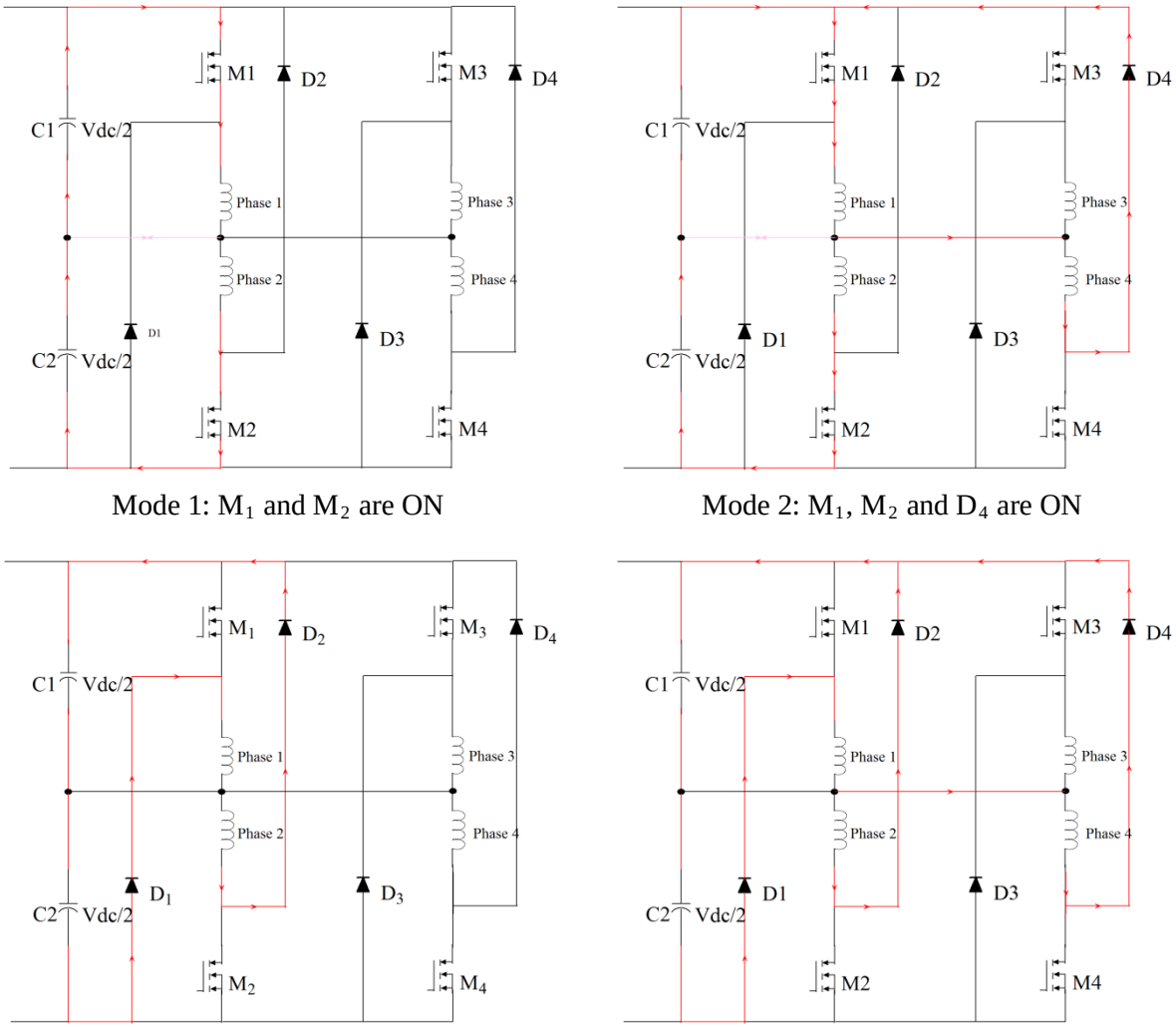

Mode 1: M_1 and M_2 are ON

Mode 2: M_1, M_2 and D_4 are ON

Mode 3: D_1 and D_2 are ON

Mode 4: D_1, D_2 and D_4 are ON

Figure 4.7 Four mode of operation of the split DC converter

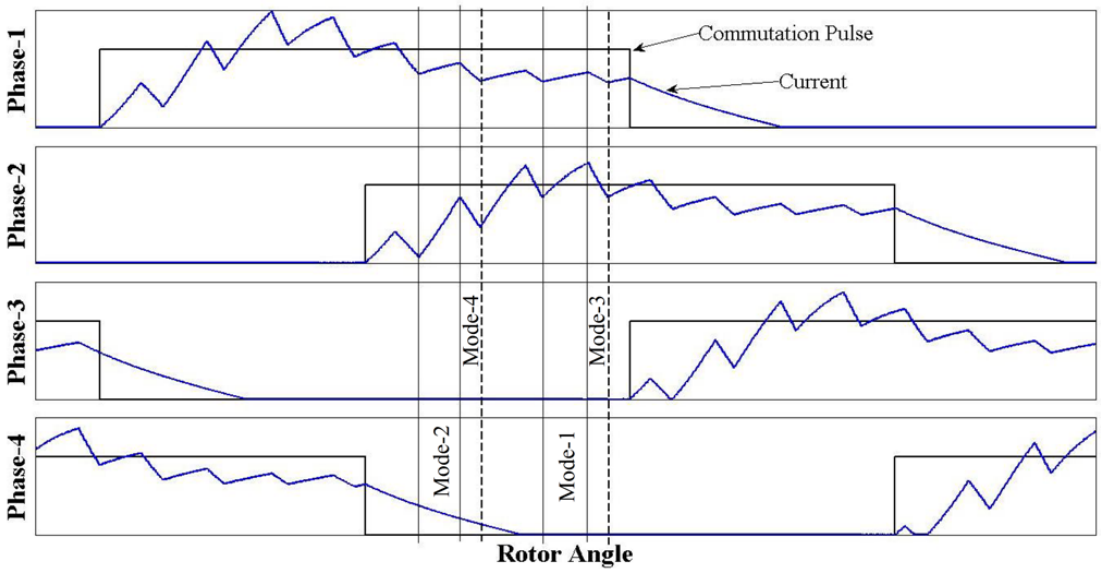

Figure 4.8 Waveform of different mode of operation of converter

4.2 AC SMALL SIGNAL MODEL OF SRM AND CONVERTER

To evaluate the performance of the SRM drive through simulation, model of the drive is required. The AC small signal model helps in design of controller of the SRM drive.

The voltage equation of the one phase winding during switches ON can be expressed as-

$$V_{ph} = R_s i_{Ts} + i_{Ts}\omega_m K_{GL} + L_A \frac{di_{Ts}}{dt} \quad (4.1)$$

During switch OFF state,

$$-V_{ph} = R_s i_{Ts} + i_{Ts}\omega_m K_{GL} + L_A \frac{di_{Ts}}{dt} \quad (4.2)$$

where, phase voltage 'V_{ph}' is equal to $V_{dc}/2$, 'R_s' is the phase resistance, 'ω_m' is the speed, 'K_{GL}' is the inductance gradient, 'L_A' is the average inductance over one switching period, 'i_{Ts}' is the average current over one switching period and 'Ts' is the switching period. Assuming 'd_u' is the duty cycle of the PWM, average voltage applied to the phase winding during one switching period can be expressed as-

$$V_{ph}.d_u - V_d(1-d_u) = R_s i_{Ts} + i_{Ts}\omega_m K_{GL} + L_A \frac{di_{Ts}}{dt} \quad (4.3)$$

or

$$V_{ph}(2d_u - 1) = R_s i_{Ts} + i_{Ts}\omega_m K_{GL} + L_A \frac{di_{Ts}}{dt} \quad (4.4)$$

To develop the model, the input voltage, phase current and duty-cycle are perturbed by small signal about their quiescent operating values. Therefore,

$$i_{Ts} = I + \delta i$$

$$d_u = D + \delta d$$

$$v_{ph} = V_{ph} + \delta v_{ph}$$

Substituting the values of V_{ph}, d_u and i_{Ts} in equation (4.4),

$$(V_{ph} + \delta v_{ph})[2(D+\delta d) - 1] = R_s(I + \delta i) + (I + \delta i)\omega_m K_{GL} + L_A \frac{d(I+\delta i)}{dt} \quad (4.5)$$

Linearizing the equation (4.5), gives the ac small signal equation for the motor drive as-

$$2\delta d V_{ph} + (2D-1)\delta v_{ph} = R_s(\delta i) + (\delta i)\omega_m K_{GL} + L_A \frac{d(\delta i)}{dt} \quad (4.6)$$

Taking the Laplace's transformation, the transfer function of the output current to duty-cycle '$G_{id} = \delta i/\delta d$' can be expressed as-

$$G_{id} = \frac{2V_{ph}}{R_s + \omega_m K_{GL} + sL_A} \quad (4.7)$$

It can be written as-

$$G_{id} = \frac{T_{id}}{1 + s/\omega_{id}} \tag{4.8}$$

where,

$$T_{id} = \frac{2V_{ph}}{R_s + \omega_m K_{GL}} \tag{4.9}$$

$$\omega_{id} = \frac{R_s + \omega_m K_{GL}}{L_A} \tag{4.10}$$

The ramp signal is compared with the control voltage 'V_c' to generate a PWM pulses, where frequency of the ramp signal decides the frequency of modulated wave while the duty cycle is decided by the magnitude of the control voltage (Vc). Transfer function of the pulse-width modulator can be written as-

$$G_{pwm} = \frac{\delta d}{V_c} = \frac{1}{V_m} \tag{4.11}$$

Where, 'V_m' is the maximum value of the comparator signal. The speed-torque equation of the SRM can be written as-

$$T_e = \frac{1}{2} i_{Ts}^2 K_{GL} = J\frac{d\omega_m}{d\theta} + B\omega_m \tag{4.12}$$

The transfer function of the speed to the current can be expressed as-

$$G_{\omega i} = \frac{\delta\omega_m(s)}{\delta i(s)} = \frac{i_{Ts}K_{GL}}{sJ + B} = \frac{i_{Ts}K_{GL}/B}{1 + s\frac{J}{B}} = \frac{Kb/B}{1 + sT_{ti}} \tag{4.13}$$

Transfer function of the PWM controlled SRM drive can be summarized from the (4.7) (4.11) and (4.13) as shown in Figure 4.9.

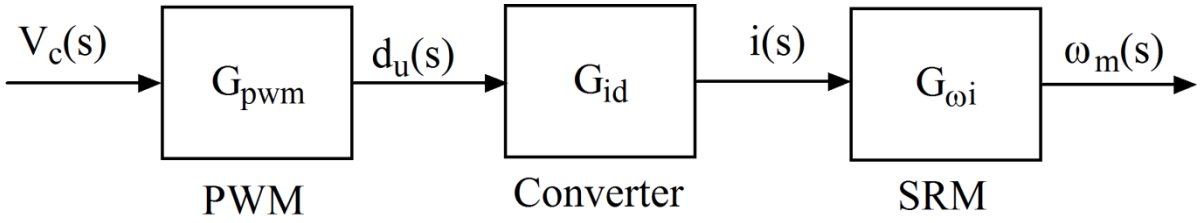

Figure 4.9 Open-loop transfer function of the PWM controlled SRM drive

4.3 DESIGN OF SPEED CONTROLLER

The purpose of designing a speed controller is to achieve stable and reliable control with desire transient response and minimum steady state error. Open-loop and closed-loop controller are designed for the prototype SRM, which have following parameters -

$R_s = 4.5\Omega$

$L_u = 19.18mH$

$L_a = 123.30mH$

$\theta_{dwell} = 30°$

$$K_{GL} = \frac{L_a - L_u}{\theta_{dwell}} = 3.47 \times 10^{-3}$$

$$T_s = 6ms$$

$$J = 1.21 \times 10^{-4} Kg \cdot m^2$$

$$B = 0.5 \times 10^{-3} N \cdot m \cdot s$$

$$\omega_m = 1000$$

$$V_{ph} = 150\ V$$

$$V_m = 1\ V$$

The basic requirement of the drive is that the motor should come to reference speed with minimum overshoot and minimum settling time. Typically, the steady state error of speed should also be less 1%. To design the controller for desired performance, the transient response of the drive for a step input of 1 rad/sec both under open loop and closed loop operating conditions is investigated using the transfer function of the drive system.

$$G_{id} = \frac{37.64}{1 + S0.219} \tag{4.14}$$

$$G_{\omega i} = \frac{6.94}{1 + S0.242} \tag{4.15}$$

$$G_{pwm} = 1 \tag{4.16}$$

Using equation (4.14)-(4.16), the overall transfer function of the open-loop system is obtained and is given by,

$$G_{OL} = \frac{260}{0.053S^2 + 0.461S + 1} = \frac{1}{0.0002038S^2 + 0.001773S + 0.003846} \tag{4.17}$$

With the additional gain of 1/260, the open-loop transfer function of the system becomes-

$$G_{OL} = \frac{1}{0.053S^2 + 0.461S + 1} \tag{4.18}$$

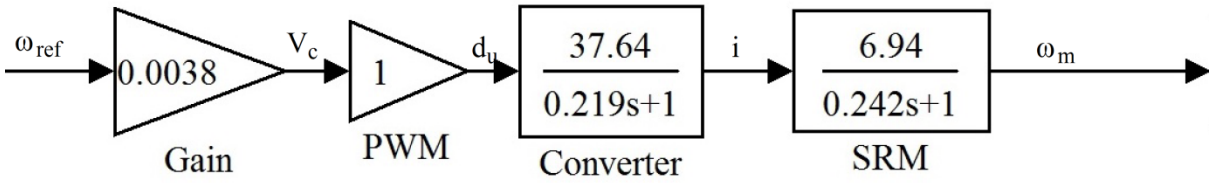

Figure 4.10 Transfer function of openloop PWM controlled prototype SRM drive

Figure 4.10 shows the transfer function diagram of the open-loop speed controlled SRM drive. The step response of the open-loop system is shown in Figure 4.11, which is an over-damped system having settling time of about 1.2 second. It shows that, open-loop PWM controller is suitable for the most of the low cost constant speed as well as variable speed application wherever precise speed control is not the prime requirement. It is also

applicable to the low power electric vehicle (E-bike) system where human being is involved in the process of the speed control. However, to meet the requirement of the constant speed in all varying load condition and against environment disturbance, closed-loop speed control is must.

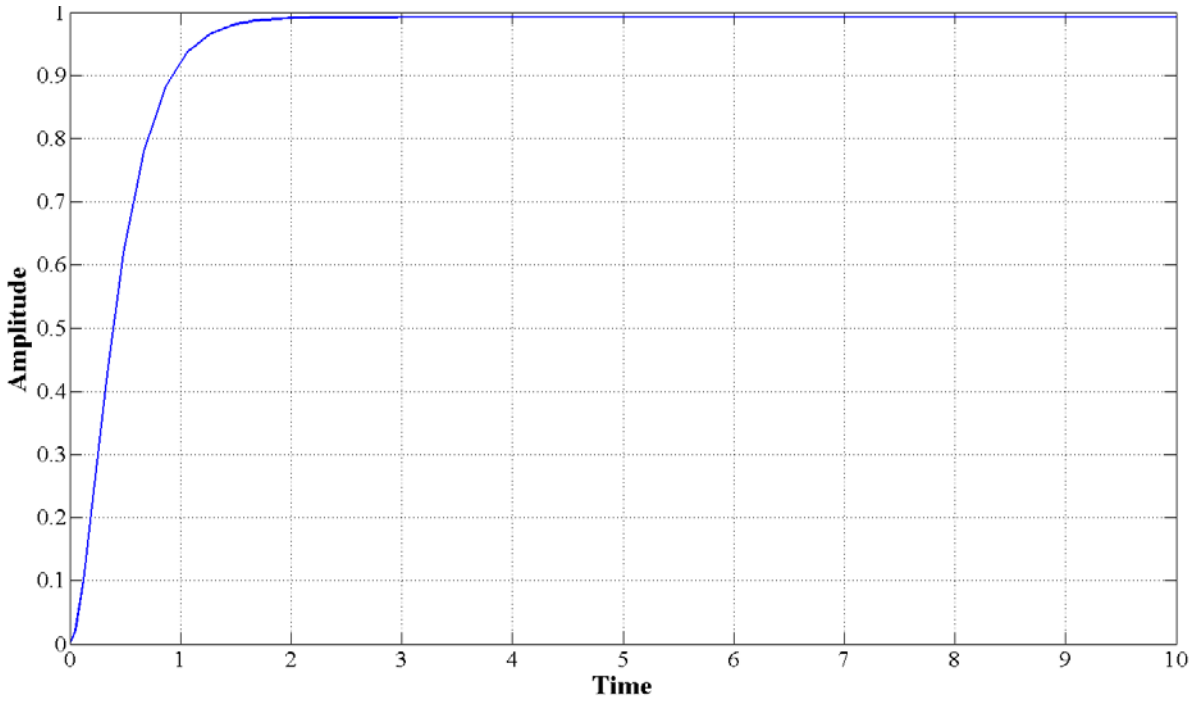

Figure 4.11 Step response of the openloop system with the gain = 0.0038.

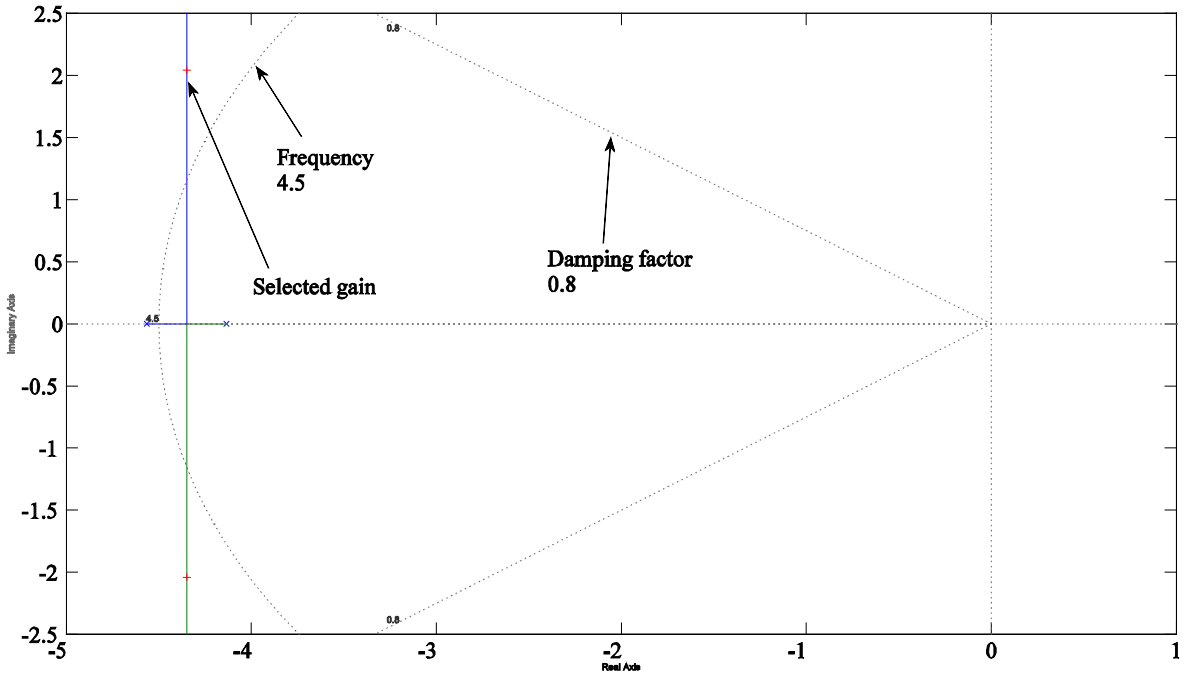

Figure 4.12 Root locus of the openloop system without PI compensator

The root locus method is used to design a closed loop speed controller, which gives closed-loop response from the open-loop root locus plot. Figure 4.12 shows the root locus

plot of the open-loop system. The two grids in the plot show the damping factor of 0.8 and frequency of 4.5 (i.e 4.5/1sec), which reflects the requirement of overshoot (<5%) and settling time (<1 sec) respectively. The intermediate gain K_p is selected as 0.217 for the proportional controller to achieve the desire response. Closed-loop transfer function with the gain K_p becomes-

$$G_{CL} = \frac{0.217}{0.053S^2 + 0.461S + 1.217} \tag{4.19}$$

The step response of the closed-loop system is shown in Figure 4.13. It is an over-damped response and settling time is also less than the required one.

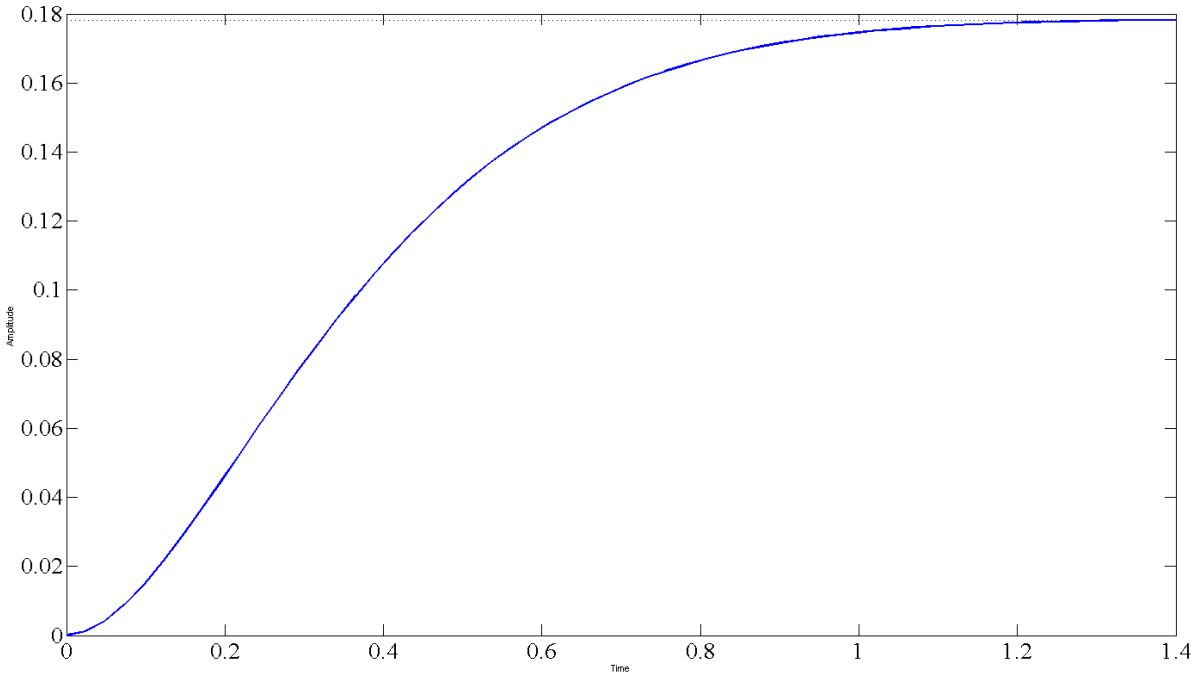

Figure 4.13 Step response of the closed-loop system with proportional gain K_p=0.217

The proportional gain K_p is required to be incresed to reduce the steady state error, which increases an overshoot and settling time. Thus proportional-integral (PI) controller is used which adds one zero and one pole in the open-loop transfer function. The PI controller transfer function is expressed as-

$$G_{PI} = K_p + \frac{K_i}{S} = \frac{K_p(S + \frac{K_i}{K_p})}{S} \tag{4.20}$$

The controller adds an asymptote which starts at the origin (pole) and end at the -K_i/K_p (zero). A fast response corresponds to points on the root locus far left to the imaginary axis. To determine the controller parameters, different combinations of K_P and K_i were selected and response of the drive was observed. For few combinations of K_P and K_i the response of the drive is shown in Figure 4.14. The overshoot and the settling time for these controller parameters are given in Table 4.3.

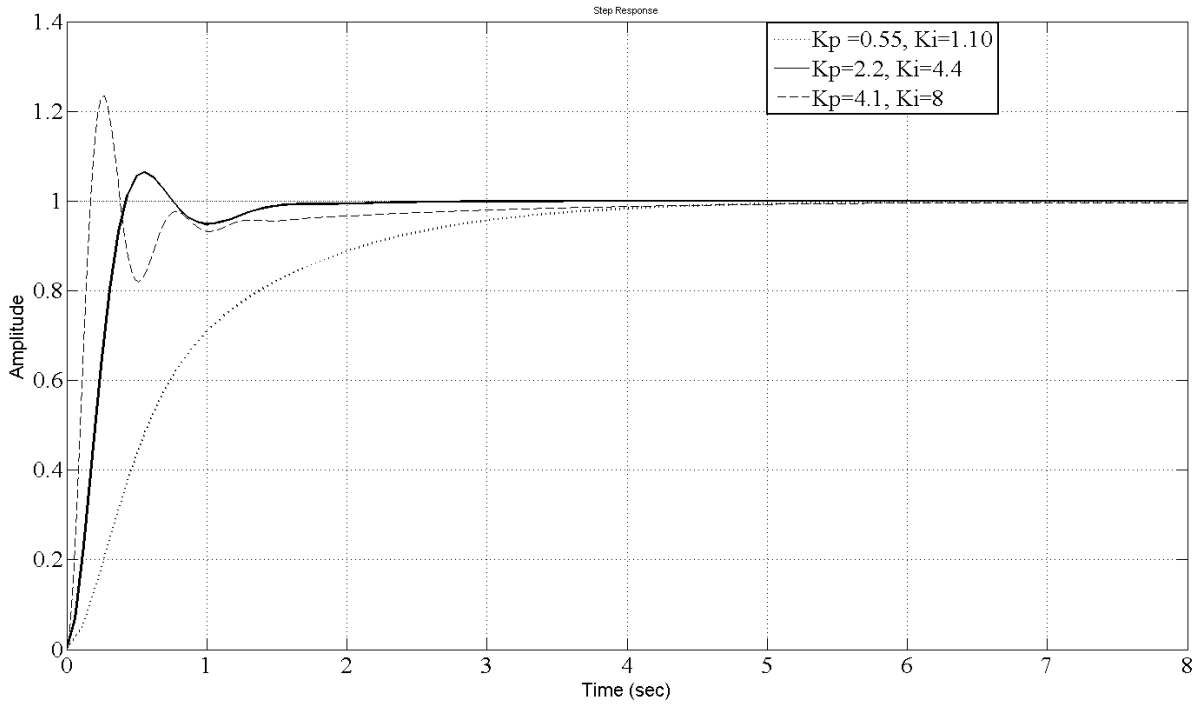

Figure 4.14 Step responses of the closed-loop system with PI speed controller

Table 4.3 Response of closed-loop system with PI speed controller

Sr. No	Controller Parameters	% Overshoot	Settling Time (sec)
1	K_p = 0.55 & K_i = 1.1	Overdamped	4
2	K_p = 2.2 & K_i = 4.4	5	1.4
3	K_p = 4.1 & K_i = 8	22	3

From the table, it is clear that for K_p = 2.2 and K_i = 4.4 the response is acceptable. Thus, these values are selected and the closed-loop transfer function becomes-

$$G_{CLPI} = \frac{2.2S + 4.4}{0.053S^3 + 0.461S^2 + 3.2S + 4.4} \tag{4.21}$$

The complete block diagram of SRM drive with the closed-loop PI speed controller is shown in Figure 4.15, where overall open-loop proportional gain of the system becomes K_p=2.2*0.038=0.084. The precise simulation model of the prototype SRM drive is derived using the MATLAB simulink environment.

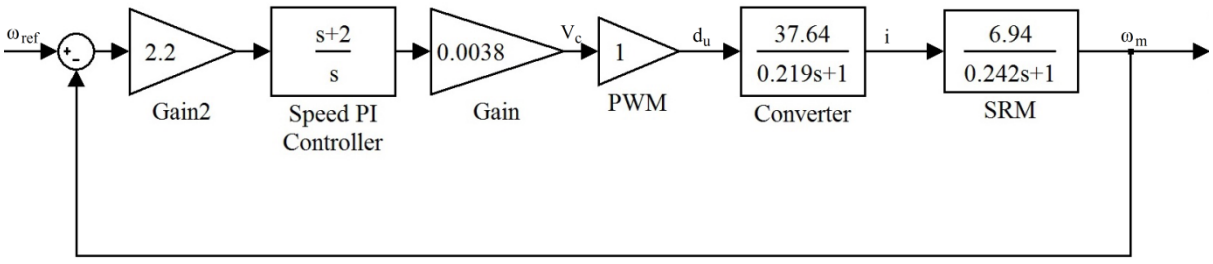

Figure 4.15 Transfer function diagram of the closed-loop speed PI controlled prototype SRM drive

4.4 SIMULATION AND MODELING OF SRM DRIVE

Precise model of the prototype SRM is derived using the modeling Method-1 as described in Chapter 3, which employs look-up table based approach to store the magnetic characteristics of the SRM. Speed laboratory's PC-SRD software is used to derive the magnetic characteristics of the SRM from the geometry and the winding details. Figure 4.16 and Figure 4.17 show the magnetic characteristics and torque characteristics of the prototype SRM, stored as a lookup table. Simulation model of the motor is developed using 'simulink' library and then converted to become compatible with the 'simpowersystem' library components, using controlled voltage source (Chapter 3). It provides ease and flexibility to model a power electronic converter.

The 'simpowersystem' library provides ready to available model of the semiconductor switches like MOSFETs, IGBTs and Diodes with the flexibility to set the parameters to match with an actual component. The split DC converter employs one MOSFET and one diode per phase. The ON state resistance and forward voltage drop of MOSFET and diode model are set according the specifications of the components used; MOSFET IRFP450A and diode MUR1560. Thus the simulation model will be more closer to the experimental SRM drive. However, GATE signal of the MOSFET is driven by the simulink signal which signifies that GATE circuit is a lossless component and it does not draw any current from the source. The simulation model of the split DC converter is shown in Figure 4.18 where A1-A2, B1-B2, C1-C2 and D1-D2 represent four phases of the motor.

PWM pulse is generated by comparing control voltage V_c with the fixed frequency (1.67KHz) ramp signal using simulink library, where maximum amplitude of the carrier signal V_m is equal to 1. The synchronized GATE pulses for the each phase are generated from the rotor position feedback to set the turn-ON and turn-OFF angles as desired. PWM pulses are combined with each of the GATE pulse using logic GATEs of the simulink library, before giving to the GATE signal of associated phase. Likewise, speed of the motor is controllable through the PWM duty cycle or says control voltage V_c. Simulation models of position sensor and PWM pulse generator are shown in Figure 4.19 and Figure 4.20 respectively. Open-loop speed control and closed-loop PI speed control system are also simulated using simulink library. Figure 4.21 shows the simulation model of the PI speed controller while simulation model of the close-loop SRM drive is shown in Figure 4.22.

The complete simulation model of the SRM drive approximates to a prototype SRM drive. It also provides full flexibility to adjust the advance angle, dwell angle, parameters of PI controller for fine tuning, PWM frequency and load torque. Power electronics converter is simulated using 'simpowersystem' library components which realize the converter losses in the modeled SRM drive. The torque developed is also measured for the different conditions.

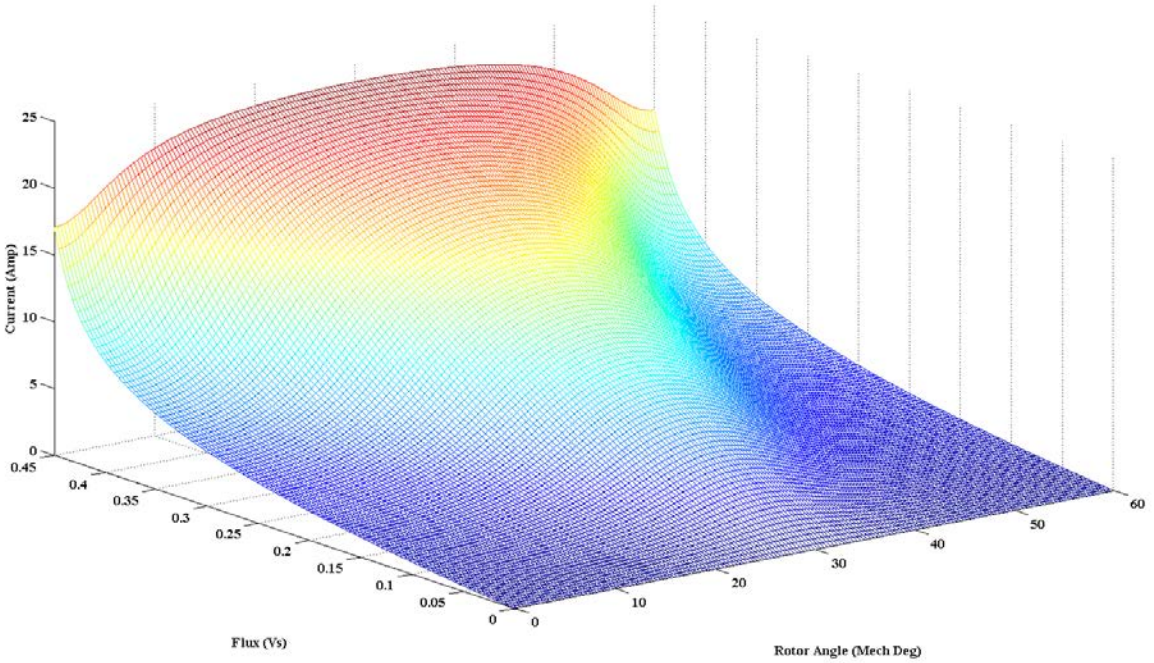

Figure 4.16 Magnetic characteristics of the prototype SRM

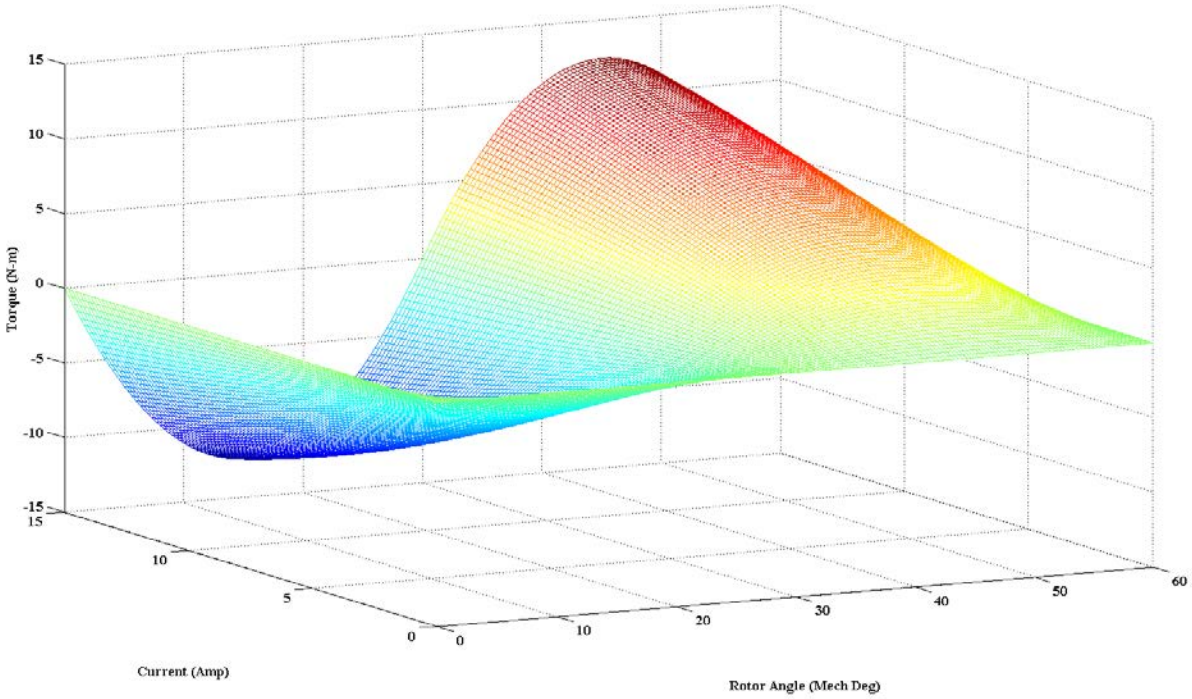

Figure 4.17 Torque-current-angle relation of the prototype SRM

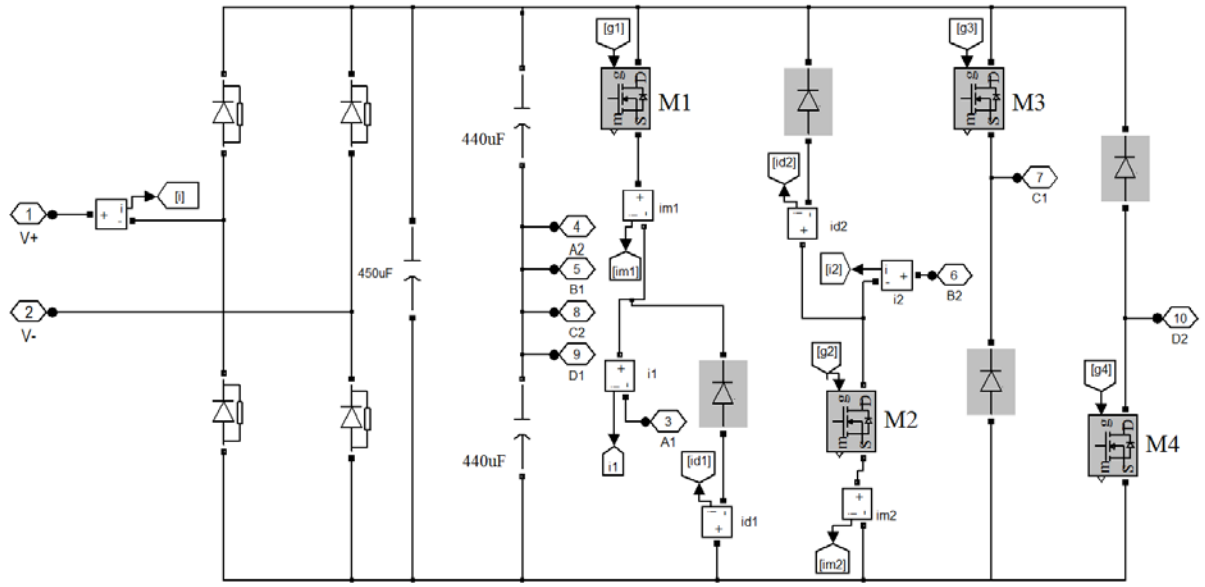

Figure 4.18 Simulation model of split DC converter

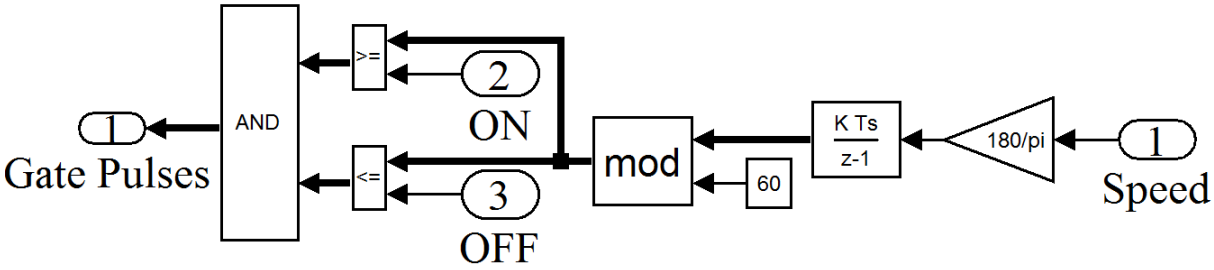

Figure 4.19 Simulation model of position sensor

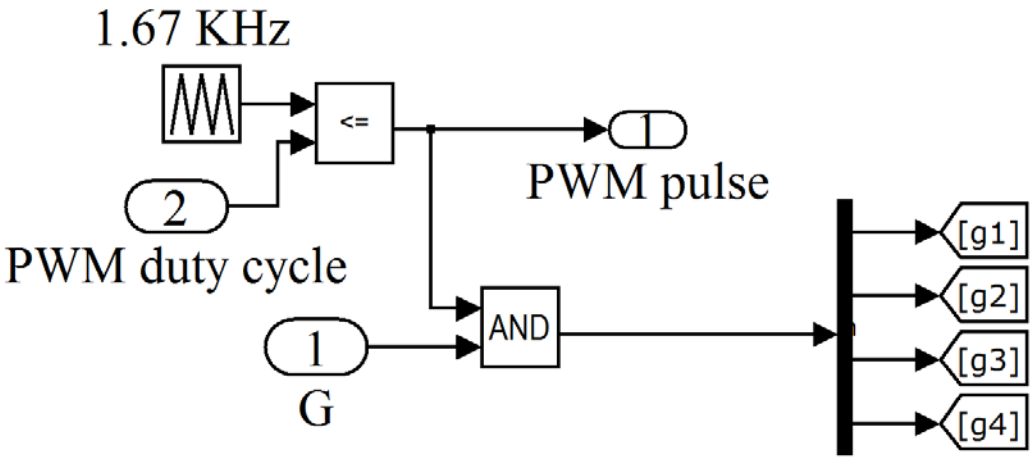

Figure 4.20 Simulation model of PWM pulse generator

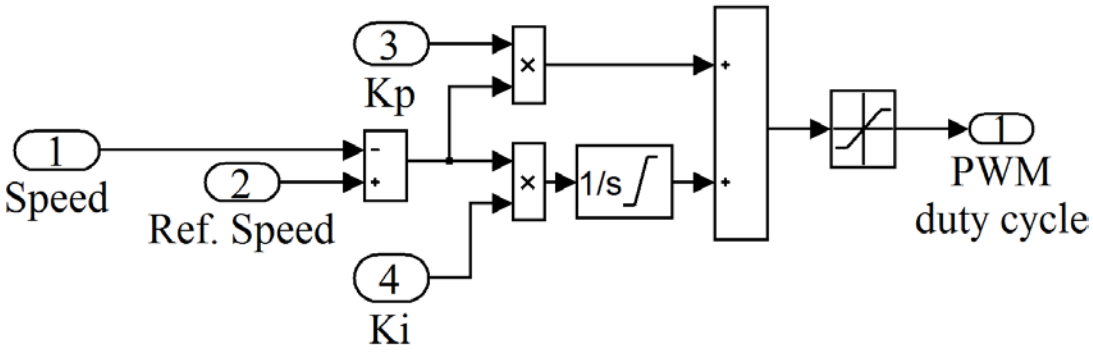

Figure 4.21 Simulation model of PI speed controller

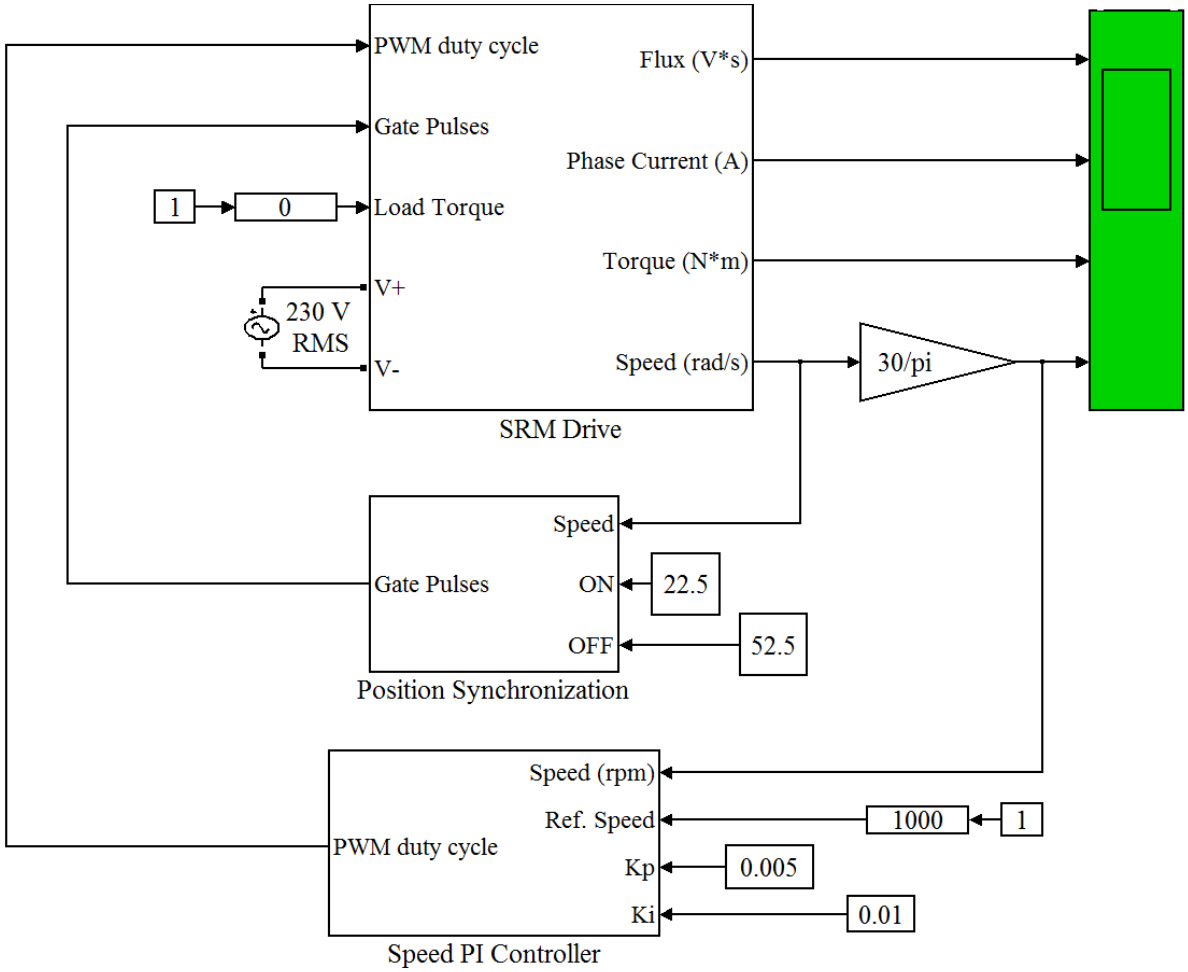

Figure 4.22 Simulation model of closed-loop SRM drive

4.5 IMPLEMENTATION OF SPEED CONTROLLER

Nevertheless, simple analog electronics can fulfill all the requirements of the controller, RT-Lab, from Opal-RT Technologies, is used as real time hardware-in-loop controller to implement a control part of the drive for the ease and flexibility. RT-Lab is a real-time simulation platform that enables real time and HIL (hardware in loop) simulation of controllers, electric plants or both, through automatic code generation methods. Automatic code generation enables very rapid deployment of prototyped controllers or HIL-simulated

plants. The process is notably very efficient when applied to I/O code because RT-LAB provides a set of simulink blocks that automatically configure common I/O functions, like analog input/outputs and time-stamping capable digital I/Os, with a resolution of 10 nanosecond. RT-LAB is equipped with a user-programmable FPGA card. Table 4.4 summarizes the characteristics of FPGA board and Table 4.5 summarize the input output cards of RT-LAB.

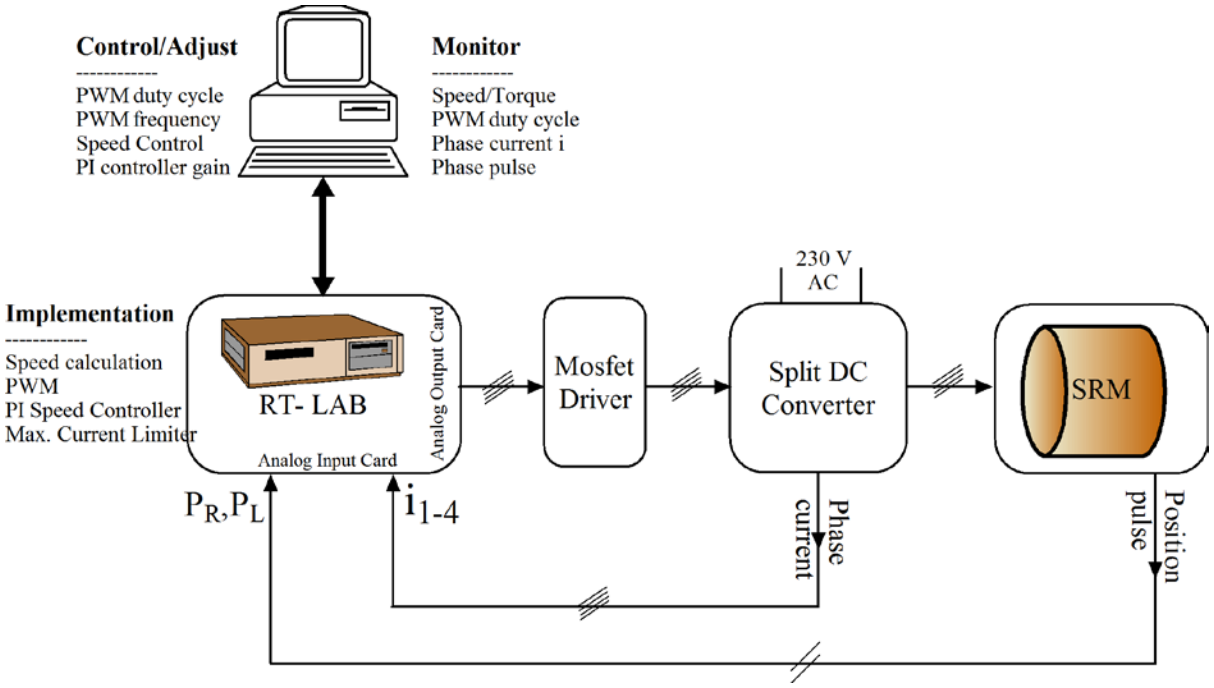

Figure 4.23 Block diagram of experimental setup of SRM drive

Table 4.4 Reconfigurable FPGA board

Model Name	**FPGA**	**Bus Type**	**FPGA Clock**	Gate	Logic Cells	**Slices**	**CLB Flip Flop**	**I/O Lines**
OP5142	Xilinx Spartan 3 XC3S500	PCI-Express 1x	100 MHz	5M	74,880 (74K)	33K	66K	296

Table 4.5 Input-output configuration

I/O Slot	**Carrier Type**	**Section A**	**Section B**
1	OP5220	OP5330 Analog Out	OP5340 Analog In
2	OP5210-S3	OP5311 Digital In	OP5312 Digital Out

The implementation of the SRM drive using RT-Lab is shown in Figure 4.23. As shown in figure, two rotor position signals are applied to the analog input card of RT- Lab. From analog output card, four gate pulses are taken out and supplied to the MOSFET driver circuit as shown. The controller is developed in the MATLAB simulink platform, which is converted and transported to the FPGA of RT-Lab using Opal-RT's compiler RT-Lab 10.3 version. Each simulink model contain two subsystem as shown in Figure 4.24, where subsystem "*SM_speed_control*" contain the model of the actual controller and input/output configuration

blocks while subsystem "*SC_speed_control*" is a model which provides user interface for online parameter control and monitor via PC with the dual core CPU. Internal model of the subsystems for the open-loop and closed-loop speed controller are shown in the Figure 4.25 and Figure 4.26 respectively, while available user interfaces for each speed controller are shown in the Figure 4.27 and Figure 4.28.

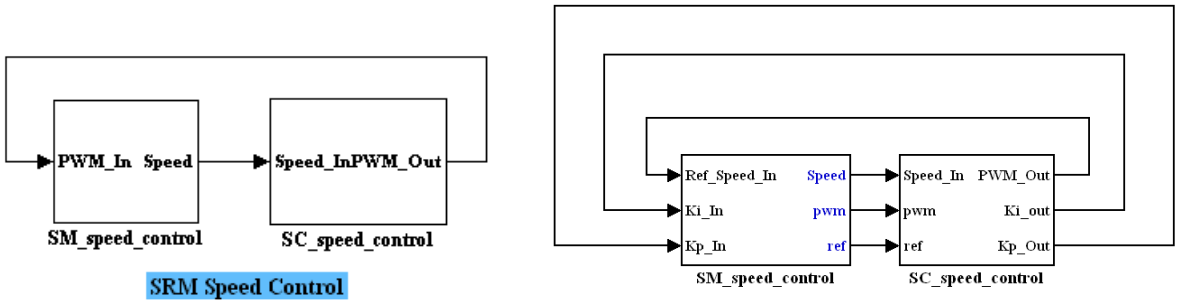

(a) (b)

Figure 4.24 MATLAB simulation model of (a)openloop and (b) closed loop speed control system

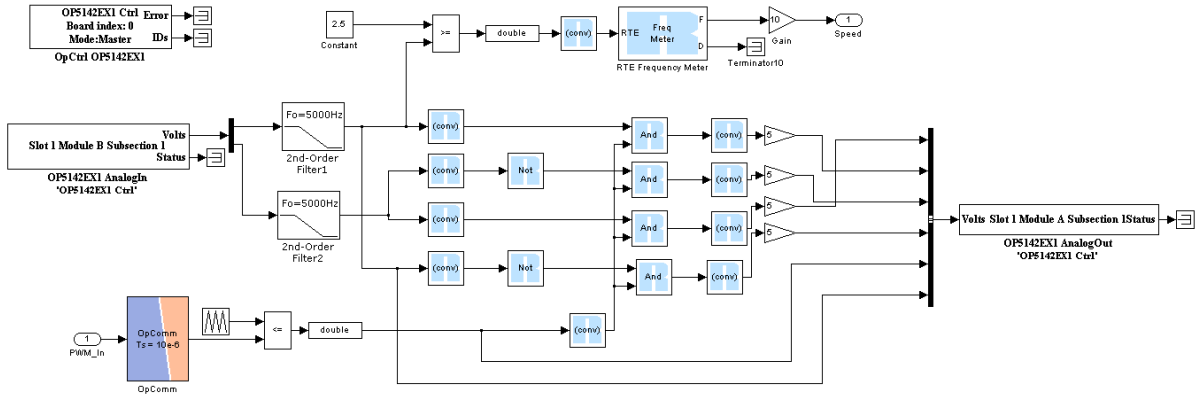

Figure 4.25 Subsystem "SM_speed_control" of open-loop speed controller

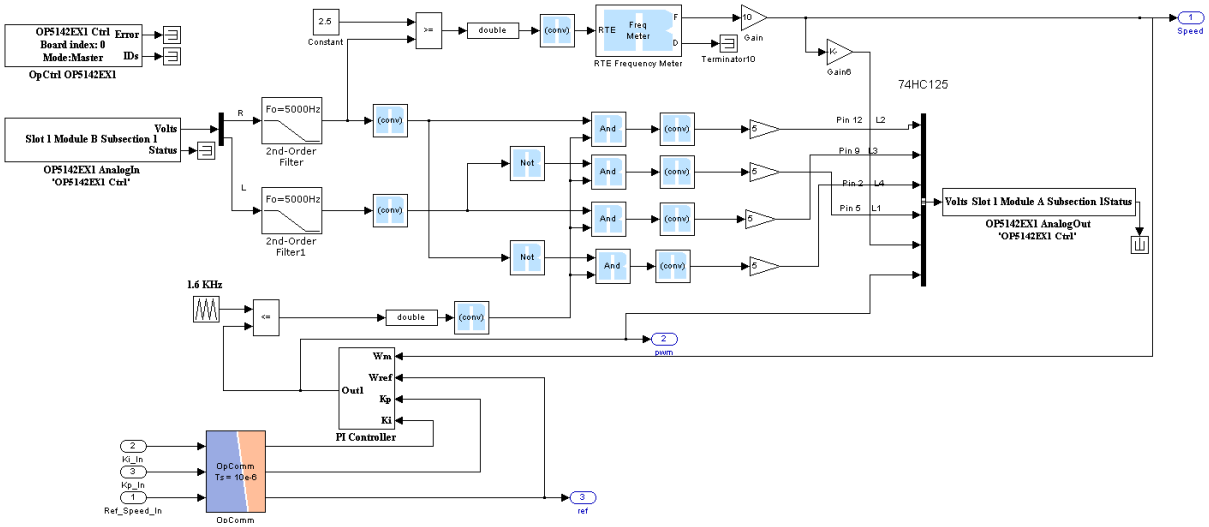

Figure 4.26 Subsystem "SM_speed_control" of closed-loop speed controller

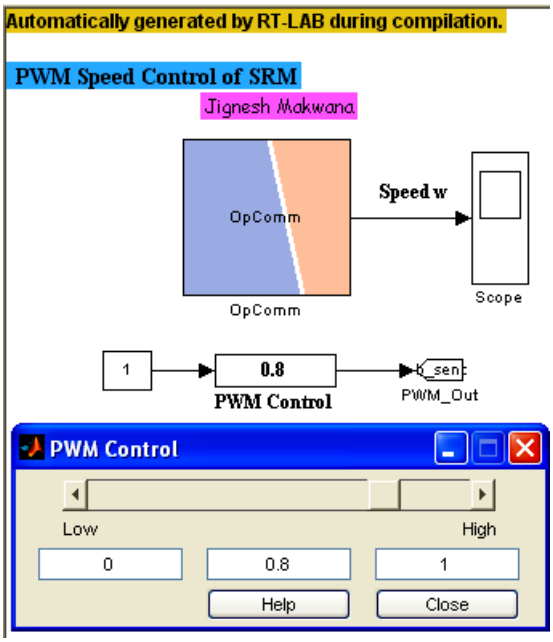

Figure 4.27 User interface with open-loop speed controller

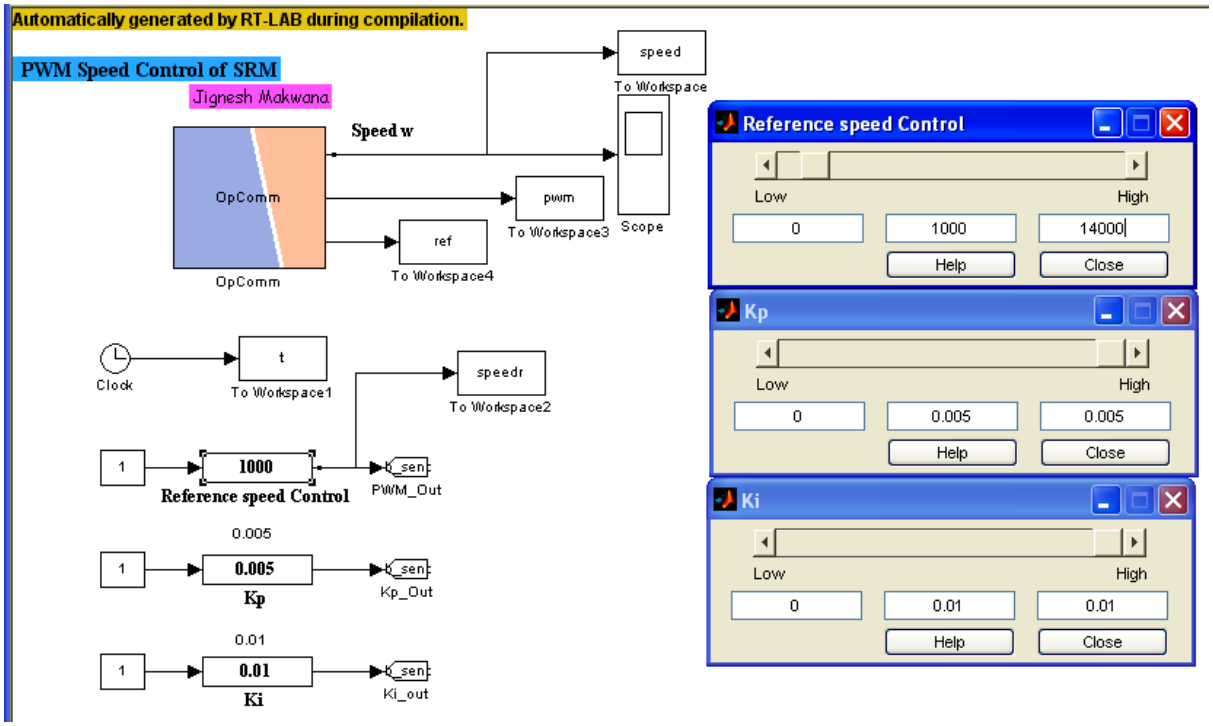

Figure 4.28 User interface with the closed-loop speed controller

The circuit diagram of the experimental setup is shown in Figure 4.29, where the numbers in red color represent a pin number of the each ICs or component. Detail hardware specification about Opal's RT-Lab is given in Appendix-B.

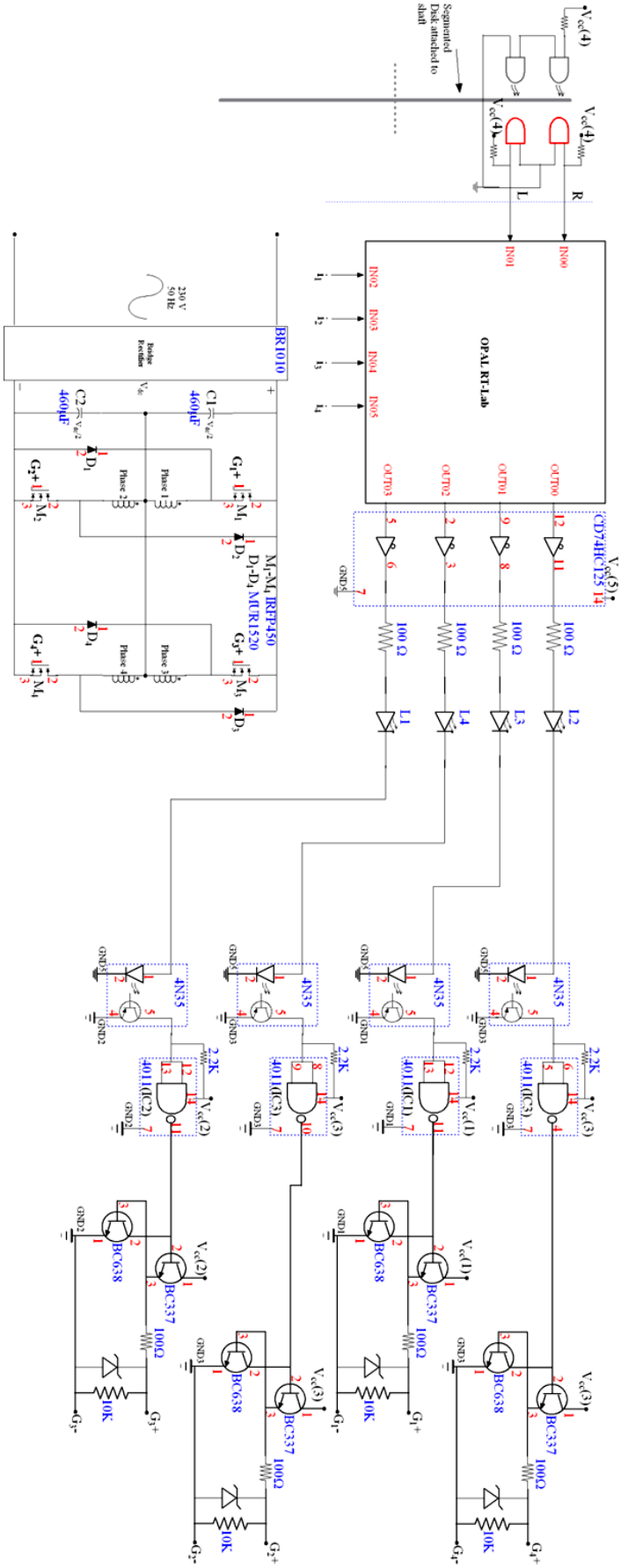

Figure 4.29 Circuit diagram of experimental setup

4.6 RESULT AND ANALYSIS

Experimental results are compared with the simulation results at each stage to analyze closeness of approximation of the modeled SRM drive to the actual one. High precision measuring instruments are used to measure, capture and store the data.

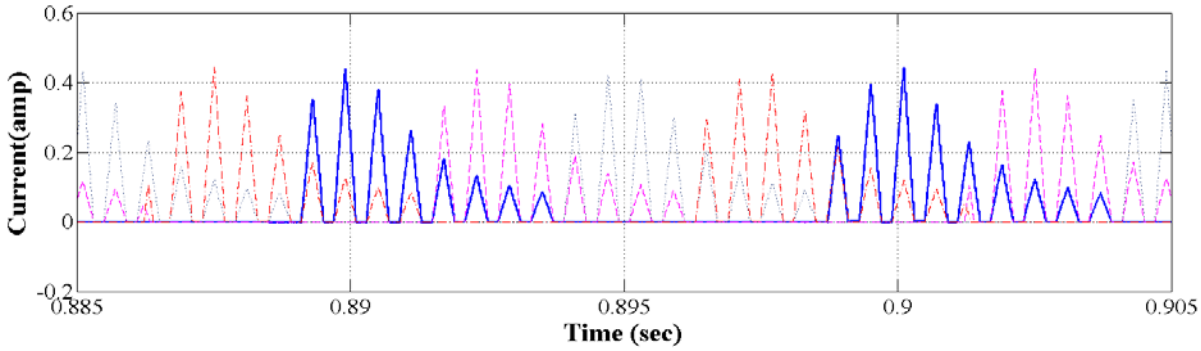

(a) Simulation

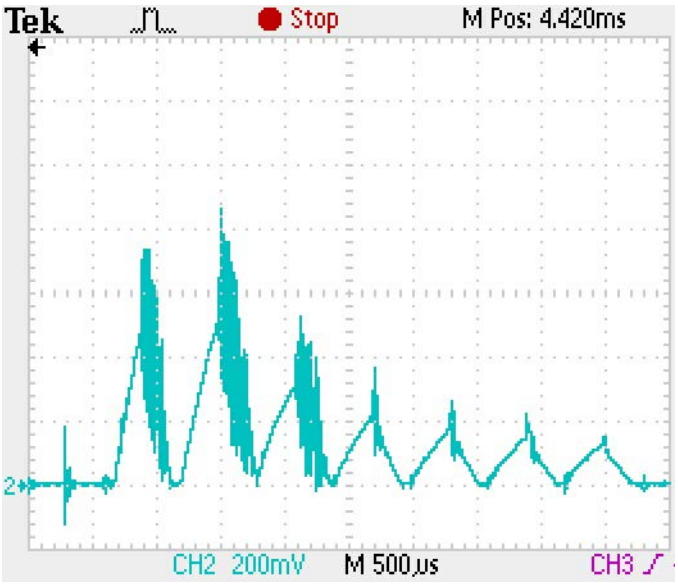

(b) Experimental (Phase curret : 0.2 amp per division)

Figure 4.30 Waveform of phase current at 1000 rpm

Figure 4.30 shows the waveform of phase current at the motor speed of 1000 rpm for the simulation as well as experimental result. The peak value of the phase current is 0.42 A for the simulation while it is 0.5 A for the experimental. It shows the closer approximation of the simulation to the prototype SRM drive. Figure 4.31 shows the waveform of input AC current for the simulation and experimental result. The peak value of the input AC current is 0.7 A for the simulation while it is 1 A for the experimental result. Furthermore, the waveform of the voltage across the phase is shown in the Figure 3.29. Theoretically, dc line voltage is 325 V for the input of 230 V AC as (230 V x √2). The voltage across the phase is 163 V during phase excitation and −163 V during freewheeling or regeneration. Likewise, the

simulation results for the phase current, input current and voltage across phase matched closely to the experimental results. This validate that the electrical properties of the simulation model including motor, converter and controller are accurate and reliable to investigate the performance of the prototype SRM drive.

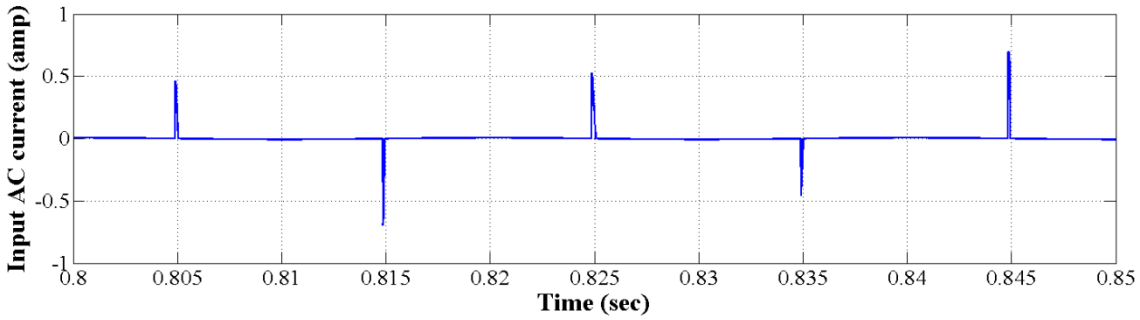

(a) Simulation

(b) Experimental (Input AC current: 1 amp per division, Time scale: 5ms per division)

Figure 4.31 Input AC current at 1000 rpm

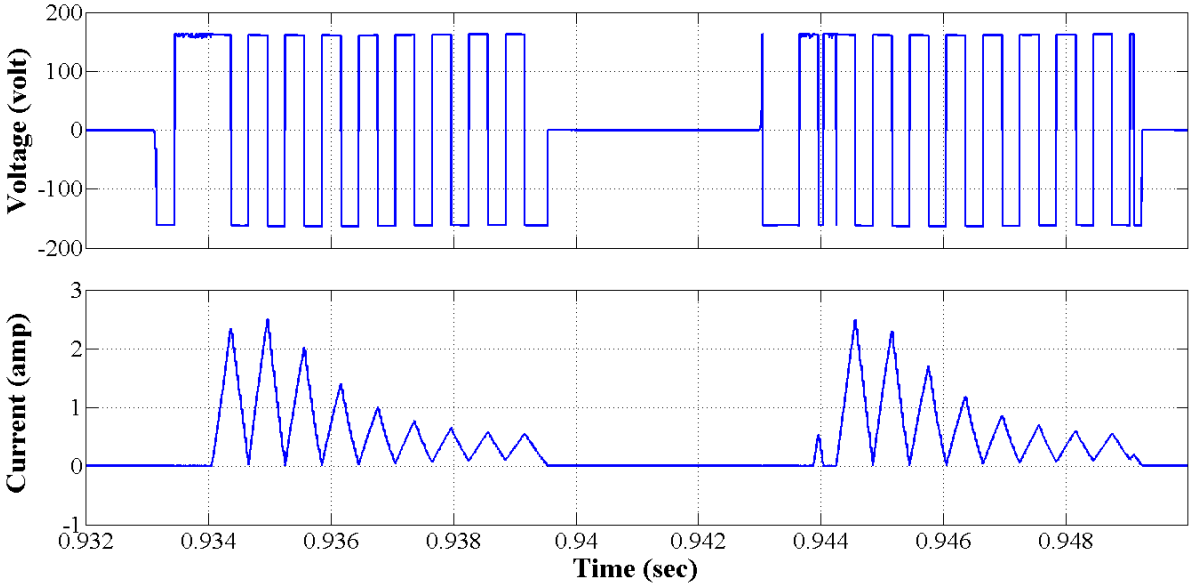

(a) Simulation

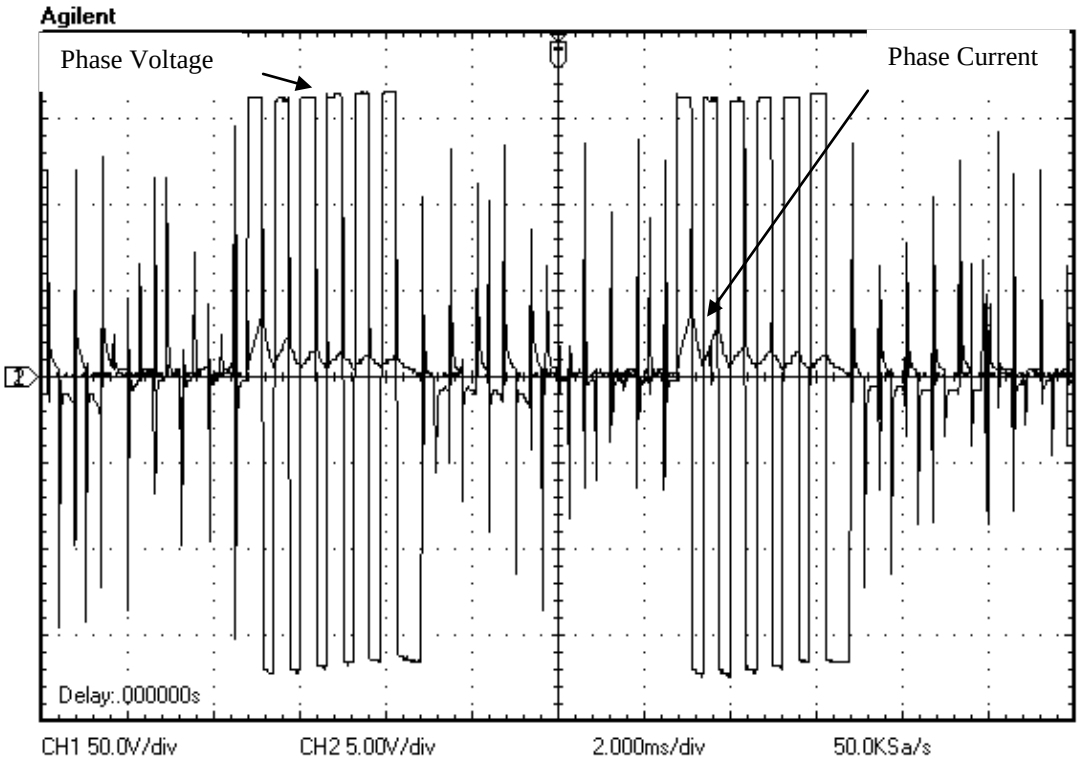

(b) Experimental (Voltage: 50 volt per division, Current: 5 amp per division)

Figure 4.32 Phase voltage at the speed of 1000 rpm and load torque of 0.618 N-m

The speed response to the step change in PWM duty cycle for the open-loop speed controller is shown in Figure 4.33. PWM duty cycle variation versus steady state speed at no-load is plotted in Figure 4.34.

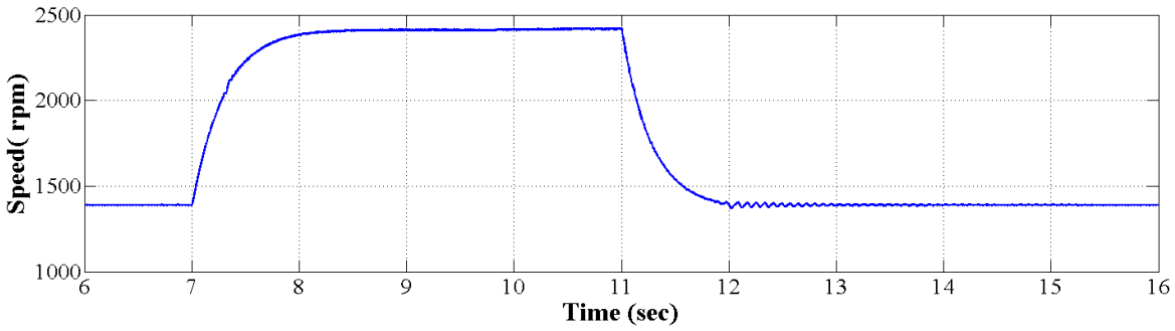

(a) Simulation

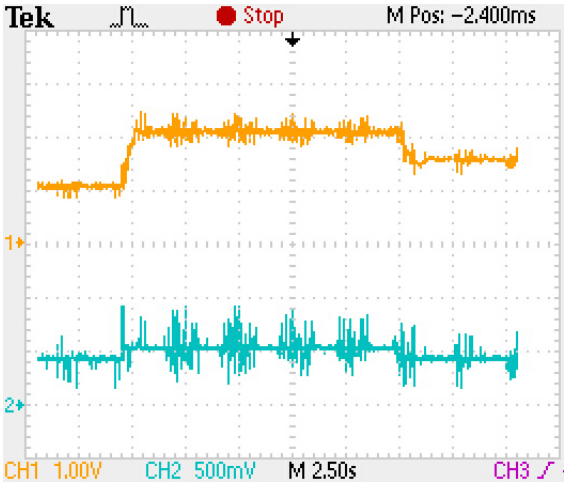

(b) Experimental (CH1: speed 500 rpm per division, CH2: duty cycle 0.25 per division)

Figure 4.33 Transient response to step change in duty cycle from 0.2 to 0.25 (Open-loop speed control)

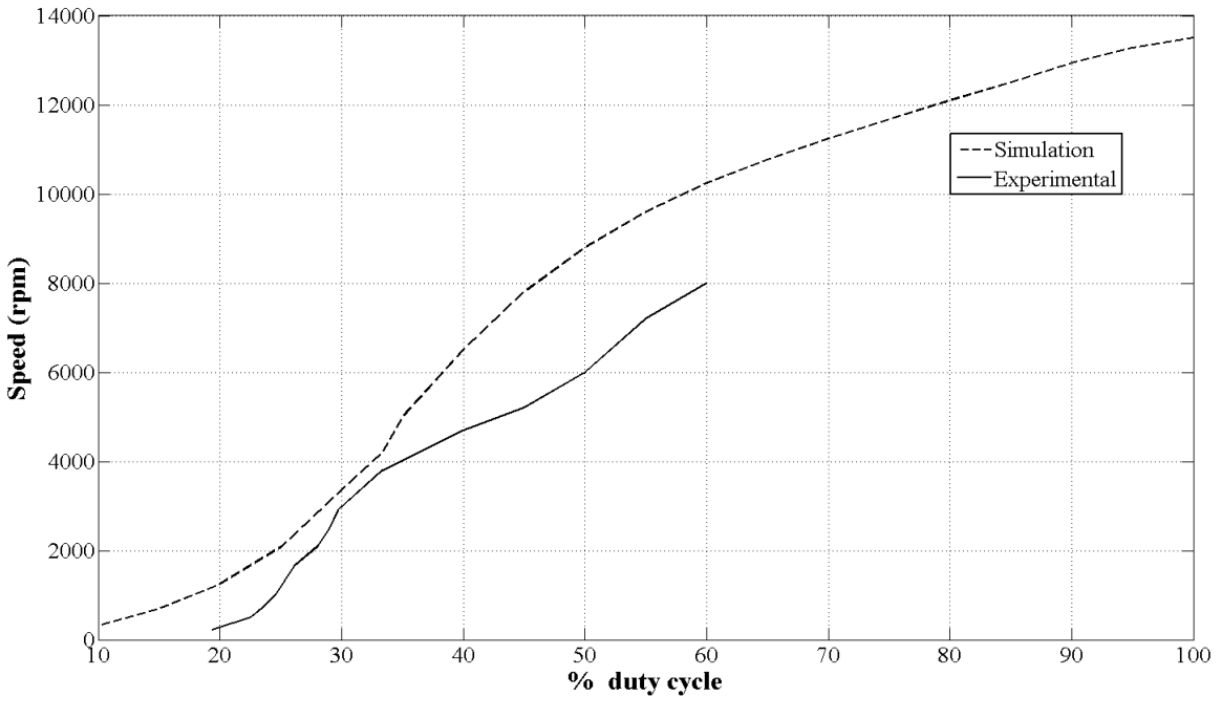

Figure 4.34 Duty cycle versus steady state speed at no-load

The response of the closed-loop speed PI controller is shown in Figure 4.35. Flexibility in real-time adjustment of gain, damping factor and settling time is used to achieve the desired transient response. Accordingly, values of the controller gain K_p and K_i are fixed to the 0.005 and 0.01 respectively. Figure 4.36 shows the transient responses of the closed loop speed controlled SRM drive, to the speed change, where simulation and experimental responses are comparable.

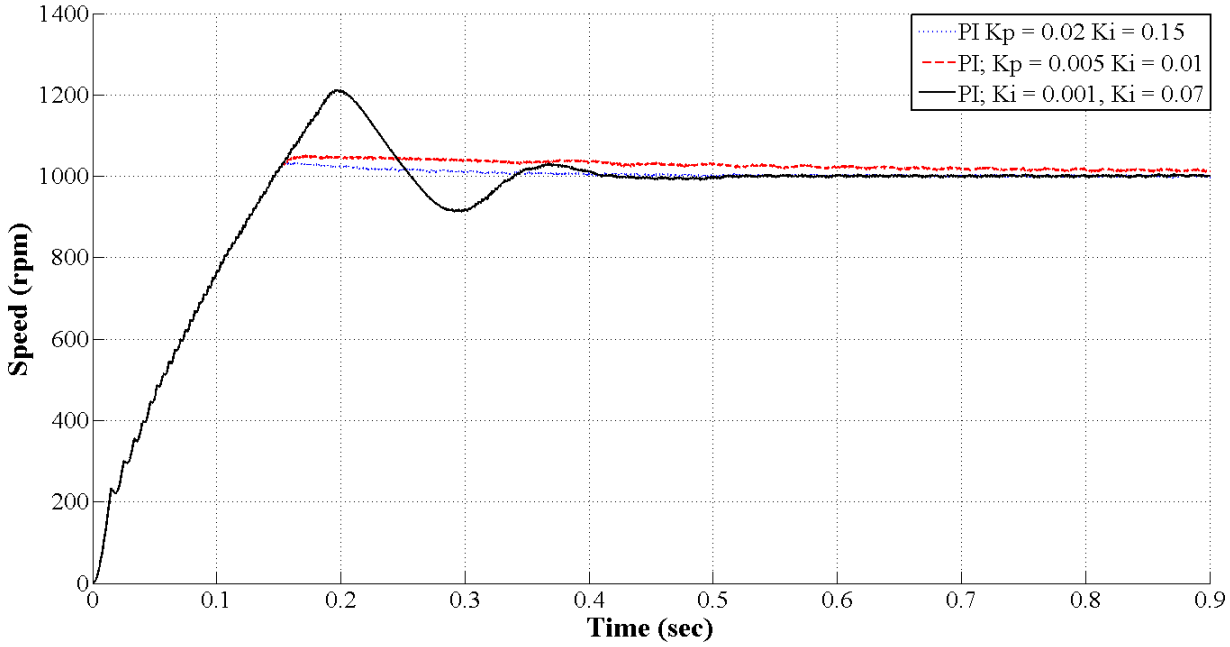

(a) Simulation

(b) K_p = 0.02, K_i = 0.15 (c) K_p = 0.005, K_i = 0.01 (d) Kp = 0.001, Ki = 0.07

Experimental (CH1: 500 rpm per division, CH2: duty cycle 0.5 per division)

Figure 4.35 Transient response with adjustable speed PI-Controller

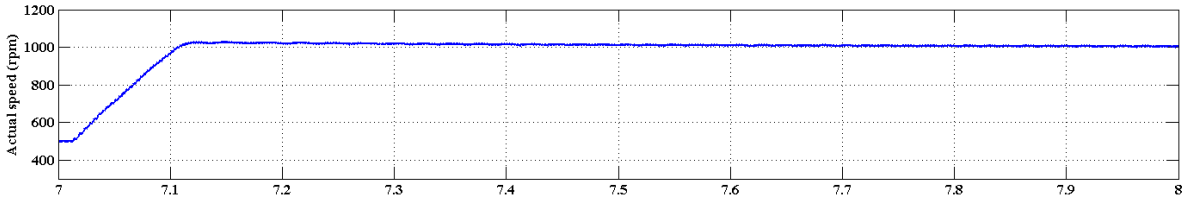

(a) Simulation: 500rpm to 1000rpm, settling time T_{sett} = 0.5 sec

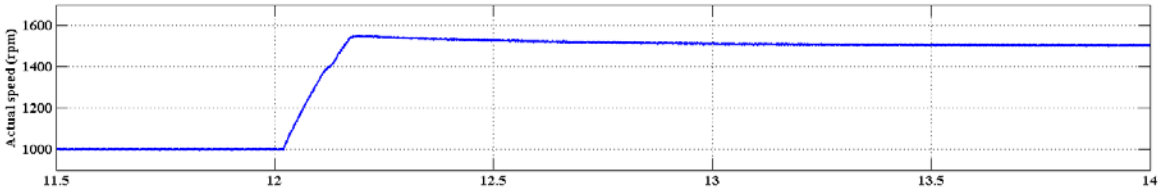

(b) Simulation:1000rpm to 1500 rpm settling time T_{sett} = 0.8 sec

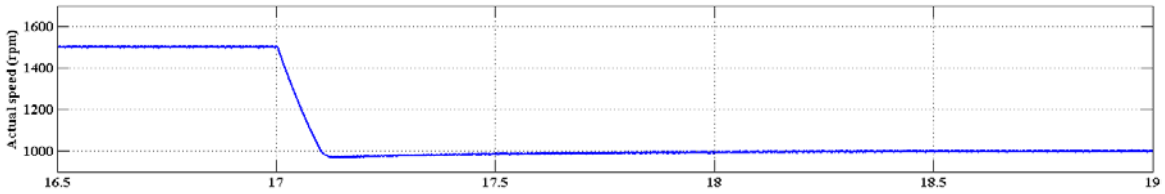

(c) Simulation: 1500 rpm to 1000 rpm settling time T_{sett} = 0.6 s

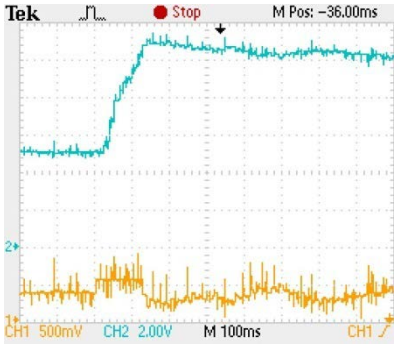

(d) Experimental: 500rpm to 1000 rpm, settling time T_{sett} = 0.9 sec ,(CH1: duty cycle 0.5 per division, CH2: speed 200 rpm per division)

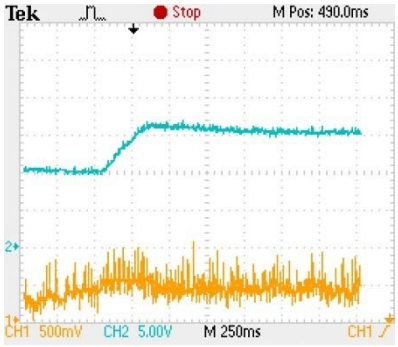

(e) Experimental: 1000 rpm to 1500 rpm, settling time T_{sett} = 1.2 sec ,(CH1: duty cycle 0.5 per division, CH2: speed 500 rpm per division)

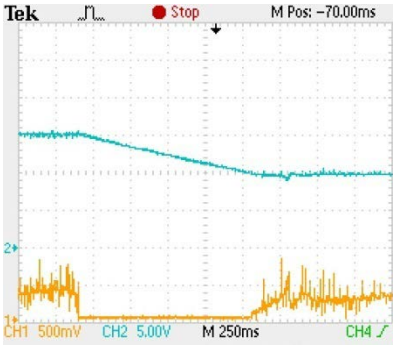

(f) Experimental: 1500 rpm to 1000 rpm, settling time T_{sett} = 1.25 sec (CH1: duty cycle 0.5 per division, CH2: speed 500 rpm per division)

Figure 4.36 Transient response to a speed change from (a)&(d) 500rpm to 1000rpm (b)&(e) 1000rpm to 1500rpm and (c)&(f) 1500rpm to 1000rpm

The retardation response of the motor is shown in Figure 4.37, where free run time required to settle down the motor speed to zero from the speed of 1000 rpm is measured with no-load condition. Experimental and simulation retardation times are comparable, which validates an approximation of the mechanical parameters, rotor inertia and friction, used in simulation model.

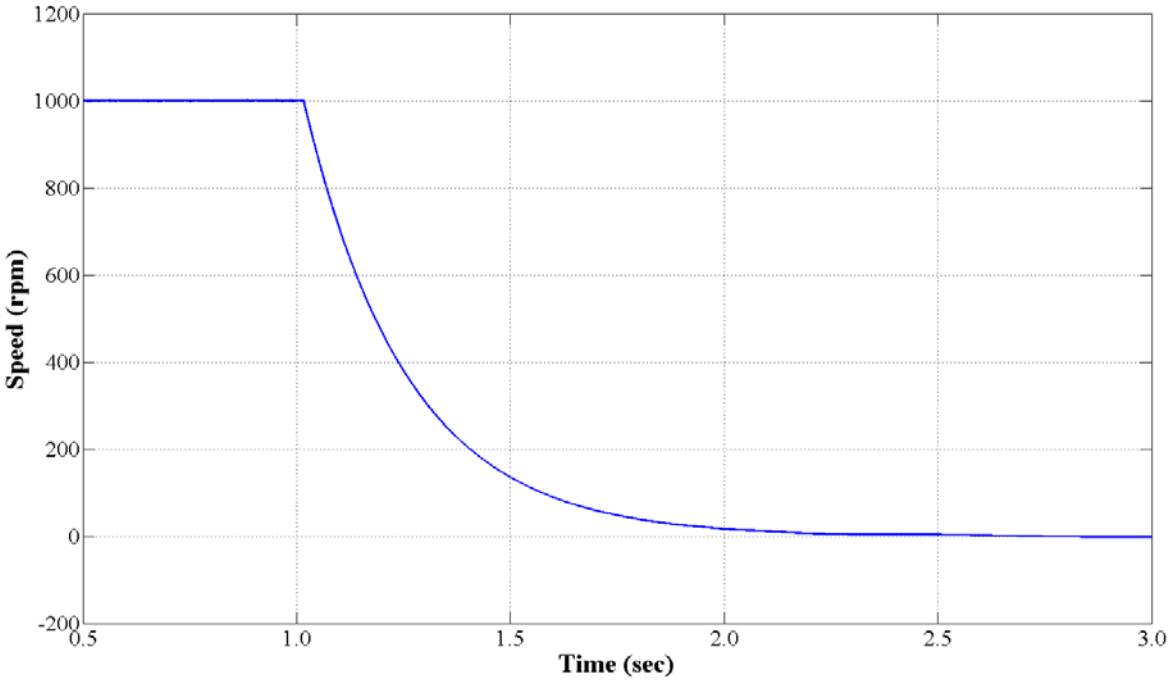

(a) Simulation: retardation time 1.4 sec

(b) Experimental: retardation time 1.8 sec (CH1: speed 500rpm per division, CH2: PWM duty cycle 0.25 per division

Figure 4.37 Retardation response (time required to settle a speed to zero from 1000 rpm)

Efficiency is measured as motor shaft output power divided by electrical AC input power to the converter thus it includes electronics and converter losses plus motor loss. High precision single phase FLUKE meter is used to measure the input AC power, current and power factor, while standard spring balance load arrangement is used to adjust and measure the torque of the motor. The motor speed is derived as N = f_{com} x 10, where 'f_{com}' is the frequency of the phase commutation pulse. Real-time monitoring of the motor speed is

possible with the dual-core CPU and RT-Lab based HIL controller. Measured efficiency versus speed plot is shown in Figure 4.38(a) while the efficiency versus load plot is shown in Figure 4.38(b). It shows the high efficiency of the drive over wide speed as well as wide load range. Figure 4.39 shows the plots of no-load power loss and no-load input AC current versus motor speed.

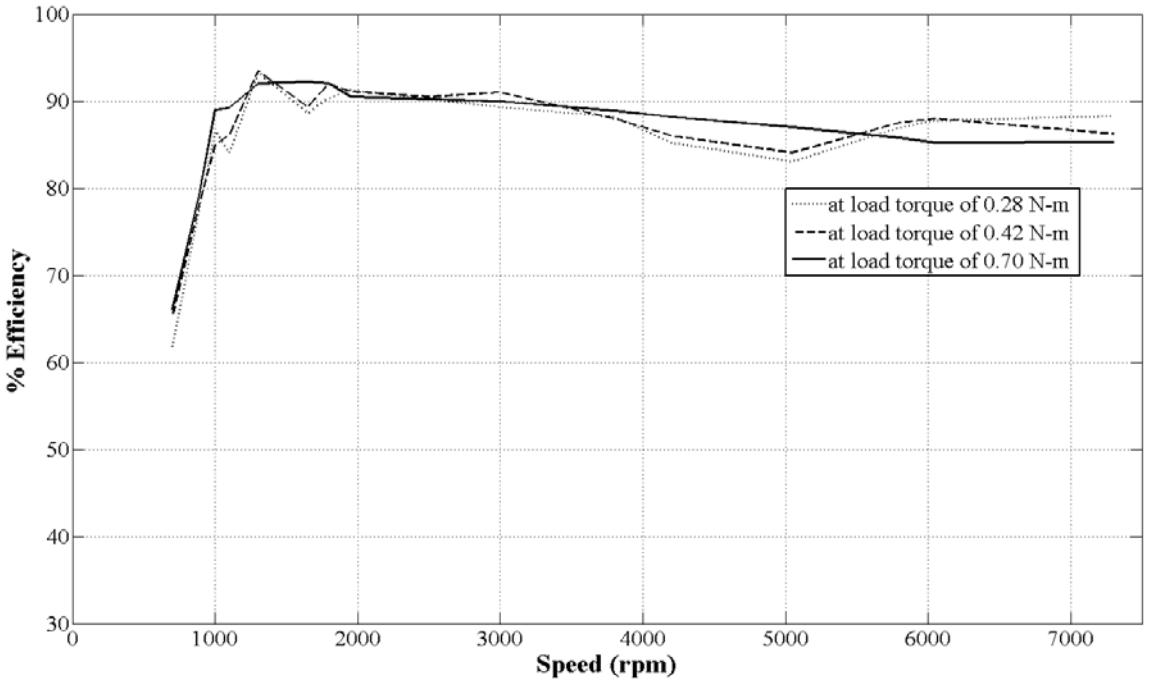

(a)

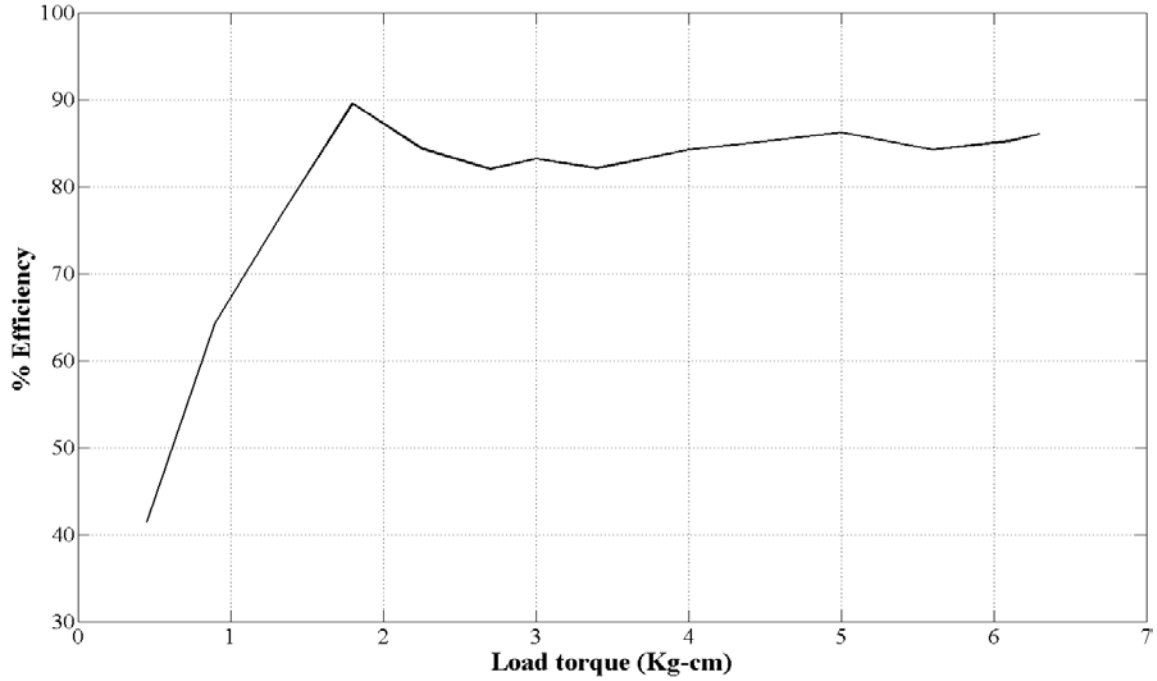

(b)

Figure 4.38 Measured efficiency of SRM drive versus (a) speed at varying load (b) load torque at constant speed of 1500 rpm

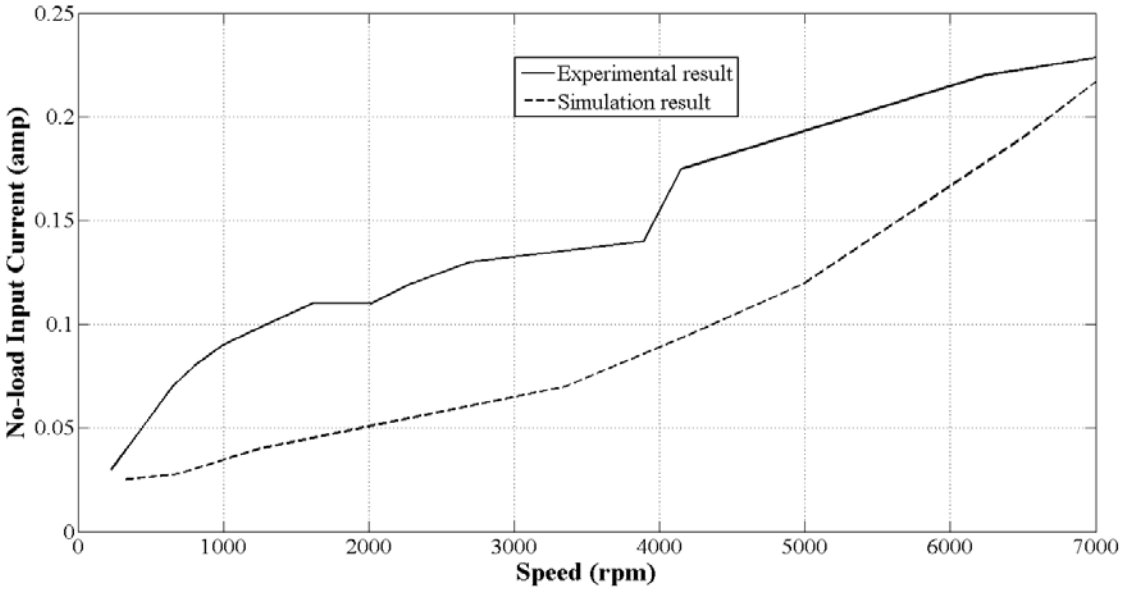

(a)

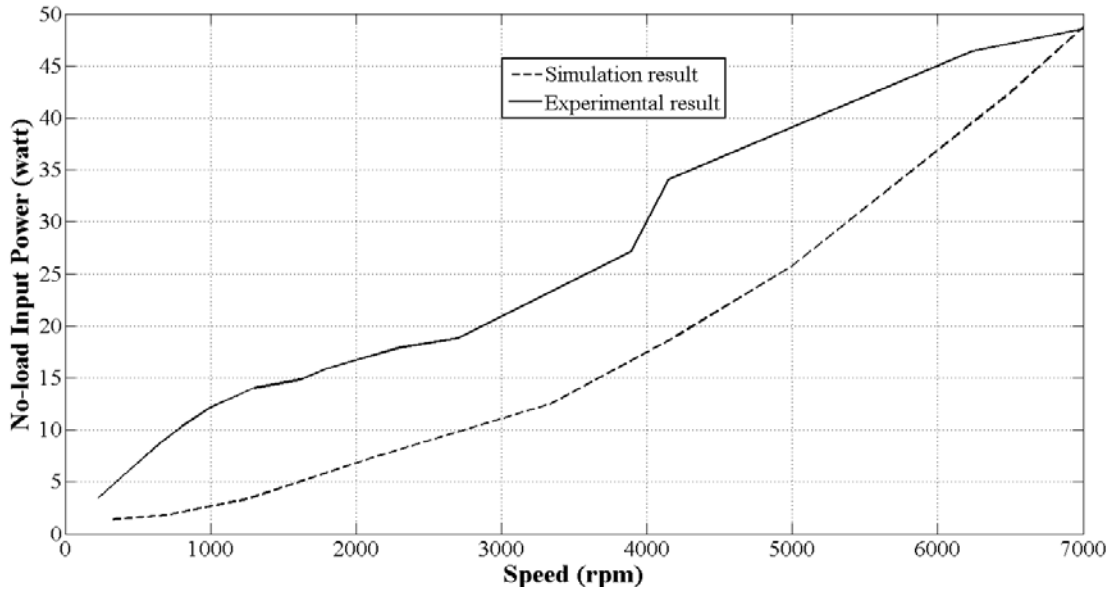

(b)

Figure 4.39 (a) No-load input current and (b) No-load input power versus speed

Torque speed characteristics of the SRM is derived using RT-Lab based real time simulation approach as described in Chapter 3, where it was used to derive the torque-speed characteristics of 60KW SRM. The characteristic is derived for the fixed commutation angle and with the fixed PWM frequency, which is shown in Figure 4.40.

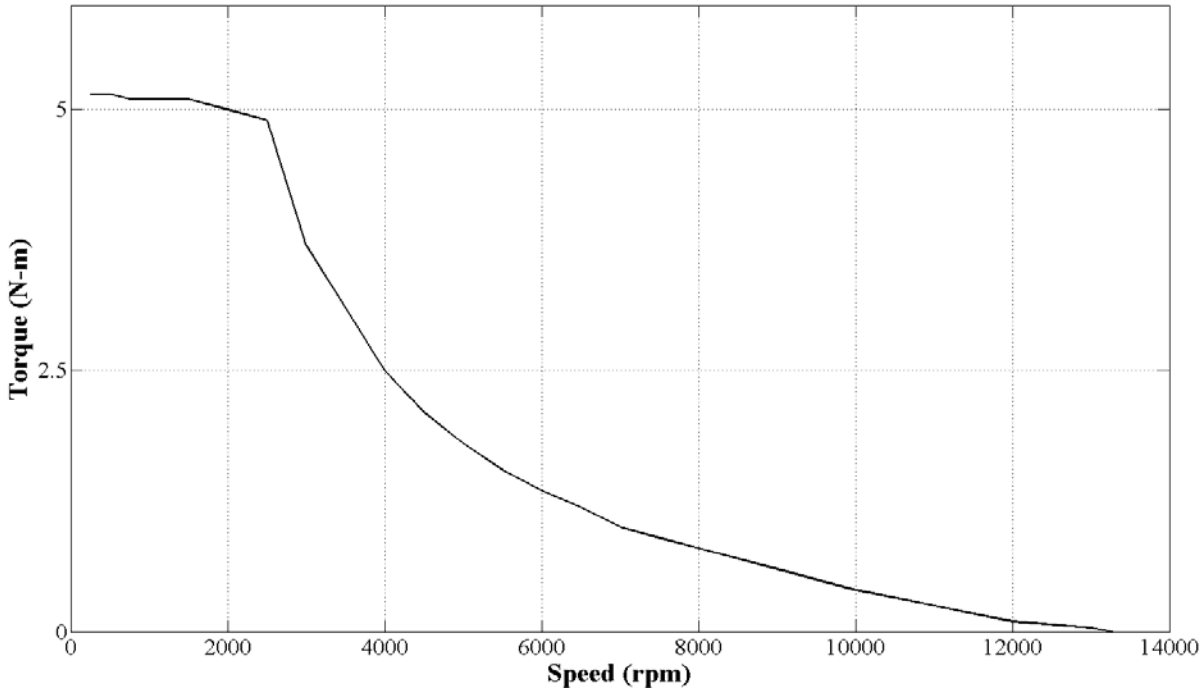

Figure 4.40 Torque-speed characteristics of the SRM

The pulsating torque of the SRM is responsible for the acoustic noise production, while a high frequency switching current also contributes to the same. Frequency spectrum analysis shows that the level of acoustic noise is less for the low frequency PWM controlled SRM drive as compared to the hysteresis current controlled drive. Frequency spectrum analysis of the phase current and motor torque for the PWM controlled drive is shown in the Figure 4.41 and Figure 4.42. While, the Figure 4.43 and Figure 4.44 shows the frequency spectrum analysis for the hysteresis current controlled drive.

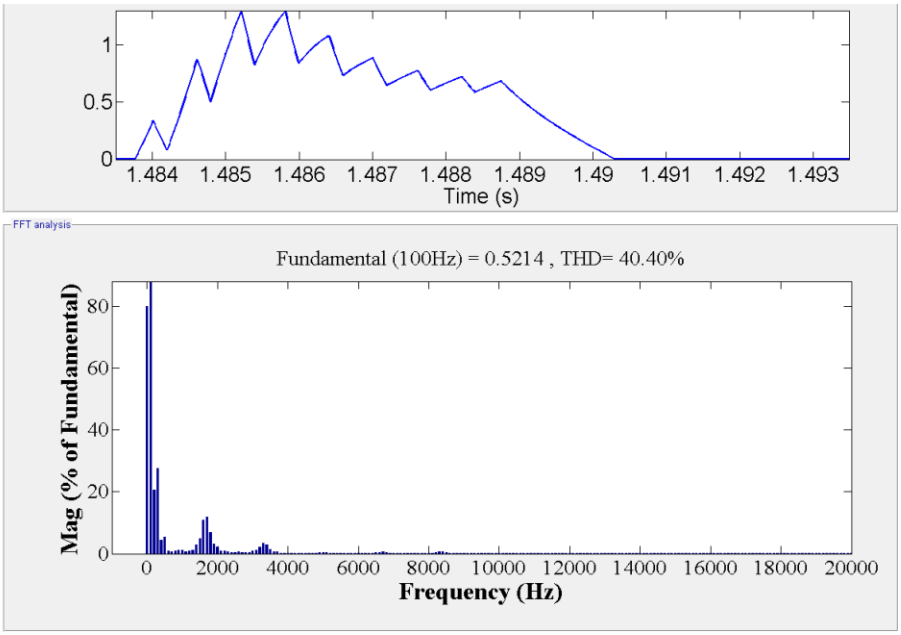

Figure 4.41 Frequency spectrum analysis of the phase current with PWM control (1.67 KHz) at 1000 rpm and 0.7 N-m load

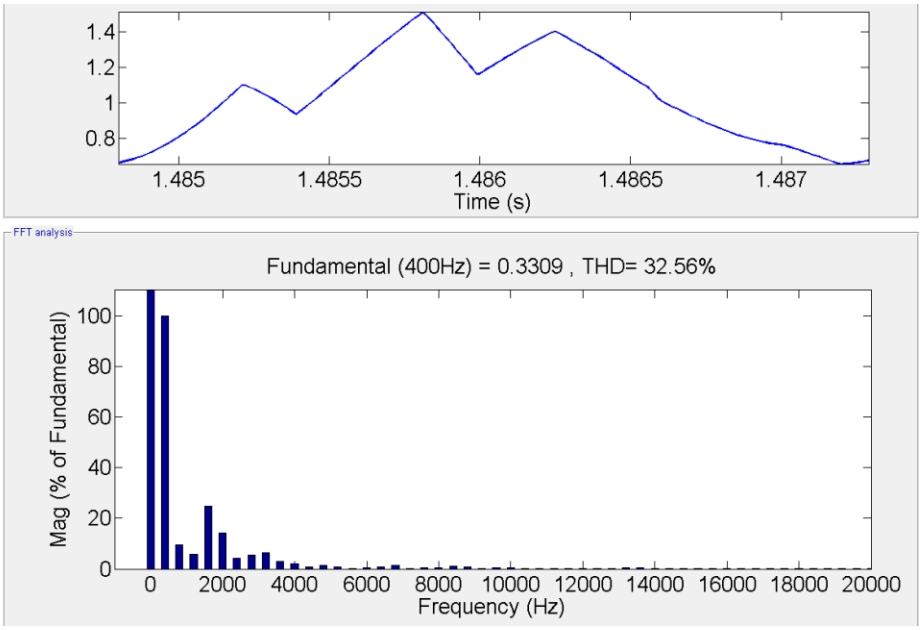

Figure 4.42 Frequency spectrum analysis of torque with PWM control (1.67 KHz) at 1000 rpm and 0.7 N-m load

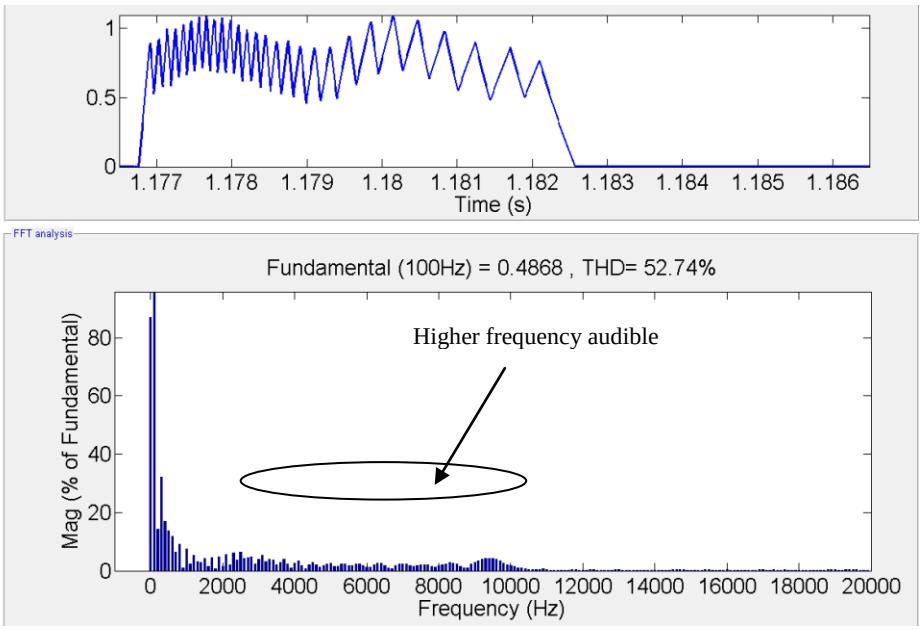

Figure 4.43 Frequency spectrum analysis of phase current with hysteresis control (hysteresis band of 0.2 amp) at 1000 rpm and 0.7 N-m load

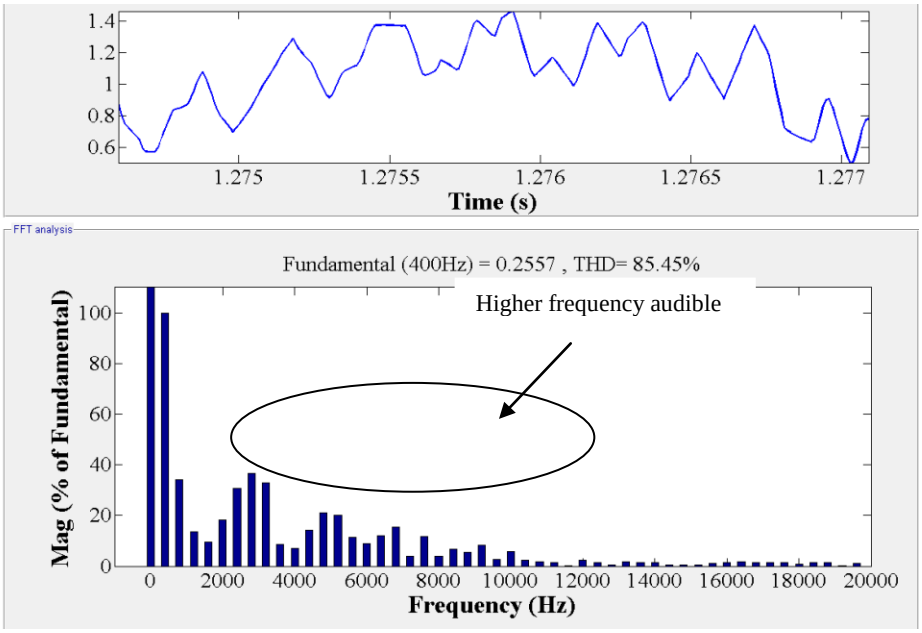

Figure 4.44 Frequency spectrum analysis of torque with hysteresis control (hysteresis band of 0.2 amp) at 1000 rpm and 0.7 N-m load

The machine analyzer MK-500, from the Kawatetsu Advantech Co. Ltd is used to measure the noise and vibrations of the motor. Figure 4.45 shows the measured noise and vibration of the SRM versus speed.

Torque ripple of the motor is measured using RT-Lab based real-time simulation approach and is given as-

$$T_{ripple} = \frac{T_{\max} - T_{\min}}{T_{avg}} \tag{4.24}$$

where 'T_{max}' is the maximum torque, 'T_{min}' is the minimum torque and 'T_{avg}' is the average torque over one electrical cycle [124]. Figure 4.46 is the result from the real time simulation of the motor which shows the waveform of phase current, current through the MOSFET, diode current and phase pulse. The motor speed, load torque as well as PWM frequency affect the amount of ripple in torque. Figure 4.47 shows the plot of torque ripple versus motor speed, while Figure 4.48 shows the plot of torque ripple versus load torque. Amount of torque ripple is reduced at the higher speed as well as for the higher load torque. Torque ripple response with the higher PWM frequency is plotted in Figure 4.49, which shows that the torque ripples are reduced with the higher switching frequency. Figure 4.50 shows the waveforms of the motor torque over one electric cycle for the varying conditions of load torque, speed and PWM frequency. The variations in motor developed torque with change in speed are shown in Figure 4.50(a) ,(b) and (c), for the constant load torque and PWM frequency. The variations in torque with change in load torque changes are shown in Figure 4.50(a) ,(d) and (e), for the constant speed and PWM frequency. The variations in

torque with change in PWM frequency for the constant speed and load torque are shown in Figure 4.50(a) ,(f) and (g),.

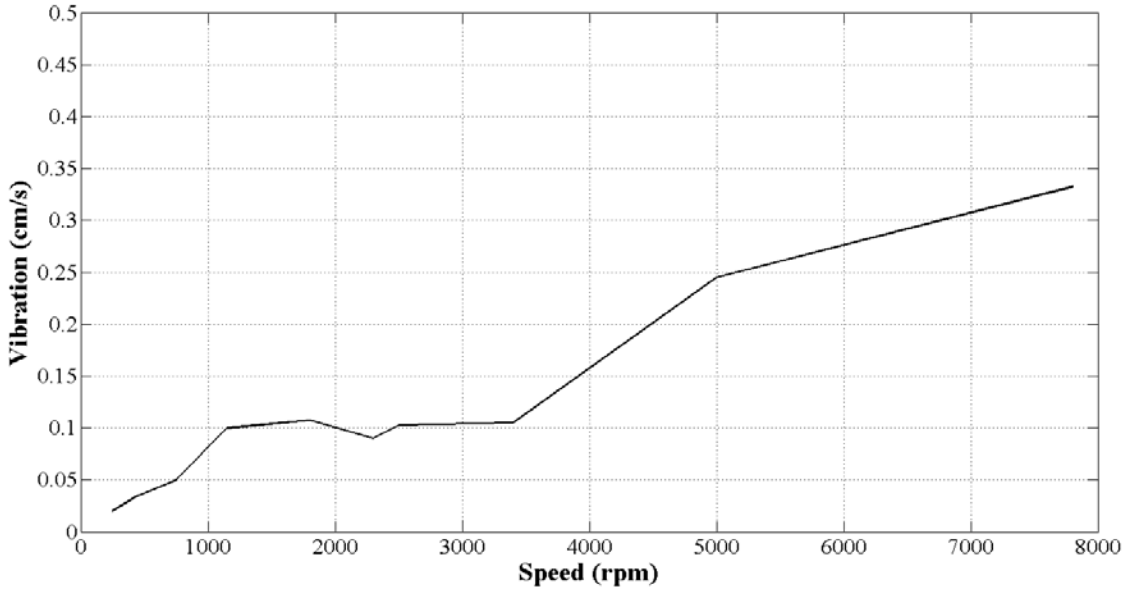

(a)

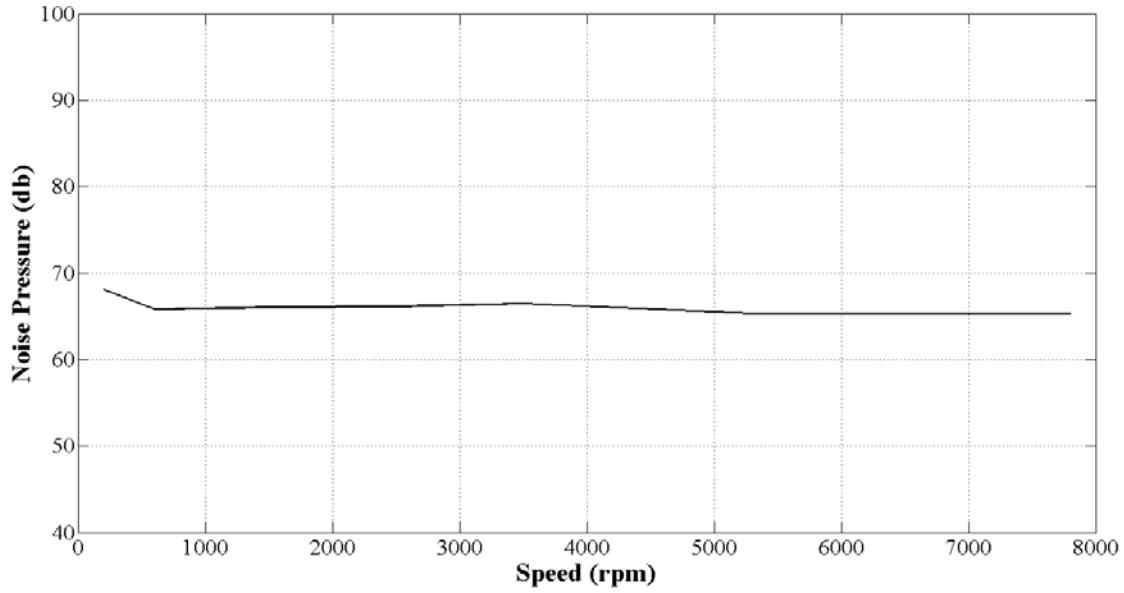

(b)

Figure 4.45 Measured (a) vibration and (b) noise response of the motor

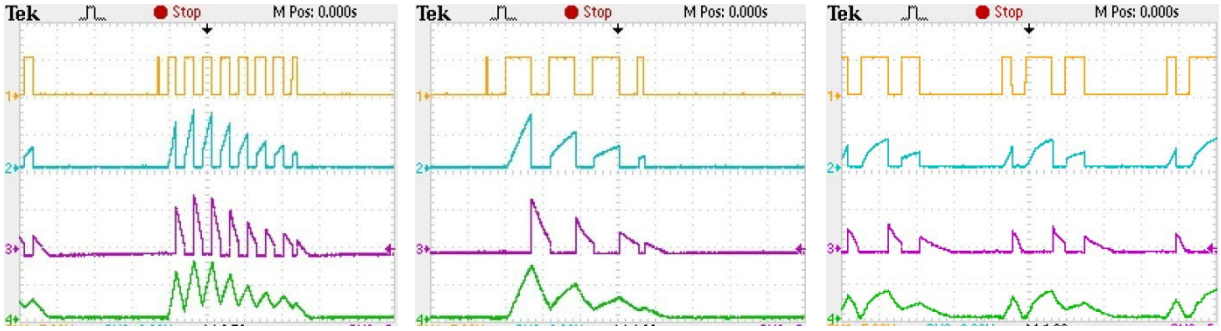

(a) at 1100 rpm (b) at 2200 rpm (c) at 4000 rpm

Figure 4.46 CH1: Phase pulse (5 volt per division), CH2: MOSFET current, CH3: diode current and CH4: phase current (2 amp per division) for the PWM frequency of 1.67 KHz, with the RT-Lab based real-time simulation approach

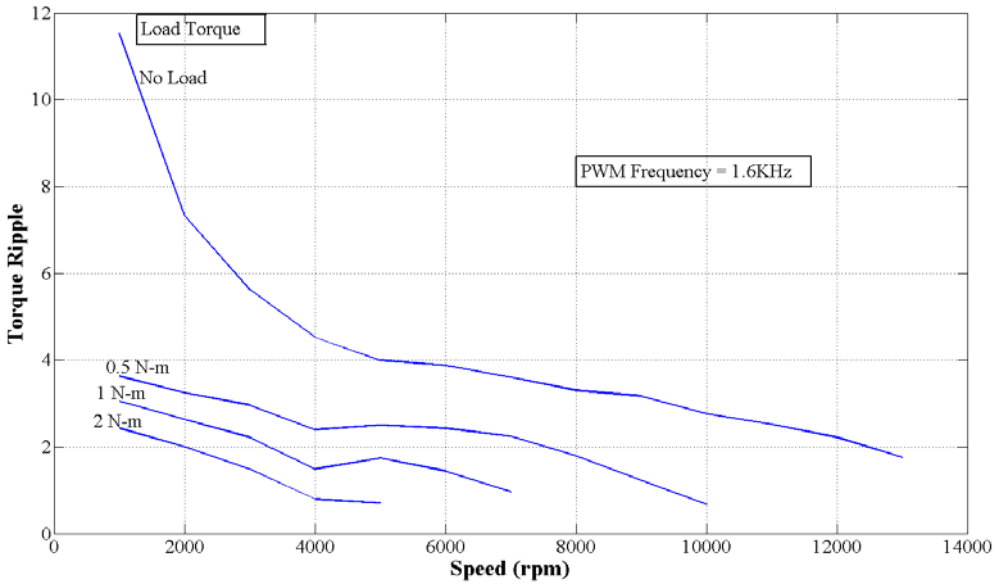

Figure 4.47 Measured torque ripple response of motor versus speed

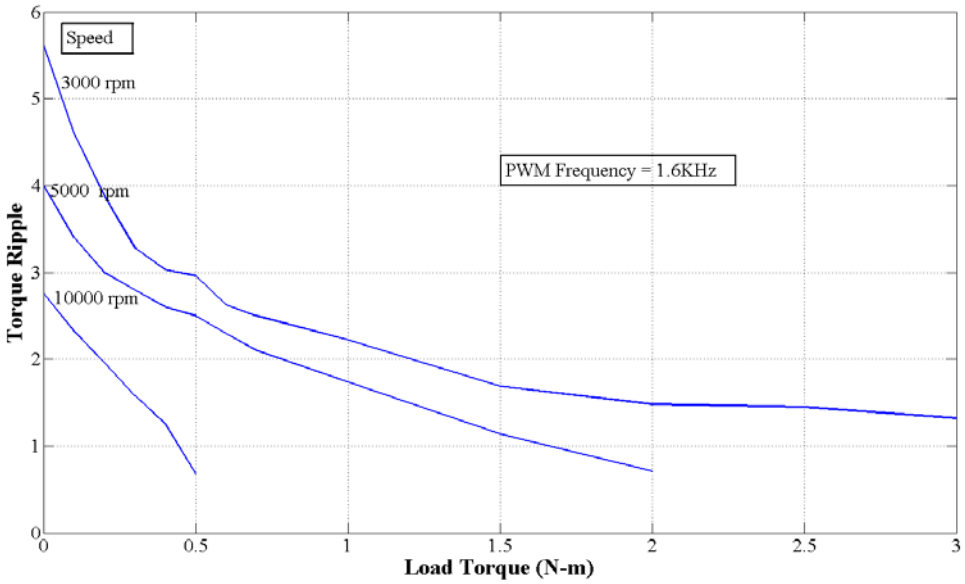

Figure 4.48 Measured torque ripple response of motor versus load torque

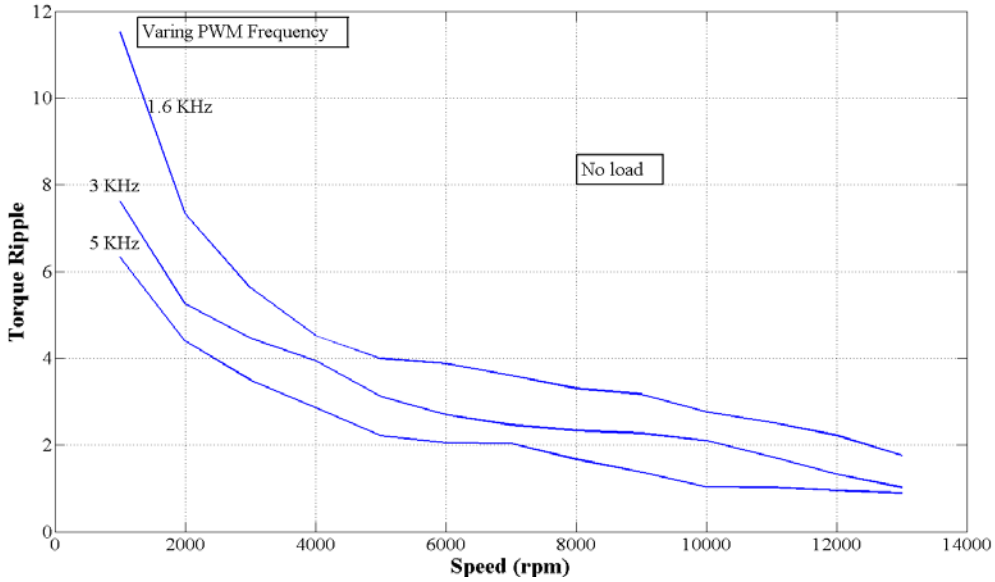

Figure 4.49 Measured torque ripple response of motor versus PWM frequency

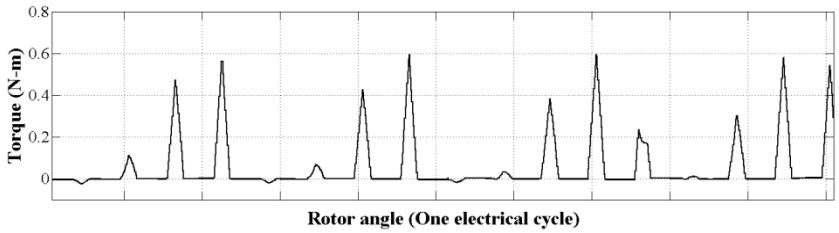

(a) at 1000 rpm, no-load and PWM frequency of 1.67KHz

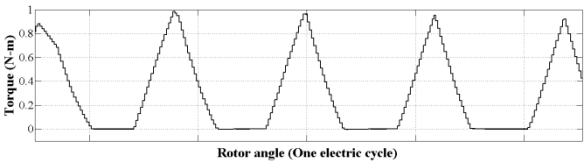

(b) at 4000 rpm, no-load and 1.67KHz

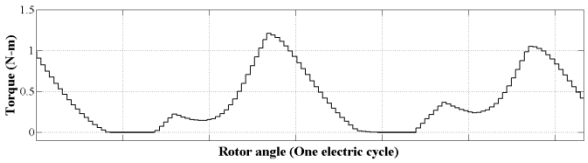

(c) at 8000 rpm, no-load and 1.67KHz

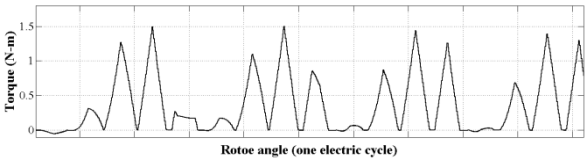

(d) 0.3 N-m load, 1000 rpm and 1.67KHz

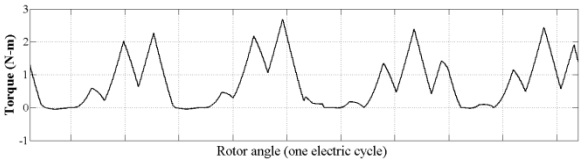

(e) 0.7 N-m load, 1000 rpm and 1.67 kHz

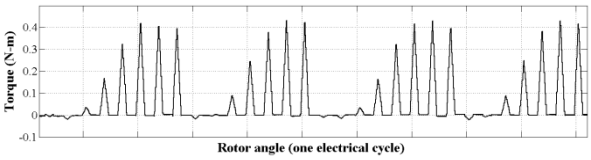

(b) PWM frequency 3KHz, no-load 1000 rpm

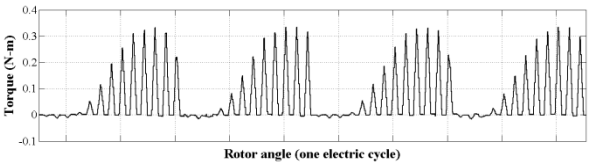

(d) PWM frequency 5KHz no-load 1000 rpm

Figure 4.50 Effect of motor speed, load torque and PWM frequency on the shape of motor torque

4.7 CONCLUSION

Rotor inertia of SRM is very low because of salient pole type construction which leads to lower weight and smaller size compared to conventional AC and DC motor and thus the response of the drive is fast enough. Motor provides higher torque compared to dc and induction motor at all speeds. Furthermore, starting torque can be made very high without the problem of excessive inrush currents. The controller of the SRM has the benefit that it does not need a bipolar (reversed) device because torque is independent of direction of current. In addition, the converter allows two-phase excitation at a time which reduces the ripple in the torque as compared to the single phase excitation scheme.

The analysis shows that the amount of acoustic noise production is less for the developed low frequency PWM controlled SRM drive as compared to the hysteresis controller. It also reduces the switching losses of converter which makes it easier and convenient to cool. The SRM drive offers high efficiency over wide speed range and even with the partial loading condition. The result shows that the developed SRM drive achieved the efficiency up to the 92%. Comparing with VFD based induction motor drive; the implementation cost of the proposed SRM drive is quite low. The performance to cost ratio of the developed SRM drove is quite high.

The investigating shows that the amount of torque ripple is depended upon the speed, load torque and PWM frequency. It is observed that the amount of torque ripple, with the no-load condition, is found 7.5 at the speed of 2000 rpm while it reduced to 2.8 at the speed of 10000 rpm. The amount of torque ripple, with the constant speed of 3000 rpm, is found 5.6 at the no-load while it reduced to 1.7 at the load torque of 1.5N-m.

Chapter 5: SENSORLESS CONTROL OF THE SRM DRIVE

The fixed-angle control scheme with the coarse position sensor fulfils all the requirements of variable speed drive, as described in previous chapter. However, a high performance drive requires high resolution position sensor to implement angle control scheme. An absolute encoder or resolver is used, in general, to obtain precise position information, which increases cost of the drive significantly. Different sensorless rotor position estimation techniques of the SRM are explored in this chapter which eliminate the requirement of mechanical position sensors. The flux linkage based technique is investigated in detail in the present chapter. The fixed-turn-off angle method is developed which makes use of minimum magnetic characteristics data to obtain coarse position information. ANN based sensorless method is also developed which provides rotor position information with accuracy and resolution. Further, an analytical method of rotor position estimation is proposed and developed which provides good accuracy of estimation without imposing burden of heavy computation and storage space on the processor.

5.1 INTRODUCTION

The high performance motor drive and motion control applications demand ripple free torque, precise speed control and optimized efficiency. It makes necessary to incorporate an optimized angle control scheme or one of the torque control algorithms like TDF(Torque Distribution Function) [33], TSF(Torque Sharing Function) [34] or look-up table based current profiling [64]. All these methods require an accurate rotor position feedback system, while low cost and low resolution arrangement like hall sensor or optical sensor together with the slotted disk is not suitable. Thus, high resolution mechanical sensors like absolute encoder and resolver are normally used to supply the position information. However, there has been enormous attention in eliminating the mechanical position sensor for reducing the cost, overall physical dimension and weight which also increases the reliability of operation in all environmental condition. A good number of sensorless rotor position estimation techniques have been proposed by the researchers over the last two decade [4, 39-41, 43, 50, 52, 58, 65, 72, 91, 92, 97] that include state observer [91, 43, 65], active probing [4, 58, 50], modulates signal injection [40, 41], flux-linkage based method [92] and current waveform monitoring technique [111, 50].

In the state observer method the model of the complete system is simulated simultaneously with the real system. The model generates a current for the applied voltage, which is compared with the actual system current. The current error adjust the gain for the three state variables; flux, speed and position. Literature shows that the linear model of the

observer has been used for the simulation [91] for simplicity**,** while non-linear model of the observer has also been presented [43] along with the experimental results. The observer based method offers high resolution position estimation but its practical implementation is quite complex. The sliding mode based observer has been appeared in literature [65] which reduces the complexity of the model. Past investigation of the state observer based sensorless method [50] shows that the accuracy of this method depends upon the mathematical model and computational power of the hardware. This method uses mathematical model of complete system including mechanical load, thus application of the designed observer model is fixed for the particular system. The real-time implementation requires complex algorithm, extra circuitry and significant amount of stored data. It greatly increases the implementation cost and speed limitation is imposed by hardware due to computation burden.

In the active probing method, the high frequency probing pulses are injected into the non-conducting phase. The magnitude of the injected current pulses are kept low to reduce the negative torque production as compared to the active torque of the motor. The phase inductance is estimated from the peak value of the probing current which is inversely proportional to the inductance. The rotor angle for the estimated phase inductance is found from the relation of rotor position versus phase inductance stored as look-up table. The main advantage of this method is that it is applicable at standstill. However, it is difficult to implement the method for a high speed operation because there is a little time for probing the pulse. Another problem that arises in the implementation is that it is very sensitive to the mutual inductance, as the current of the active phase induces voltage in unenergized phases, which distorts the probing pulse. It is also required to have prior information about phase inductance as a function of rotor position. The variation in the phase inductance is flat near to the unaligned position, thus it is difficult to estimate the rotor position in this region. The major drawback of the method is that it deteriorates the efficiency of the drive because of negative torque production by the probing pulses.

The modulated signals, used in communication systems employing techniques like frequency modulation, amplitude modulation and phase modulation; are used to estimate the phase inductance of unenergized phase [40, 41]. In [40], an unenergized phase is connected to the oscillator which is designed such that the frequency is inversely proportional to the phase inductance, and by measuring frequency, inductance is estimated. Also, the sinusoidal voltage with the fixed frequency and amplitude is applied to an unenergized phase via resistor [41]. The inductance is measured by detecting change in phase displacement between voltage and current. The method is applicable at standstill and offers reasonably good accuracy. This method suffers due to mutual effect of energized phase, speed limit and requires knowledge about the specific inductance of the phase. The

method requires a multiplexer to connect and disconnect the modulator from the power circuit. The external modulator and isolation circuit increases the cost and component required compared to previous method.

5.2 FLUX-LINKAGE BASED SENSORLESS ROTOR POSITION ESTIMATION

Flux-linkage based sensorless method is the most accurate sensorless method because it uses an actual motor magnetic characteristic to estimate a rotor position. Lyons made use of magnetic characteristics of the SRM first time in 1991 to estimate the rotor position [92]. The method use a set of magnetization curves stored in a multi-dimensional table. The basic theory of the flux-linkage based sensorless method is based on the fact that, the magnetic characteristics is a three dimensional non-linear relation amongst current, flux-linkage and rotor angle, thus if any of the two variables are known then the third can be found from the stored magnetic characteristics. A typical magnetic characteristic is shown in Figure 5.1 where few magnetic curves for different rotor position are shown for the simplicity.

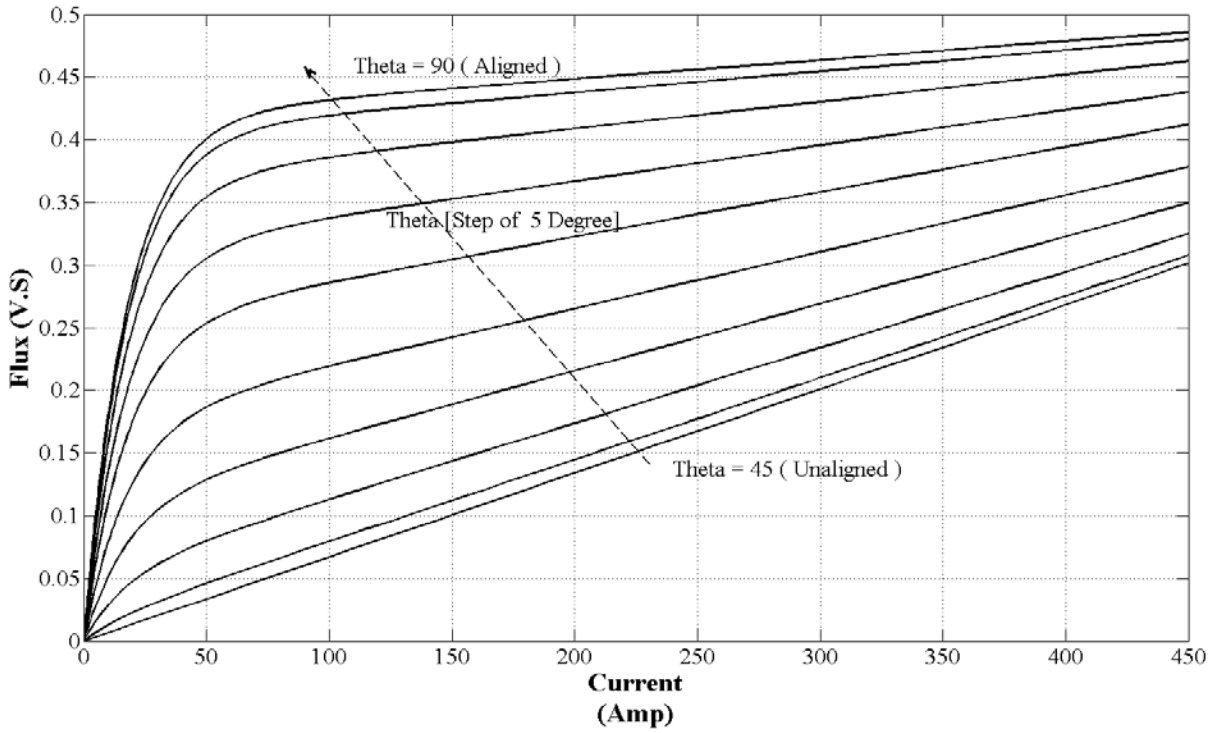

Figure 5.1 Magnetic characteristic of the 60KW 3-phase 6/4 pole SRM

High resolution rotor position estimation requires large number of magnetic curves to store. It is to be noted that half an electrical cycle is enough to represent the complete magnetic characteristics of the motor from the unaligned to aligned position because unaligned position is a case which occur at the middle of the electrical cycle for the regular motor. The magnetization curve at unaligned position is the straight line while at aligned position it shows two deflections, one at current of 40 amperes and other one at 250 amperes. First

deflection is mainly due to magnetic saturation of the stator and rotor pole corners and second deflection is due to magnetic saturation of the stator and rotor core (yoke). The large numbers of magnetic characteristics are stored as 3-dimentional look-up table where phase current and flux-linkage are used as indices to find the respective values of the rotor position. The flux is calculated using (5.1). The block diagram of the sensorless method is shown in Figure 5.2. The rotor position can be derived from the instantaneous values of phase voltage and phase current as the flux-linkage can be derived from the phase voltage and phase current.

$$\psi(t) = \int (V_{ph} - i_{ph} R_s) dt \tag{5.1}$$

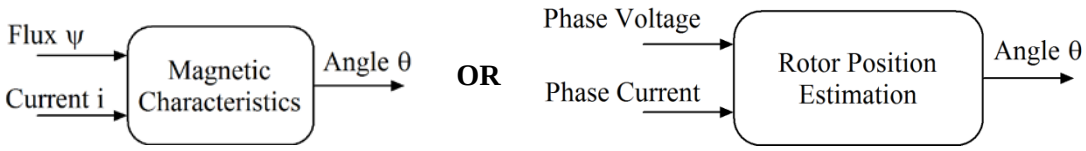

Figure 5.2 Basic block diagram of the flux-linkage based sensorless method

This method requires experimental setup and takes time to measure the magnetic characteristic of the motor for the range of position [100]. The accuracy of the position estimation depends up on the stored data, that means more data is required for higher resolution. The rotor position can be estimated from the active phase only which might be used to commutate the same conducting phase or to energize the succeeding phase.

Performances of the following flux-linkage based sensorless methods have been investigated using simulation analysis.

- Fixed turn off angle method
- ANN based sensorless method
- An analytical method

The fixed turn-off angle method of rotor position estimation is proposed which store only one magnetic curve instead of all rotor position. The method gives the coarse rotor position, which decides the turn-OFF instant of the conducting phase. The ANN (artificial neural network) is used to represent magnetic characteristics of the motor in the ANN based sensorless method. An analytical sensorless method is proposed which store two magnetic curves, one at mid position and the other at aligned rotor position. The method reduces the significant amount of stored data to estimate continuous rotor position.

The simulation model of 6/4 pole three phase SRM is used with conventional bridge converters and hysteresis current controller to investigate the performance of the sensorless methods. These methods are described in detail in the following sections.

5.2.1 Fixed turn-off angle method

The block diagram of the fixed-turn-off angle sensorless method is shown in Figure 5.3. The magnetic curve at the reference rotor angle 85° is stored as a look-up table. The reference rotor angle is selected to provide advance phase commutation. The phase voltage and phase current are measured continuously, from which an instantaneous flux for each phase is calculated in real-time using (5.1). The phase current is used as an index to generate the reference flux ψ_{ref} from the look up table. The calculated flux ψ_{cal} is compared with the reference flux ψ_{ref}, which generates a flux difference ψ_{diff}. The commutation logic block generates an individual phase commutation pulse from the flux difference.

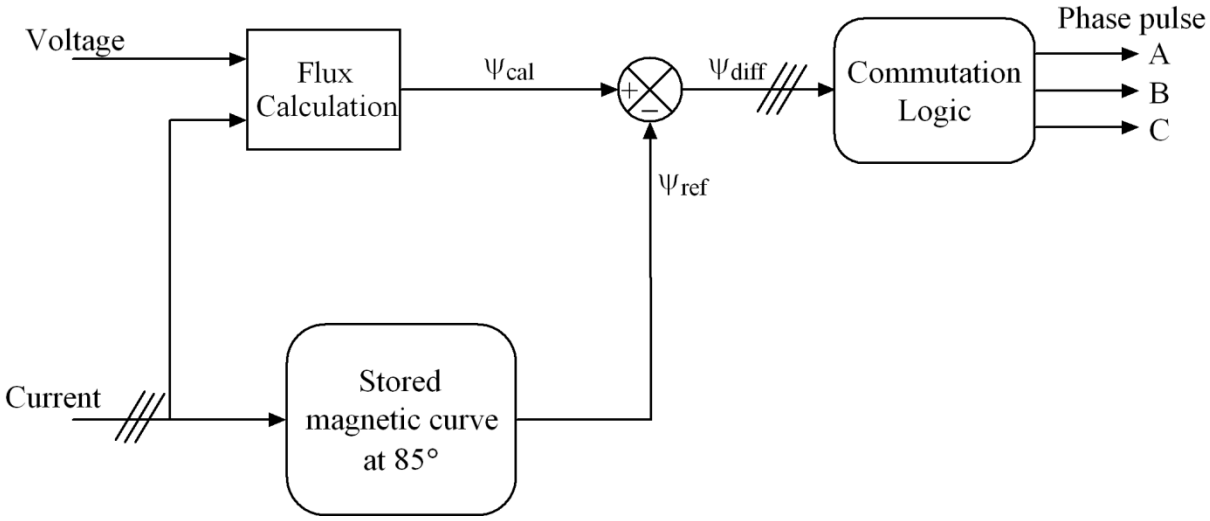

Figure 5.3 Block diagram of fixed turn-off angle method

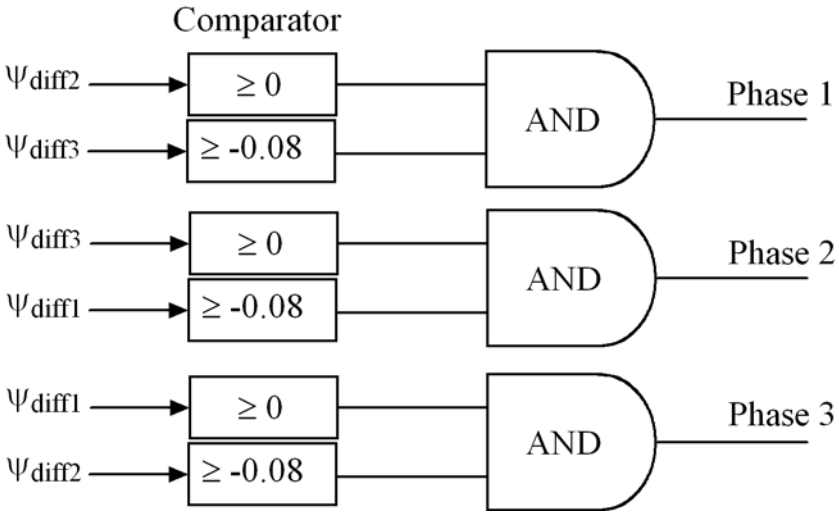

Figure 5.4 Commutation logic of the fixed turn-off angle method

It is assumed that the initial rotor angle is 45° (unaligned position). If the phase-1 is excited at an unaligned rotor position then the difference between ψ_{cal} and ψ_{ref} becomes maximum, which reduces as rotor moves toward aligned position. The ψ_{diff} becomes zero at

a reference rotor angle that is 85°. The flux difference increases again with further increase in rotor angle that is from 85° to 90°. However, the conducting phase is commutated when

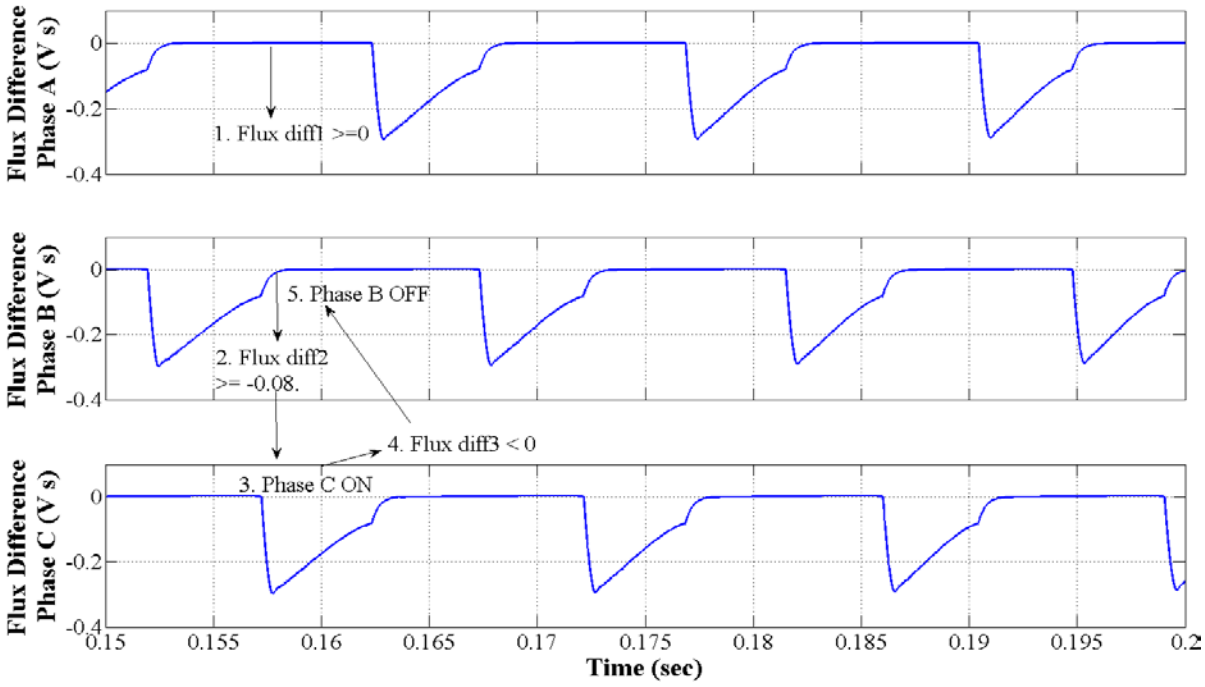

(a)

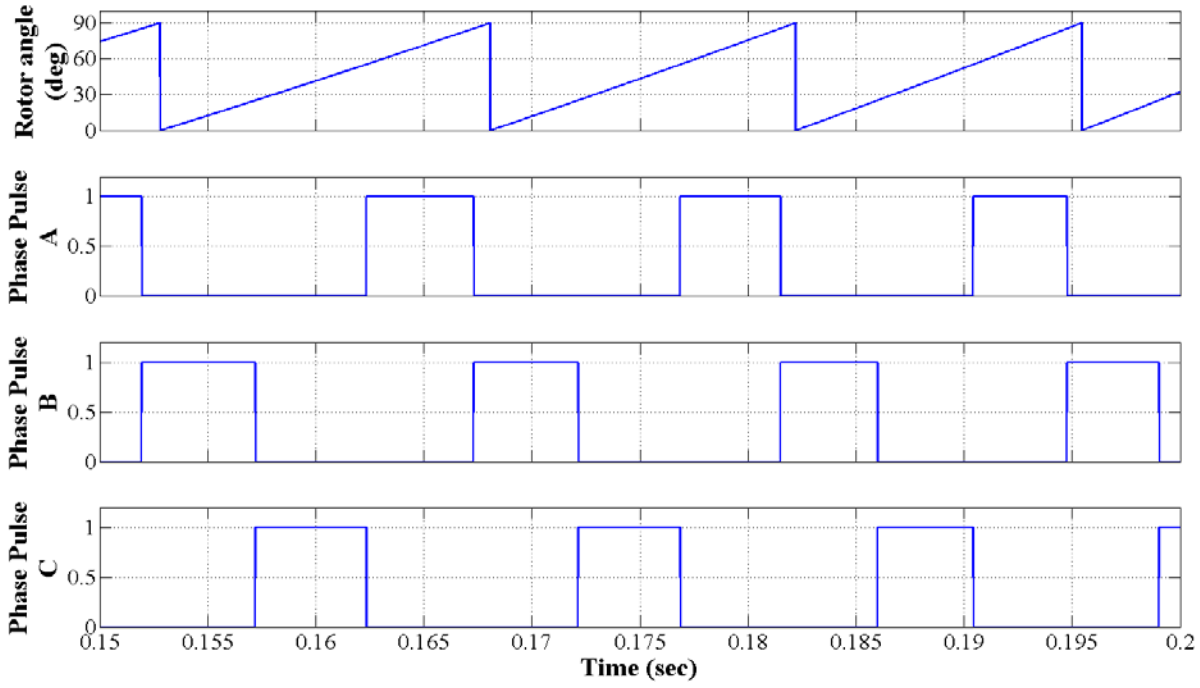

(b)

Figure 5.5 Waveform of (a) flux difference and (b) commutation pulse of each phase

ψ_{diff} becomes zero and subsequent phase is turned ON at the same time. Thus the phase conduction is advanced by the same degree as the commutation advance. The flux difference of the commutated phase is zero as ψ_{cal} and ψ_{ref} both are zero. If the conduction

sequence is assumed to phase1-phase2-phase3, and flux differences for the each respective phases are ψ_{diff1}, ψ_{diff2} and ψ_{diff3}, then the phase-1 is commutated and phase-2 is excited at a condition ψ_{diff1}=0.

The logic of commutation is implemented as shown in Figure 5.4. The comparator output is logic '1' if the specified condition is TRUE else '0'. The waveforms of flux difference and phase commutation pulses are shown in Figure 5.5. At the instant when only phase-2 is ON, the ψ_{diff2} is negative which approaches to zero as rotor angle increases, while ψ_{diff1} and ψ_{diff3} are zero. At an instant, when ψ_{diff2} is close to zero (>= -0.08), phase-3 will turn ON as both the inputs of the AND gate are at logic '1'. Consequently ψ_{diff3} becomes negative which dissatisfies the condition for phase-2 to remain ON. Likewise, each respective ψ_{diff} turns ON the succeeding phase and self commutates as shown in Figure 5.5.

The waveform of the flux, phase current and torque are shown in Figure 5.6 for the sensorless operation of the drive. The result shows that the method gives the same performance as provided by the coarse mechanical sensors like Hall Effect and optical interrupter.

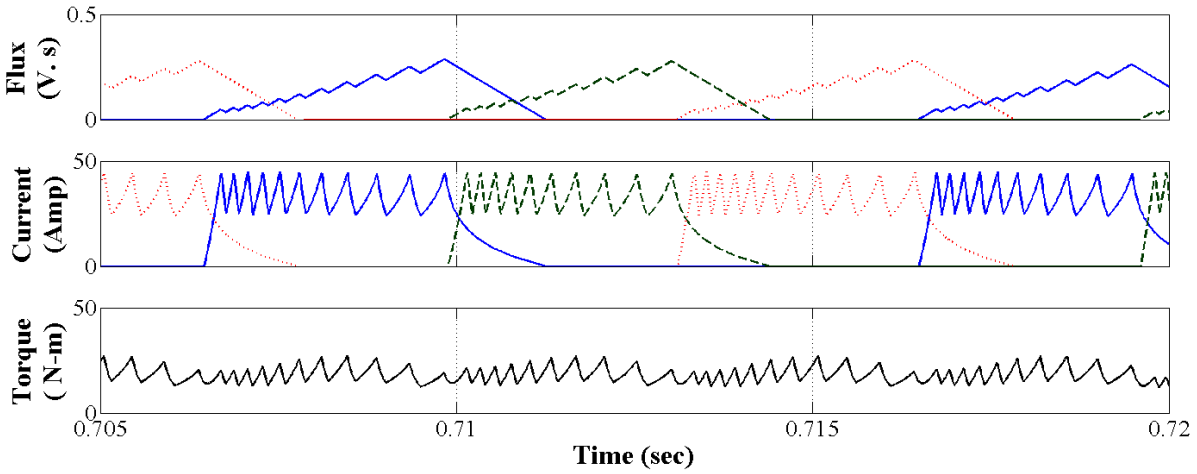

Figure 5.6 Waveform of the flux, phase current and torque at the speed of 1500 rpm

The method is simple, cost effective and easy to implement as it does not involve any complex computation and require very less amount of data to store. The method also offers high accuracy with the wide speed range operation.

The angle control and multi-phase excitation are not possible. However reference angle can be selected to achieve desire phase advance. More than one magnetic curves can be stored to have flexibility in selecting mode of operations like low speed, medium speed or high speed. The dwell angle cannot be increased which deteriorates the peak torque capability in high speed operation.

The method is suitable for the applications where the use of a mechanical sensor seems to be unreliable due to harsh environmental conditions.

5.2.2 ANN based sensorless method

The ANN technique is applied to estimate the continuous rotor position of SRM. The ANN forms a very efficient mapping structure which utilizes to map a non-linear magnetic characteristic of the SRM.

5.2.2.1 *An introduction to ANN*

Artificial neural networks are composed of simple neuron operating in parallel which inspire from the operation of the human brain [60, 163]. Figure 5.7 shows the model of simple neuron introduced by the McCulloch & Pitts which compose of inputs X_1 & X_2, weights W_1 & W_2, bias 'b', summing function and activation function. Weights can acquire & store the experimental knowledge which also called synaptic weights because its function is identical to the synapses in biological neuron. The activation function is used for limiting the output of a neuron while the bias has the effect of lowering the net input of the activation function. Mathematically it can be described as follow.

$$Net = X_1 \times W_1 + X_2 \times W_2 + b \times W_b \tag{5.2}$$

$$Output = f(Net) \tag{5.3}$$

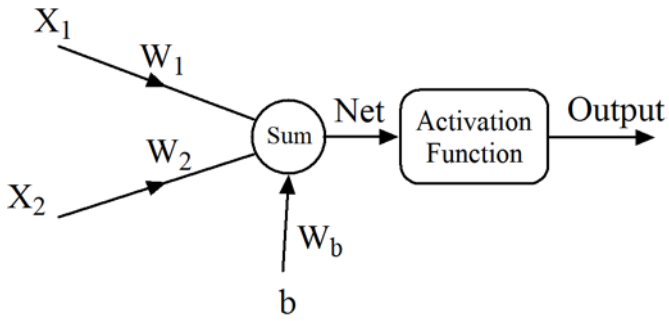

Figure 5.7 Simple neuron model

Process of acquiring knowledge is called learning or training which required large number of input and target output patterns. Figure 5.8 shows typical learning process of the neural network. The first pattern of input and targeted output is applied by selecting the initial weights randomly. Calculated output for this input pattern is compared with the applied targeted pattern which generates an error. The weight adjustment mechanism modifies the current weight to reduce an error. Modified weights are used for calculating the output for the next pattern of input and compared with the next pattern of targeted value, which generates the new error and modify the weight again. The process goes on until results are get satisfactory. The ways that neurons are interconnected, categorizes the neural networks in different type. Different learning techniques are also published which may associate with some particular type of the neural network. Choosing an appropriate activation function is a

vital part of the designing a neural network. Neural networks are capable to solve different types of problems mainly function approximation, pattern reorganization and classification.

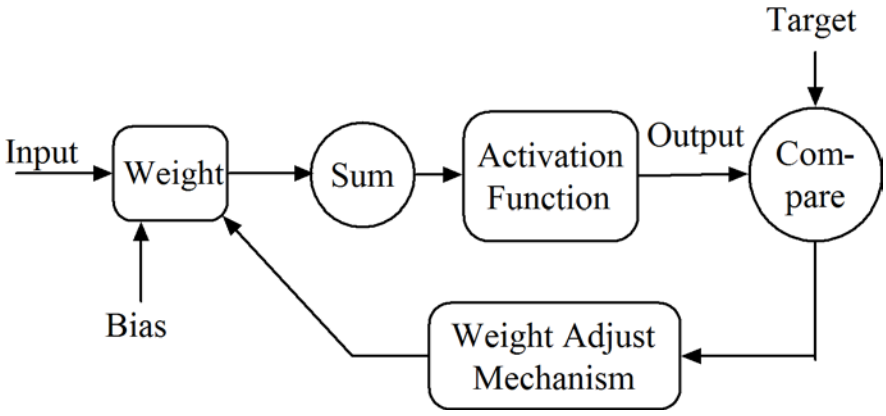

Figure 5.8 Learning process of the neural network

5.2.2.2 *Neural Network Design for rotor position estimation*

The neural network is designed to estimate a rotor angle from the applied phase current and flux linkage for 6/4 pole three phase SRM. Basically, ANN replaces the stored multidimensional look-up table from the basic flux-linkage based method by providing a complex mathematical structure to represent a non-linear magnetic characteristic of the SRM. Accuracy of the mapping function depends upon preciseness and amount of data available to train the neural network. The training is done offline which requires having magnetic characteristics of the motor. Magnetic characteristic with the 46 magnetic curves at an angle difference of one degree is used to train the neural network.

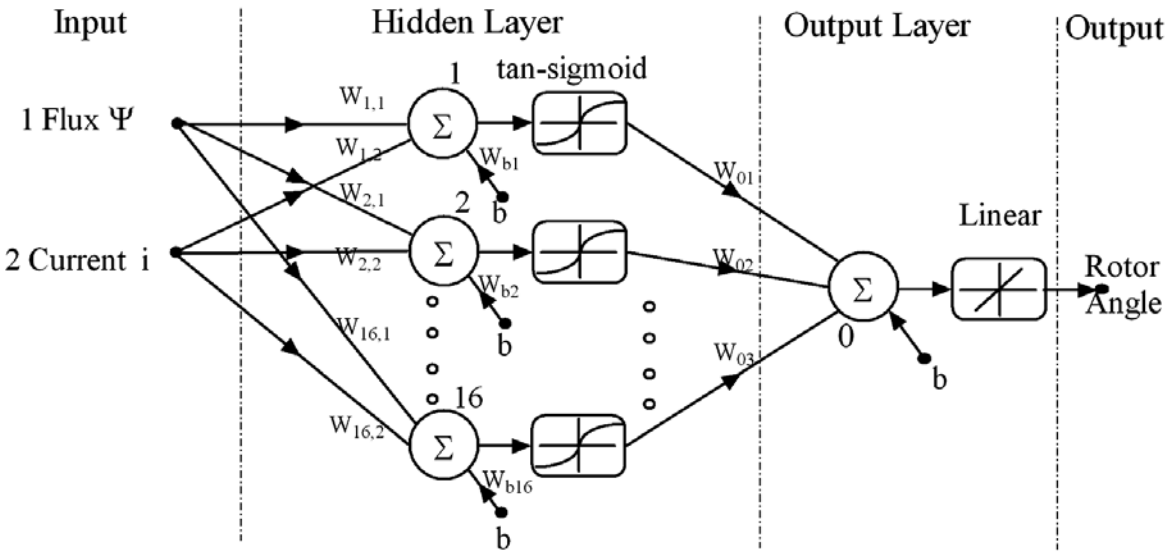

Figure 5.9 Feed-forward neural network structure

The feed-forward neural network structure is used as it found useful for most of the function approximation problem [163]. The structure of neural network used is shown in

Figure 5.9 which has two inputs and one output, while there is one hidden layer and one output layer. The tan-sigmoid transfer function and linear transfer function are used as activation function of the hidden layer and output layer respectively. Sixteen neurons are preferred for the hidden layer for the given problem. More neuron in the hidden layer allows the network to solve more complicated problems, but more neuron requires more computations. Number of neurons in hidden layer is decided after covering some simulation experiments with different number of neuron for the present problem. Feed-forward neural network is designed & trained using '*nftool'* of the MATLAB [62].

The Levenberg-Marquardt technique is used as a training algorithm which reduces the training time as compared to back-propagation technique [97]. The required training data is available in term of 46 magnetic curves. Total data is divided in to two vectors called input vector of the dimension 2x4646 and the target vector of dimension 1x4646. The input vector represents the flux linkage and current while output vector represents the rotor angle θ. Input vector and output vector are randomly divided in three sets such that 70% are used for training, 15% are used to validate that the network is generalizing and to stop training before over-fitting and 15% are used as a completely independent test of network generalization. During training, all the input vectors to the network appear at once in a batch. One can also change the training style to present the input vector one at a time. Training is stopped when validation error increase for six continuous iteration which occurred at 678 iteration. Figure 5.10 shows the training performance which is a plot of training error, validation error and test error. It shows that final mean square error is small, while test set error and validate set error have very similar characteristic and no significant over fitting has occurred by iteration 672 where the best validation performance occurred. Figure 5.11 shows linear regression performance of the trained neural network between network output and corresponding targets. It shows that the output tracks the targets very well for training, testing and validation and the R-value is over 0.99 for the total response. Result of training performance and regression performance dictate that response of the neural network is satisfactory and it is ready to estimate rotor position for any input vector. Since network model and simulink model of the neural network is generated, weight matrix of the hidden layer and output layer for the generated neural network are (5.4) and (5.5) respectively where bias b=1.

Input vector [2x4646] is applied to the designed neural network to generate the estimated rotor position as an output [1x4646]. Figure 5.12 is a three dimensional plot of the magnetic characteristics which shows the comparison between actual magnetic characteristic of the motor and the magnetic characteristic represented by the designed ANN, where only 10 magnetic curves are shown for simplicity. It shows that the magnetic characteristic of the motor is mapped with good accuracy by the designed ANN.

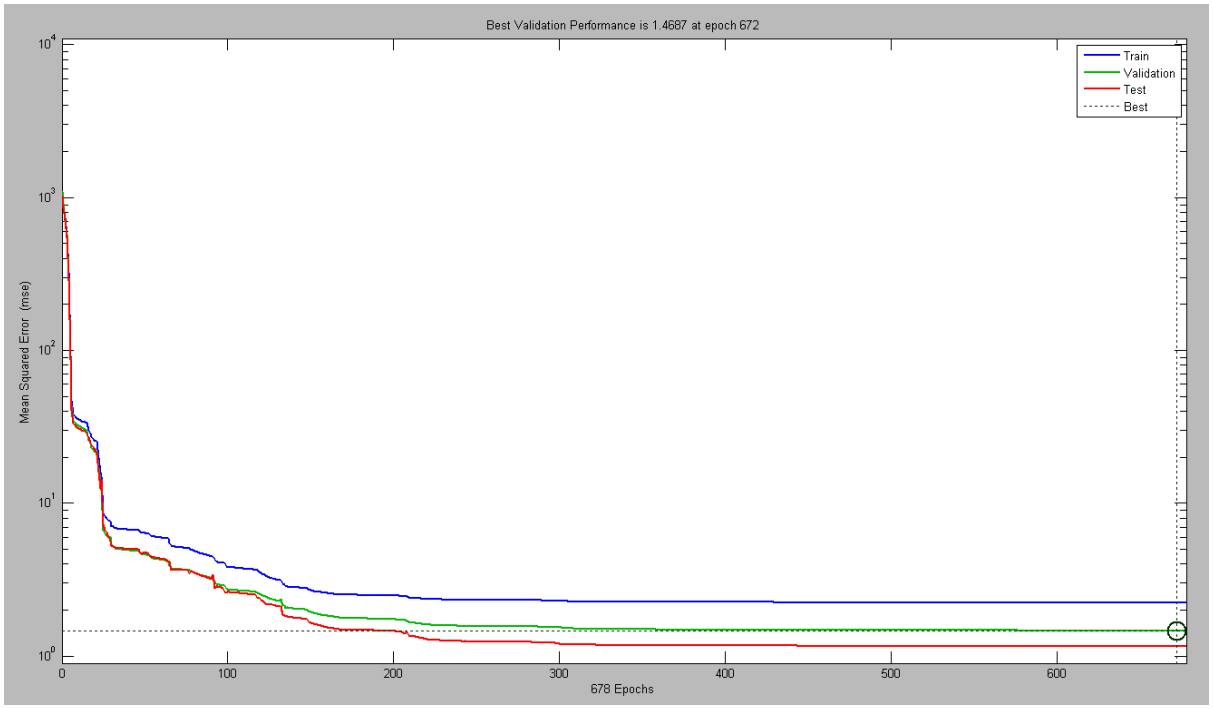

Figure 5.10 Training performance

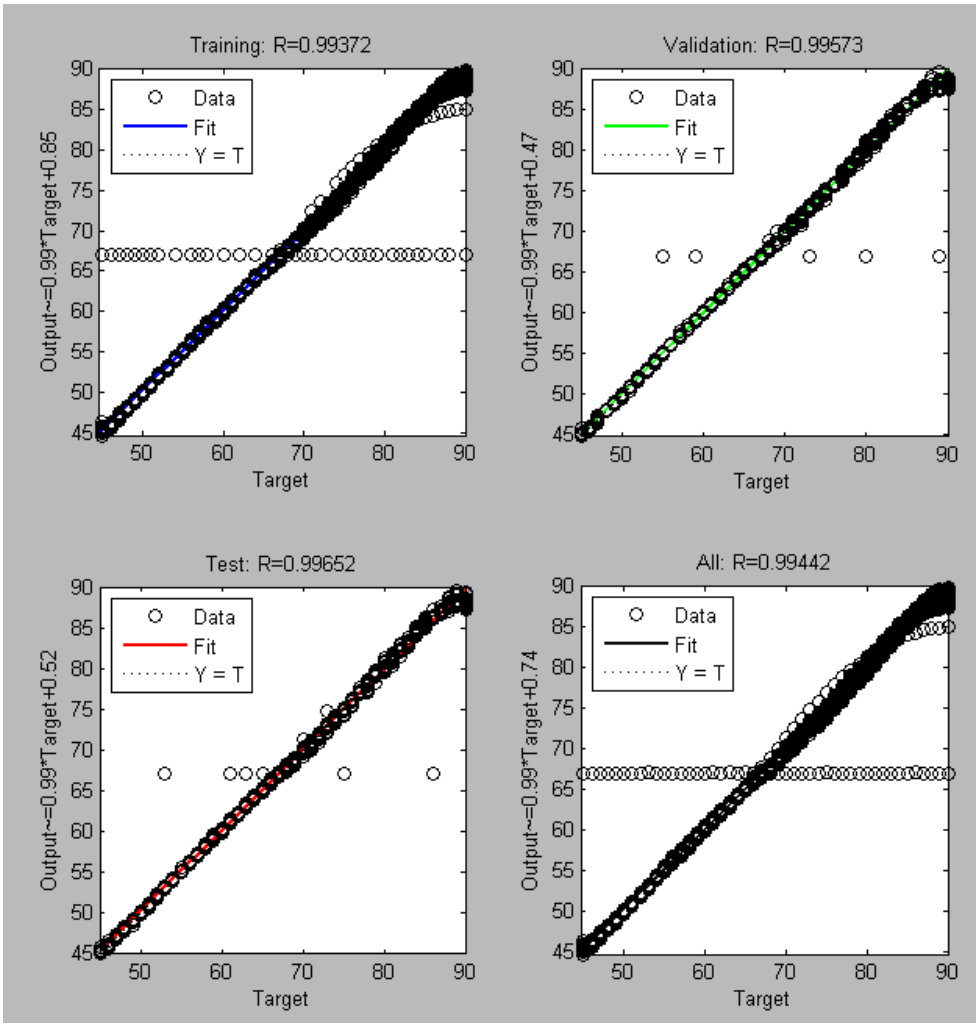

Figure 5.11 Performance analysis of the trained neural network

$$
\begin{array}{c} \\ 1 \\ 2 \\ 3 \\ 4 \\ 5 \\ 6 \\ 7 \\ 8 \\ 9 \\ 10 \\ 11 \\ 12 \\ 13 \\ 14 \\ 15 \\ 16 \end{array}
\begin{array}{c}
\begin{array}{ccc} W_i & W_\psi & W_b \end{array} \\
\left[\begin{array}{ccc}
-0.5934 & 91.9621 & 93.72433 \\
2.0181 & -1.8513 & -2.2939 \\
-11.9593 & -10.4382 & -24.51922 \\
-72.1254 & 72.0190 & 3.1407 \\
-21.8693 & 1.3566 & -20.5761 \\
-0.0307 & -0.2781 & 0.2933 \\
0.0031 & 0.1908 & -0.6741 \\
-22.0188 & 1.3744 & -21.5185 \\
-30.8701 & 1.9483 & -29.8403 \\
298.2586 & -8.9400 & 289.2668 \\
-43.2982 & 6.5196 & -44.4028 \\
9.7924 & -8.4773 & -3.9596 \\
272.3772 & -8.1442 & 264.4790 \\
1.1323 & -6.3322 & 5.5901 \\
238.9472 & -7.1274 & 232.8433 \\
-6.8095 & 32.9698 & -33.2169
\end{array}\right]
\end{array}
\qquad (5.4)
$$

$$
\begin{array}{cccccccccccccccccc}
W_{01} & W_{02} & W_{03} & W_{04} & W_{05} & W_{06} & W_{07} & W_{08} & W_{09} & W_{10} & W_{11} & W_{12} & W_{13} & W_{14} & W_{15} & W_{16} & W_b \\
[31.18 & -27.47 & -21.30 & 33.05 & -9.35 & 17.506 & 41.35 & 57.78 & -28.53 & -44.28 & 7.15 & -39.85 & 119.93 & -0.15 & -201.18 & 4.31 & 23.22\ ]
\end{array}
\qquad (5.5)
$$

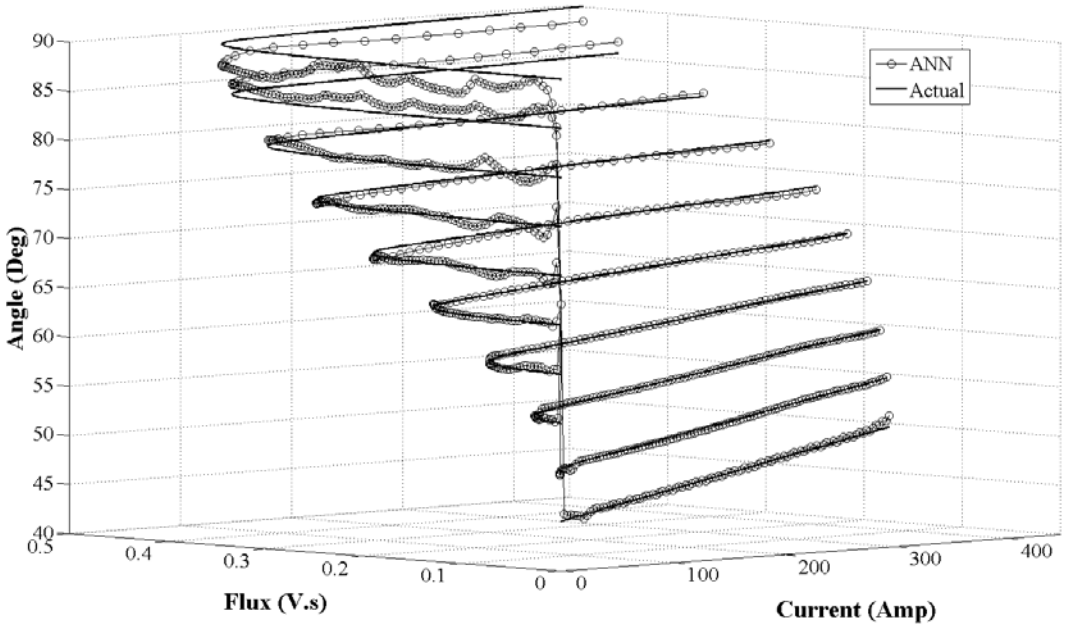

Figure 5.12 Three dimensional view of the actual magnetic characteristics and the characteristic represented by the ANN

Figure 5.13 shows the two dimensional views of the magnetic characteristics represented by the designed neural network. These characteristics are also compared with each ones in the same figure. These characteristics show the high accuracy of the mapping over full range of rotor angle. However, angle-flux and angle-current view of the characteristics show that the accuracy of the mapping is somewhat low at very low value of flux, i.e below 0.02 (V.s), at very low value of current and also close to the aligned rotor position, i.e from 85° to 90°. The effective region is defined as the region of the mapped magnetic characteristic where the accuracy of the estimated rotor angle is of more concern.

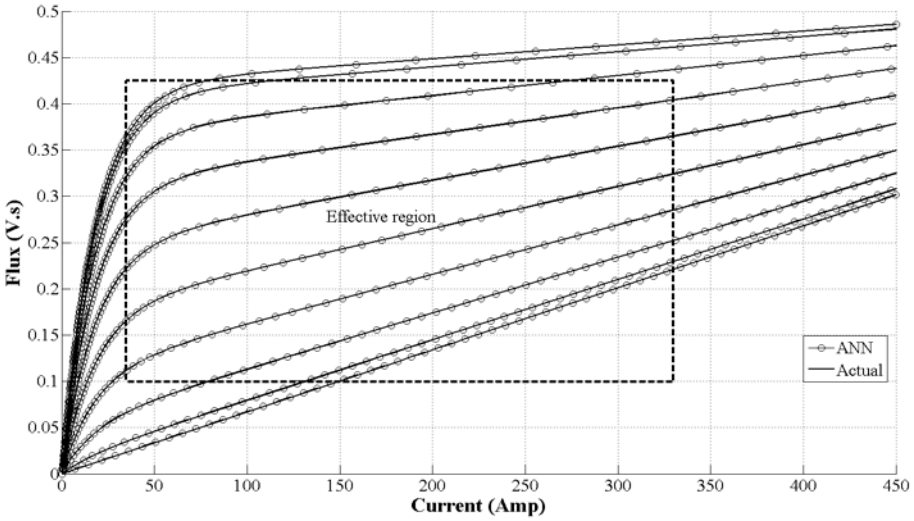

(a) Flux Vs current

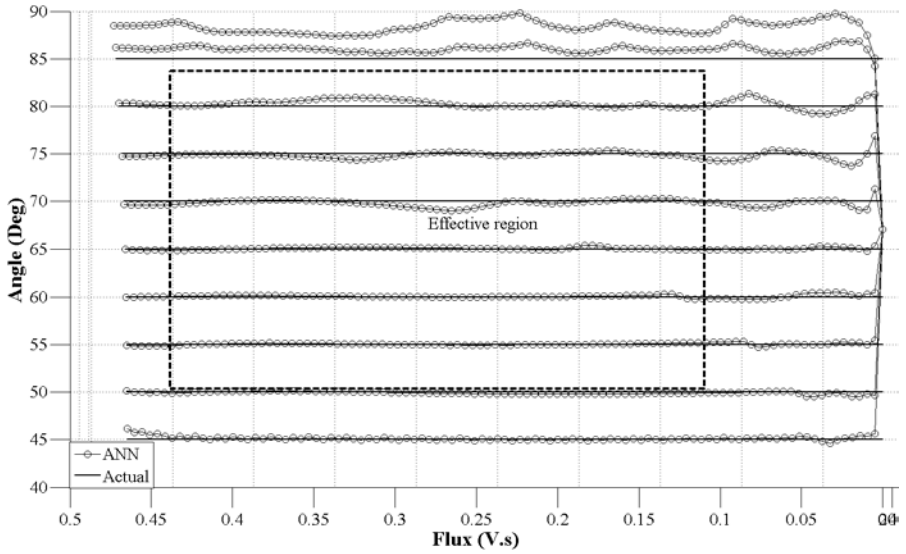

(b) Angle Vs flux

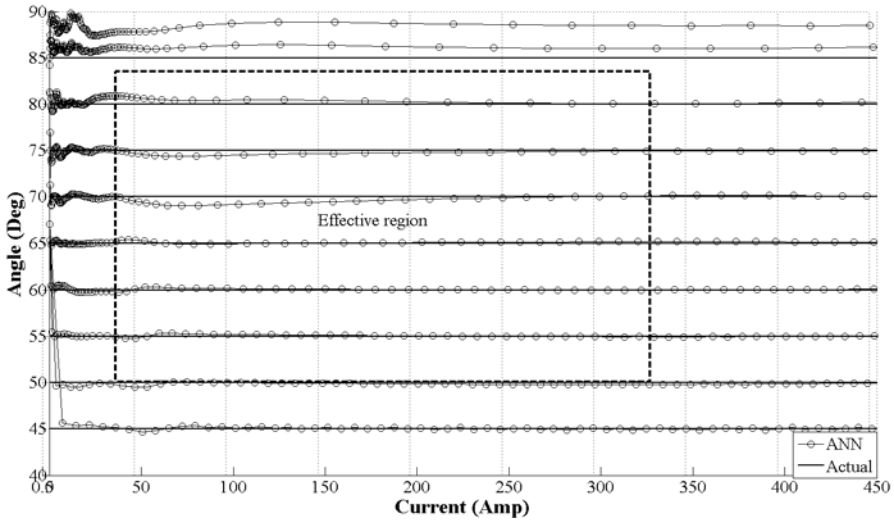

(c) Angle Vs current

Figure 5.13 Two-dimensional view of the magnetic characteristic

The effective region is derived based on general requirement of commutation process. The phase commutation logic is derived from the estimated rotor angle. However, all the estimated rotor positions are not required to generate commutation pulse. The basic requirement of the commutation process can be summarized as follow.

1. The rotor position from the active phase is required to turn ON the next subsequent phase and to commutate the current excited phase.
2. It is required to commutate the excited phase, slightly before the aligned position of the rotor, to prevent the negative torque production during current freewheeling or regeneration mode.
3. The phase commutation needs to be done little bit in advance to ensure the appropriate level of current to produced desire torque.

The first statement is applicable to all the flux-linkage based sensorless techniques. Other two statements are general requirement of the SRM drive. It all dictates that the rotor position at close to the unaligned position and at very close to the aligned position are not used in the commutation process. It also reflects that the rotor position estimated during phase transaction will also not be used for the commutation where magnitude of current and flux are relatively low. Figure 5.13 shows that the accuracy of the estimated rotor angle is good at all range of angle-current for the effective region.

5.2.2.3 *Simulation of ANN based sensorless SRM drive*

The simulation model of the designed ANN is used along with the simulation model of the three phase SRM drive to obtain the performance of the complete sensorless SRM drive. Block diagram of the ANN based sensorless scheme is shown in Figure 5.14, where ANN is

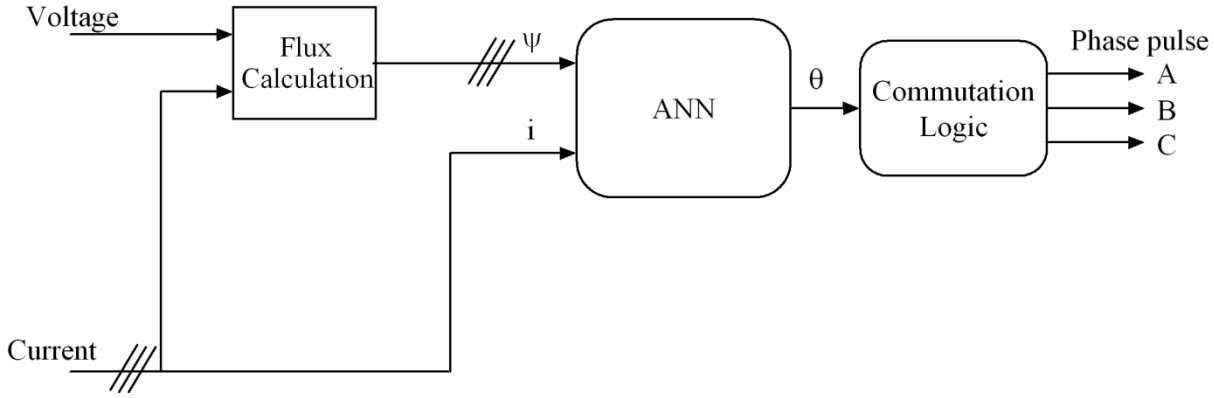

Figure 5.14 Block diagram of ANN based sensorless method

used to estimate a rotor position from the calculated flux and measured current. The estimated rotor angle is compared with actual rotor angle in Figure 5.15. Figure 5.16 shows the waveform of flux, current and torque while motor is running at the speed of 1500 rpm and with the load torque of 15 N-m. The result shows that the ANN based method provides good

accuracy of estimation. Thus, this method can be used to replace the resolver or absolute encoders to provide the rotor position information required for the commutation process.

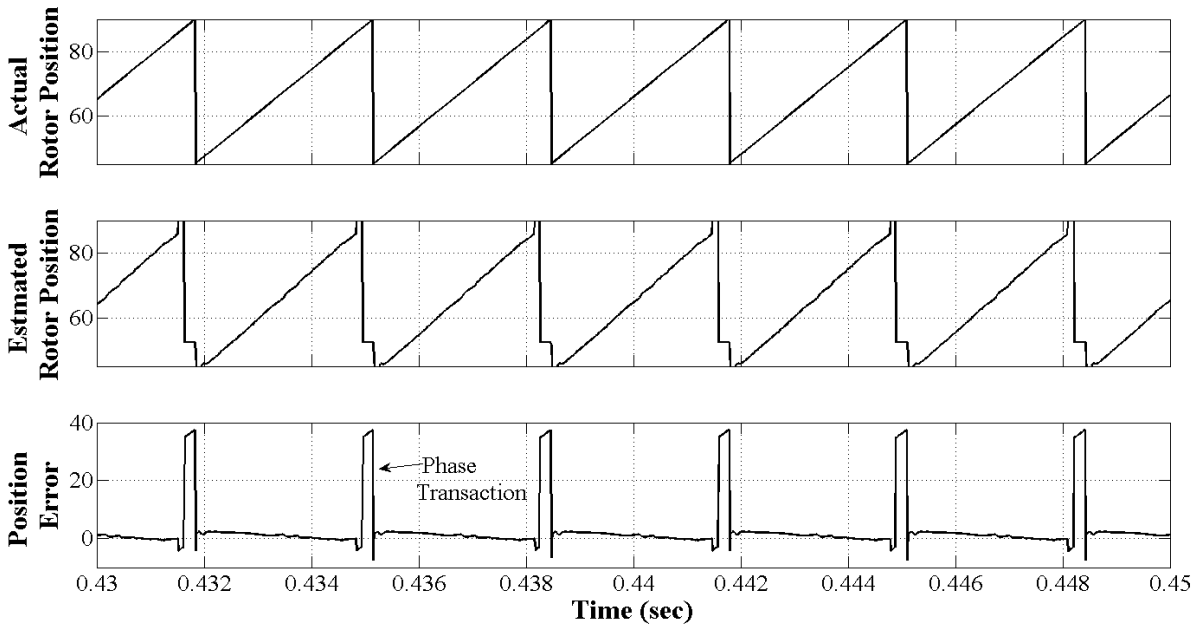

Figure 5.15 Error in rotor position estimation

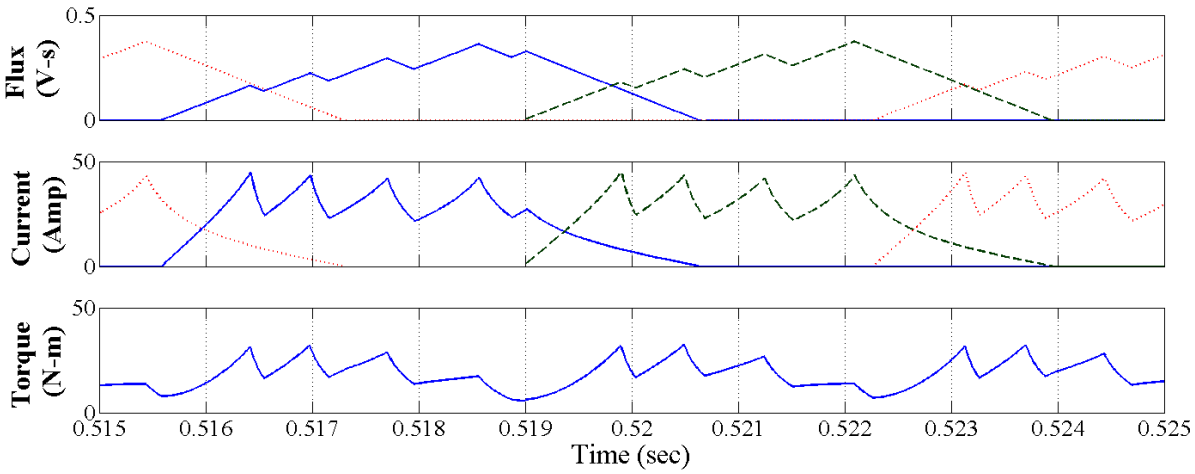

Figure 5.16 Waveform of flux, current and torque at the speed of 1500 rpm and load torque of 15 N-m

The continuous rotor position estimation is possible with the ANN based sensorless method. It offers high accuracy of the rotor position estimation and that of the commutation process. Both the advance angle control and dwell angle control are possible. The method is suitable for the application that requires precise speed control. It is also suitable where the wide range of speed-torque is required, which demands variation of advance angle and dwell angle to adjust a speed-torque characteristics. However, implementation of the torque control or optimum efficiency algorithm does not allow the phase transaction error in rotor position. An additional ANN based flux estimator can be used to eliminate the error, which estimates the flux from the estimated rotor angle and measured phase current [97]. The

difference between estimated flux and calculated flux can be used to compensate for the angle error.

The accuracy of the estimation can be increased with larger amount of training data, however it increases the training time. Also, it requires more time and cost to obtain the magnetic curves at more precise rotor angle. The accuracy of the feed-forward neural network can be increased by selecting the higher number of neurons for hidden layer; however it increases the complexity, and demands higher computational capability. It is to be noted that the relation between accuracy of the mapping and numbers of neuron is not a linear. Thus selection of training data and numbers of neuron are the key feature of the method which should be decided according to hardware capability.

5.2.3 An analytical method of rotor position estimation

A method of continuous rotor position estimation is proposed in the present work to reduce the computation burden and an amount of data to be stored. It connects the magnetic characteristic of the motor to an analytical expression to estimate the rotor position. The block diagram of the sensorless method is same as an ANN based sensorless method, except that an analytical expression is used to derive the rotor angle from the input flux and current, instead of neural network.

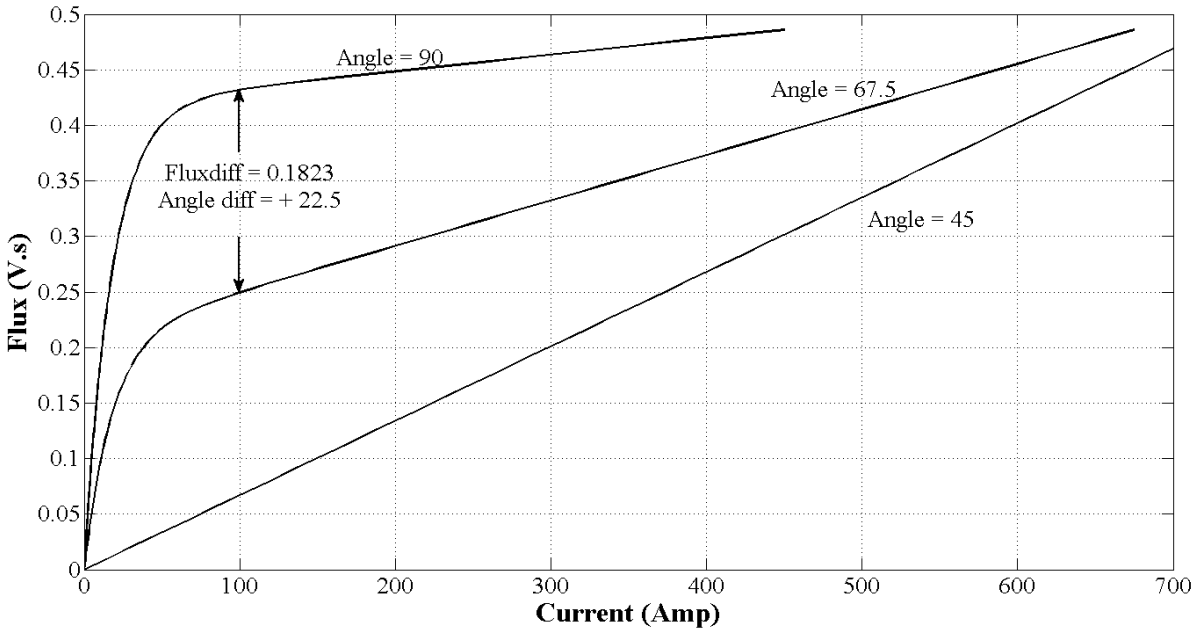

Figure 5.17 Magnetic curves at an aligned, unaligned and mid rotor position

The method requires only two magnetic curves to store, one at mid rotor position (67.5°) and other at aligned rotor position (90°). Expression for the rotor position estimation is derived from the physical reasoning about distribution of flux-angle over current range. Figure 5.17 shows the required magnetic curves of the motor. At low current level (below saturation), small flux difference represents a large angle difference, while at the higher

current level, (after saturation) the flux difference is comparatively large to represent the same angle difference. The aim is to map a distribution of flux difference over entire current range, using a simple mathematical algorithm.

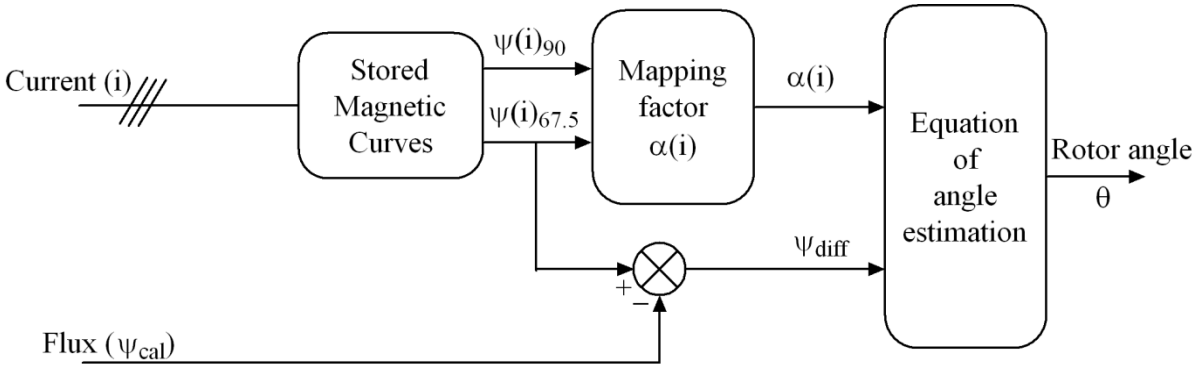

Figure 5.18 Block diagram of rotor position estimation using analytical method

Figure 5.18 shows the block diagram of analytical method of rotor position estimation. Similar to previous method, all phase currents and voltages are measured continuously, and flux is calculated online. The current is used as an index to find the flux $\psi(i)_{90}$ and $\psi(i)_{67.5}$ from the stored magnetic curves. Mapping factor $\alpha(i)$ represents the ratio of angle difference and flux difference as a function of current, and is expressed as-

$$\alpha(i) = \frac{90 - 67.5}{\psi(i)_{90} - \psi(i)_{67.5}} \tag{5.6}$$

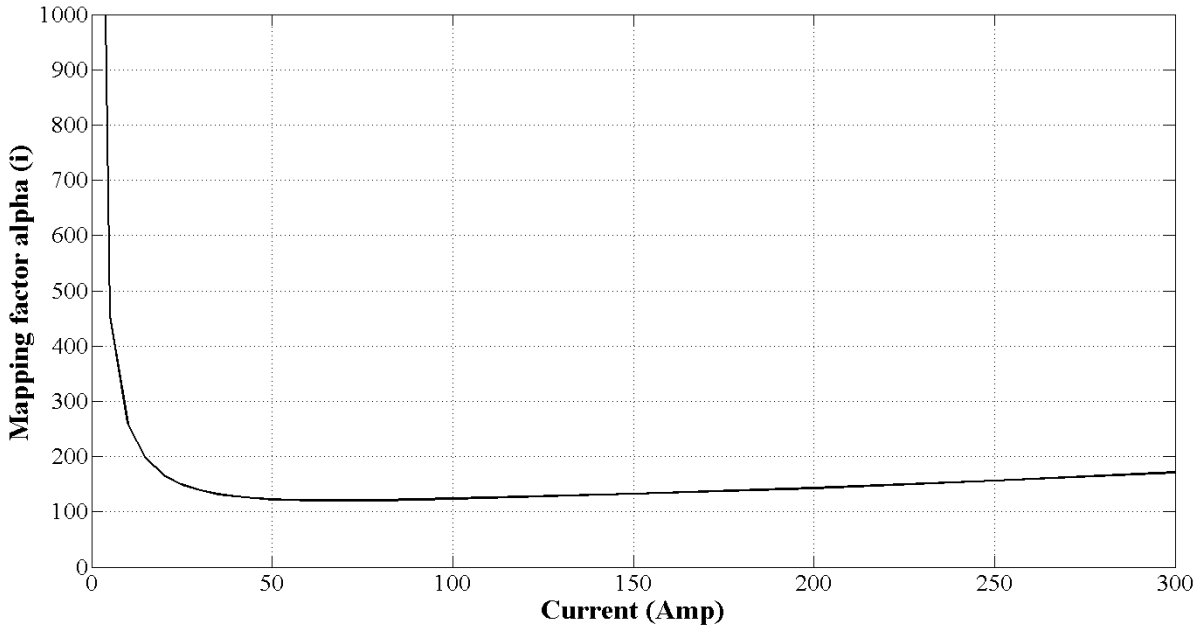

Figure 5.19 Variation of mapping factor α(i) over current

Mapping factor $\alpha(i)$ maps the nonlinearity in the relation of flux difference versus angle difference as function of current. The plot of mapping factor versus current is shown in Figure 5.19. The Flux $\psi(i)_{67.5}$ is taken as reference which is compared with calculated flux to

generate flux difference ψ_{diff}. The rotor angle is estimated form the mapping factor α(i) and flux difference ψ_{diff} as-

$$\theta = 67.5 + \psi_{diff} \cdot \alpha(i) \tag{5.7}$$

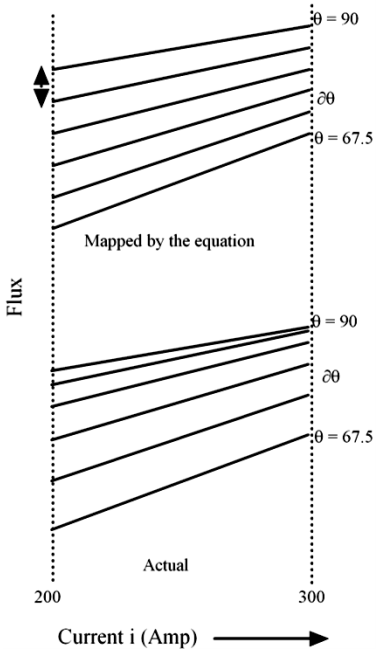

Figure 5.20 Magnetic characteristic mapped by an analytical equation

The equation (5.7) revels that the magnetic curves for the rotor angle 45° to 90° are distributed in equal segments. Figure 5.20 shows the difference between actual magnetic characteristics and that mapped by an analytical equation. Further, an analytical equation produces a zero error in estimation at an angle θ = 67.5° as ψ_{diff} is zero, and at θ = 90° as ψ_{diff} is maximum. The respective positive and negative errors are present at the rotor positions below and above to the reference position.

Simulation results of an analytical sensorless method are shown in Figure 5.21 where motor is running with minimum dwell angle of 30°. It shows the difference between actual rotor position and position estimated by an analytical method at a current of 50 A. The error is zero at an angle of 67.5° while it is progressive in nature with increment/decrement of the rotor angle.

The rotor angle error is good enough to provide the continuous rotor position which can be used for the adjustment of advance angle and dwell angle. The method offers low cost and easy to implement solution for the rotor position estimation. It is suitable for the applications which require flexibility in torque speed characteristic. The method is not suitable to incorporate efficiency optimize algorithm and torque control scheme as they require precise position information throughout the electric cycle and for the entire range of

speed. However, the error in estimated position is almost linear in nature, which can be easily compensated over linearized current.

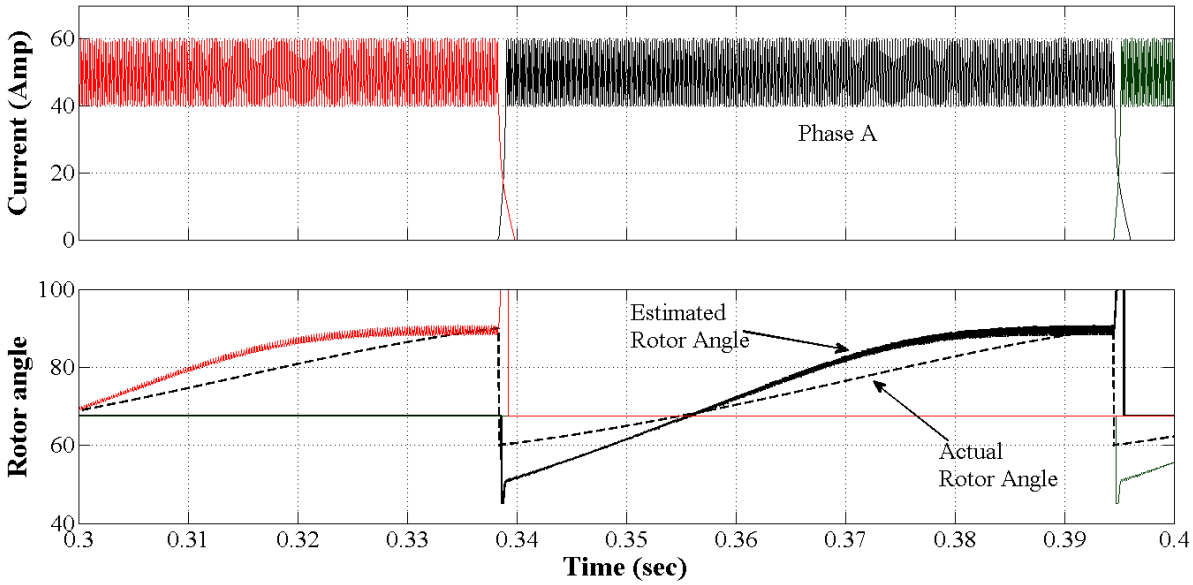

Figure 5.21 Comparison of estimated rotor angle and actual rotor angle

The error in estimated rotor angle can be compensated as-

$$\theta_{new} = \theta_{est} + \Delta\theta \tag{5.8}$$

where 'θ_{est}' is the estimated rotor angle, '$\Delta\theta$' is required correction in angle and 'θ_{new}' is the corrected rotor angle. The required correction $\Delta\theta$ is a function of estimated rotor angle θ_{est} and phase current, however the effect of current is negligible compared to the rotor angle. Even, assuming constant current (i=50 A), the dependency of $\Delta\theta$ on estimated rotor position is not linear. One possible solution is to store the relation between $\Delta\theta$ and θ in a look-up table. Instead of storing relation in a look-up table, higher order polynomial method can be used for the curve fitting. The non-linear relation is linearized over four segments of rotor angle, as shown in Figure 5.22(a). The first section represents a small linear region where negative error increases with increase in rotor angle, thus it requires positive correction as rotor angle increase. After that error reduces linearly increases up to the mid rotor position, thus required correction is added as shown in section-2. Likewise the linear correction is added in section-4. The correction $\Delta\theta$ is added as a function of square of the current in section-3. Consequently, the corrected rotor angle is shown in Figure 5.22(b) which is a function of estimated rotor angle.

Figure 5.23 shows the simulation result of the analytical sensorless method with the compensation in estimated rotor angle. It shows that the accuracy of the angle estimation is reasonably good to incorporate with the efficiency optimization technique and torque control algorithms. The Figure 5.24 shows the error in estimation of rotor angle at the higher current (speed) than the compensator is designed for.

Overall the analytical method offers a simple and effective solution to the rotor position estimation which also considers a magnetic non-linearity of the motor.

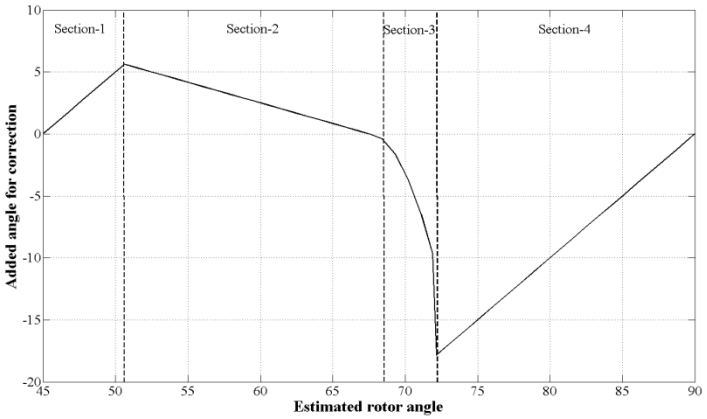

(a)

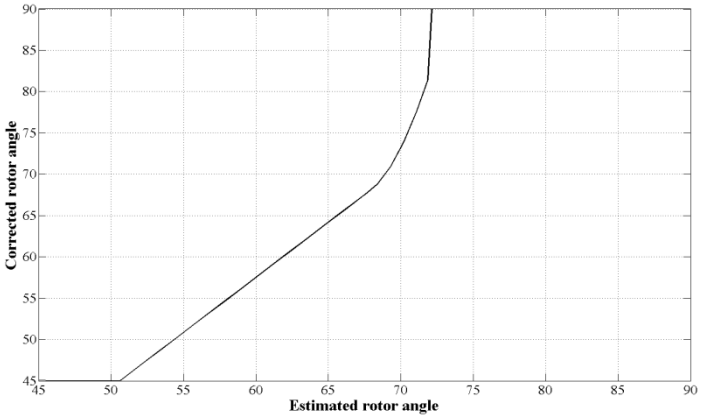

(b)

Figure 5.22 (a) Correction added $\Delta\theta$ and (b) Corrected rotor angle θ_{new} versus estimated rotor angle

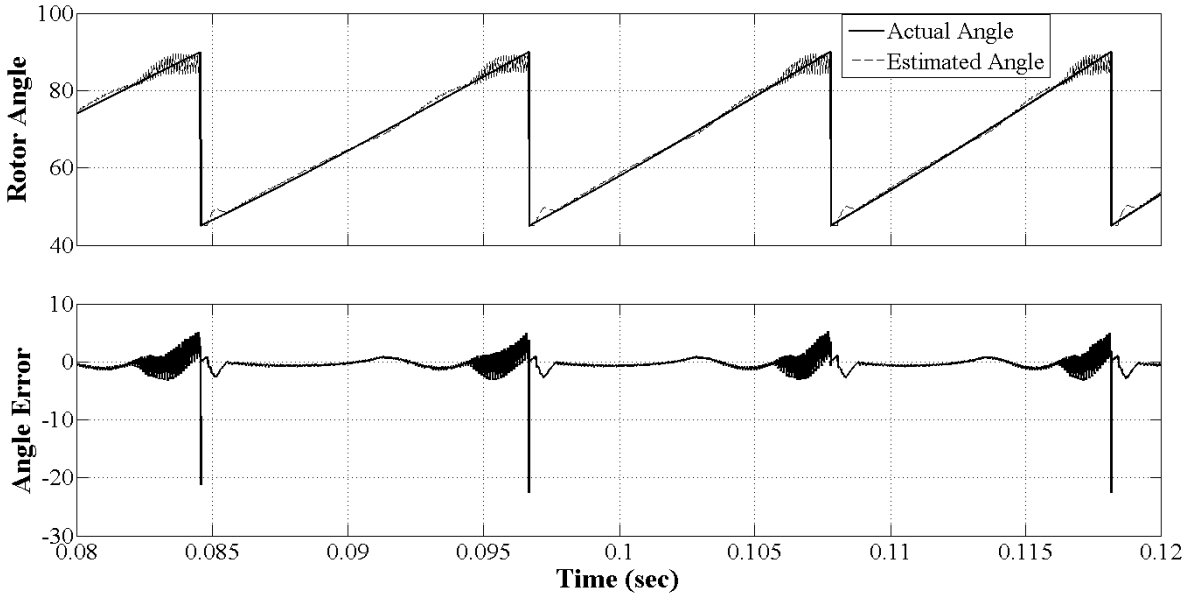

Figure 5.23 Estimated rotor angle after correction at the speed of 1500 rpm

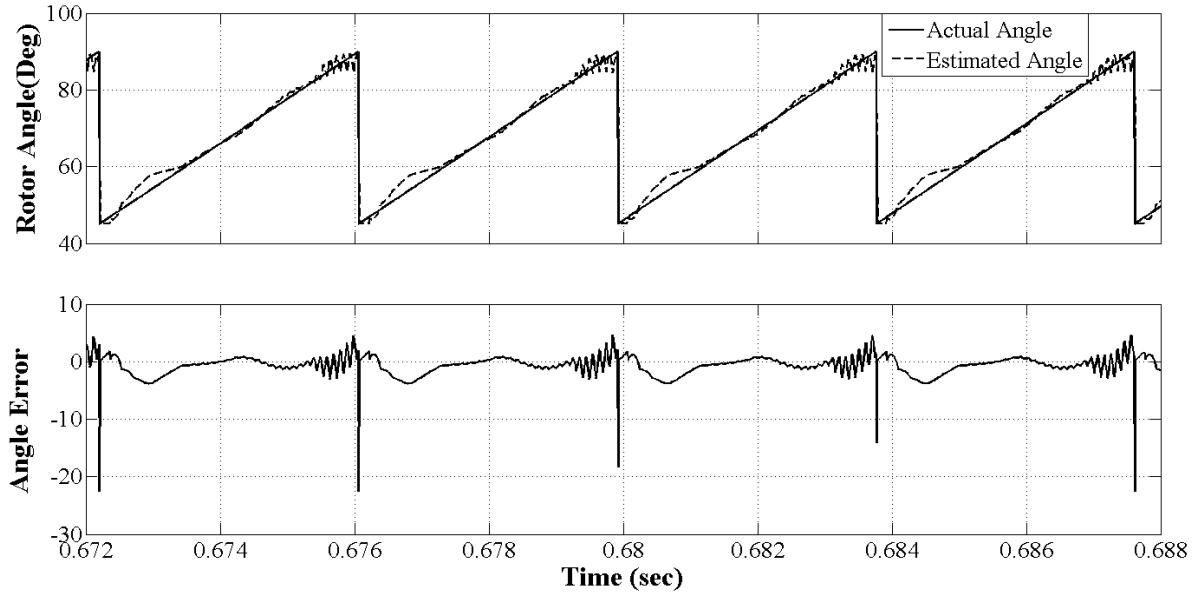

Figure 5.24 Estimated rotor angle with compensation at the speed of 3000 rpm

The method reduces computation burden as well as it requires less stored data to estimate continuous rotor position. The accuracy of the method is good and comparable to the ANN based technique. Advance angle control and dwell angle control is possible however compensation in angle estimation is required to implement the torque control and/or torque ripple minimization technique.

5.3 CONCLUSION

The major advantages of the flux-linkage based sensorless technique are good accuracy, wide speed operation and immunity to the saturation effect. Load torque, inertia and viscous damping do not have any impact on the operation of estimating methods unlike observer based method. An initialization routine is always required because the method is not applicable at standstill. One phase excitation or two phase excitation at a time are the general methods adopted for the initial startup. It sets the initial rotor position aligned to the excited phase or at the known intermediate position. Active probing method or modulated signal injection method can also be incorporated to get the initial position. The problem of ageing effect on the magnetic characteristics is always associated with the flux linkage based method. The method also suffers from the error in calculation of flux-linkage at very low speed and that is due to temperature effect on resistance value. However, the on-line resistance estimation scheme can be incorporated to eliminate this effect.

More or less all the methods required prior information about magnetic characteristics of the motor. Special care has to be taken in the measurement of magnetic characteristics of the motor because the accuracy of the method is highly depended upon it. The flux-linkage based methods are applicable to the specific motor only for which it is designed. Even

motors with the same specification could also have a bit variation in magnetic characteristics during the bulk production.

The sensorless methods based on the current waveform do not require any prior knowledge of the magnetic characteristics and also do not suffer from the problem of applicability to the specific motor unlike flux-linkage based method.

Chapter 6: CURRENT GRADIENT SENSORLESS METHOD

Various sensorless control techniques are explored in this chapter. These techniques are independent of the motor magnetic characteristics. Performance of the current gradient sensorless method (CGSM) is investigated experimentally. Design and implementation of the standard CGSM with the low-frequency PWM controlled SRM drive was found difficult and unreliable. To overcome the problem of standard CGSM modified CGSM is proposed and investigated.

6.1 INTRODUCTION

Most of the sensorless methods require the prior information about the motor magnetic characteristics to incorporate sensorless algorithm with the motor. The magnetic characteristic of the motor can be obtained experimentally. Accuracy of the magnetic characteristic is quite important because performance of the sensorless methods depend upon it. However, measurement technique and accuracy of instruments used affect the determinant magnetic characteristics and in turns the performance of the sensorless method. Besides, these methods also require intensive computation and bearing burden of lots of storage space on processors. Cost of implementation of sensorless scheme, for the medium size EMDS, becomes higher than twice of cost of the motor plus converter, which is not feasible. This has motivated search of a sensorless method which is economical and easy to implement.

Some interesting sensorless methods have been proposed in the late 90's which do not require any prior knowledge of motor magnetic characteristics except the rotor and stator pole configuration [32, 35, 81, 82, 107, 123, 155]. These methods basically monitor the phase current and detect the instant for one rotor position per stroke. Sensorless methods of this category include chopping current waveform [123], regenerative current [155] and current gradient sensorless method (CGSM) [82, 107]. All these methods can be easily implemented on any motor having same stator-rotor pole topology without prior knowledge of magnetic characteristics or electrical parameters.

Sensorless method based on chopping of current waveform is applicable only when current is regulated through hysteresis current control loop. In this method rotor position is detected by calculating rise time and fall time of chopping waveform which is a function of incremental inductance. However, due to uncertainty of the phase resistance and back EMF, which depends on speed and rotor position, the calculation of rise time and fall time becomes difficult. Furthermore, as the incremental inductance is current dependent it contributes extra complexity in the rotor position estimation. It is applicable to only low speed

operation, where current regulation is possible thus single pulse operation is not possible. As the resolution of rotor position is inversely proportional to the speed, the high speed control is quite difficult.

In regenerative current method, the current is monitored continuously and a phase is de-energized in response to reversal of current. To control the drive, phase current is turned off for constant period when it exceeds the reference value. The current control is performed in soft chopping mode by observing the slope of the current through the freewheeling diode. When rotor passes the aligned position, slope of the current changes from negative to positive because inductance starts falling. Efficiency of this method is poor because of considerable negative torque produced during de-energized mode. Other drawback is that turn-off angle cannot be advanced so speed is limited below base speed.

6.2 CURRENT GRADIENT SENSORLESS METHOD

CGSM (Current Gradient Sensorless Method) is applicable where current is controlled through voltage PWM techniques. First sensorless method with PWM control is applied in [155], which monitors the rate of change of phase current (di/dt) in each PWM period. Thus, rotor position can be estimated, since di/dt is a function of incremental inductance. However, it is clear that this method also suffers from uncertainty of the incremental inductance at higher current level and error introduced by the back EMF. Also single pulse operation is not possible.

6.2.1 Principle of CGSM

The CGSM, as proposed by [107] and then implemented and analyzed [82], provides low cost solution for the rotor position estimation of the SRM. It detects position θ_{pdp} where rotor and stator pole begin to overlap by observing change in *di/dt*. A typical current waveform for fixed frequency PWM controlled three phase SRM drive is shown in Figure 6.1. It shows the current and ideal inductance of phase-A, while other phase currents are not shown for simplicity. PWM duty cycle is constant throughout the phase commutation period. Rotor positions at different angular positions are shown in Figure 6.2. Angular positions of stator/rotor and phase excitation condition at different angular position are tabulated in Table 6.1.

Sequence of phase excitation is taken as A-B-C with phase overlap which results rotor rotation in anti-clockwise direction. Phase-A is energized at an instant θ_u where the inductance value is at minimum L_u and ideally remains constant till θ_{pdp}. The phase equation can be expressed as;

$$V_{ph} = R_s i_{ph} + \omega_m L_{ph} \frac{di_{ph}}{dt} + \omega_m i_{ph} \frac{dL_{ph}}{d\theta} \quad (6.1)$$

Where, 'L_{ph}' is phase inductance, 'R_s' is phase resistance, 'i_{ph}' is phase current, 'ω_m' is speed, and 'θ' is rotor position.

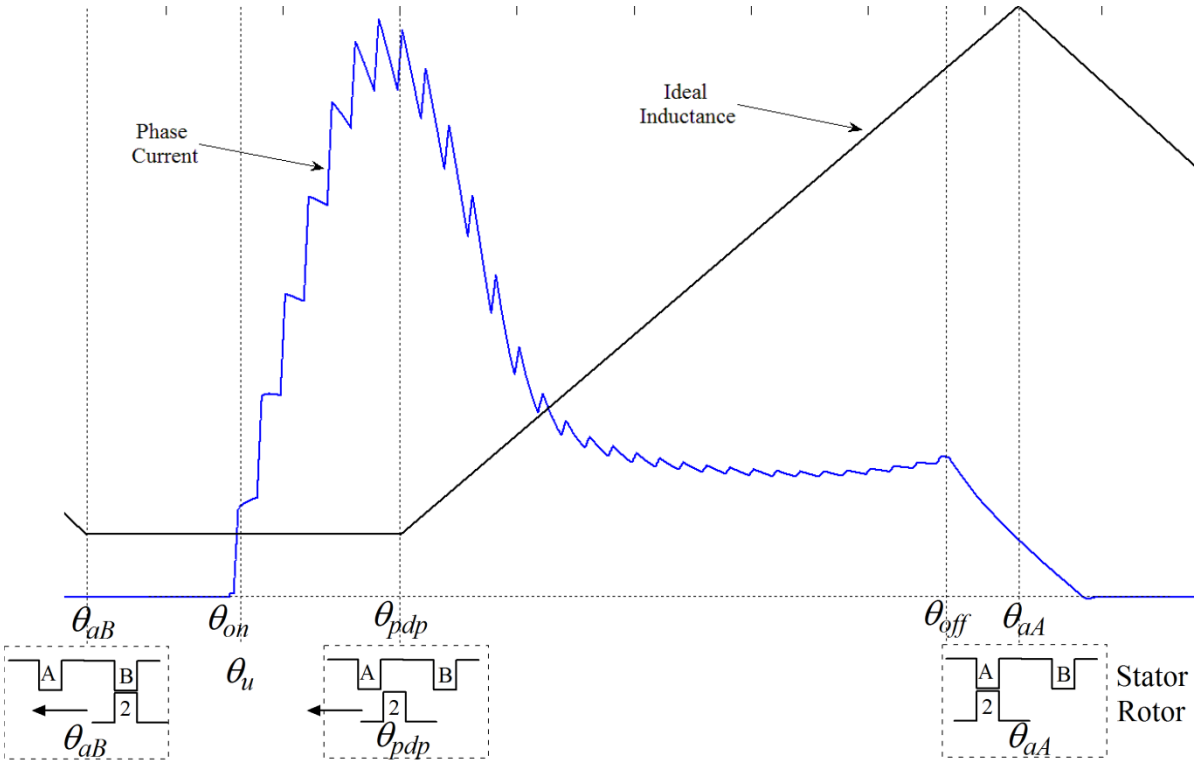

Figure 6.1 Phase current and phase inductance for voltage PWM controlled drive

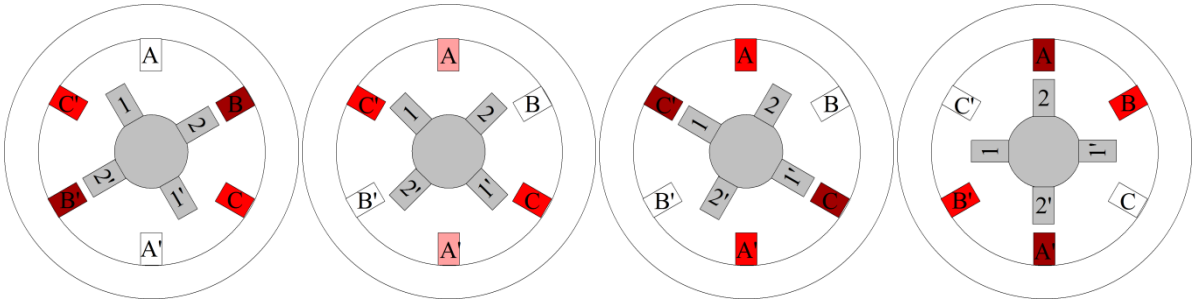

Figure 6.2 Rotor position at (a) θ_{aB} (b) θ_u (c) θ_{pdp} (d) θ_{aA}

Two situations are considered for the analysis, one just before reaching θ_{pdp} referred to as 'pdp-' and other just after passing θ_{pdp} referred to as 'pdp+'. Phase equation for these two situations, neglecting voltage drop across resistance, become -

$$v_{pdp-} = \omega_m L_u \frac{di_{pdp-}}{dt} + \omega_m i_{pdp-} \frac{dL_u}{d\theta} \quad (6.2)$$

$$v_{pdp+} = \omega_m L_u \frac{di_{pdp+}}{dt} + \omega_m i_{pdp+} \frac{dL_u}{d\theta} \quad (6.3)$$

When 'pdp-' inductance is constant, $dL_u/d\theta = 0$. Equation **(6.2)** can be rewriten as -

$$v_{pdp-} = \omega_m L_u \frac{di_{pdp-}}{dt} \quad (6.4)$$

Since, voltage is maintained constant throughout the commutation period -

$$v_{pdp-} = v_{pdp+} \quad (6.5)$$

Combining equation **(6.3)**, **(6.4)** and **(6.5)** results in,

$$\left(\frac{di_{pdp-}}{dt} - \frac{di_{pdp+}}{dt} \right) = \frac{i_{pdp+} \left(\frac{dL_u}{d\theta} \right)}{L_u} \quad (6.6)$$

Table 6.1 Mechanical position of stator/rotor and phase excitation at the different instant of angular position

Angle	Mechanical Position	Phase A	Phase B	Phase C
θ_{aB}	Rotor pole pair 2-2' is fully aligned with stator pole pair B-B'	Not energized	Ending of commutation period	Fully energize
θ_u	Stator pole pair A-A' (phase-A) is in fully unaligned position.	Starting of phase conduction	Not energized	Fully energized
θ_{pdp}	Stator pole pair A-A' and rotor pole pair 2-2' is just begin to overlap.	Fully energized	Not energized	Ending of commutation period
θ_{aA}	Stator pole pair A-A' is fully aligned with rotor pole pair 2-2'.	Ending of commutation period	Fully energized	Not energized

Since, all the variables on the right-hand-side in (6.6) are positive, condition (6.7) is always true.

$$\left(\frac{di_{pdp-}}{dt} - \frac{di_{pdp+}}{dt} \right) > 0 \quad (6.7)$$

and thus,

$$\frac{di_{pdp-}}{dt} > \frac{di_{pdp+}}{dt} \tag{6.8}$$

It states that the slope of phase current is always greater for $\theta < \theta_{pdp}$. This is the principle of CGSM that detects the instant when rate of change of current (*di/dt*) changes from positive to negative value, that means at the instant θ_{pdp} rate of change of current becomes zero (*di/dt = 0*) and value of phase current i_{ph} is reached to its peak.

It is clear that the pulse per stroke can be produced by monitoring *di/dt* and by checking condition (di/dt=0). These pulses are called "peak detection pulse (*pdp)*" because it imitates an instant of current peak.

6.2.2 Rotor position estimation & phase commutation

Implementation of the sensorless SRM drive based on theory of CGSM requires continuous estimation of rotor position from the peak detection pulse. Figure 6.3 shows the basic block diagram of PWM controlled sensorless SRM drive based on CGSM. Main role of the sensorless scheme is to produce a phase commutation pulse by monitoring and processing the phase current. Sensorless scheme of CGSM is divided into two major blocks named 'Current Peak Detection' and 'Commutation Logic'. The first block output is current peak detection pulse (*pdp*) as explained earlier. The continuous rotor position is obtained from the peak detection pulse, and accordingly phase commutation pulses are produced from it. Detailed block diagram of sensorless scheme is shown in Figure 6.4.

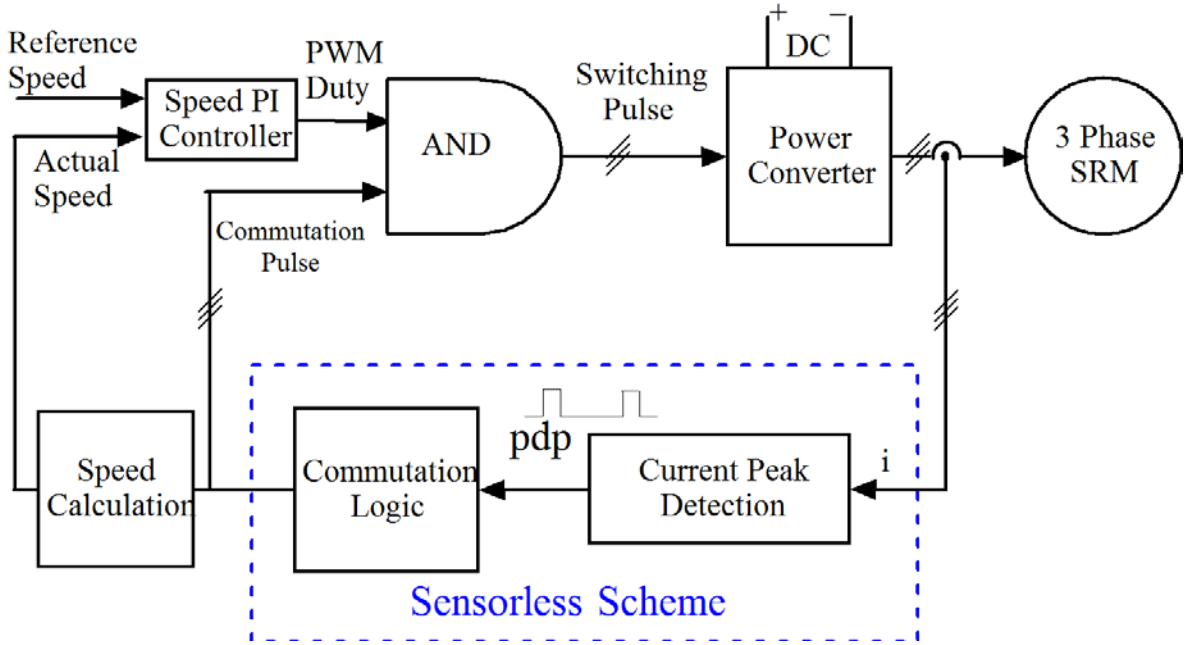

Figure 6.3 Block diagram of Voltage PWM controlled sensorless drive based on CGSM

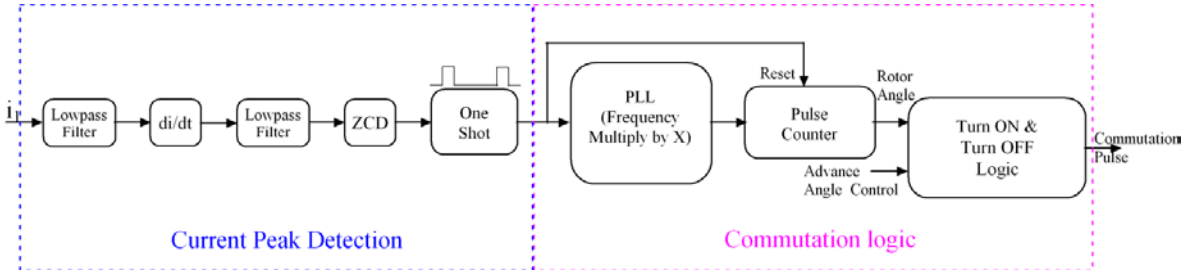

Figure 6.4 Block diagram of sensorless scheme

6.2.2.1 *Current peak detection*

Current peak detection stage is comprised of low-pass filters, differentiator, zero-crossing detector and one-shot. Process starts with sensing phase current with the help of current sensors. Low pass filters are added to filter out the switching frequency and noise. Cutoff frequency of the filter is decided by frequency of the PWM. Differentiator is used to monitor the rate of change of current (*di/dt*) and zero-crossing-detector (ZCD) followed by the one shot that produces a pulse at the instant when *di/dt = 0*. Here, it is apparent that fully analog implementation of the current peak detection stage is a simple, reliable and cost effective solution.

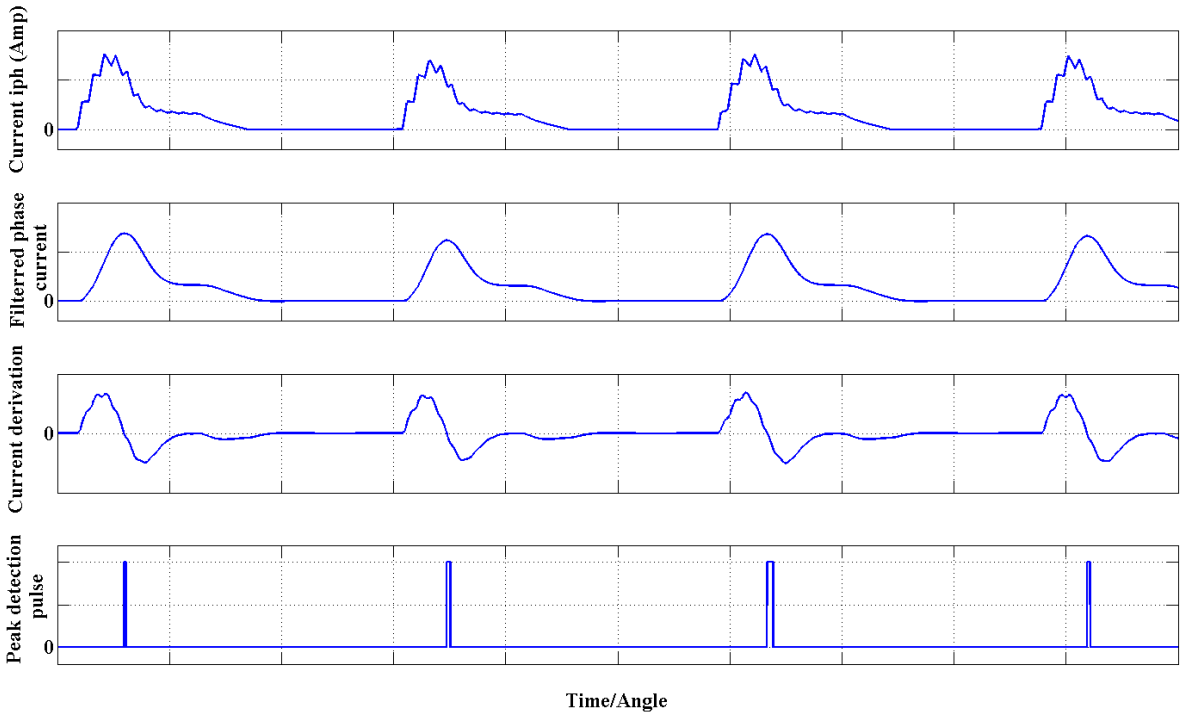

Figure 6.5 Waveform of current peak detection stage

Waveforms for current peak detection at different stages are shown in Figure 6.5. It consist of phase current sensed by the current sensor, current filtered by filter, current derivative and peak detection pulse by the ZCD, with one-shot. Only a single phase waveforms are shown here since, each phase produces a pulse at regular interval, that is 90° (mechanical) for the three phase 6/4 SRM. However, for all phases, peak detection

pulses are produced at each stroke that is 30° (mechanical) for the same case. Peak detection pulses produced from each phase should be processed further to obtain continuous rotor position. Final commutation pulse for each phase can be generated from the rotor position so obtained for the desired direction of the torque.

6.2.2.2 *Commutation logic*

Commutation logic decides the turn-ON and turn-OFF instant for each phase by producing the commutation pulse. In most of the sensorless methods commutation logic is obtained from the continuous rotor position estimation. The continuous rotor position is estimated from the peak detection pulse and then commutation logic is derived from that in the conventional way.

Commutation logic starts with PLL (phase-lock-loop) which multiplies the frequency of peak detection pulse with the condition that phase and frequency are locked to input. Block diagram of PLL is shown in Figure 6.6. PLL detects a difference in phase and frequency of input and output. Error in phase and frequency adjusts the input voltage of VCO to control the output frequency. Frequency of output is divided by M_f times in the feedback loop and compared with input (peak detection pulse) to achieve the frequency multiplication. PLL matches the frequency of compared signal with the peak detection pulse with zero phase difference. As a result, frequency of output signal becomes M_f times multiple of input signal's frequency. Mathematically it can be explained as;

If $f_{compare} = \frac{f_{out}}{M_f}$ (6.9)

then $f_{out} = M_f \times f_{in}$ (6.10)

because $f_{in} = f_{compare}$ when phases are locked, where $f_{compare}$ = frequency of compared signal, f_{out} = frequency of output and f_{in} = frequency of input signal. The output of the PLL is shown in Figure 6.7 which indicates M_f pulses in the time interval of $1/f_{in}$ second.

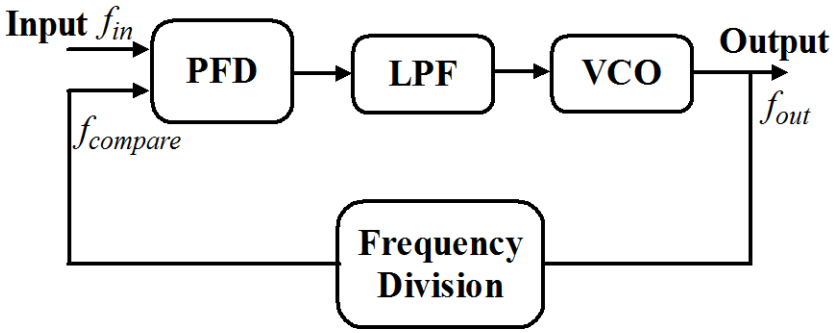

Figure 6.6 Phase lock loop

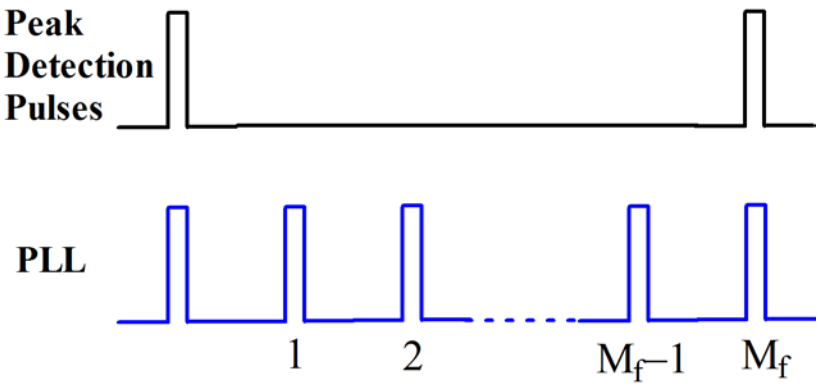

Figure 6.7 Frequency multiplication using PLL

The main purpose to multiply the frequency of peak detection pulse is to estimate the rotor angle in between the two peak detection pulses by interpolation. Figure 6.8 shows the current peak detection pulse for all three phases with respect to conduction period of each phase. Peak detection pulses from each phase represents an angle of 90° (mechanical) (i.e stroke angle*Number of phases) while considering combine peak detection pulses for all phases, each next pulse is separated by an angle of 30° (mechanical) (i.e stroke angle). If the frequency of peak detection pulses of each phase is multiplied by an integer M_f using PLL, then minimum rotor angle that can be discriminated by the PLL's output pulse will be (stroke angle*Number of phase /M_f)° or say (90/M_f)° for the case. As shown in Figure 6.4, pulse counter is used to estimate a rotor position from the high frequency pulse which results from the PLL output stage. Count value is incremented by one at each low-to-high transaction and counter will reset to zero on low-to-high transaction of the peak detection pulse. Accordingly, resolution ($\theta_{\min}$) of rotor angle estimation can be calculated as,

$$\theta_{\min} = \frac{\varepsilon * m}{M_f} \tag{6.11}$$

Where, 'ε' is stroke angle, and 'm' is number of phase and 'M_f' is frequency multiplier. Figure 6.9 shows the waveform for the rotor position estimation using PLL and counter for M_f = 90. The 6/4 pole three phase SRM will give resolution of 1°(mechanical)., It is apparent from the Figure 6.8 that zero count value represents a rotor angle of 60°(mechanical) or say θ_{pdp} thus estimated rotor angle is -

$$\theta_{estd} = CV \bullet \theta_{\min} + \theta_{pdp} \tag{6.12}$$

Where, 'θ_{estd}' is estimated rotor angle in mechanical degree, 'CV' is count value and '$\theta_{\min}$' is the minimum rotor angle that can be estimated by the scheme.

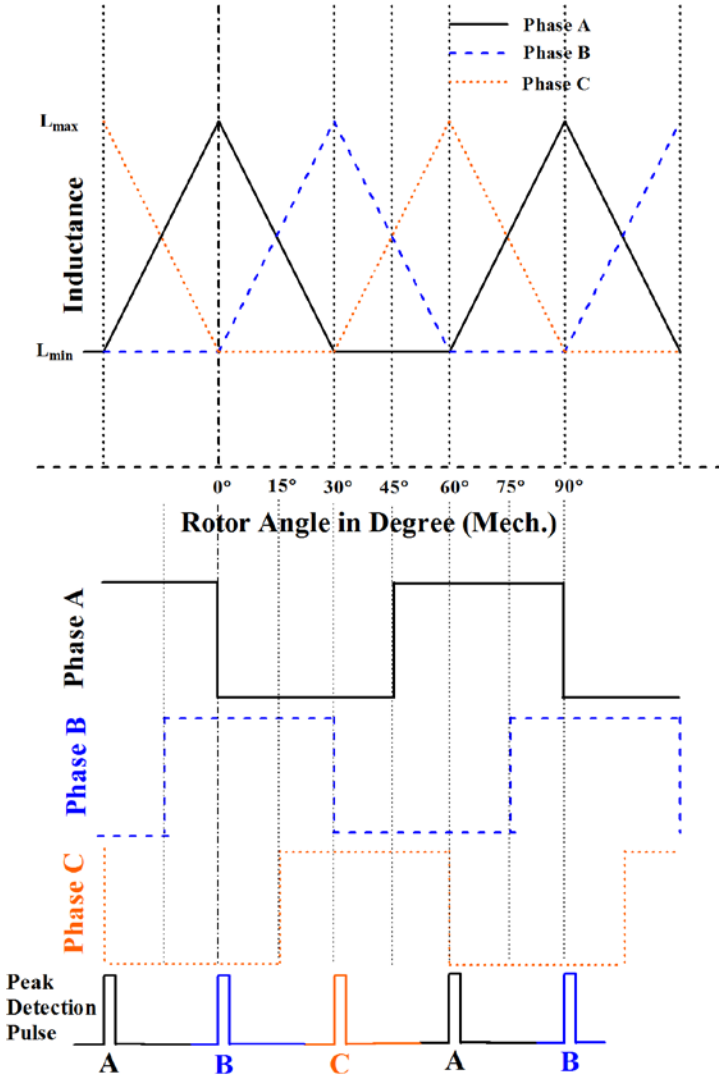

Figure 6.8 Current peak detection pulses

It is apparent from the above that any single phase detection is enough for rotor position estimation and commutation pulse can also be derived from it. However, it is true only when motor is running with mechanical position sensor or by some other position sensing arrangement. Furthermore, if combined peak detection pulses are used to estimate a rotor position using PLL and counter stage then resolution increases by 1/m times, and equation (6.11) becomes:

$$\theta_{\min} = \frac{\varepsilon}{M_f} \tag{6.13}$$

It gives a resolution of 0.333°. Even though it gives accurate rotor position estimation, it is quite difficult to implement the sensorless SRM drive using commutation pulses obtained from it. This is due to the fact that during transaction from initial start-up to the sensorless control, operating parameters like speed, commutation angle and torque vary which may cause the instability and loss of synchronization. However, sensorless control is possible only if these parameters remain constant during changeover, but practically it is not possible.

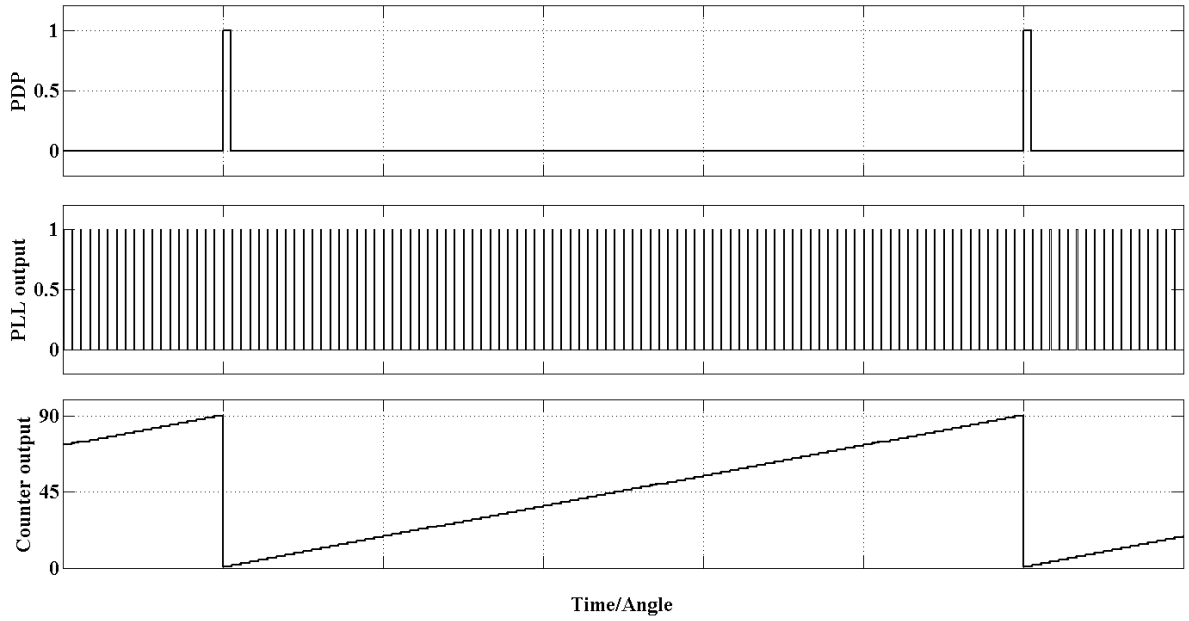

Figure 6.9 Output of pulse counter

Keeping in view the above analysis, following rules are made to decide commutation logic of any sensorless method which is based on principle of active phase monitoring. These rules are formed to avoid any misinterpretation and misleading appreciation regarding the sensorless operation of SRM.

Rule1. *Rotor angle information derived from active phase must be used to energized (turn ON) the next subsequent phase and it is applicable even for continuous rotor position estimation scheme.*

Rule2. *To de-energized (turn OFF) the excited phase rotor angle information derived from the same phase or from the next subsequent phase can be used depends upon whether the commutation overlap is required or not.*

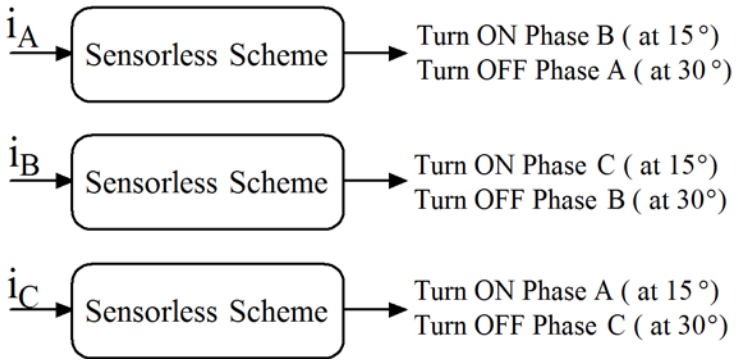

Figure 6.10 Phase commutation logic

The above rules are applicable in all sensorless methods where rotor position is derived from the energized phase.

Peak detection pulses are derived for each phase to follow the compliance of the above rules, as shown in Figure 6.10. In this scheme estimated rotor angle from each phase will decide self turn OFF instant and turn ON instant of next successive phase. Thus, each phase will turn ON the next phase after 15° and itself turn OFF after 30°.

6.2.2.3 *Speed estimation*

Speed can be calculated from the frequency of peak detection pulse or phase commutation pulse. But, peak detection pulses are used in practice to derive the speed of the motor because the phase commutation pulses are the outcome of the peak detection pulse in sensorless method. In the case of 6/4 pole three phase SRM, frequency of peak detection pulse is 4 cycle per revolution. If one revolution per second is the speed, then 4 cycle will appear in one second. Thus speed of the motor can be represented as -

$$N_s = \frac{f_{pdp} * 60}{4} \tag{6.14}$$

Where, ' f_{pdp} ' is frequency of peak detection pulse and ' N_s ' is motor speed in rpm.

In general speed can be defined as-

$$N_s = \frac{f_{pdp} * 60}{n_{cr}} \tag{6.15}$$

where ' n_{cr} ' is number of cycle of peak detection pulse per revolution, which can be calculated as -

$$n_{cr} = \frac{360}{\varepsilon * m} \tag{6.16}$$

Speed can be obtained from the peak detection pulse of any phase using equation (6.15) and (6.16).

6.3 DESIGN AND PERFORMANCE INVESTIGATION OF CGSM

Implementation of current gradient sensorless method can be accomplished with only analog electronic circuits as the algorithm is simple. Nevertheless, major issues of CGSM, associated with design, implementation and performance are investigated for indepth analysis. These include current peak detection, rotor position estimation and commutation logic. Non linear inductance characteristics, effect of low PWM frequency, use of low pass filter and PLL are the main concern. Each of the problem and cause is described in detail with the possible solution.

6.3.1 Effect of rotor/stator pole arc

Three phase SRM having six stator pole and four rotor pole is being considered in all previous discussion related to CGSM. It can also be observed from Figure 6.1 and Figure 6.8 that both rotor and stator pole arcs are 30° for the three phase SRM. However, any difference in pole arcs affects inductance profile as well as angular position of current peak. Three phase 6/4 pole SRM having dissimilar rotor and stator pole arc is considered to demonstrate the effect. Phase current and inductance variation of the SRM (Model 1-chapter 3) is shown in Figure 6.11.

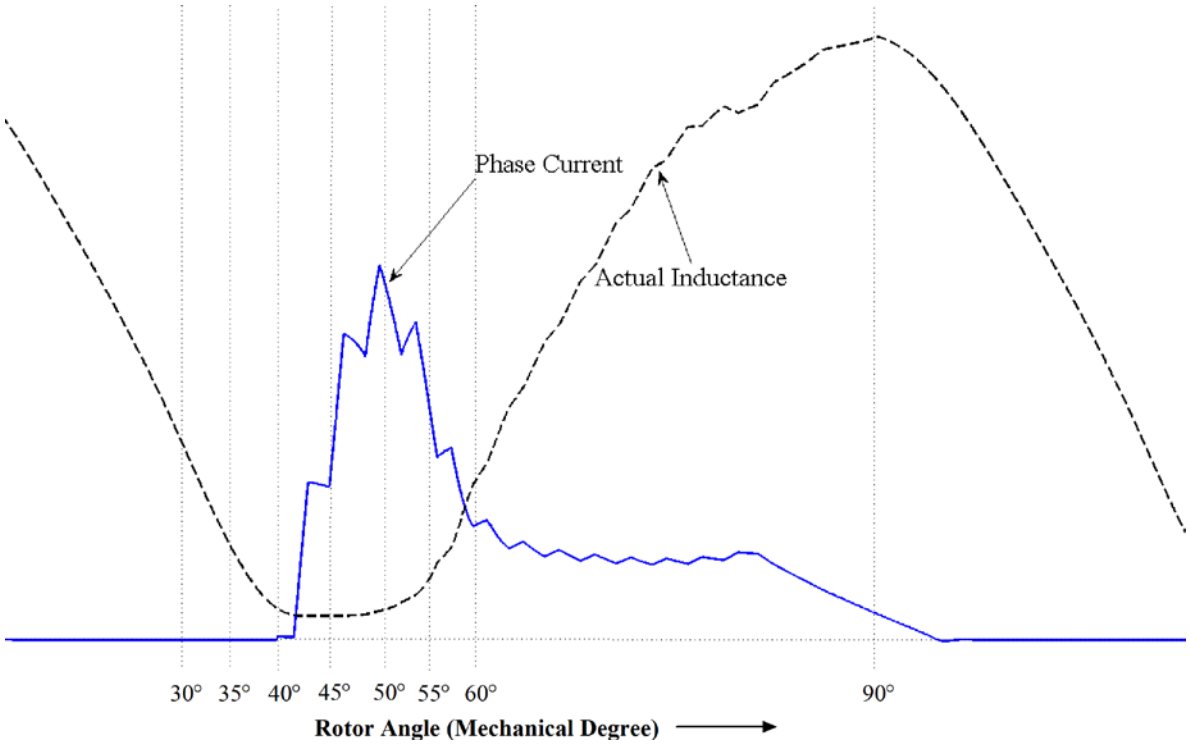

Figure 6.11 Phase current and inductance variation of 60KW, 6/4 pole, 3 phase SRM

Rotor pole arc (θ_r) and stator pole arc (θ_s) of motor are 45° and 32° respectively. Hence, rotor angle (θ_{pdp}) at which stator and rotor poles just begin to get aligned, will advance more than that in the previous case, where both θ_r and θ_s were 30°. Comparison of both the cases is shown in Figure 6.12 from which it is obvious that θ_{pdp} is advanced by an angle of 8.5° (i.e 7.5° + 1°) for the case compared to previous one. Hence, θ_{pdp} will become 51.5° for the three phase SRM. For the 6/4 pole three phase motor, θ_{pdp} can be derived as -

$$\theta_{pdp} = 60 - (\theta_r - 30 + \theta_s - 30) \tag{6.17}$$

or

$$\theta_{pdp} = 120 - \theta_r - \theta_s \tag{6.18}$$

For 8/6 pole four phase motor, rotor angle θ_{pdp} can be derived as-

$$\theta_{pdp} = 90 - \theta_r - \theta_s \tag{6.19}$$

In general, equation for rotor angle θ_{pdp} can be written as-

$$\theta_{pdp} = (2 * \varepsilon + 60) - \theta_r - \theta_s \tag{6.20}$$

where 'ε' is a stroke angle.

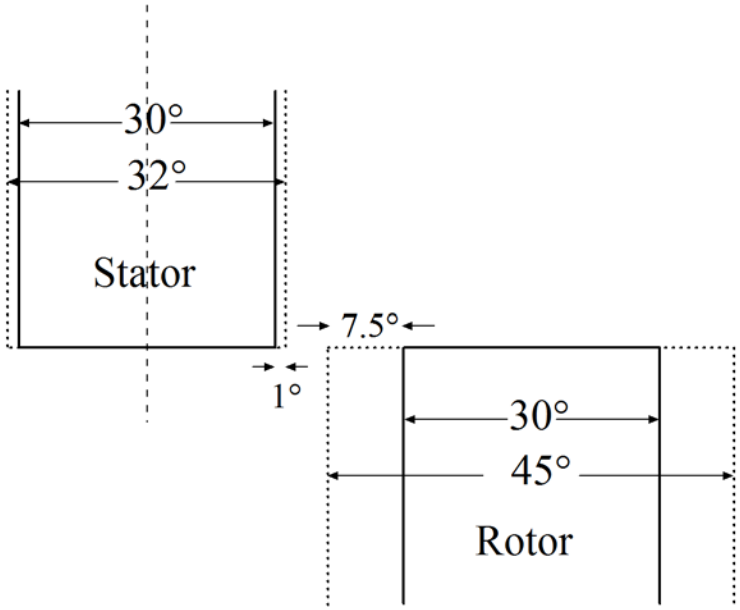

Figure 6.12 Rotor and stator pole arc

Since, the performance of the CGSM depends on the instant of peak detection pulse only, other motor parameters like phase inductance, resistance, temperature and magnetic characteristics do not affect the CGSM. Thus, it is easy to design a generalized CGSM, which can work for most of the motor topologies with or without minor changes in equation (6.12) and (6.20). Parameters required to implement a CGSM are number of phases, number of rotor/stator pole and pole-arcs.

6.3.2 Current peak detection

Accuracy of the sensorless method depends on the instant of current peak detection. However, current peak detection stage requires only few components including op-amp as a base to implement. Low-pass filters are used in the current peak detection stage for eliminating switching frequency, thus cut-off frequency (f_{coff}) of low-pass filters should be designed based on selected PWM frequency. Wide range of f_{coff} will produce the same performance for high frequency (greater than 10 KHz) PWM control. The cut-off frequency of filter is generally chosen as,

$$f_{coff} = \frac{f_{pwm}}{2}, to, \frac{f_{pwm}}{3} \tag{6.21}$$

Filters add delay in current peak detection instant, which is directly proportional to the speed of the motor and inversely proportional to the cut-off frequency of the filter. However,

in high frequency PWM controlled drive, this delay is less than 1°, which is negligible and even some times it becomes helpful to compensate the advance effect in peak detection instant due to corner flux. The scenario looks different with the low frequency PWM drive, which is meant for energy efficient solution. The delay produced in peak detection instant is prominent with the low PWM frequency and cannot be neglected. On the other hand, PWM frequency is set to 1.6 KHz in the low cost efficient PWM controller, designed in chapter 4. Design and performance of CGSM for such a low frequency PWM drive is investigated**.** Simulation diagram of current peak detection stage in MATLAB simulink environment is shown in Figure 6.13, where f_{coff} is selected to 400 Hz and 1000 Hz for the PWM frequency of 1.6 KHz and 5 KHz respectively. Issues related to the current peak detection stage are described in the following sub-sections.

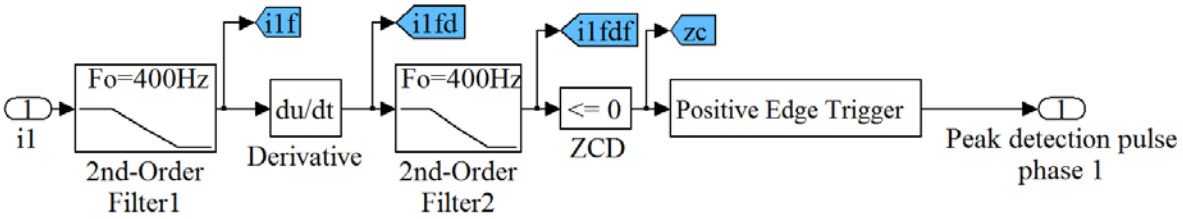

Figure 6.13 Simulation diagram of current peak detection stage

6.3.2.1 *Effect of current chopping method*

Soft chopping and hard chopping are two basic modes of operation to control the phase current. Figure 6.14 and Figure 6.15 show the waveforms for current peak detection stage with soft chopping and hard chopping techniques respectively, when applied to simulation model of SRM with PWM frequency of 5 KHz at no load. In the soft chopping mode, phase voltage is zero during current freewheel, while in the hard chopping mode, full reversed voltage will appear across phase during regeneration mode. Therefore, current decays more slowly in soft chopping mode as compared to hard chopping, and thus current is discontinuous particularly at light load with the hard chopping mode, especially for the low frequency PWM. It requires more filtering as compared to soft chopping and consequently delay produced in peak detection pulse is also more. The required duty cycle of PWM is less in soft chopping mode as compared to the hard chopping for the same speed. It is because of less peak current required in soft chopping mode to maintain the same average current. Although, the soft chopping mode is more suitable for implementation of CGSM, performance of CGSM for SRM with the split DC converter (hard chopping mode) is also investigated later on.

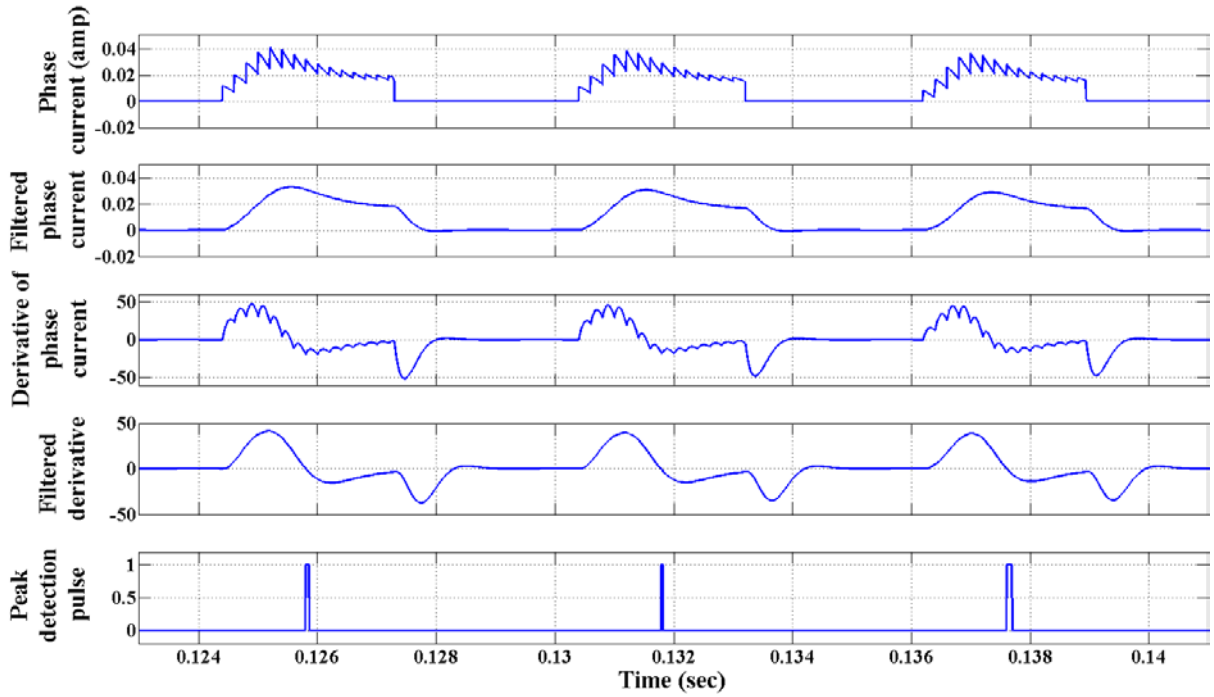

Figure 6.14 Waveform for current peak detection stage with soft chopping

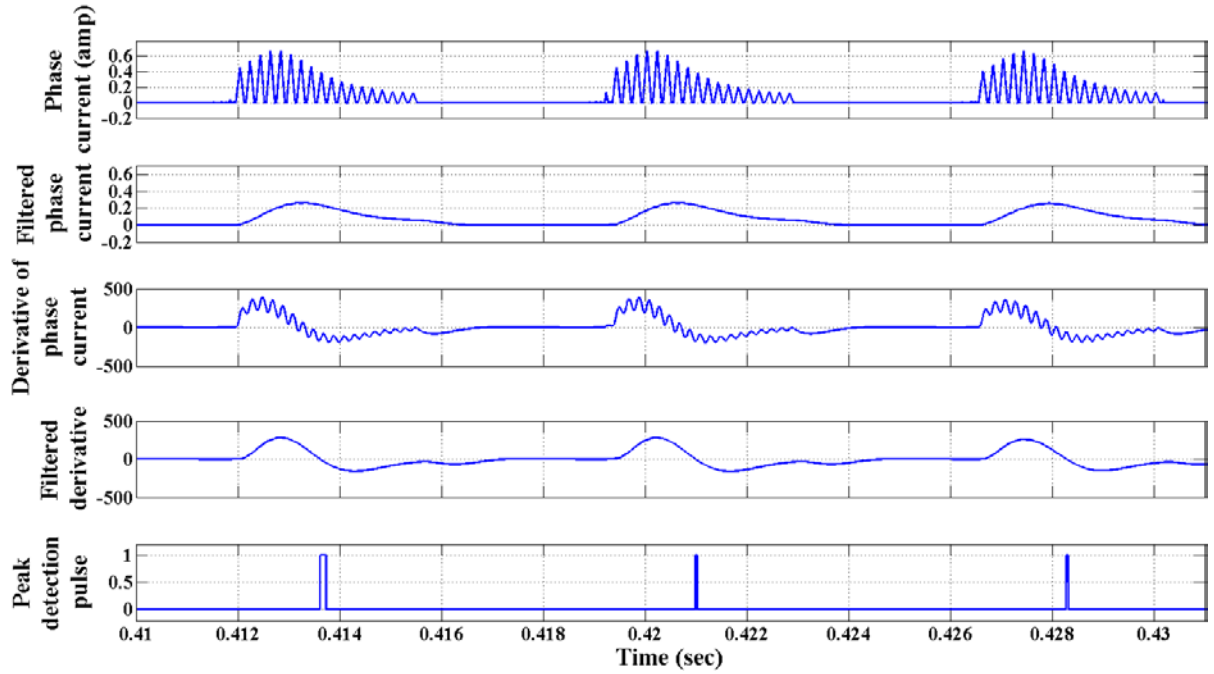

Figure 6.15 Waveform for current peak detection stage with hard chopping

6.3.2.2 *Delay in peak detection pulse*

Simulation model of PWM controlled SRM drive with split DC converter is used to analyze the current gradient sensorless method. The peak detection angle θ_{pdp} for the 8/6 pole four phase SRM is obtained as 30°(mech) using equation (6.20). Various waveforms of the current peak detection stage for the phase-1 and at no load are shown in Figure 6.16, where PWM frequency is 1.6 KHz and speed of the motor is 1300 rpm. Ideally current peak

detection pulse (PDP) should indicate the rotor angle of 30° (θ_{pdp}) irrespective of turn ON angle, speed and load. But, phase delay produced in current peak detection due to second order filter, adds an error in estimation of rotor angle. Furthermore, delay produced in peak detection pulse is directly proportional to the motor speed.

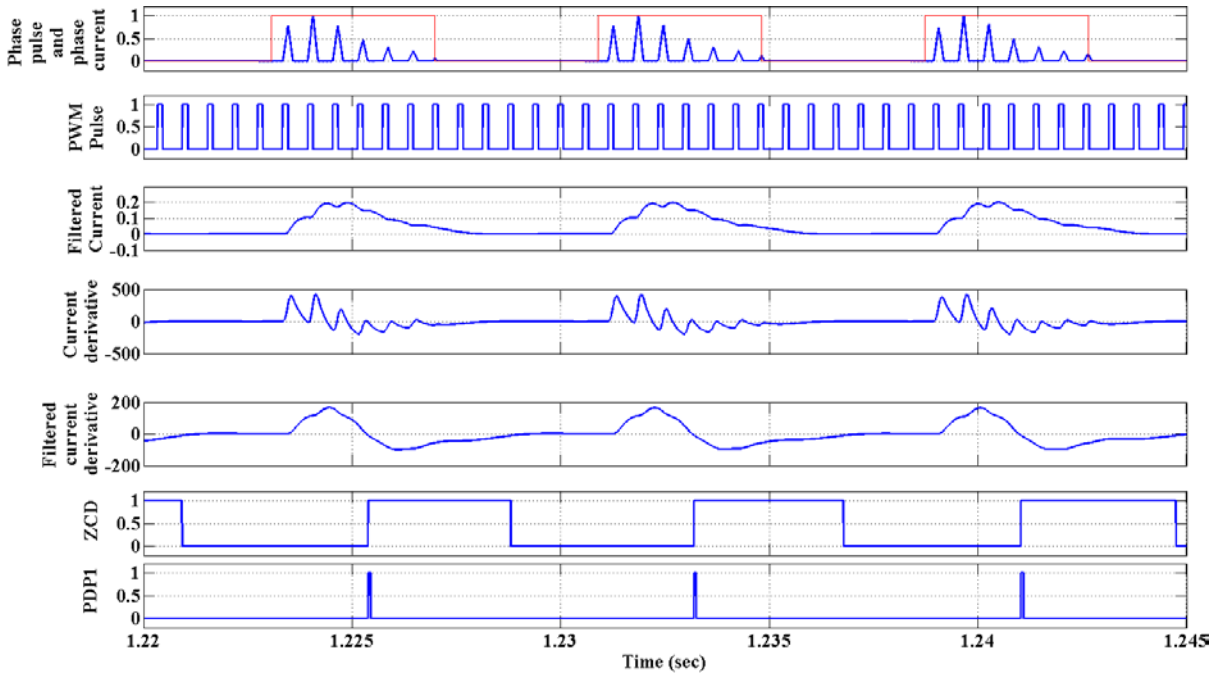

Figure 6.16 Waveforms of the current peak detection stage for phase-1 at no load and 1300rpm with PWM frequency of 1.6KHz

The transfer function of the second order filter and current peak detection stage are obtained as given below,

$$TF_{filter}(s) = \frac{1}{1.583e^{-7}S^2 + 0.0007958S + 1} \tag{6.22}$$

$$TF_{pds}(s) = \frac{1}{2.506e^{-14}S^4 + 2.52e^{-10}S^3 + 9.499e^{-7}S^2 + 0.001592S + 1} \tag{6.23}$$

Frequency response of the filter and peak detection stage is shown in Figure 6.17. Delay in current peak detection is a function of rotor speed, while variation in delay due to the load current is very small and can be neglected.

If an error, introduced in the rotor angle estimation, is θ_{error}, then rotor angle pointed by the peak detection pulse (θ_{pdp_new}) can be expressed as-

$$\theta_{pdp\_new} = \theta_{pdp} + \theta_{error} \tag{6.24}$$

Variation of rotor angle, indicated by the peak detection pulse (PDP) for the PWM frequencies of 1.6 KHz and 5 KHz are shown in Figure 6.18 and Figure 6.19 respectively. Error produced in the current peak detection pulse can be compensated during the rotor angle estimation by replacing θ_{pdp} with θ_{pdp_new} in the equation (6.12). Experimental results represent the measured value of rotor angle which is non-linear in nature. For the continuous

rotor angle estimation for control of SRM, an approximate linear equation is derived from the measured rotor angle as shown in Figure 6.18 and Figure 6.19.

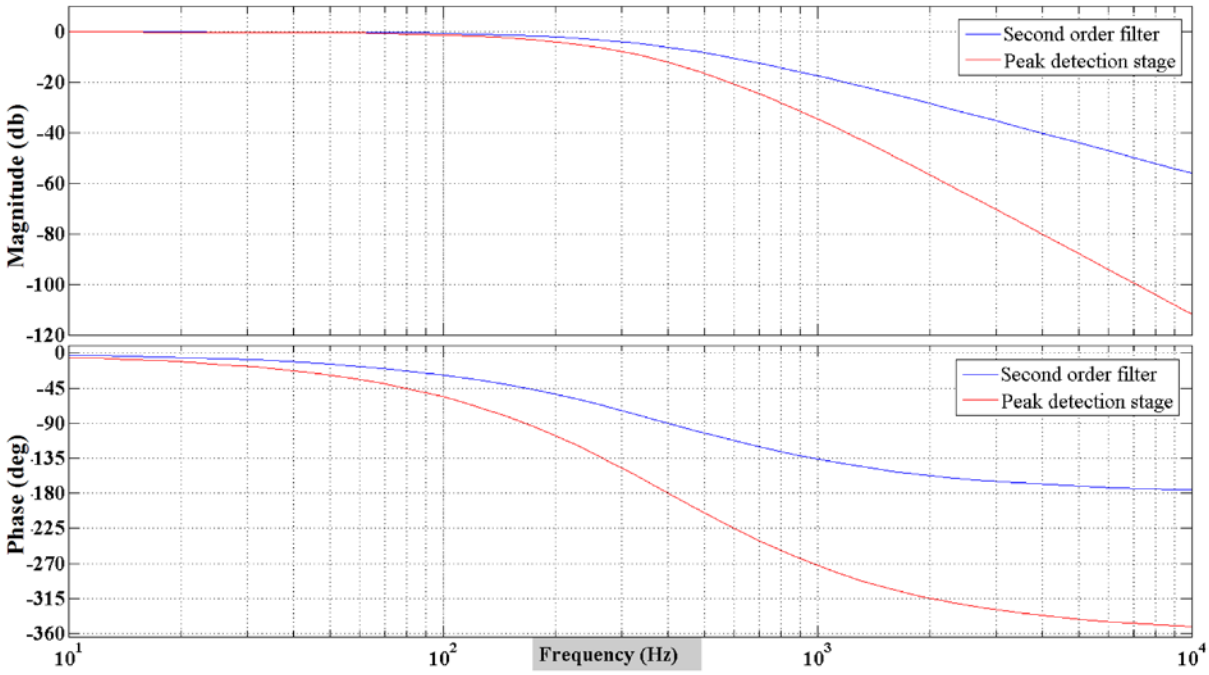

Figure 6.17 Frequency response of second order filter and current peak detection stage

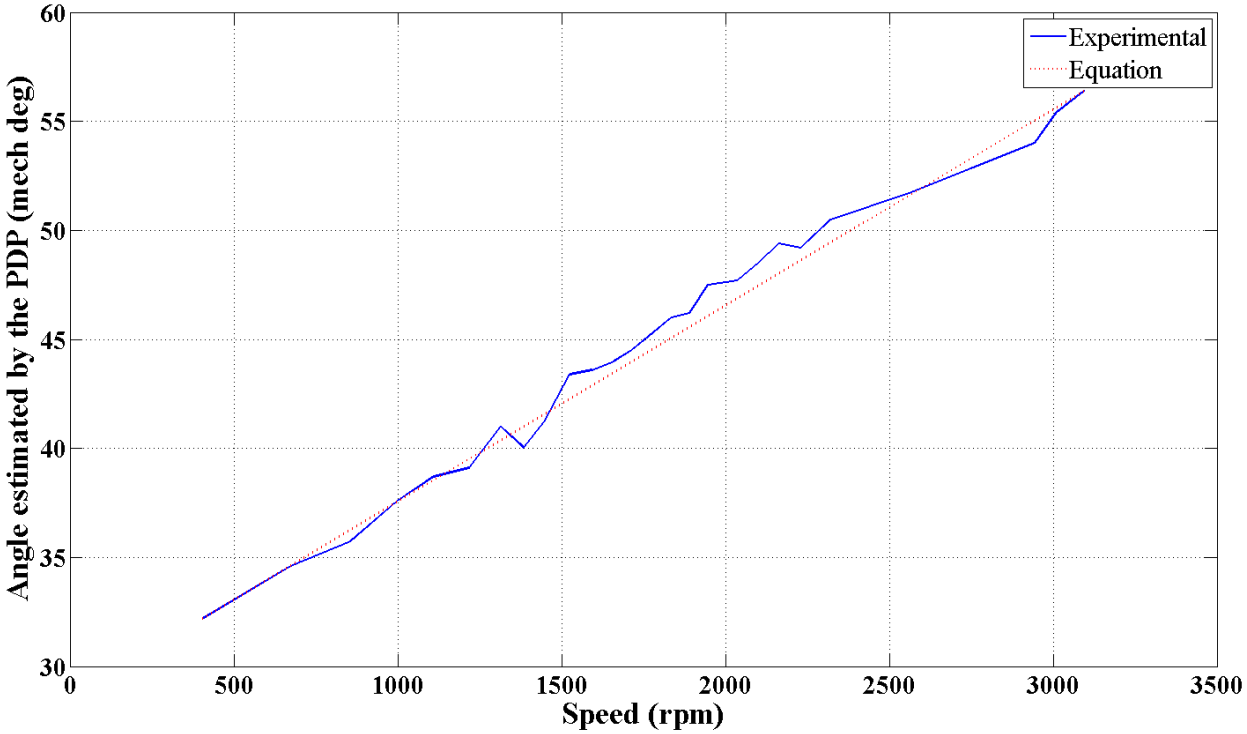

Figure 6.18 Variation in angle estimation with motor speed for the PWM frequency of 1.6KHz

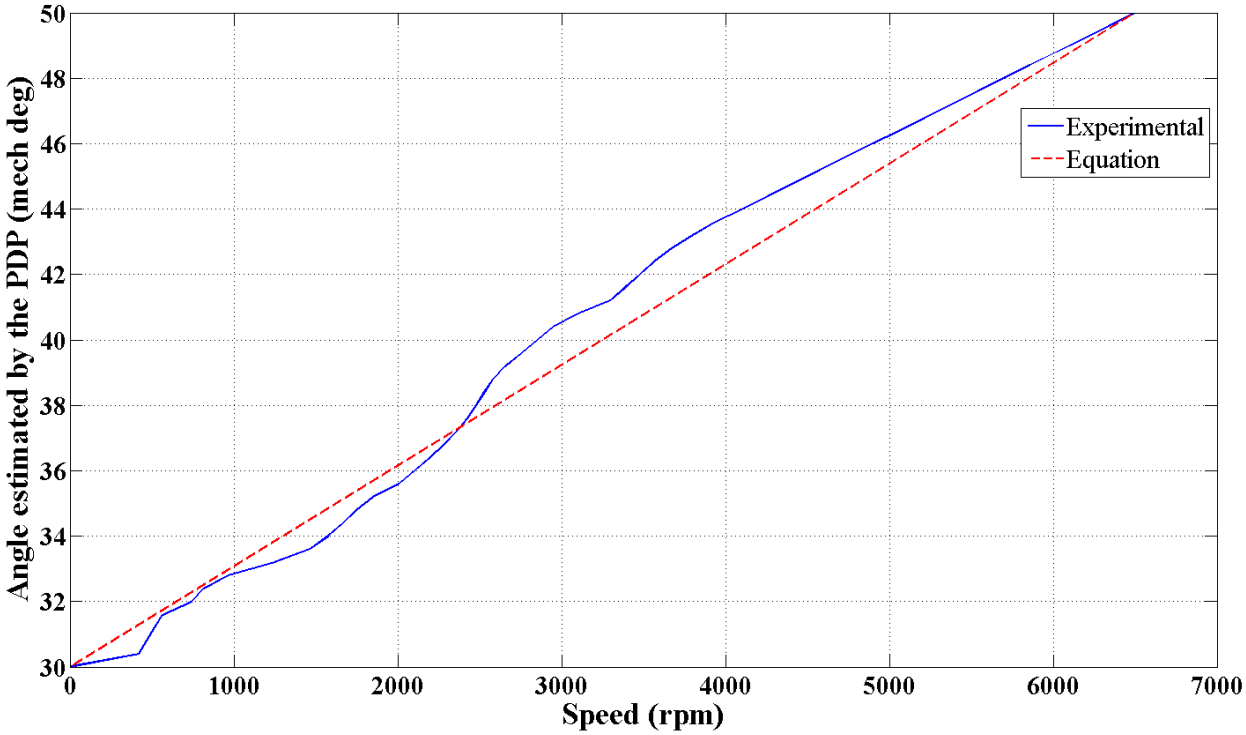

Figure 6.19 Variation in angle estimation with motor speed for the PWM frequency of 5KHz

6.3.2.3 *Error in peak detection instant due to non synchronized PWM pulse*

A specific problem arises with the low frequency PWM control, particularly at a higher speed. Frequency of commutation pulse f_{com} is a function of motor speed, while PWM frequency f_{pwm} is constant throughout. Because, f_{com} is same as frequency of peak detection pulse f_{pdp}, it can be expressed as-

$$f_{com} = \frac{N_s \times n_{cr}}{60} \tag{6.25}$$

Frequency of commutation pulse increases with increase in motor speed. Consider a case shown in Figure 6.20 for the high speed operation, where f_{com} is greater than $f_{pwm}/10$, while it is assumed that, duty cycle of PWM pulse remains constant throughout the commutation period and current is discontinuous. It is a general practice to generate a PWM pulse independently with or without frequency control. However, Figure 6.20(a) shows the case where it is assumed, that PWM pulse is always in synchronism with commutation pulse. With the rising inductance profile and constant duty cycle, current peak at each PWM pulses gets reduced. Thus, the angle θ_{pdp} can be obtained accurately from the peak detection pulse. However, in real practice, PWM pulses are not synchronized and so effective duty cycle is not constant throughout the commutation period, as shown in Figure 20(b)&(c). Consider a case shown in Figure 20 (b), for which first current peak is less in magnitude as compared to the second one, even with increase in inductance. This is due to the fact, that effective duty cycle is less for the first pulse due to non synchronized PWM,

while effective turn ON instant θ_{on} is not altered. It will introduce an error in the angle directed by the peak detection pulse thus, the rotor angle directed by the peak detection pulse will always be higher than the actual angle θ_{pdp}. But, for the case shown in Figure 6.20 (c), current peak reduces with the increase in inductance while, it produces delay in turn ON instant. Consequently, low frequency non-synchronized PWM pulses results in wide variation in estimated rotor angle particularly at higher speed. Furthermore, the compensation of the error produced in rotor angle estimation becomes difficult because, variations of peak detection instant and effective turn ON angle both are independent in nature and may vary for each commutation period even with constant speed.

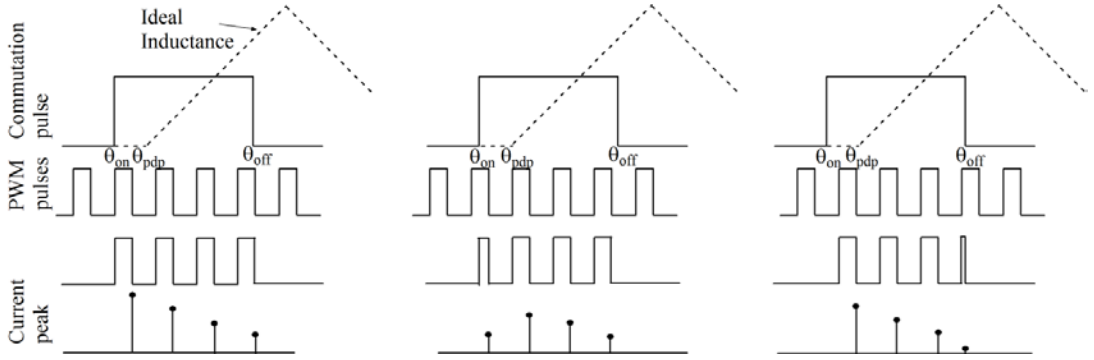

Figure 6.20 Effect of non synchronized PWM pulse on instant of current peak (a) synchronized PWM pulse (b) & (c) non-synchronized PWM pulse.

Simulation model of 8/6 pole four phase SRM with PWM frequency of 1.6 KHz for the non-synchronous PWM are shown in Figure 6.21 and Figure 6.22, where turn ON angle θ_{on} = 22.5° and turn OFF angle θ_{off} = 52.5°.The figures shows the variation in instant of current peak. Figure 6.21 explicate a case (b) of Figure 6.20, where error is produced in peak detection, due to variation in effective duty cycle during commutation interval. Figure 6.22 shows the case (c) of Figure 6.20, where delay is produced in turn ON angle. Rotor position directed by current peak detection pulse is varying at each commutation interval. As a result, implementation of CGSM with the low frequency PWM controller is quite difficult for the high speed operation. Figure 6.23 shows the waveform of phase current at a speed of 10440 rpm. This phenomenon limits the lower value of the PWM frequency for desired motor speed. Irrespective of motor winding parameter and motor magnetic characteristics, lower limit of PWM frequency can be constrained by following equation for the implementation of current gradient sensorless method.

$$f_{pwm} > 10 \times f_{com} \tag{6.26}$$

From equation (6.25)

$$f_{pwm} > \frac{N_s \times n_{cr}}{6} \qquad (6.27)$$

Minimum PWM frequency for the desired motor speed can be derived from equation (6.27). However, if PWM pulses are synchronized with the phase commutation pulse, then CGSM can give errorless rotor position estimation even for $f_{pwm} = f_{com}$.

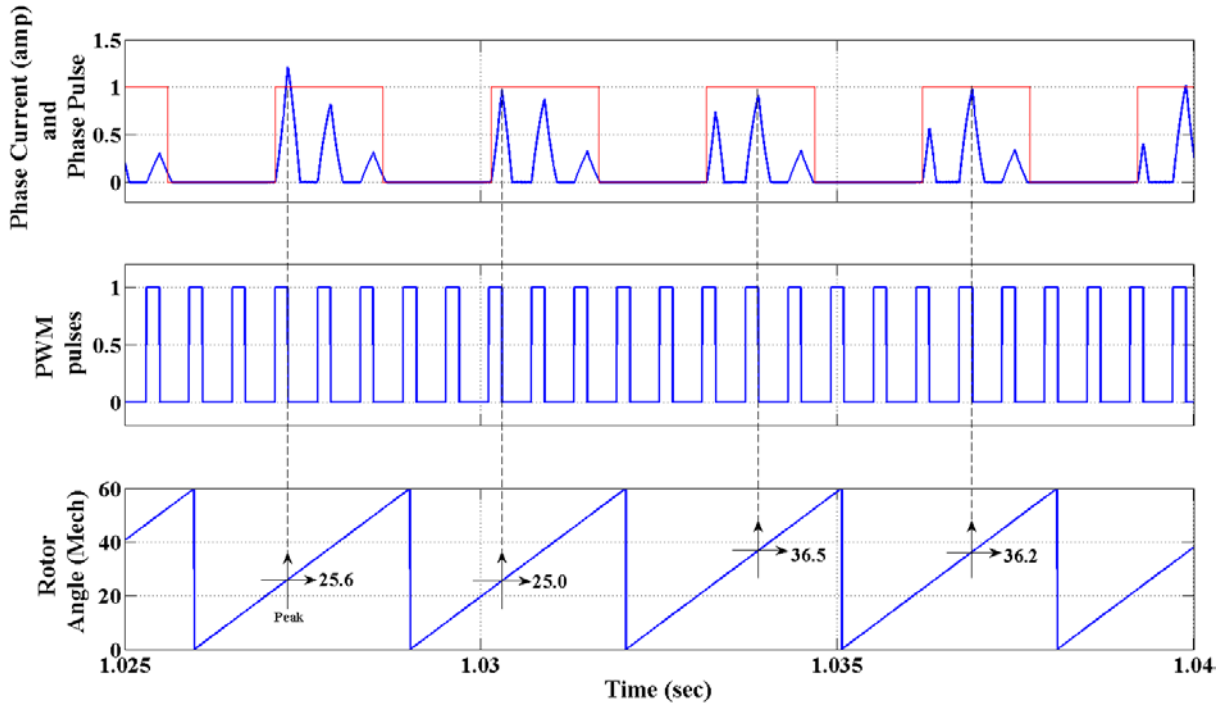

Figure 6.21 Variation in an instant of current peak for the non-synchronous PWM at no load with duty cycle of 30% and speed of 3300rpm

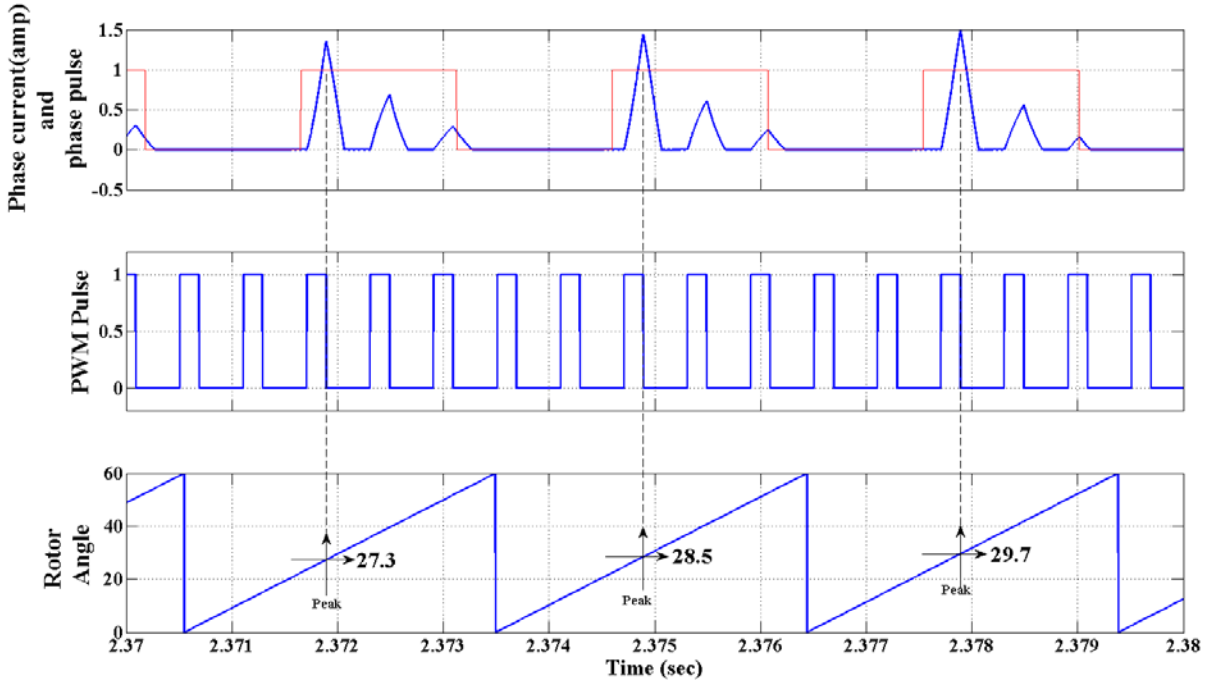

Figure 6.22 Variation in an instant of current peak for the non-synchronous PWM at no load with duty cycle of 30% and speed of 3400rpm

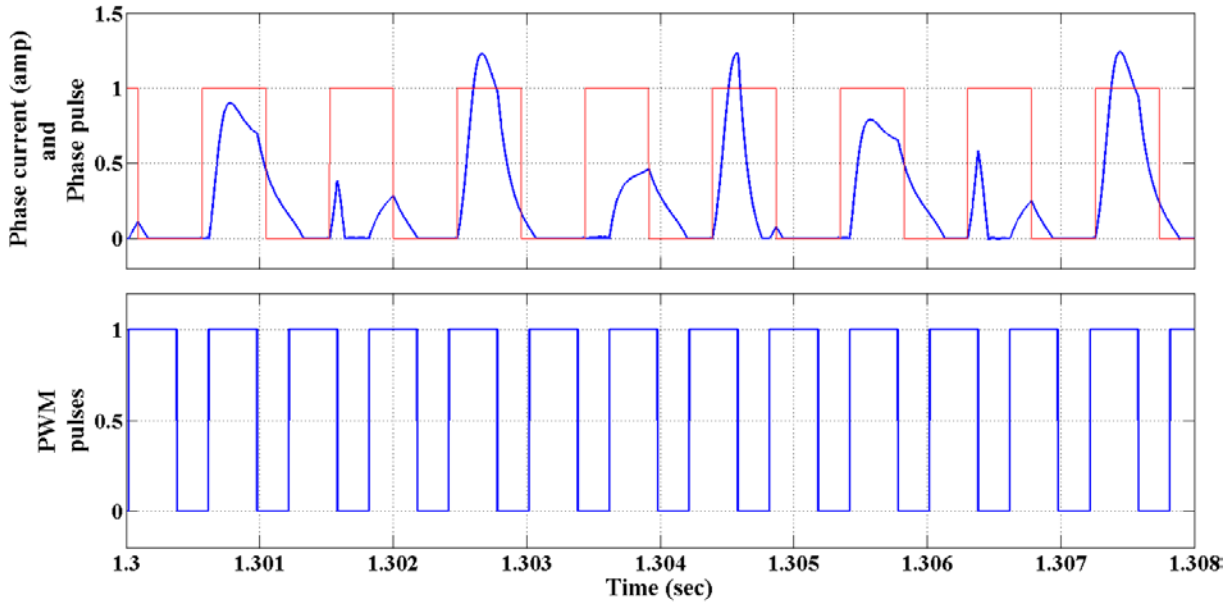

Figure 6.23 Variation in an instant of current peak for the non-synchronous PWM at no load with duty cycle of 60% and speed of 10440 rpm

Phase locked loop can be used to synchronize the PWM pulses with the commutation pulses. Another simplest way to achieve synchronization is to reset PWM chip, at the rising edge of commutation pulse. However, practical implementation of both the methods is much complex because of the fact that the commutation pulses are derived from the peak detection pulses. Thus it is a better choice to limit the PWM frequency for desired motor speed. Moreover, synchronized PWM techniques can be used to derive an accurate delay produced in current peak detection, where commutation pulses should be result of the accurate mechanical position sensing arrangement.

6.3.3 Phase lock loop

A PLL (Phase-locked-loop) system is a closed-loop electronic circuit that controls an oscillator so that it provides an output signal that maintains a constant phase angle with respect to a reference signal, which can range from a fraction of Hz to many GHz.

6.3.3.1 *Basic PLL circuit theory*

Basic block diagram of PLL system is shown in Figure 6.24. It starts with phase detection system (PD) which detects a phase difference ($\Delta\varphi$) between input (V_{in}) and output (v_{out}) signals through the feedback system. Phase error is then smoothed out by low pass filter (LPF) which adjusts the phase of output with the help of voltage controlled oscillator (VCO).

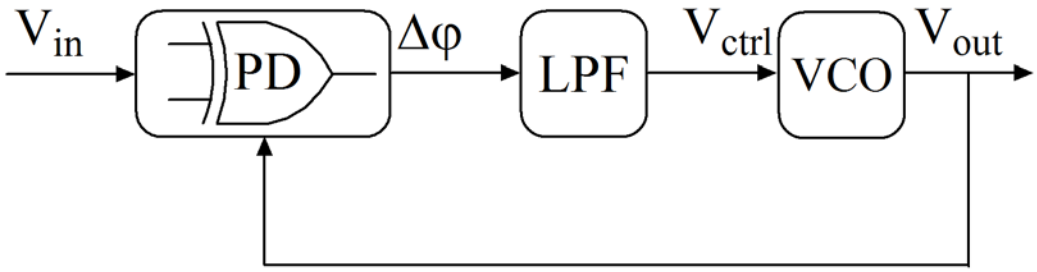

Figure 6.24 Basic block diagram of PLL

A simple phase detection circuit for a square (pulse) signal can be realized with a single XOR gate which outputs a phase error as-

$$\Delta\varphi = \begin{cases} 1\, for V_{in} \neq V_{out} \\ 0\, for V_{in} = V_{out} \end{cases} \quad (6.28)$$

for an input 'V_{in}' and output 'V_{out}' as shown in Figure 6.25. LPF module smoothes the phase error to generate control signal (V_{ctrl}). Control voltage V_{ctrl} is directly proportional to the phase difference Δφ.

VCO is a circuit module that oscillates at a controlled frequency (ω). The oscillation frequency is controlled using voltage 'V_{ctrl}'. Frequency of oscillation (ω) can be expressed as-

$$\omega = \omega_0 + K_v \cdot V_{ctrl} \quad (6.29)$$

Where, 'K_v' is proportionality constant of VCO module in rad/s/V and 'ω_0' is initial (minimum frequency) frequency at zero control voltage. Operation of the PLL can be summarized as, if V_{in} and V_{out} are out of phase (Unlocked), then the PD module detects the error and LPF module smoothes the error signal. The control signal (Vctrl) slows down or speeds up the VCO module; hence, the phase is corrected (Locked). Graphical representation of PD and VCO module are shown in Figure 6.26. Initial phase difference φ_0 produces a control voltage 'V_1'. Frequency of oscillation changes to 'ω_1' which corresponds to control voltage 'V_1' and thus phase difference changes to a new value. This process continues until phases are being locked. Mathematically phase locked condition can be represented as-

$$\frac{d}{dt}(\varphi_{in} - \varphi_{out}) = 0 \quad (6.30)$$

where 'φ_{in}' and 'φ_{out}' are phase delays of input and output respectively. This implies that

$$\omega_{in} = \omega_{out} \quad (6.31)$$

where 'ω_{in}' and 'ω_{out}' represents frequency of input and output signals respectively.

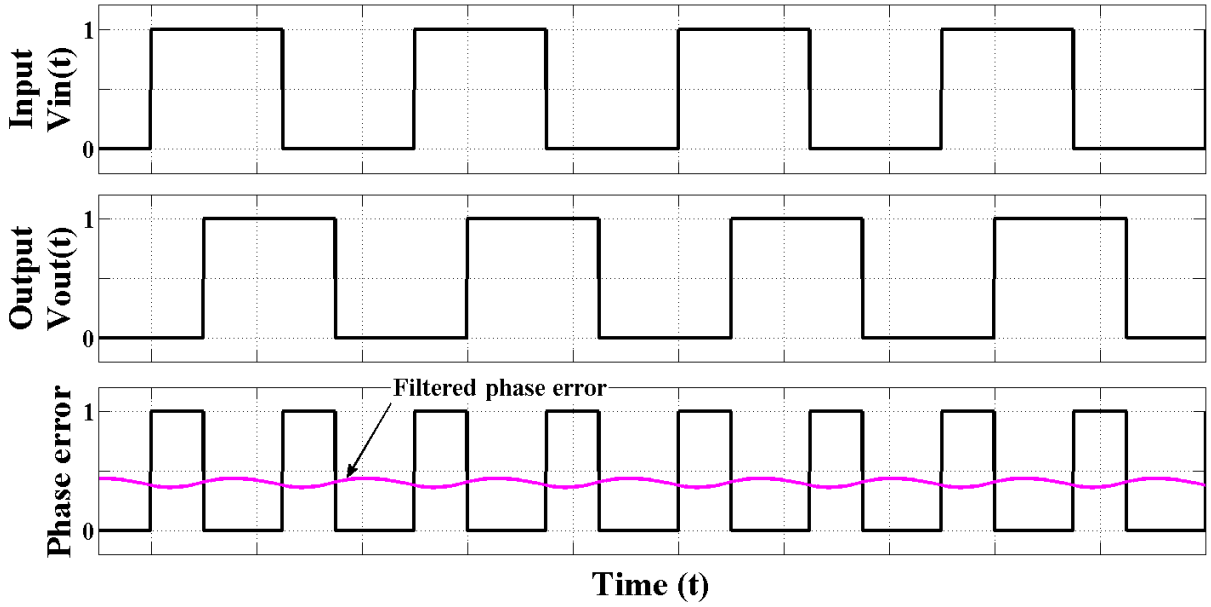

Figure 6.25 Waveforms of phase detection circuit

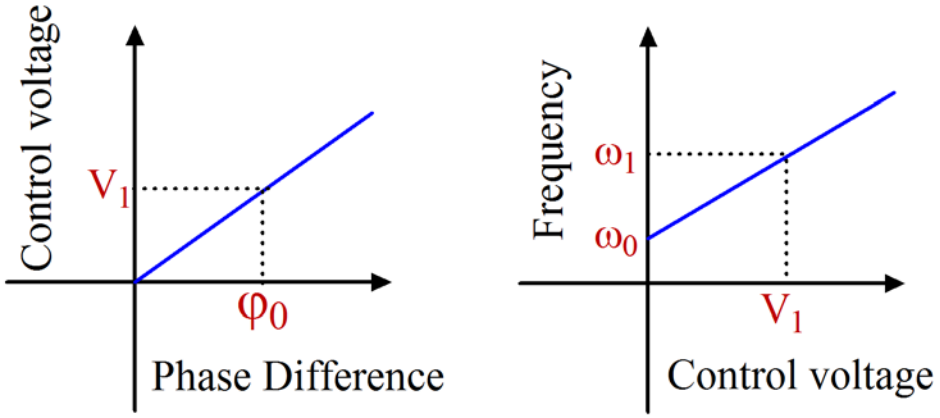

Figure 6.26 Graphical representation of PD and VCO

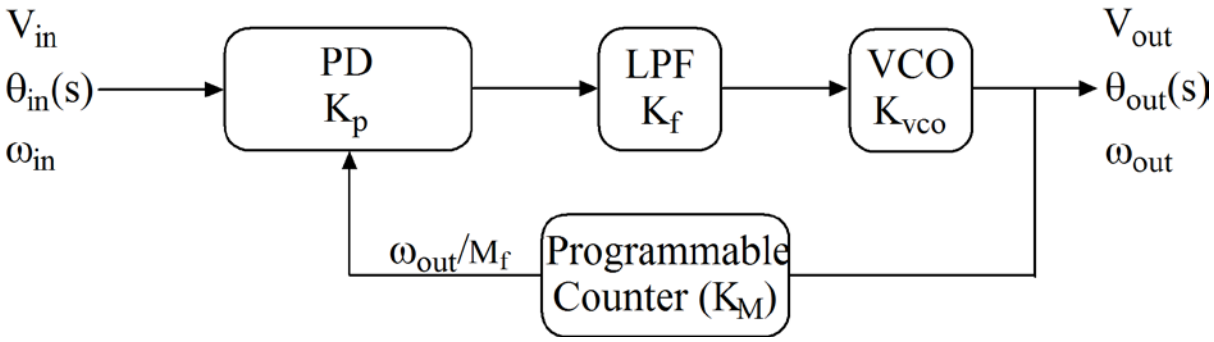

Figure 6.27 PLL with frequency multiplication

6.3.3.2 *Design analysis of PLL*

Design problem of PLL is approached using Laplace Transform technique. The Laplace Transform permits representation of time response f(t) of the system in complex domain F(s). The Laplace Transform of input and output phases are given as,

$$\varphi_{in}(t) \rightarrow \theta_{in}(s) \tag{6.32}$$

$$\varphi_{out}(t) \rightarrow \theta_{out}(s) \tag{6.33}$$

The phase detector, filter and VCO comprise the feed forward path, while the feedback path contains the programmable divider as shown in Figure 6.27. Since, the VCO produces a frequency proportional to its input voltage, any time variant signal appearing as control signal will modulate the frequency of VCO. Thus, the output frequency during phase locked condition is -

$$f_{out} = M_f \times f_{in} \tag{6.34}$$

and therefore,

$$\omega_{out} = M_f \times \omega_{in} \tag{6.35}$$

where 'ω_{in}' and 'ω_{out}' denote the frequency of input and output in rad/s. Transfer function of programmable counter can be represented as-

$$\frac{\theta_{out}(s)}{\theta_c(s)} = K_M = \frac{1}{M_f} \tag{6.36}$$

The phase error is given as,

$$\theta_e(s) = \theta_{in}(s) - \theta_c(s) \tag{6.37}$$

Phase detector produces a voltage proportional to the phase error $\theta_e(s)$. If $V_p(s)$ is a voltage produced by a phase detector then -

$$\frac{V_p(s)}{\theta_e(s)} = K_p \tag{6.38}$$

Where, 'K_p' is a proportional gain of the phase detector in volt/rad. This filtered voltage is used as control signal (V_{ctrl}) for the VCO. Transfer function of filter stage is represented as-

$$\frac{V_{ctrl}(s)}{V_p(s)} = K_f(s) \tag{6.39}$$

Where, $K_f(s)$ is a filter transfer function. The transfer function of VCO is given as-

$$\frac{\theta_{out}(s)}{V_{ctrl}(s)} = K_{vco}(s) = \frac{K_v}{s} \tag{6.40}$$

Where, 'K_v' is proportional constant of VCO, expressed in rad/s/V. Transfer function of PLL is a result of equation (6.36) to (6.40) as expressed in Figure 6.28.

By using control theory, open loop transfer function of the system is given as,

$$G(s)H(s) = K_p K_f(s) K_{vco}(s) K_M = \frac{K_p K_f(s) K_v K_M}{s} \tag{6.41}$$

Different *types* (1, 2 or 3) of system can be realized by selecting appropriate filter gain $K_f(s)$. The *type* of system refers to the number of poles of the open loop transfer function G(s)H(s)

located at the origin. Typical open loop transfer function for the type 1, type 2 and type 3 are presented in Table 6.2.

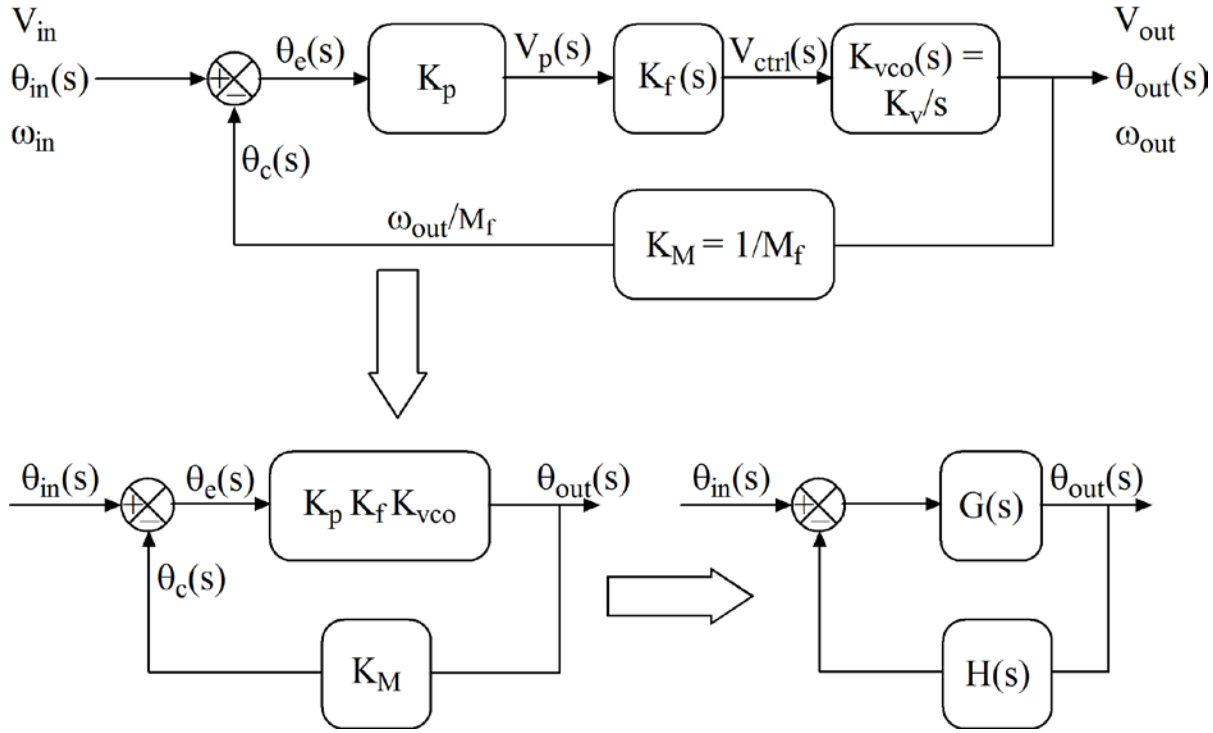

Figure 6.28 Transfer function model of PLL

Table 6.2 Typical open loop transfer function for the type 1, type2 and type 3

Type of the system	Open-loop transfer function G(s)H(s)
Type 1	$\frac{K}{s(s+a)}$
Type 2	$\frac{K(s+a)}{s^2}$
Type 3	$\frac{K(s+a)(s+b)}{s^3}$

In evaluating the system, phase error $\theta_e(s)$ must be examined in order to determine the optimum or satisfactory steady state error and transient characteristics. Using transfer function theory, phase error is equated as-

$$\theta_e(s) = \frac{1}{1+G(s)H(s)} \cdot \theta_{in}(s) \tag{6.42}$$

The steady state evaluation can be simplified with the use of final value theorem associated with Laplace transformation. This theorem permits finding the steady state error $\theta_e(s)$ resulting from the input $\theta_{in}(s)$ without transforming back to the time domain. It states -

$$\lim_{t\to\infty}[\theta(t)] = \lim_{s\to 0}[s\theta(s)] \tag{6.43}$$

The input signal $\theta_{in}(s)$ is characterized as follows -

For step position

$$\theta_{in}(t) = C_p \qquad t \geq 0 \tag{6.44}$$

or in Laplace transformation,

$$\theta_{in}(s) = \frac{C_p}{s} \tag{6.45}$$

Where, 'C_p' is the magnitude of phase step in radians. This corresponds to shifting the phase of incoming reference signal by C_p radians.

For step velocity

$$\theta_{in}(t) = C_v \cdot t \qquad t \geq 0 \tag{6.46}$$

or in Laplace transformation,

$$\theta_{in}(s) = \frac{C_v}{s^2} \tag{6.47}$$

Where, 'C_v' is the magnitude of rate of change of phase in radian per second. This corresponds to input a frequency that is different than the feedback portion of VCO frequency. Thus C_v is a frequency difference in radian per second seen at the phase detector.

For step acceleration -

$$\theta_{in}(t) = C_a \cdot t^2 \qquad t \geq 0 \tag{6.48}$$

Or, in Laplace transformation, -

$$\theta_{in}(s) = \frac{2C_a}{s^3} \tag{6.49}$$

Where, 'C_a' is the magnitude of rate of change of frequency in radian per second per second. This corresponds to time variant frequency input.

Steady state error of the system can be determined for a given input signal type from the equation (6.42) and (6.43) as-

$$\theta_{ess} = \lim_{s \to 0}[s \cdot \frac{\theta_{in}(s)}{1 + G(s)H(s)}] \tag{6.50}$$

By applying the different inputs to the type 1, 2 and 3 system and utilizing final value theorem, following Table 6.3 can be constructed which shows respective steady state phase errors.

A zero phase error identifies phase coherence between the two input signals at the phase detector. A constant phase error identifies a phase difference between the two input signals at the phase detector. Magnitude of this differential phase error is proportional to the loop gain and magnitude of the input step while, a continuously increasing phase error identifies time rate change of phase. This is an unlock condition for the phase loop.

Table 6.3 Steady state phase error for various system types

Step Input	Type 1	Type 2	Type 3
Position	Zero	Zero	Zero
Velocity	Constant	Zero	Zero
Acceleration	Continuously increasing	Constant	Zero

Using Table 6.3, system type can be determined for specific input. PLL is used to achieve the objective of frequency multiplication for the case. It is required that, the frequency of output signal should be multiple of the input signal. Here, input signal is a peak detection pulse or phase commutation pulse. Thus frequency of input signal is a function of motor speed and therefore, any speed change results in corresponding change in frequency of input at the phase detector. Minimum of type 2 system is required for PLL, to trace a reference frequency with zero phase error. Therefore, open loop transfer function G(s)H(s) must take the form of-

$$G(s)H(s) = \frac{K(s+a)}{s^2} \tag{6.51}$$

Or, from the equation (6.41),

$$\frac{K_p K_f(s) K_v K_M}{s} = \frac{K(s+a)}{s^2} \tag{6.52}$$

The parameters thus far determined include K_p, K_v, K_M leaving only K_f as the variable for design. Thus K_f must take the form -

$$K_f(s) \propto \frac{(s+a)}{s} \tag{6.53}$$

in order to provide all of the poles and zeros for the required G(s)H(s).

Considering type-2 system, stability analysis of the system is analyzed. The root locus technique of determining the position of system poles and zeros in the s-plane is often used to graphically visualize system stability. Stability of the system requires that all poles must lie in the left half of the s-plane.

Root locus for the open loop transfer function G(s)H(s) of type two system (eq. 6.51) is constructed in Figure 6.29. It has two branches beginning at origins with one asymptote located at 180°. The root locus lies on the circle centred at (s = −a), and continuous on all portion of the negative real axis to left of the zeros. The breakaway point is (s = −2a). It should be noted, that zero added to the type 2 system provides stability. Without zero, the poles would movie along the jω axis as a function of gain and the system at all time would be oscillatory in nature.

The *order* of a system refers to the highest degree of the polynomial equation -

$$1 + G(s)H(s) = 0 \tag{6.54}$$

which is termed as the *characteristics equation*(C.E). The roots of characteristics equation

become closed loop poles of overall transfer function -

$$\frac{\theta_{out}}{\theta_{in}} = \frac{G(s)}{1+G(s)H(s)} \tag{6.55}$$

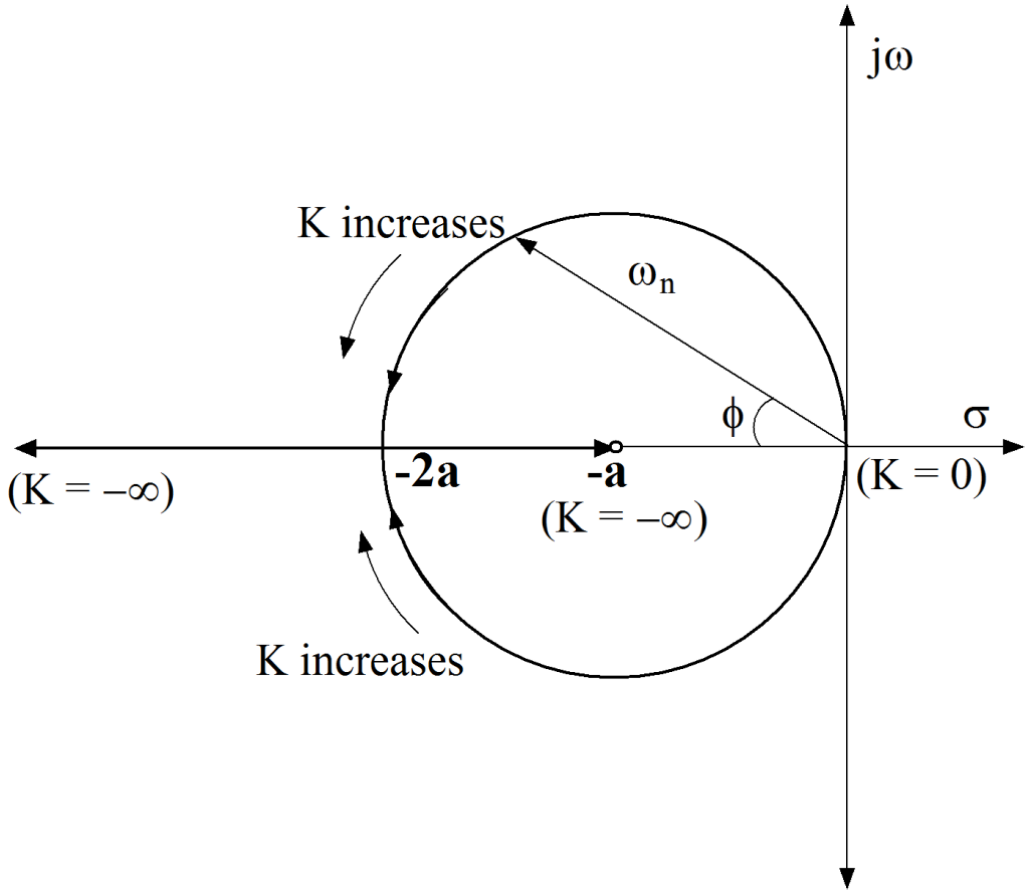

Figure 6.29 Root locus contour for type 2 second order system

The characteristic equation for the type 2 system of equation 6.51 is derived as-

$$s^2 + Ks + Ka = 0 \tag{6.56}$$

which is a second order polynomial. Thus type 2 second order system is obtained. The second order characteristic equation is normalized to a standard form -

$$s^2 + 2\xi\omega_n s + \omega_n^2 = 0 \tag{6.57}$$

Where, the damping ratio $\xi = \cos\phi$, $(0° \le \phi \le 90°)$ and 'ω_n' is the natural frequency as shown in Figure 6.29.

The phase or output frequency response of this type 2 second order system to a step position (phase) or velocity (frequency) input is shown in Figure 6.30. The required value of ω_n can be determined by the use of graph for specific damping factor ξ and lock-up time.

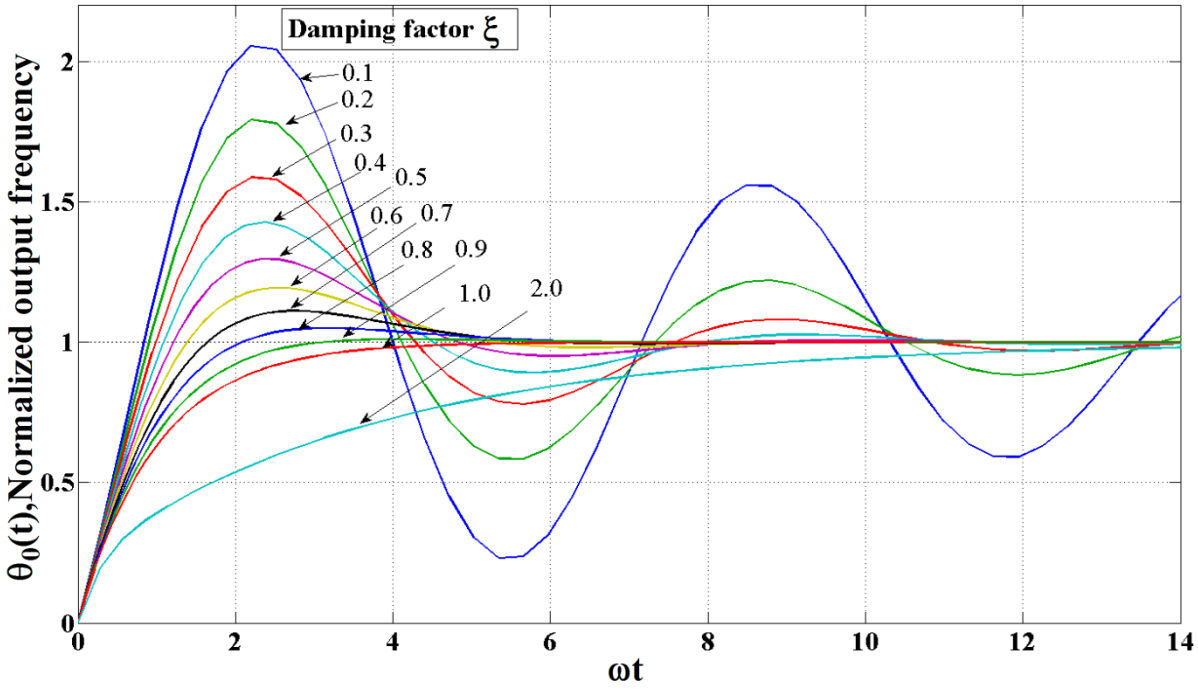

Figure 6.30 Step response of type 2 second order system

PLL is designed to achieve a resolution of 1° for the 8/4 four phase SRM, considering following parameters-

$$K_m = \frac{1}{60} \tag{6.58}$$

$$K_p = 0.1\ V/rad \tag{6.59}$$

$$K_v = 10\times10^6\ \ rad/s/V \tag{6.60}$$

$$K_f = \frac{K(s+a)}{s} \tag{6.61}$$

From the equation 6.52 G(s)H(s) can be written as -

$$G(s)H(s) = \frac{16.7\times10^3}{s}\cdot\frac{K(s+a)}{s} \tag{6.62}$$

and characteristic equation of the system becomes -

$$1+G(s)H(s) = s^2 + 16.7\times10^3\cdot K\cdot s + 16.7\times10^3\cdot K\cdot a \tag{6.63}$$

Here, two unknown constants 'K' and 'a' need to be determined.

Comparing characteristic equation with the standard second order form (eq.6.57),

$$\omega_n^2 = 16.7\times10^3\cdot K\cdot a \tag{6.64}$$

$$2\xi\omega_n = 16.7\times10^3\cdot K \tag{6.65}$$

From the above two equations, 'K' and 'a' are determined as -

$$2\xi\omega_n = \frac{\omega_n^2}{a} \tag{6.66}$$

$$\omega_n = 2\xi a \tag{6.67}$$

For ξ = 0.8, peak overshoot is less than 20% and will settle within 5% at $\omega_n t$ = 4.5.

Required lock-up time is considered as 1ms.

$$\omega_n = \frac{4.5}{t} = 4.5\times10^3 \ \ rad/s \tag{6.68}$$

The selected values of constant 'K' and 'a' for desired performance are given as,

$$a = 2.8125\times10^3 \tag{6.69}$$

$$K = 0.4311 \tag{6.70}$$

The open loop transfer function of the system is given by equation 6.71.

$$G(s)H(s) = \frac{16.7\times10^3 \cdot 0.4311 \cdot (s + 2.8125\times10^3)}{s^2} \tag{6.71}$$

Figure 6.31 and Figure 6.32 show the root locus contour and simulation diagram of the PLL system.

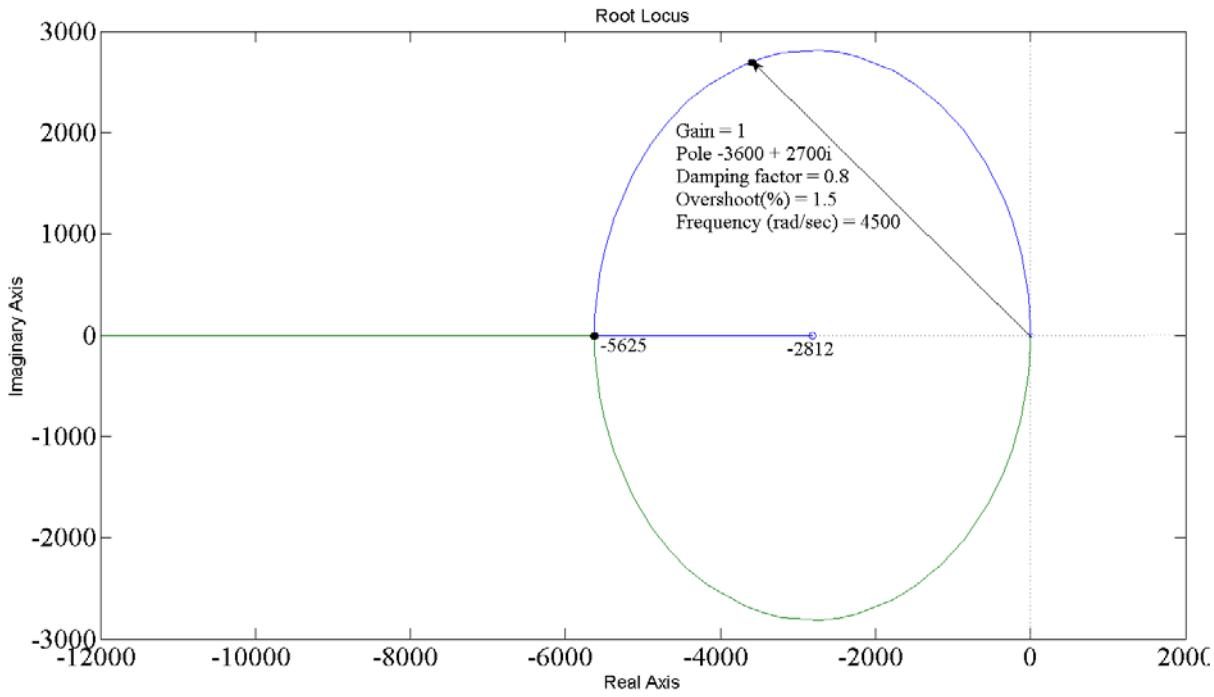

Figure 6.31 Root locus contour of the designed PLL system

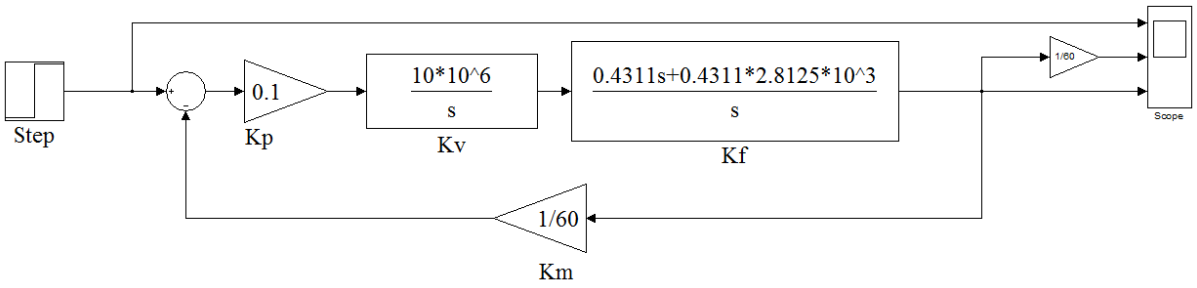

Figure 6.32 Simulink diagram of the PLL system

6.3.3.3 *Charge pump PLL*

Basic PLL system with only phase detector (PD) suffers from the problem of lock acquisition. If the output frequency is far away from the input frequency, when the PLL is turned ON, it is possible that PLL would never lock. Modern PLL uses frequency detector (FD) in addition to PD. Figure 6.33 shows the possible implementation of the module which detects both phase and frequency difference. Phase and frequency detector (PFD) module uses two edge triggering modules of D- Flip Flop. This module senses the rising transition in A or B. If A becomes "1" then flip-flop A is set (QA = "1") and when B becomes "1", the flip-flop B is set (QB = "1"). If both flip-flops are set, AND gate resets both output QA and QB to "0". Figure 6.34 shows that the waveform for the case A leads to B. Similarly, if B leads to "1", then QB = "1", when A becomes "1", then QA = "1", momentarily, while AND gate resets both output QA and QB to "0". The V_{out} is average of (QA - AB) is used to phase and frequency difference. Basic block diagram of PLL with phase frequency detector (PFD) is shown in Figure 6.35 which contains PFD, LPF, differential amplifier and VCO with negative feedback system.

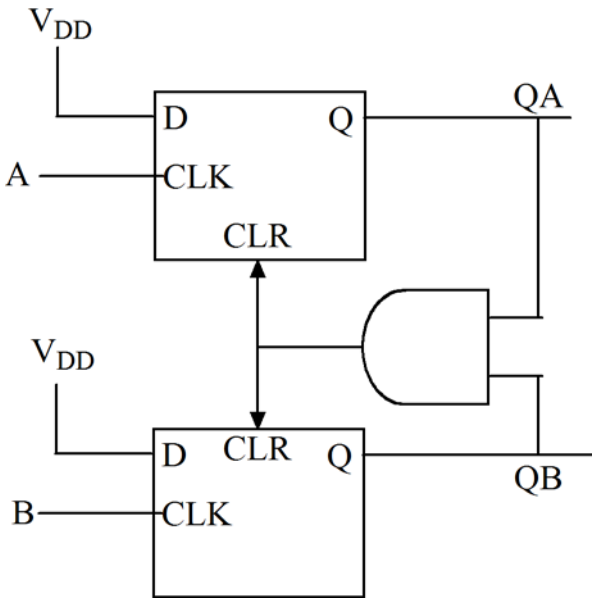

Figure 6.33 Phase and frequency detector (PFD) module

PLL module with PFD and differential amplifier is sensitive to noise and offset voltage, and it also leads to ripples in $V_{control}$. Charge pump PLL module does not suffers from the above problem. Block diagram of charge pump PLL is shown in Figure 6.36. Main structure consists of PFD, two switches, capacitor and VCO with negative feedback. Two switches are controlled by QA and QB, which charge or discharge the capacitor.

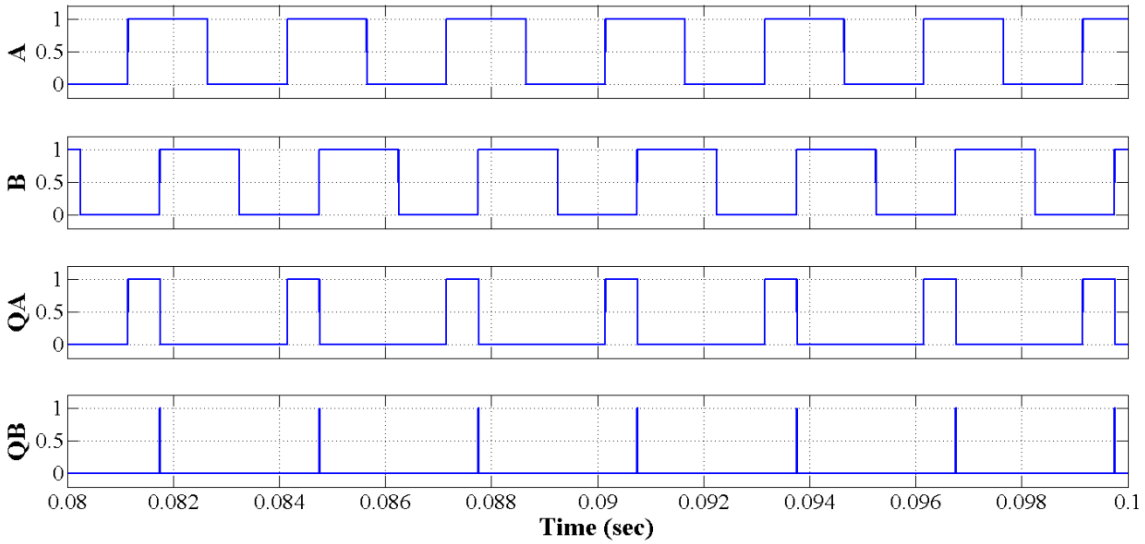

Figure 6.34 Waveform of PFD module

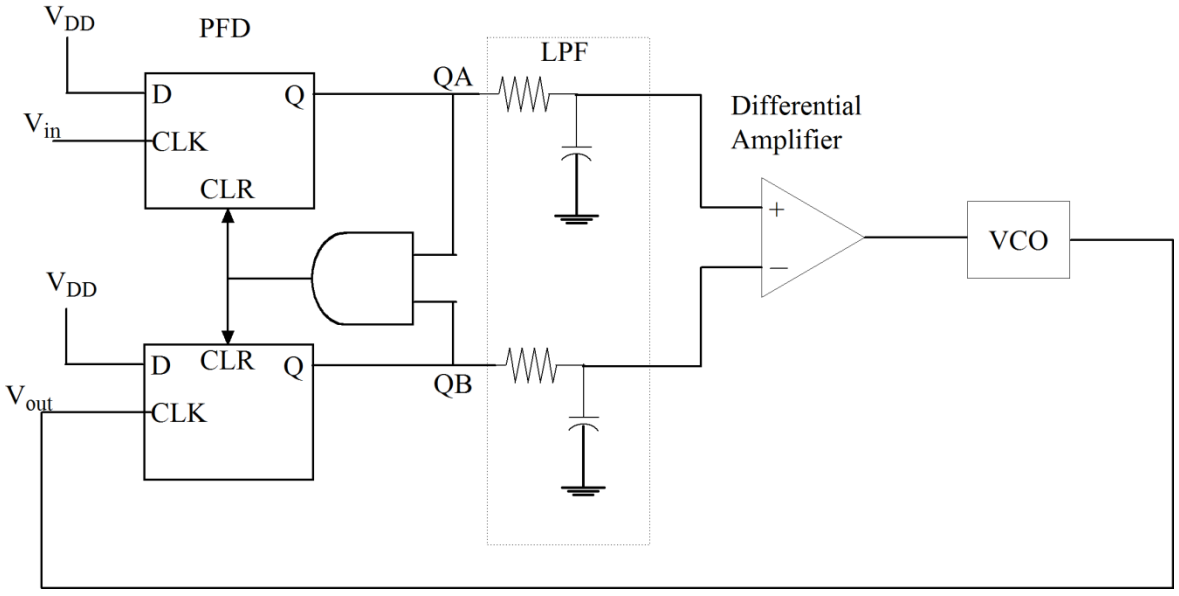

Figure 6.35 PLL module with PFD

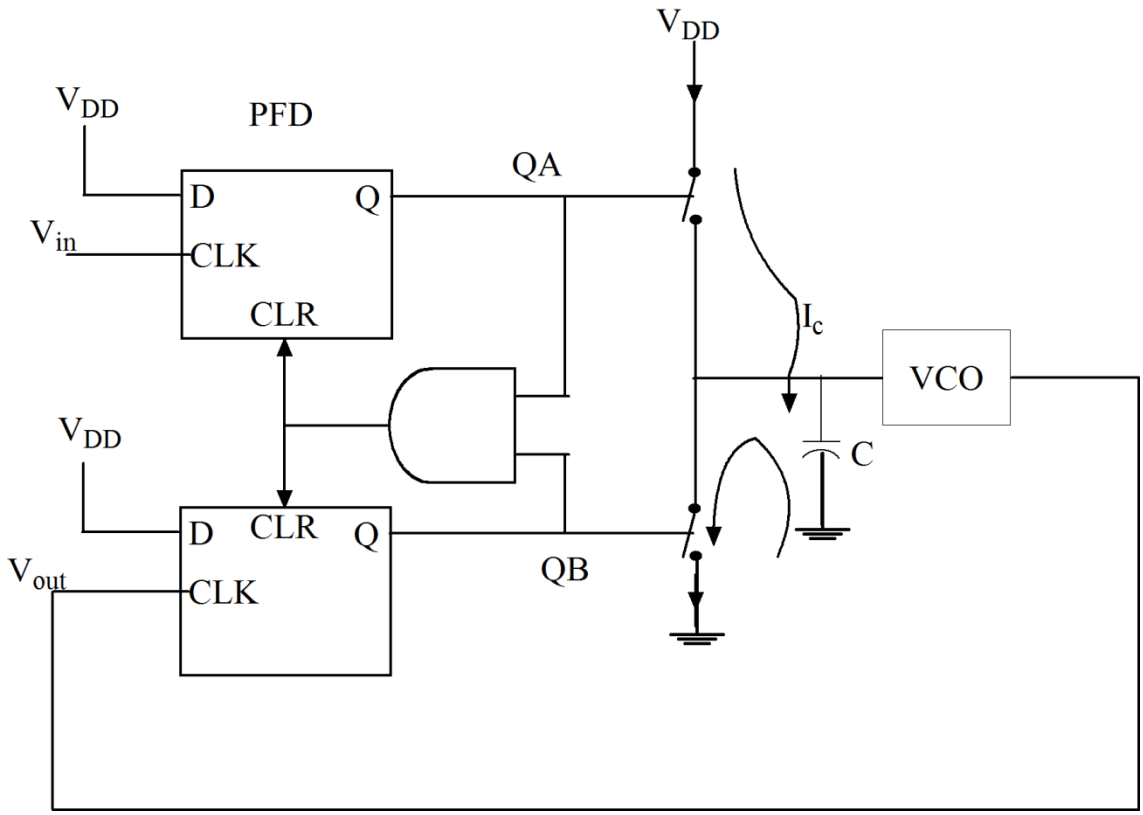

Figure 6.36 Charge pump PLL

6.3.4 Implementation and Results

The model of 500W, 8/6 pole, four phase SRM with split DC converter is used, as described in chapter 4, with the low frequency (1.6 KHz) PWM controller. The current peak detection stage is simulated for each phases as shown in Figure 6.13, which gives four individual peak detection pulses (PDP). Experimental results for the delay in peak detection instant are shown in Figure 6.18, recorded from real time hardware-in-loop (HIL) simulation approach. Figure 6.37 and Figure 6.38 show the waveform of current peak detection stage for the motor phase, at speeds 1300 rpm and 3500 rpm respectively. The waveforms clearly show that a delay is produced in peak detection instant at higher speed. The charge pump PLL is used with the counter to form a frequency divider feedback system. PLL outputs the multiple frequency pulse for the input of phase pulse. The gain of VCO is compensated for the motor speed using lookup table, providing fast tuning and wide speed range. Four separate counters count the multiple frequency pulse, outputs from the PLL. Each counter is reset by the peak detection pulse of respective phase. The rotor angle for each phase is derived from the individual count value using linear equation as shown in Figure 6.18, which is also compensated for the delay produced in peak detection instant. It gives individual rotor position for each phase. Commutation logic for each phase is derived from the rotor position of previously conducting phase. Commutation logic for the phase '2' is derived from the

estimated rotor position of the phase '1' as shown in Figure 6.39. Figure 6.40 shows the error in rotor position estimation at the constant speed of 1000 rpm.

Commutation pulse

Phase Current

Filtered phase current

Peak detection pulse

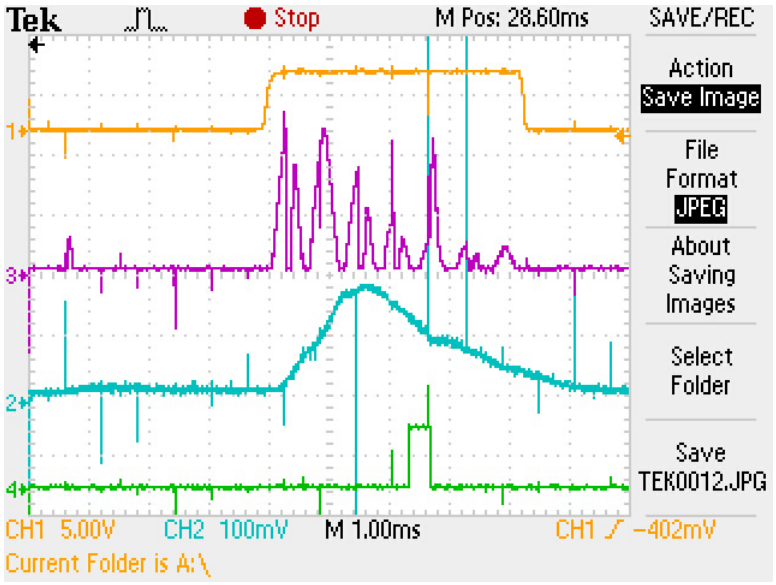

Figure 6.37 Peak detection pulse at 1300 rpm

Commutation pulse

Phase Current

Filtered phase current

Peak detection pulse

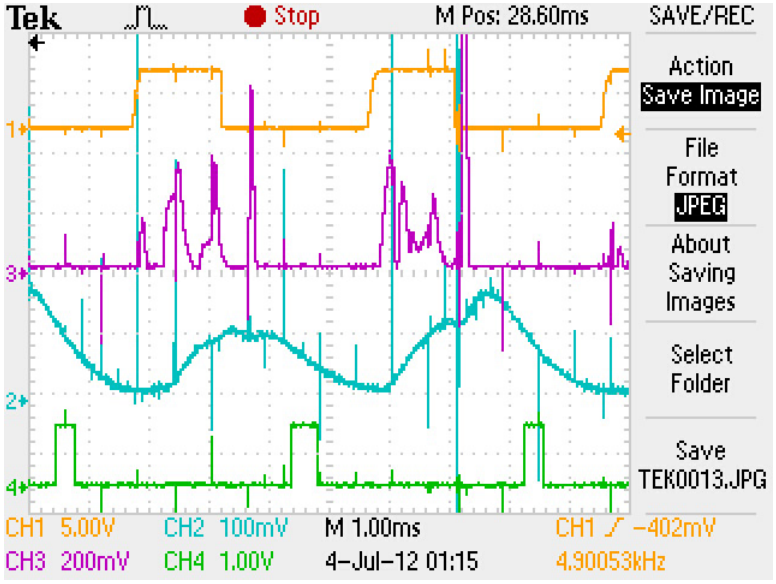

Figure 6.38 Peak detection pulse at 3500 rpm

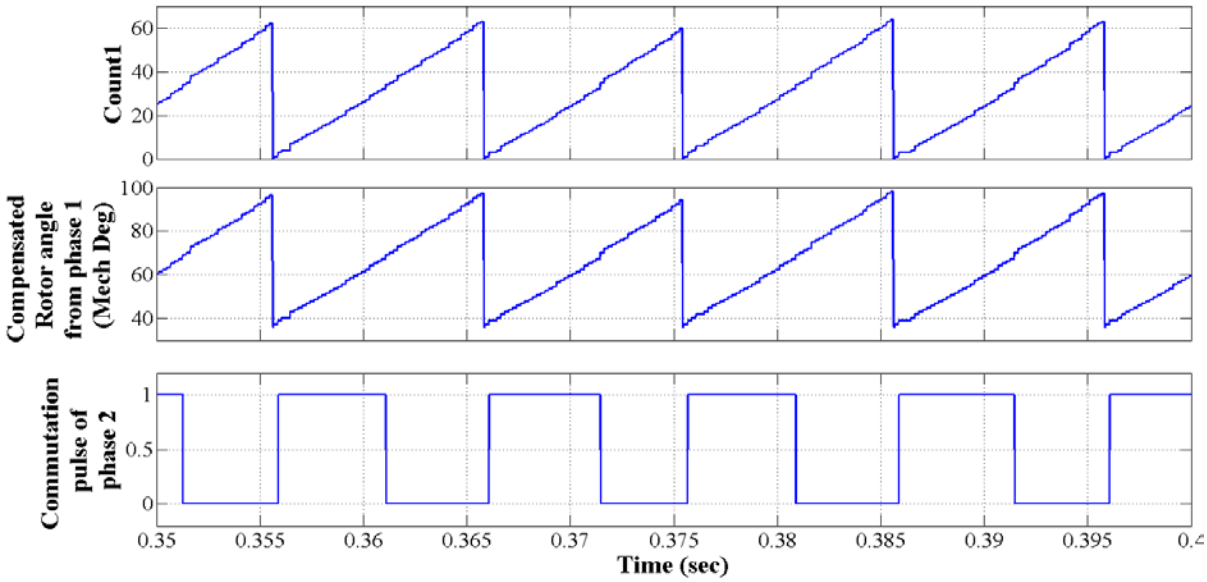

Figure 6.39 Rotor position estimation and commutation logic

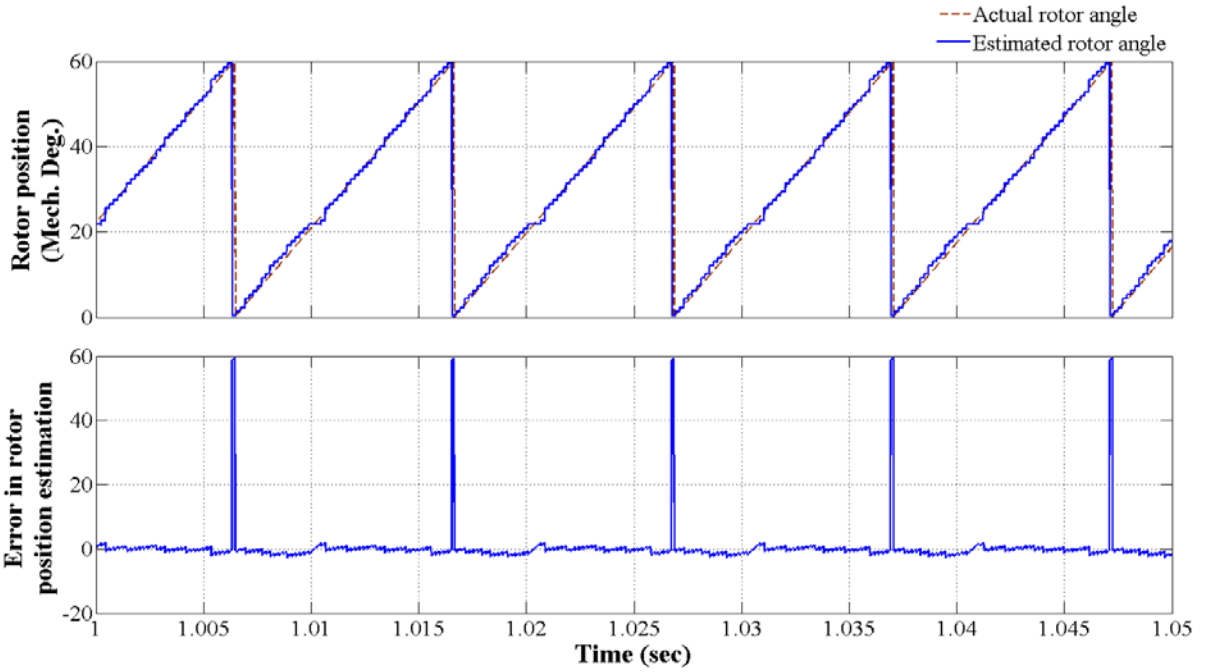

Figure 6.40 Error in rotor position estimation

Performance of the CGSM is investigated with the open-loop and closed-loop speed control scheme. A fixed angle control scheme is used for the initial startup with the turn ON angle of 22.5° and turn OFF angle of 52.5°. Ripples in the torque, PLL tuning and delay in the peak detection instant depend upon the speed of the motor, which deteriorates the dynamic performance of the CGSM with the openloop speed control system. On the other hand, rotor position can be estimated from the active phase only using this method, which makes it necessary to follow the rules derived to produce the commutation logic in section 6.2 of this chapter. Rotor position information derived from the phase is used to turn ON the next successive phase and to commutate the same phase. It limits the maximum possible

speed of the motor, even an error in rotor position estimation due to delay in peak detection instant is compensated for the speed. Maximum turn ON angle is restricted to 30° or less for the constant dwell angle of 30° to eliminate the negative torque production. Rotor angle represented by the previously conducting phase for the maximum turn ON angle is 45°, because each phase is lagging by 15°. The maximum possible speed for the maximum turn ON angle is 1700 rpm as shown in Figure 6.18. However, for the higher PWM frequency of 5 KHz, speed limit is also high i.e. 4500 rpm. Any further increase in the speed increases the effective turn ON angle, which results in negative torque production. It may lead the system towards instability. Any sudden change in speed or load torque also affects the stability of the system.

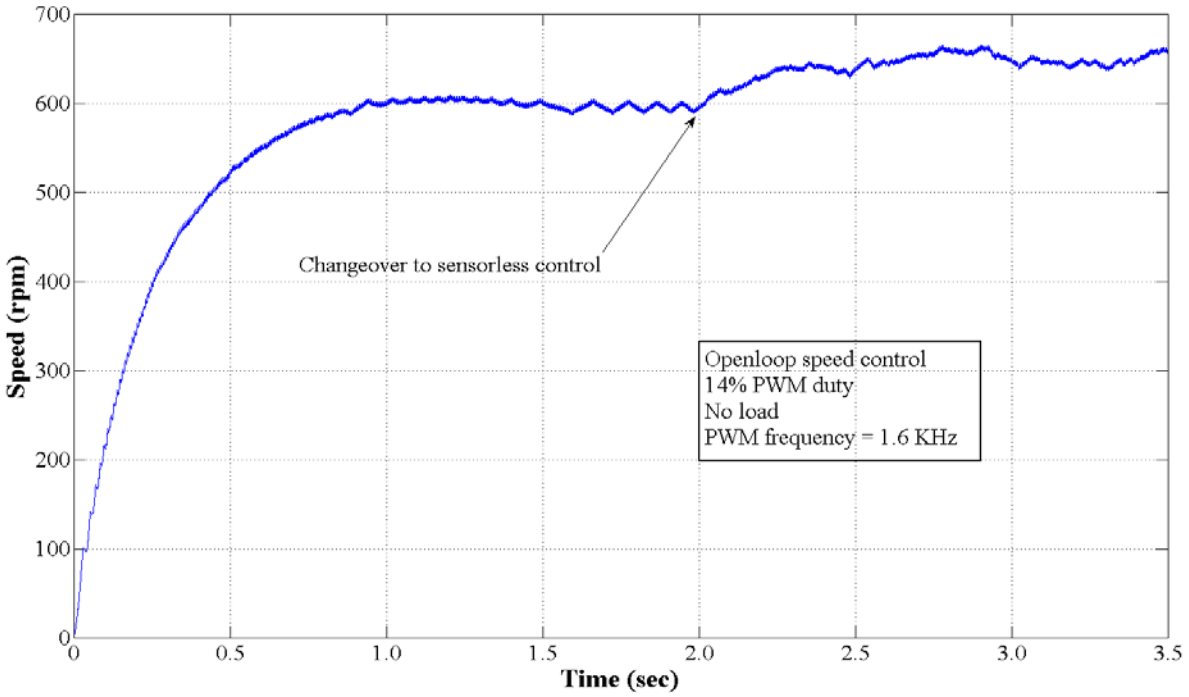

Figure 6.41 Open-loop performance of CGSM with 14% PWM duty

Performance of the sensorless method with the openloop speed control scheme is shown in Figure 6.41 to Figure 6.45. Both the advance angle and dwell angle are kept constant throughout. Changeover from the initial startup to the sensorless control makes sudden change in the motor speed due to the change in advance angle and dwell angle. The motor is started with the fixed angle position sensing arrangement and then changeover to the sensorless control with the same advance angle and dwell angle is shown in Figure 6.41. A small error in the rotor position estimation causes the transient in speed during the changeover to achieve the new steady state value. It is due to the reflection of error in calculation of turn ON and turn OFF angle. This error can easily be compensated during conversion of the estimated rotor angle into the phase commutation pulse to eliminate the speed transient during changeover. However, general method used for the initial startup is

feedforward method, in which train of pulses with the initial frequency is applied to the motor

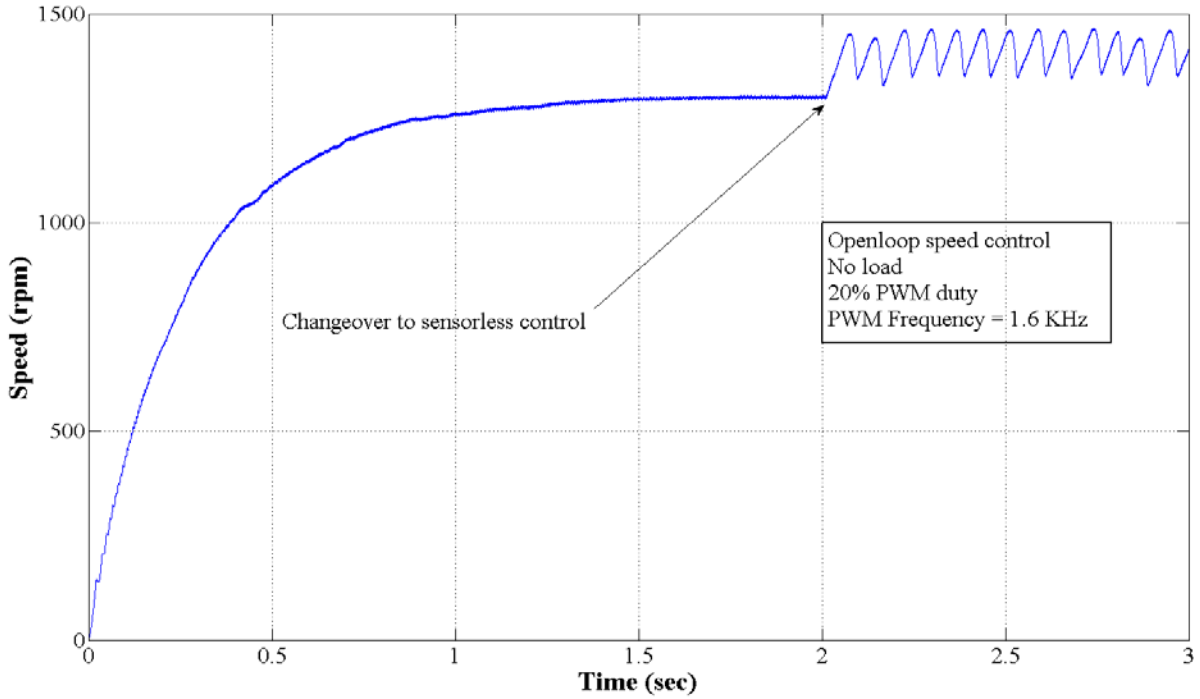

Figure 6.42 Open-loop performance of CGSM with 20% of PWM duty

with 100% PWM duty cycle. The frequency is increased linearly and the PWM duty cycle is reduced to speed-up the motor. The motor generates the enough torque to accelerate the speed, at which peak detection pulse can be detected. A turn ON angle and turn OFF angle both vary to a large extent during initial startup. Thus motor always experiences a transient in the speed during changeover, even with the general startup method. With the fixed turn ON angle of 22.5°, maximum speed of 1200 rpm can be achieved without change in the turn ON angle. This case is shown in Figure 6.41 where changeover takes place at a speed of 600 rpm with the PWM duty cycle as 14% throughout. Here, increase in speed is observed due to change in the advance angle during changeover. At the higher speed, increase, both in the turn ON angle and turn OFF angle, is proportional to the speed of the motor, even if advance angle and dwell angle are fixed. The case is shown in Figure 6.42, where changeover takes place at the speed of around 1300 rpm with the PWM duty cycle of 20%. Here, increase in speed is observed, but at that time speed is oscillating because both the advance angle and the dwell angle are varying with the speed. At a higher speed, turn ON angle increases and reach near 30° or even higher, which produces the negative torque. It limits the motor speed to increase further with the sensorless method. The case is shown in Figure 6.43 where changeover takes place at a speed of 1900 rpm with the PWM duty cycle of 33%. Speed is reduced and oscillates around 1600 rpm, nevertheless it could be much higher with the position sensing scheme (initial startup scheme) compared to sensorless method with the same advance angle and PWM duty cycle. Figure 6.44 shows the case of

changeover to the sensorless method with load torque of 0.1 N-m. Dynamic response of the system is shown in Figure 6.45 with change in PWM duty cycle. However, large change in PWM duty cycle or load torque results in loss of stability of CGSM with the open-loop speed control system.

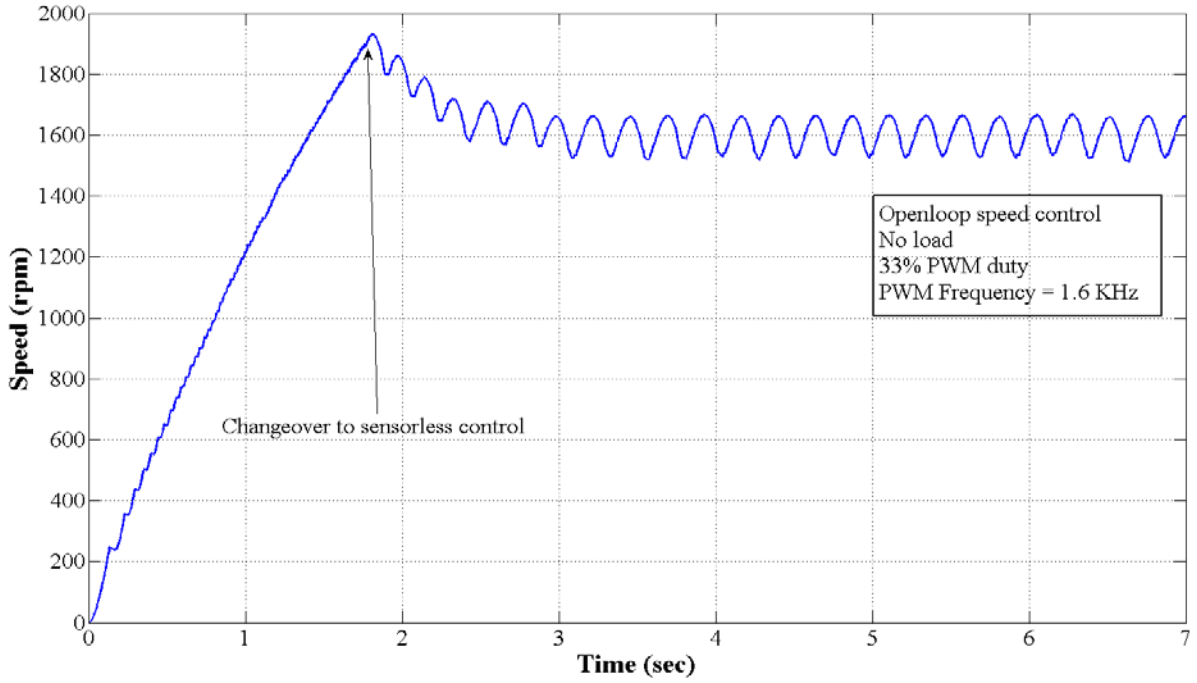

Figure 6.43 Open-loop performance of CGSM with 33% of PWM duty

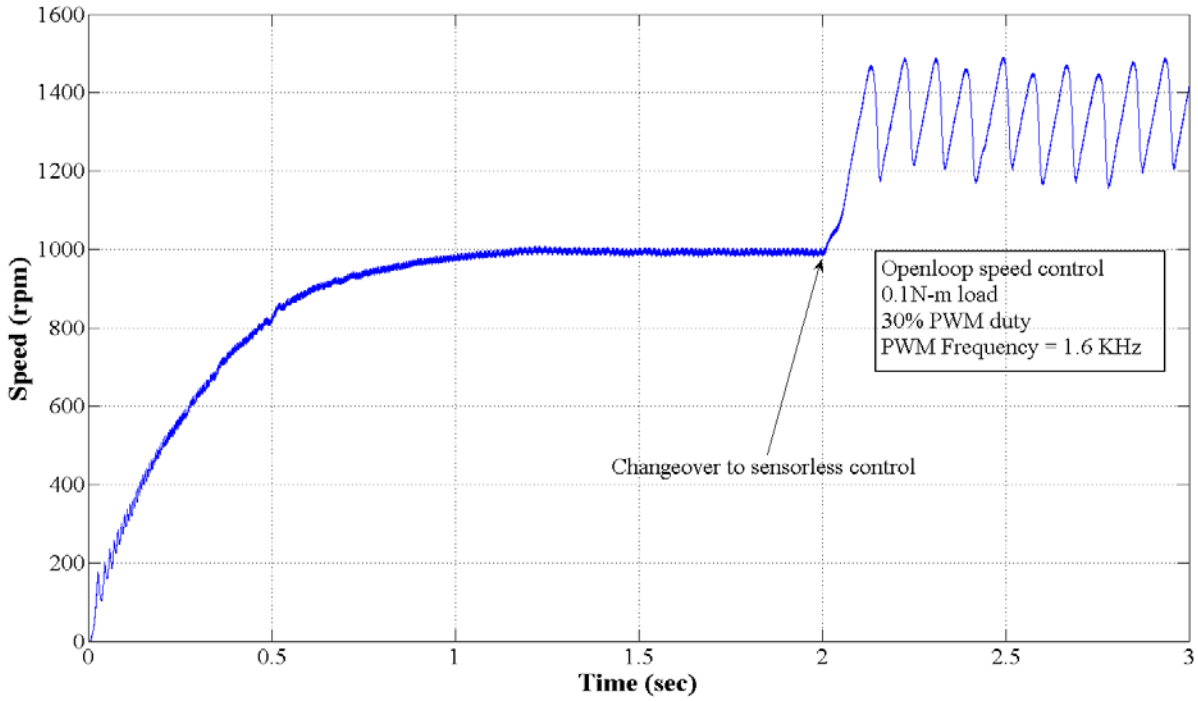

Figure 6.44 Open-loop performance of CGSM with 30 % of PWM duty and 0.1 N-m load

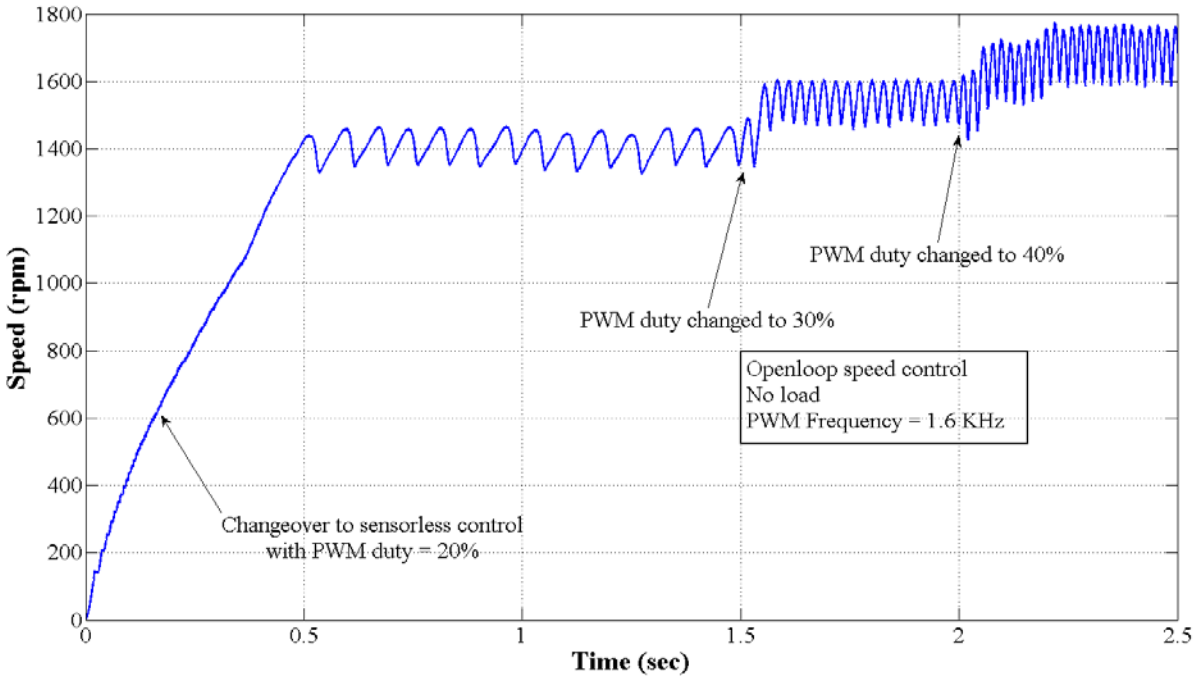

Figure 6.45 Open-loop performance of CGSM with varying PWM duty

Performance of the CGSM with closed-loop speed control system is shown in Figure 6.46 to Figure 6.49. The speed PI controller adjusts the PWM duty cycle to compensate for the error in speed, from initial startup to the sensorless operation. It is because the speed controller compensates the change in speed during changeover by adjusting the PWM duty cycle. Figure 6.46 shows the changeover to the sensorless method with no-load and with load torque of 1 N-m respectively. Transient response to a load torque step of 0.2 N-m is shown in Figure 6.47. PWM duty cycle is adjusted by the speed PI controller, and it compensates the effect of load change. Transient response to a speed step of 200 rpm is shown in Figure 6.48 with no-load and with the load torque of 0.2 N-m. The analysis of the results shows that the steady state as well as dynamic response of the CGSM is better with the closed-loop speed control scheme. However higher speed limit, imposed due to the negative torque production, still remains with the closed-loop speed controller. Figure 6.49 shows the transient response to a speed change from 1300 rpm to 1400 rpm. The turn ON angle is nearer to 30° with the constant dwell angle, therefore it produces negative torque. It results in average torque reduction, which reduces the motor speed. At the same time PI speed controller increases the PWM duty cycle to maintain the constant speed. But, with the increases in PWM duty cycle, negative torque magnitude also increases, which results in speed dip and oscillation. Reduction in the efficiency and speed oscillation restricts the high speed operation.

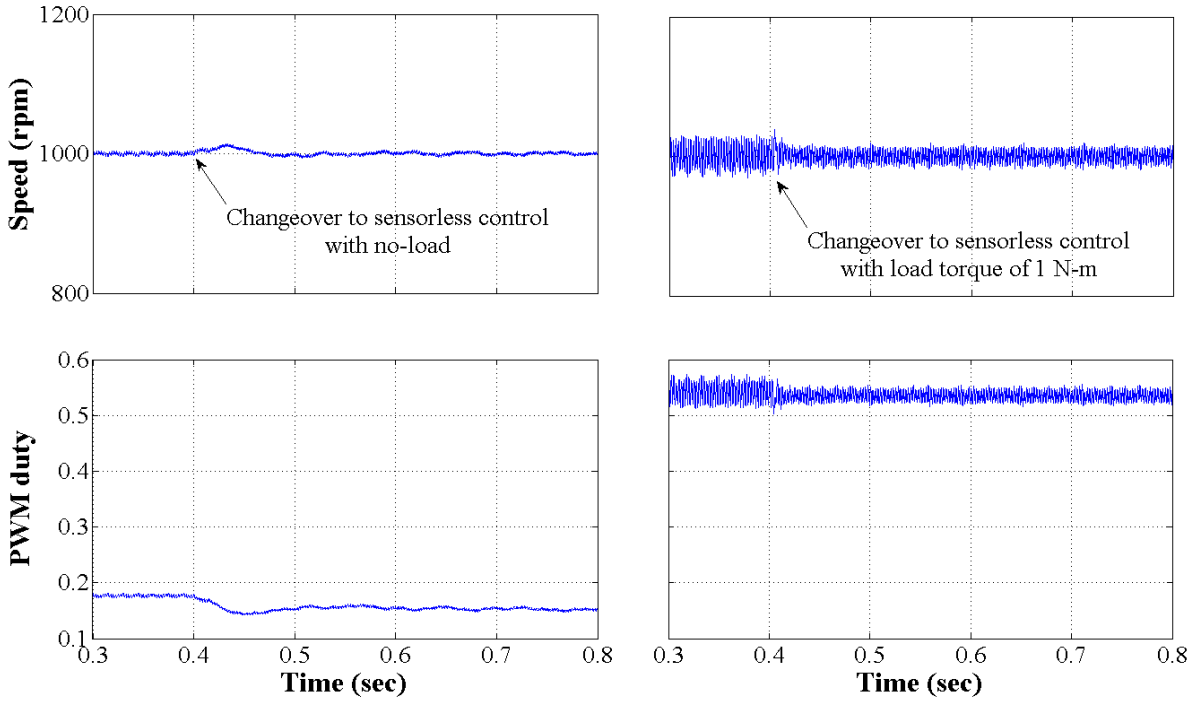

Figure 6.46 Closed-loop performance of CGSM with no-load

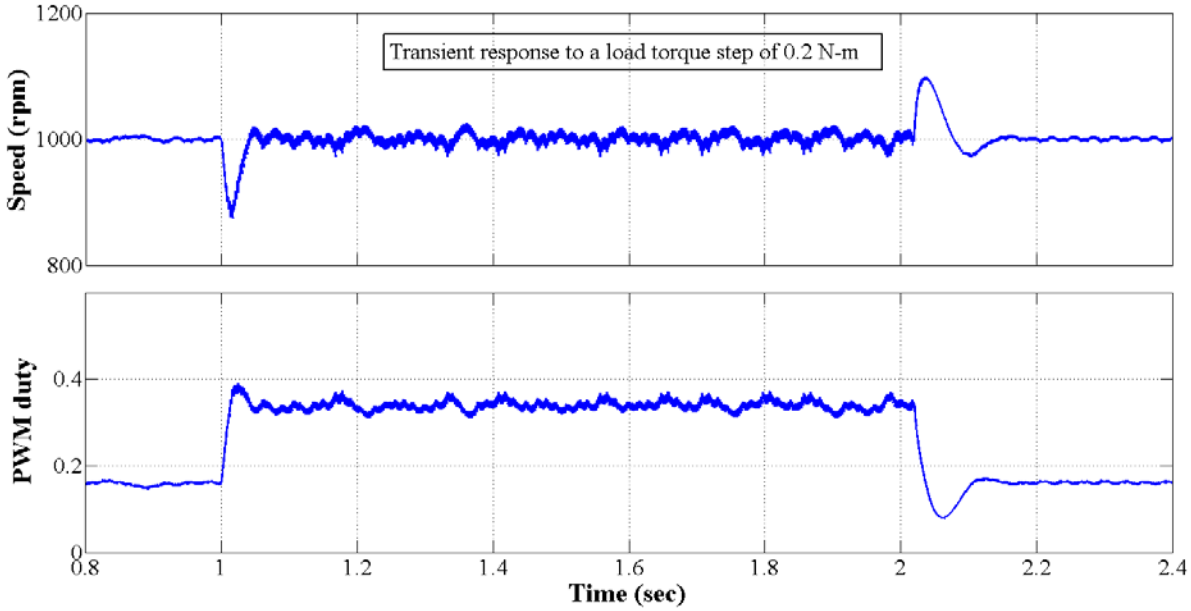

Figure 6.47 Closed-loop performance of CGSM for load transient

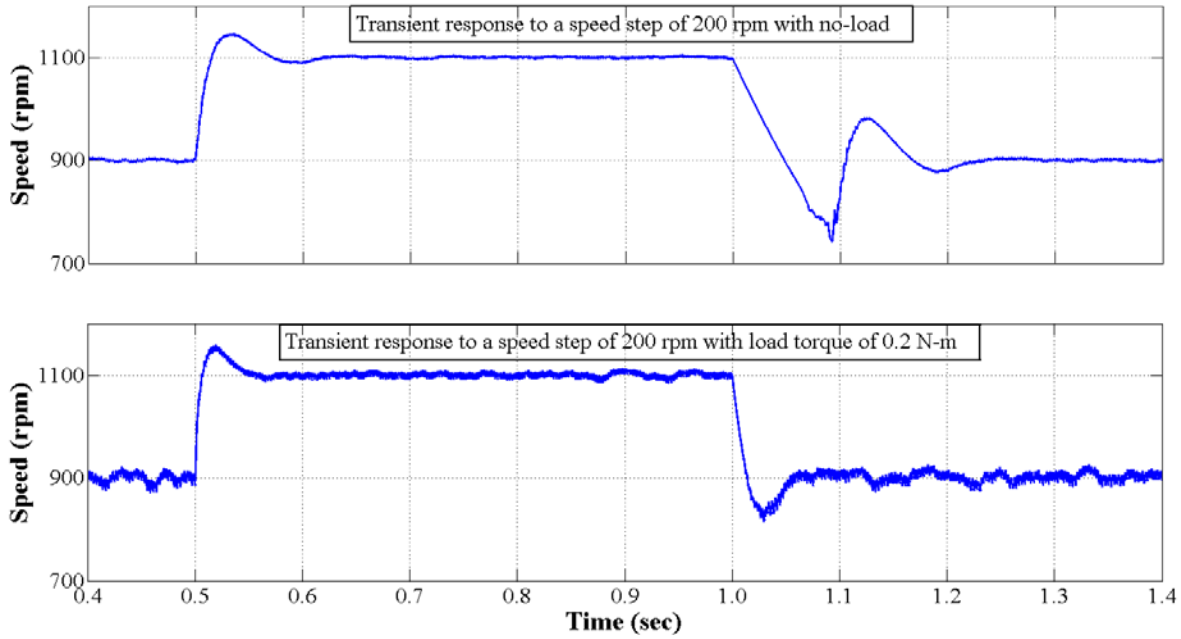

Figure 6.48 Closed-loop performance of CGSM for speed transient at no-load

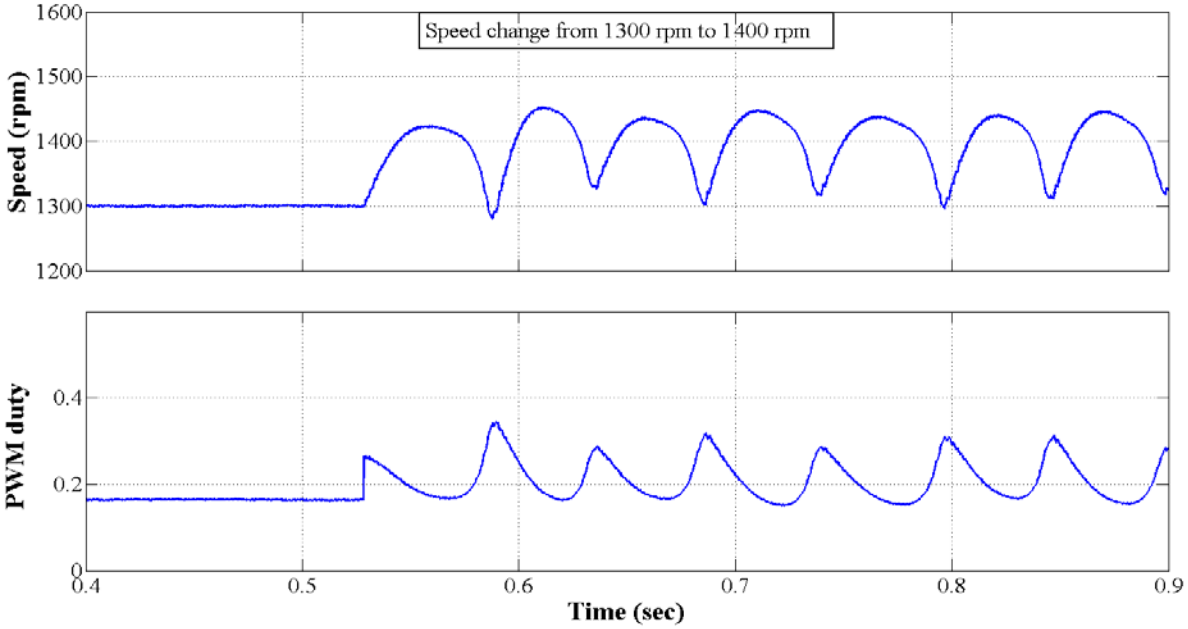

Figure 6.49 Closed-loop performance of CGSM at higher speed

Simulation and experimental results confirm the theory and prove the concept of the CGSM. Guidelines for the practical implementation of the CGSM are prepared from the results of investigation. It covers design and performance issues along with the summary of basic requirement and limits and are as under -

- ✓ Method is applicable with PWM voltage control scheme.
- ✓ No prior knowledge of motor parameters is required except the pole configuration.

- ✓ Indeed, it estimates one rotor position per phase, while PLL position interpolation is used to derive intermediate rotor angle.
- ✓ Implementation requires only few Op-amp, resistors and capacitors.
- ✓ Low-pass filter is not necessary for single pulse operation
- ✓ Feasibility with both closed-loop as well as open loop speed controller.
- ✓ Closed-loop speed control system remains stable with speed as well as torque transient.
- ▪ It is required to incorporate any initial startup method with CGSM.
- ▪ PWM frequency limits the upper speed due to delay produced in peak detection pulse by filter.
- ▪ Oscillations in higher speed are observed with open-loop speed control system, due to variation in turn-ON and turn-OFF angle.
- ▪ Open-loop speed control system is unstable for the torque transient.
- ▪ Closed-loop speed control system does not remain stable for the large transient in speed or torque. This is due to negative torque production at the higher turn ON angle and error produced due to delayed tuning of PLL.

Overall the implementation of the CGSM is quite challenging, particularly with the low frequency PWM controller as compared to the high frequency PWM controller.

6.4 MODIFIED CURRENT GRADIENT SENSORLESS METHOD

A new CGSM is proposed particularly for the low frequency PWM controller, called modified current gradient sensorless method (MCGSM). It eliminates the use of PLL from the commutation stage and improves the stability of the system.

6.4.1 Design principle of MCGSM

Proposed MCGSM differs with the conventional CGSM in the design of current peak detection stage and the method used to produce the commutation logic. Basic block diagram of the speed control system with the MCGSM is same as shown in Figure 6.3. Block diagram of MCGSM is shown in detail in Figure 6.50. Sensorless scheme for only one phase is shown, for the convenience, while it is used for each phase current to derive individual phase commutation pulse. In the conventional method, PLL is used to produce train of multiple frequency pulses from the peak detection pulse, which produces intermediate rotor position, and then phase commutation pulse is derived from continuous rotor position. Proposed method eliminates requirement of PLL or any other frequency multiplying techniques. Details of current peak detection stage and commutation logic are described as below;

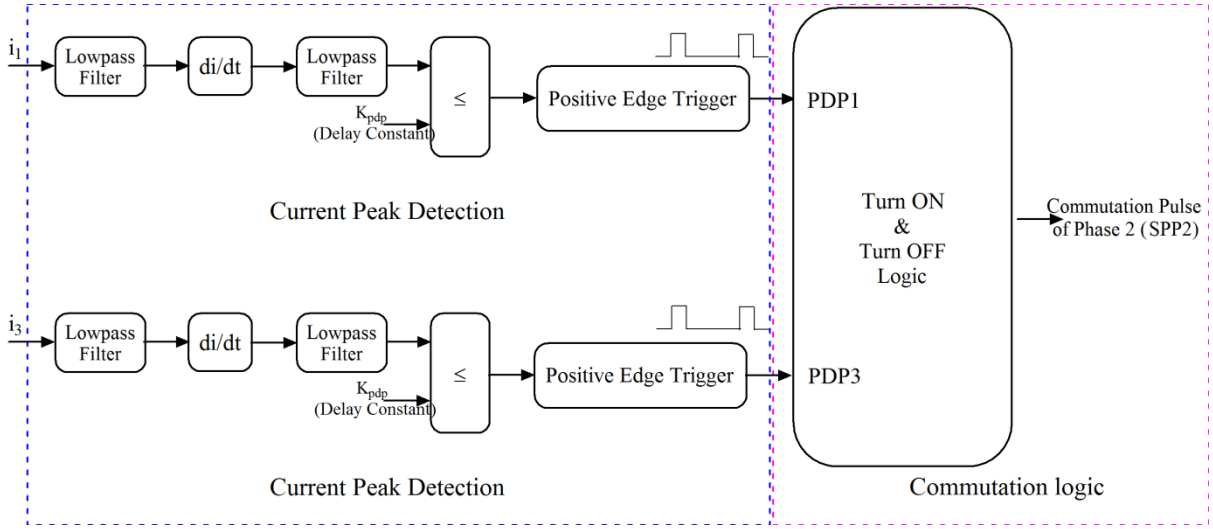

Figure 6.50 Block diagram of MCGSM

6.4.1.1 *Current peak detection*

Process of current peak detection involves obtaining one pulse per stroke at the instant of current peak and it is same as in conventional CGSM. However, filter adds a delay in peak detection instant which is more prominent for the low frequency PWM controller. Proposed method takes advantage of delay produced in current peak detection to derive commutation logic, rather than compensating for error. ZCD of the conventional current peak detection stage is replaced by the comparator. Further, the delay in peak detection instant can be introduced by varying delay constant (K_{pdp}) of the comparator. Waveform for the current peak detection stage is shown in Figure 6.16 where K_{pdp} is zero, while it is apparent that more negative value of K_{pdp} adds more delay in peak detection instant.

6.4.1.2 *Commutation logic*

Commutation logic generates an individual phase commutation pulse to ensure the torque production in the positive direction. Phase commutation pulses are derived directly from the peak detection pulse in the MCGSM. Consider a Figure 6.51 which shows a phase commutation and peak detection pulse of the each phase with K_{pdp} = 0, while motor is running with the constant turn ON angle of 22.5° and turn OFF angle of 52.5° at the constant speed of 1300 rpm. Assuming constant motor speed, PDP of the active phase decides turn ON instant of the next successive phase, and PDP of the same successive phase decides turn OFF instant of the previously conducting phase. As shown in Figure 6.51, PDP1 turns ON phase-2, while PDP2 turns OFF phase-1. Figure 6.50 shows the commutation process of the phase-2 where PDP1 turns ON phase-2, and PDP3 turns it OFF. Phase commutation pulses from the sensorless operation are compared with the commutation pulse from the fixed position sensing arrangement in Figure 6.52. Delay in peak detection instant is a

function of speed which results in variation of advance angle with the motor speed. Advance angle is inversely proportional to the motor speed, thus both turn ON and turn OFF angles increase with the speed. Maximum and minimum turn ON angles are bound to 30° and 20° respectively to ensure the positive average torque. Measured commutation angles for the simulation and experimental results are plotted in Figure 6.53 and Figure 6.54, respectively.

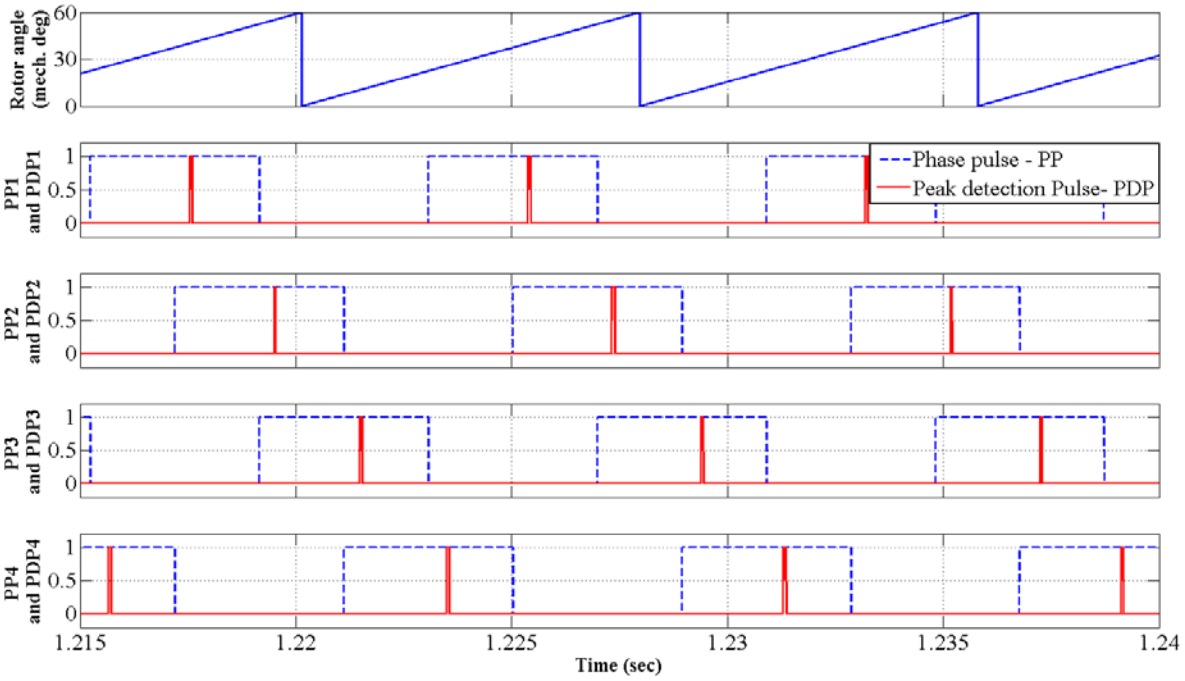

Figure 6.51 Phase pulse and peak detection pulse

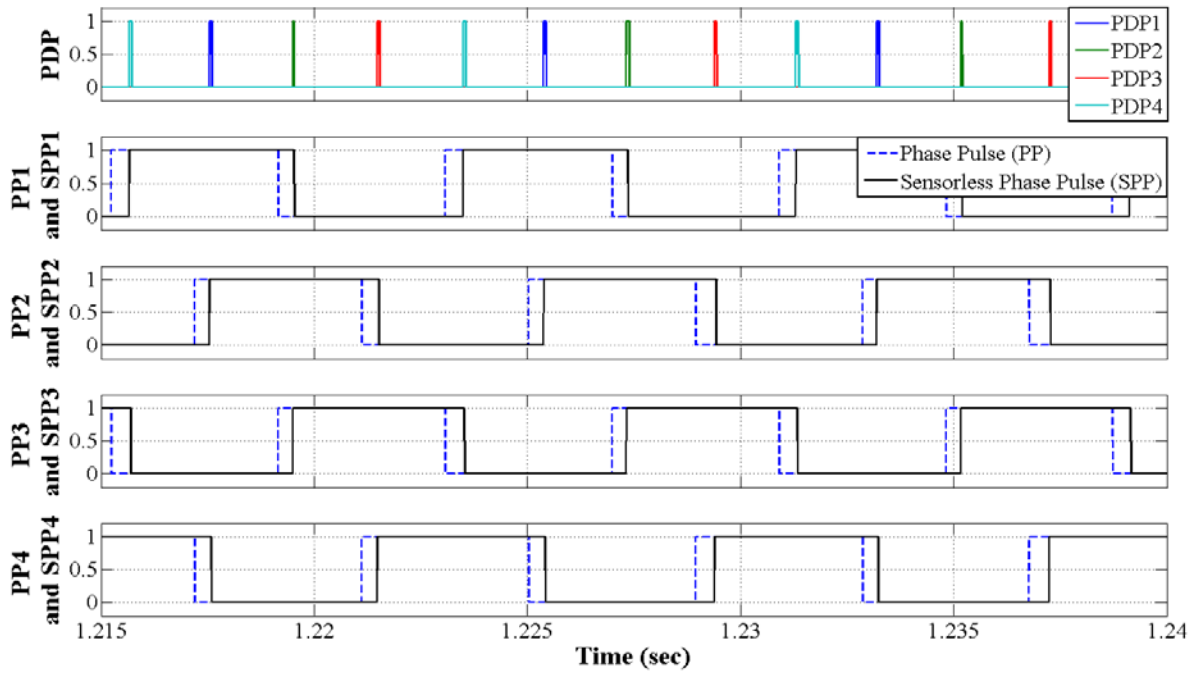

Figure 6.52 Commutation logic from peak detection pulse

Effect of angle variation on the motor speed can be controlled by controlling PWM duty cycle with the closed-loop speed controller; however it needs to compensate this effect with the open-loop speed controller. Even with the closed-loop speed controller, motor speed is bound for the uncompensated commutation angle. Effect of angle variation can be compensated by controlling delay constant K_{pdp}. Consider a phase -2 where PDP1 decides turn ON instant, which is bound by upper and lower limits. Reflected upper and lower limits for the PDP of phase 1 become 45° and 35° respectively, which decide range of peak detection pulse. Ideally PDP represent rotor angle of 30°, while in practice delay is added by the filter which is proportional to the motor speed. In general, it is required to add a minimum delay even at very low speed, which can be accomplished by reducing K_{pdp}; however, it is not applicable for the case of low frequency PWM controller. The delay factor K_{pdp} can be set constant to achieve optimum angle with the closed-loop speed controlled, constant speed drive applications. Effect of load torque can be neglected to map a linear relation between K_{pdp} and motor speed, to compensate variation in commutation angle to some extent, for the variable speed drive application demands wide speed range of operation. Variation of commutation angles for high frequency (5 KHz) PWM controller is shown in Figure 6.55. Both the upper and lower speed limits are higher compared to low frequency PWM controller. Thus additional delay must be added to the peak detection instant at low speed even with the constant speed drive.

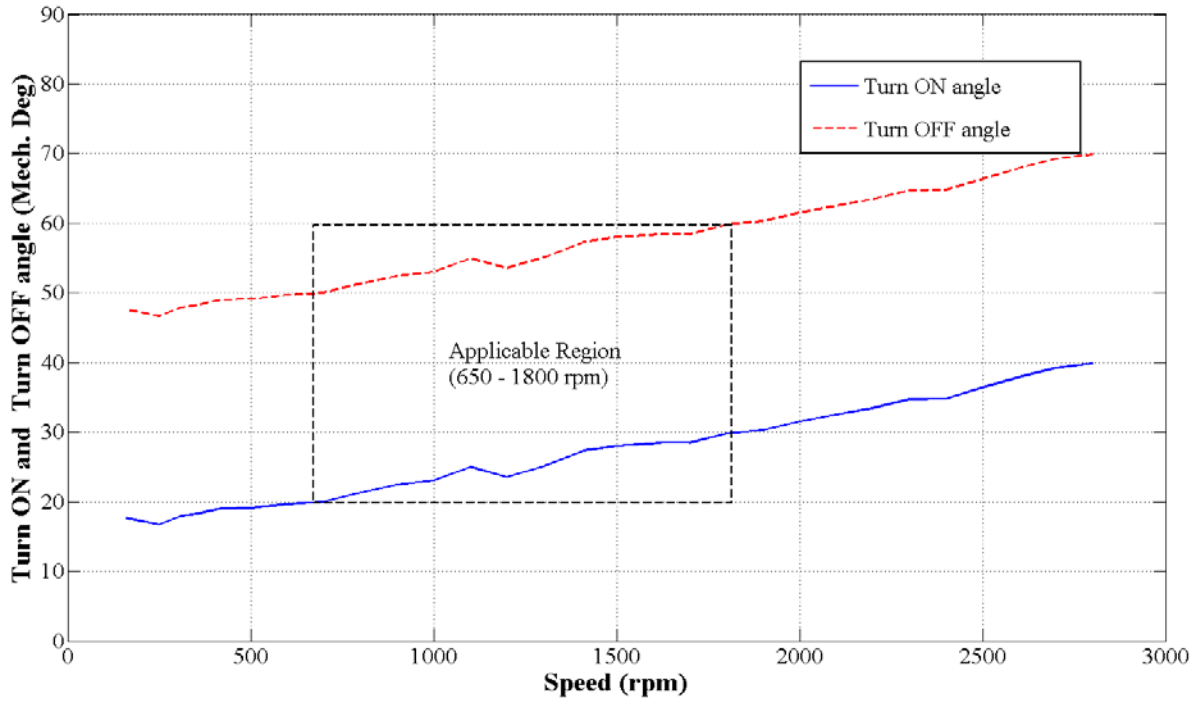

Figure 6.53 Variation of commutation angle with motor speed (Simulation)

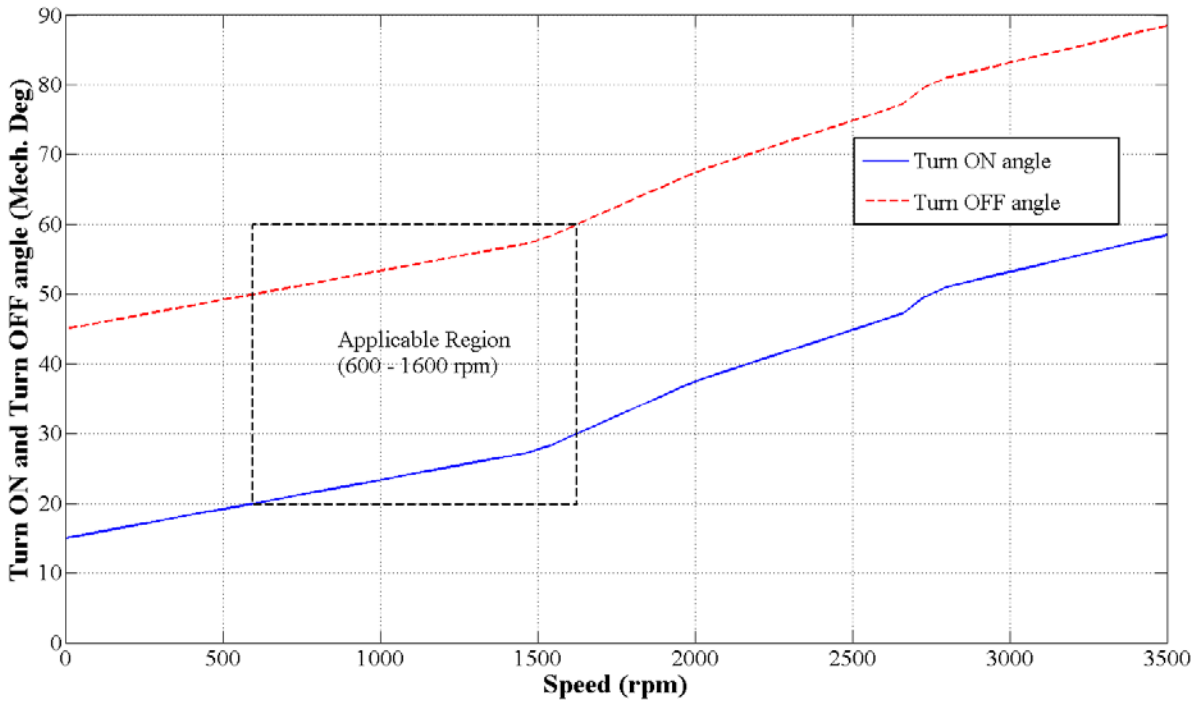

Figure 6.54 Variation of commutation angle with motor speed (Experimental)

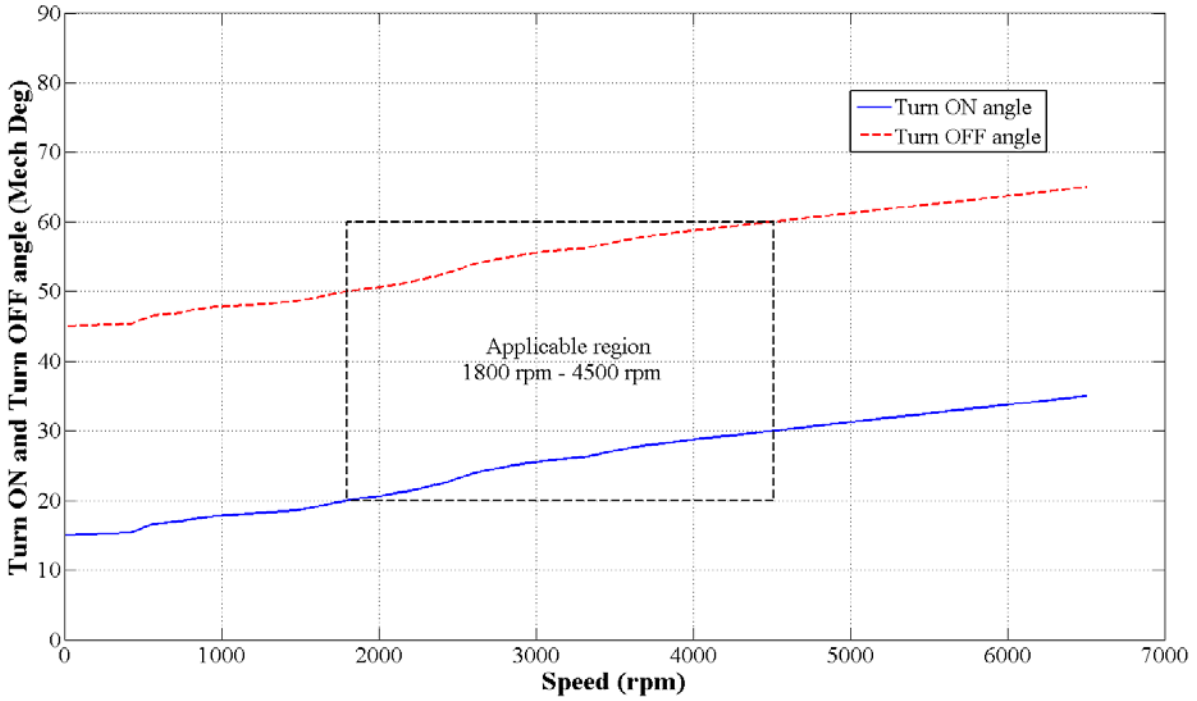

Figure 6.55 Variation of commutation angle with PWM frequency of 5 KHz (Simulation)

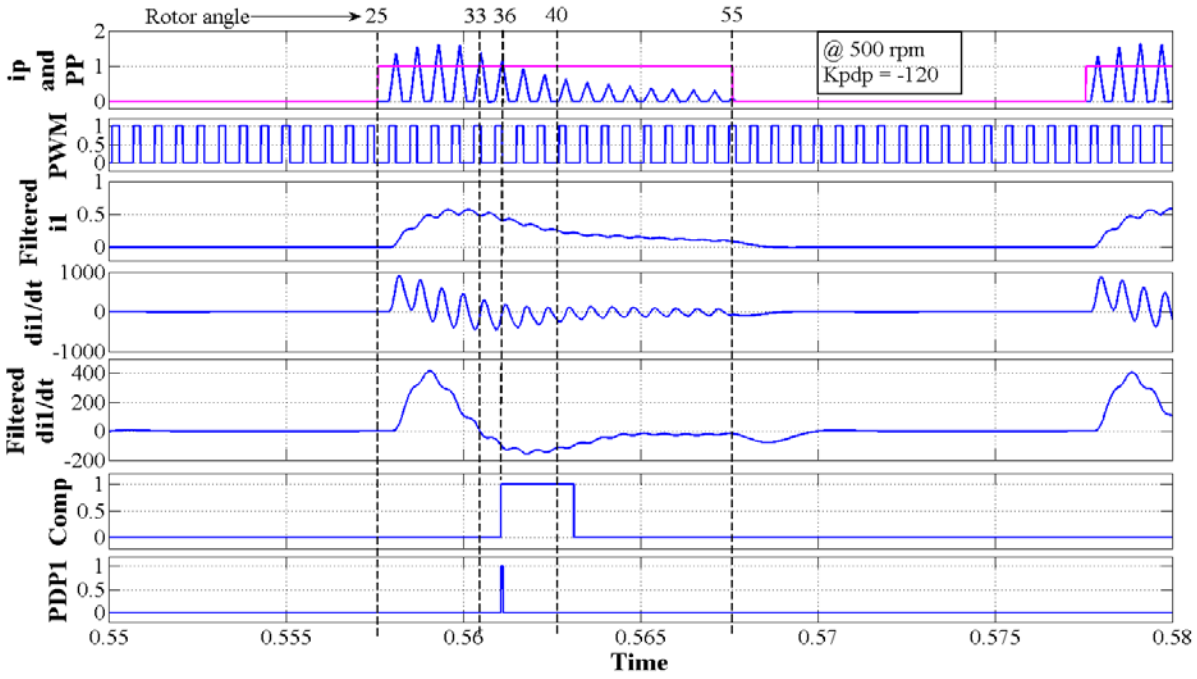

(a)

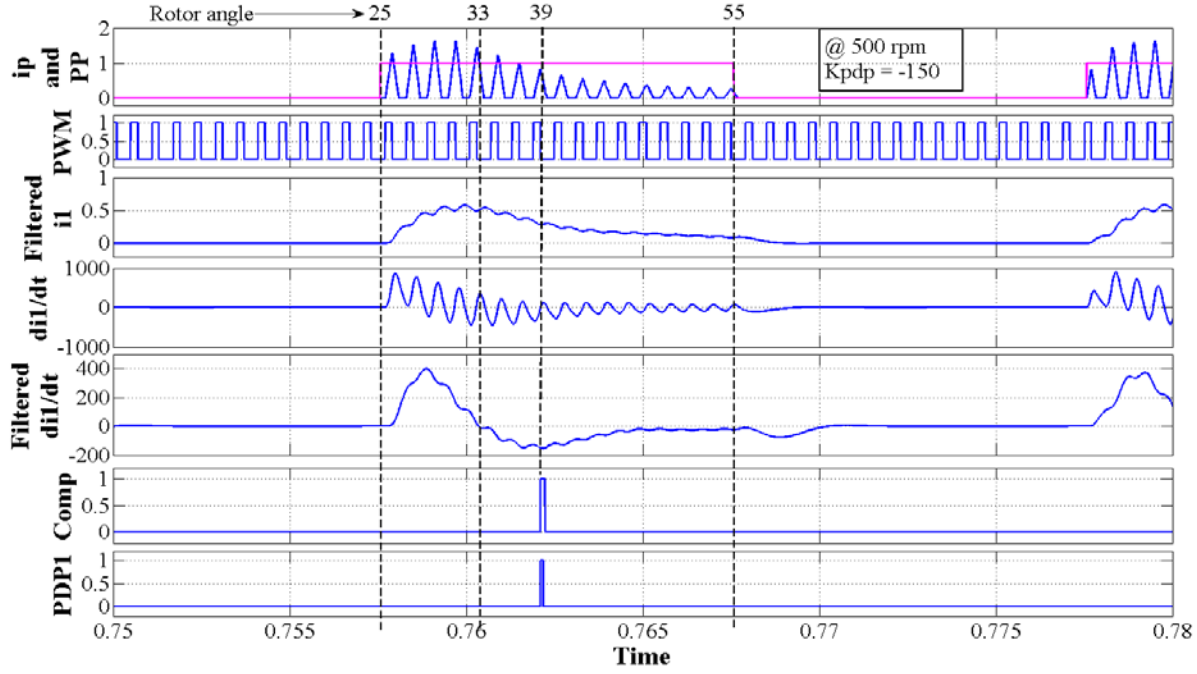

(b)

Figure 6.56 Waveform of peak detection stage at the motor speed of 500 rpm (a) K_{pdp} = – 120 and (b) K_{pdp} = – 150

MCGSM is also able to perform with the K_{pdp} = 0 or say, with ZCD instead of comparator to complete a peak detection stage for the limited speed bandwidth and with the compromised efficiency. The delay factor K_{pdp} can be designed to set optimum angle to improve efficiency for the constant speed drive applications, while for the variable speed drive application, K_{pdp} can be linearized for a limited speed band to improve the efficiency. It

reduces a large variation in commutation angle with motor speed, to a constant narrow bandwidth of 1° to 3°, which can be treated as nearly constant commutation angle, as desired. However, large variation in load torque affects bandwidth of commutation angle. The delay factor K_{pdp} can be represented as-

$$K_{pdp} = K_{ca} \times N_s + K_0 \qquad (6.72)$$

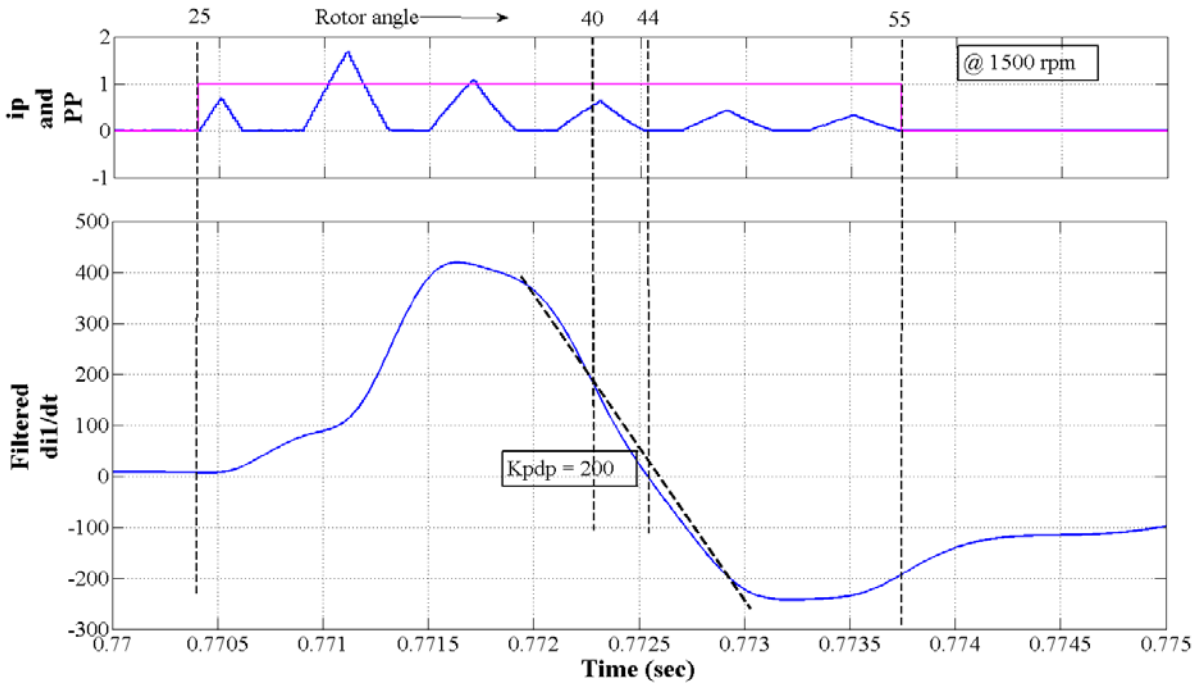

Figure 6.57 Rate of change of current at the speed of 1500 rpm

Particular commutation angle, where 'K_{ca}' is the constant, depends on the required commutation angle, 'N_s' is the motor speed in rpm and 'K_0' is the initial constant. Consider a case of constant commutation angle with the turn ON angle of 25° and constant dwell angle of 30°, shown in Figure 6.56. It shows waveform of entire peak detection stage for phase-1 at a speed of 500 rpm. Ideally, the PDP1 should represent a rotor angle of 40° to maintain a constant turn ON angle of 25°, because it decides turn ON instant of phase-2. However, the turn ON instant is 33° for the K_{pdp}=0 (ZCD), which demands reduced value of K_{pdp}, to maintain the PDP1 to 40°. The PDP1 reflects an angle of 36° for the K_{pdp} = -120, while it is 39° for maximum possible delay factor of K_{pdp} = -150, as shown in Figure 6.56. It is required to reduce a delay in PDP at higher motor speed, to maintain PDP1=40° as shown in Figure 6.57, which can be fulfilled by increasing the K_{pdp}. The PDP1 reflects an angle of 44° for the K_{pdp} = 0, at the motor speed of 1500 rpm, which reduces to 40° at the K_{pdp} = 200, as shown in Figure 6.57. The delay factor K_{pdp} can be linearized as shown in Figure 6.58 from the measured values. However, it is quite difficult to map nonlinearity among K_{pdp}, phase current and motor speed. The MCGSM is intended to be incorporated with low cost PWM controlled drive, therefore, it is preferable to allow a small variation in commutation angle which

reduces a computation burden and implementation cost, nevertheless efficiency is not optimized. Implementation and results for the MCGSM with and without compensation of commutation angle are explained in next section for the open-loop as well as closed-loop speed controller.

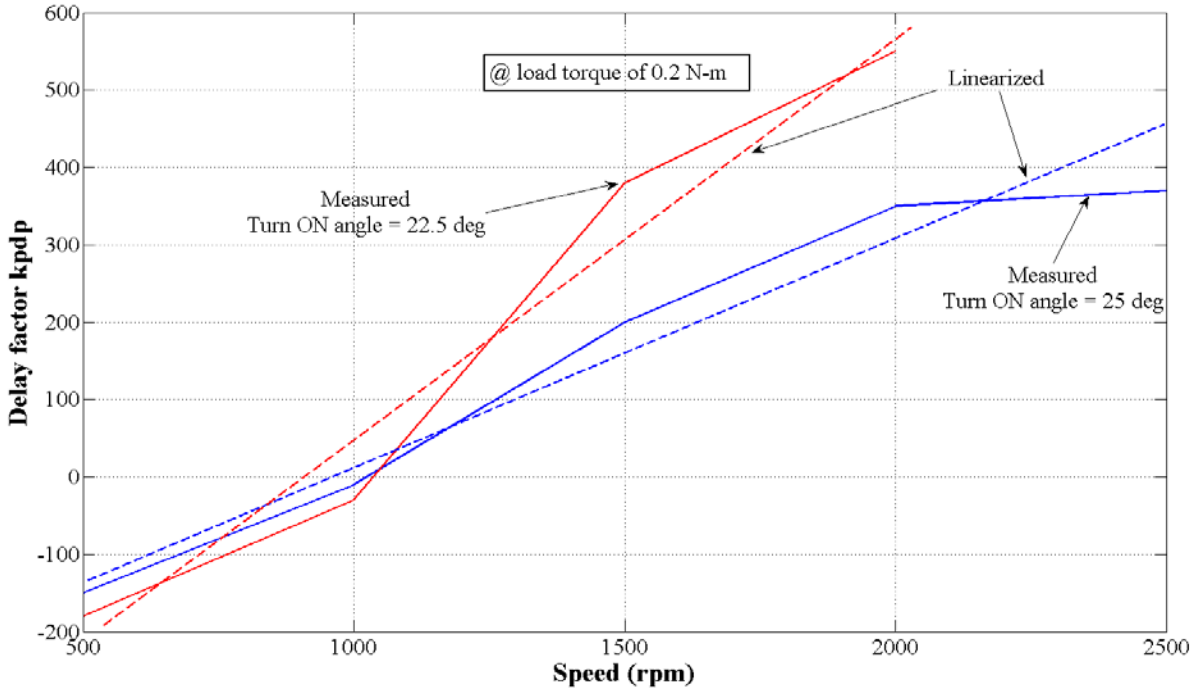

Figure 6.58 Variation in delay factor K_{pdp} with motor speed

6.4.2 Implementation and Results

Prototype model of MCGSM with 500 W, four phase SRM, split DC converter and low frequency PWM controller is developed. The transitions from the initial startup to the sensorless control with the open-loop control and with no compensation in commutation angle are shown in Figure 6.59 and Figure 6.60. The torque developed by motor during transition should be greater than the load torque. It might be possible that the torque developed with the initial startup method is higher than that of the sensorless method for the same speed as well as constant PWM duty cycle, and it is because of the difference in commutation angle. However, the torque can be increased by increasing the PWM duty cycle during the transition if required. Consider the case shown in Figure 6.59, where transition takes place at a speed of 880 rpm and with the constant duty cycle of 20% at no-load. It shows the transition from fixed commutation control (θ_{on} = 22.5°) to the variable commutation angle scheme (θ_{on} proportional to speed) with the constant dwell angle and duty cycle. It is evident that, average torque becomes more at the instant of transition, which increases the motor speed. This variation in θ_{on} with the motor speed results in the stable oscillatory behavior of the speed. Figure 6.60 shows the operating condition when the motor torque becomes less than the load torque just after the transition, which reduces the average

torque and motor speed. The turn ON and the turn OFF angles both reduce with the reduction in motor speed which increasingly reduces the average motor torque. However, stable

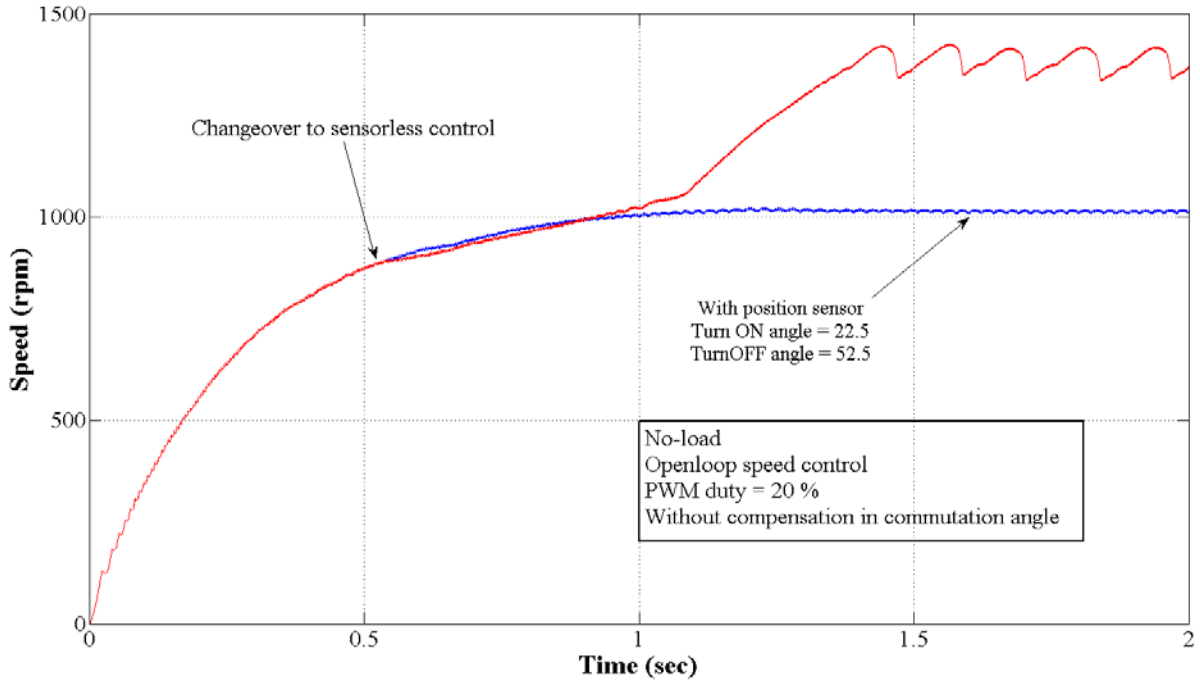

Figure 6.59 Changeover to sensorless control at the speed of 880 rpm

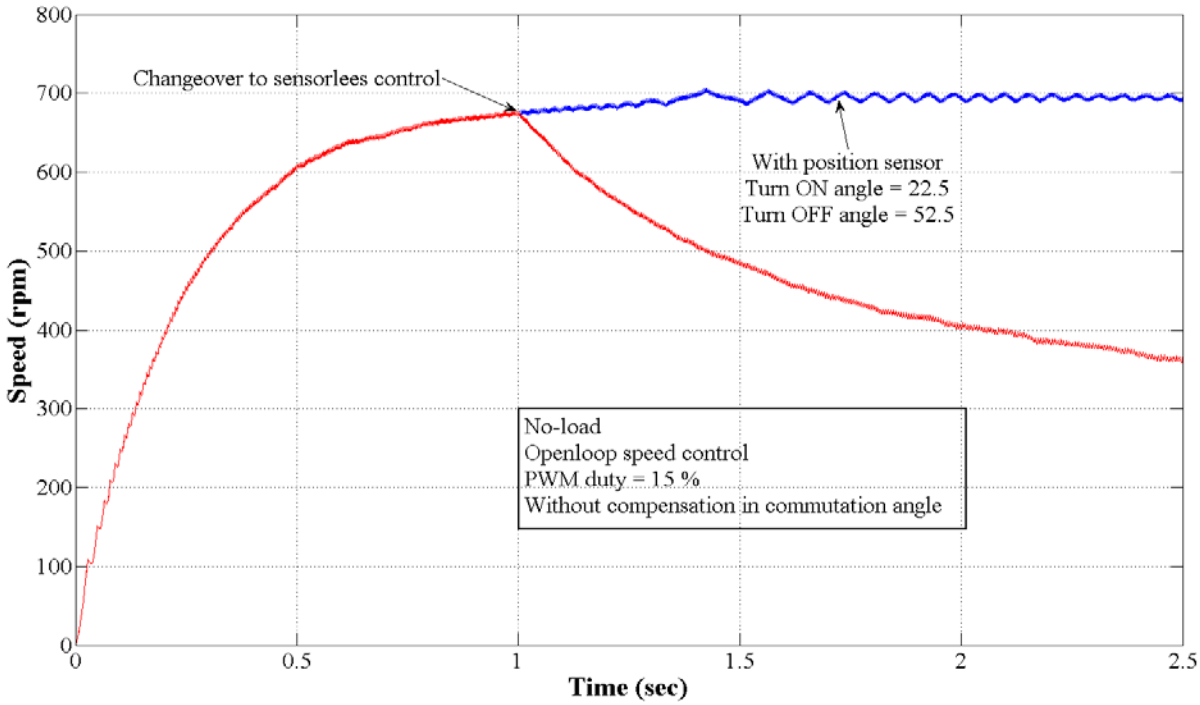

Figure 6.60 Changeover to sensorless control at the speed of 680 rpm

operation can be achieved for the same case by increasing duty cycle after transition. The transient response to a speed change with the open-loop speed control is shown Figure 6.61. Any sudden change in duty cycle leads a system towards instability, because if motor

speed increases beyond the limit, then torque gets reduced at higher turn ON angle. It imposes the limit on the PWM duty cycle to keep the speed below maximum limit, thus maximum possible duty cycle is dependent and proportional to the load torque. The open-loop response of the MCGSM is comparable with that of the CGSM. The motor speed is having oscillatory behavior and there is significant reduction in motor efficiency beyond the speed limit. Torque transient is not allowed with open-loop control. The transition from initial startup to the sensorless method for the open-loop speed control, with the compensation in commutation angle, is shown in Figure 6.62. Compensation in the commutation angle with the linearized delay factor results in performance improvement of the open-loop control system, which includes significant increase in motor efficiency, higher speed limit, better speed transient response and allows torque transient. However, prior knowledge about motor parameters is required to implement the compensation with linearized delay factor.

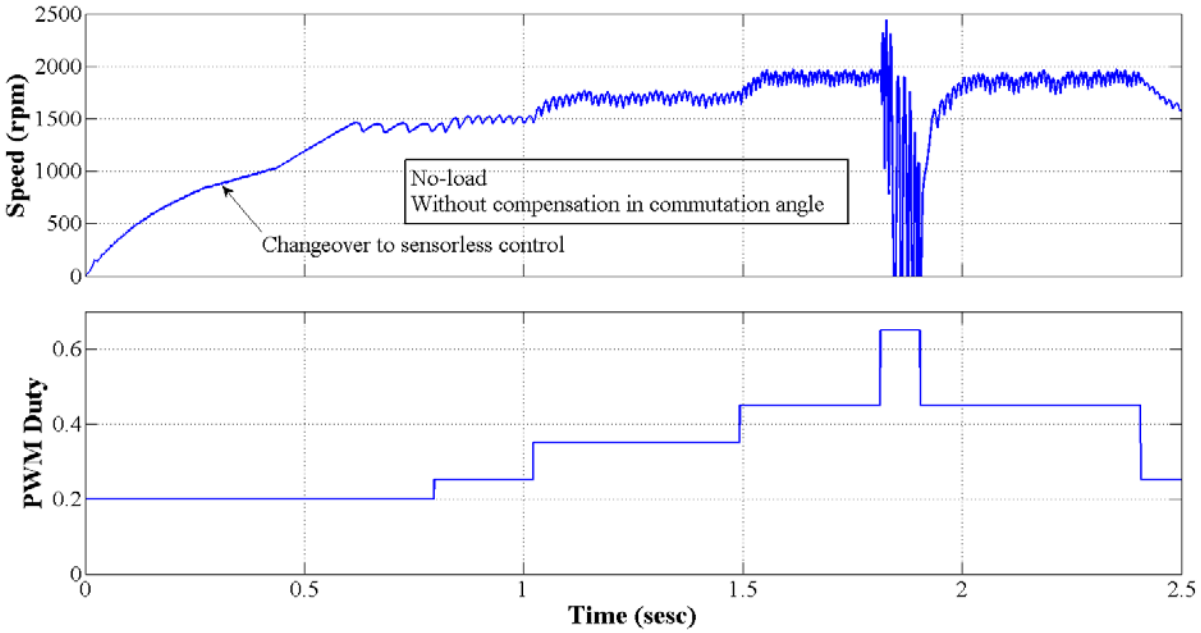

Figure 6.61 Transient response to a speed change with open-loop control

The performance of the MCGSM with the closed-loop speed control system and without compensation in commutation angle is shown in Figure 6.63 to Figure 6.65. It shows smoother transition from initial startup to the sensorless control. Transient response to a large speed step is also better with MCGSM particularly with light load condition. CGSM does not allow even small load transient (0.3 N-m maximum for the case) while MCGSM can withstand large torque transient as shown in Figure 6.65. A linearized delay factor or a constant delay factor with the continuous speed drive can be implemented with the closed-loop control for efficiency improvement.

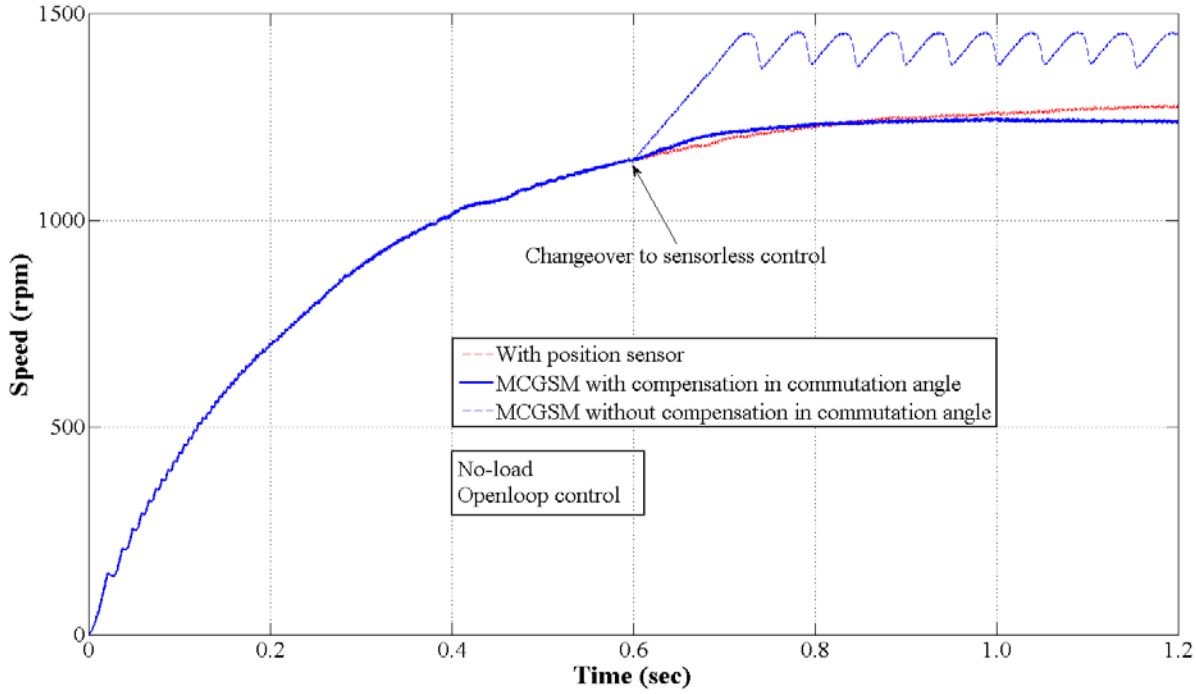

Figure 6.62 Changeover to sensorless control with compensation in angle

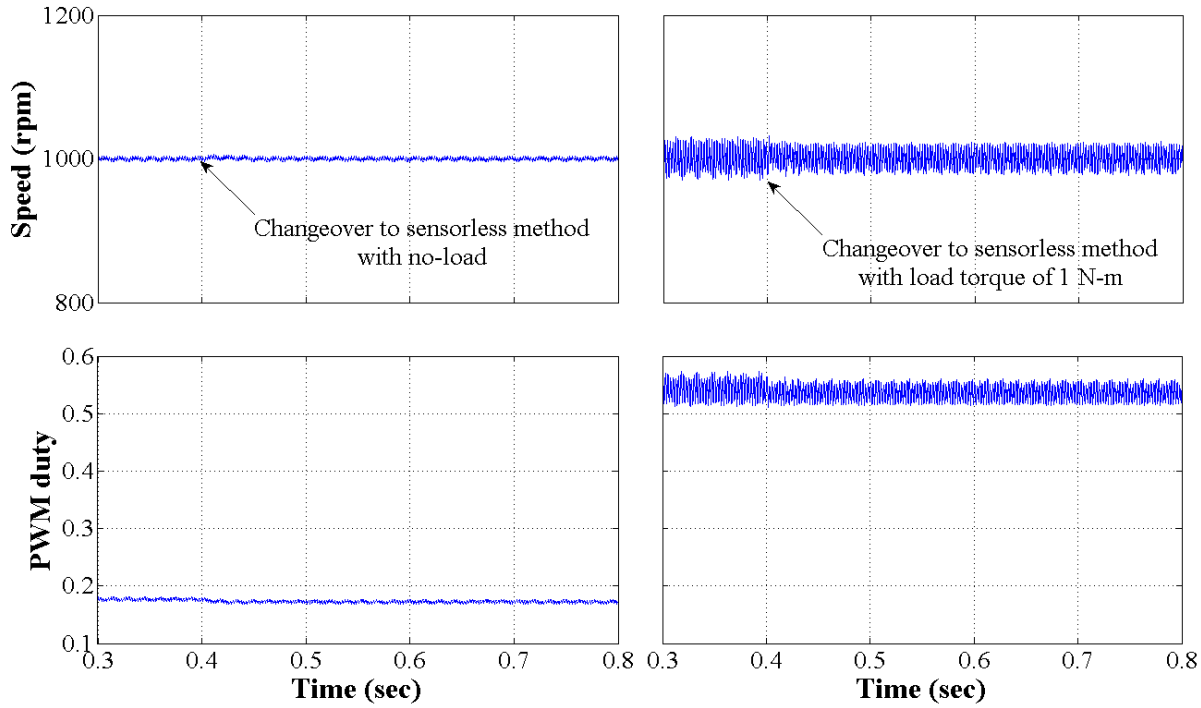

Figure 6.63 Changeover to sensorless control with closed-loop speed control

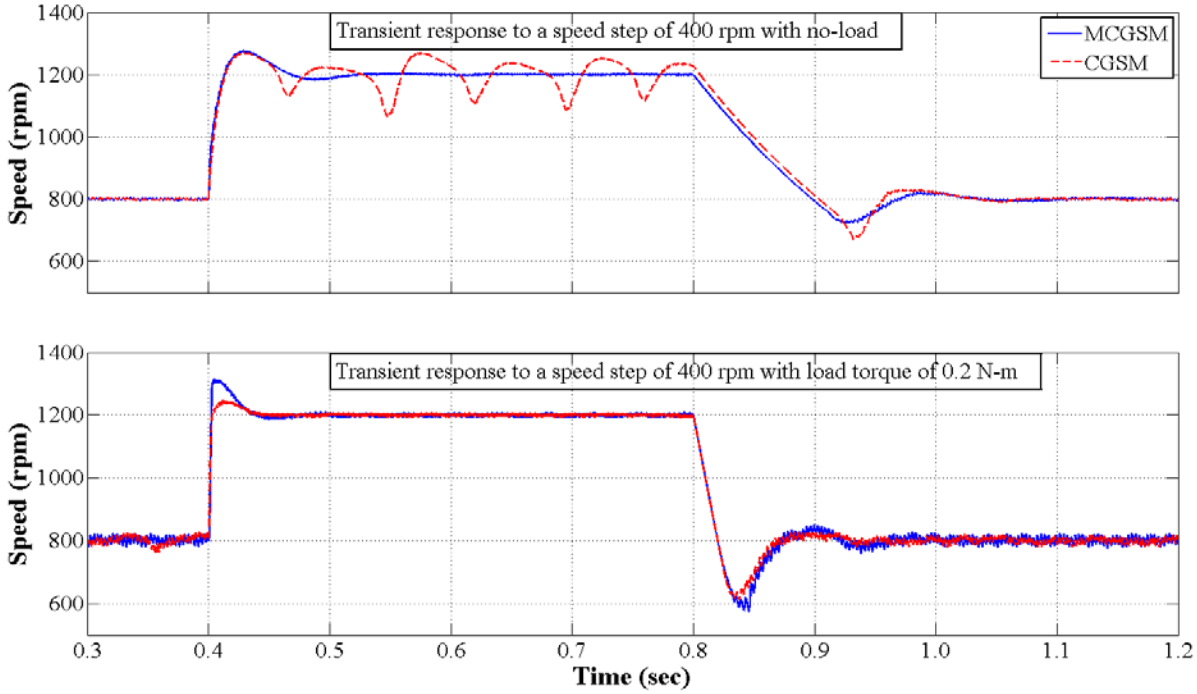

Figure 6.64 Transient response to a speed change with closed-loop control

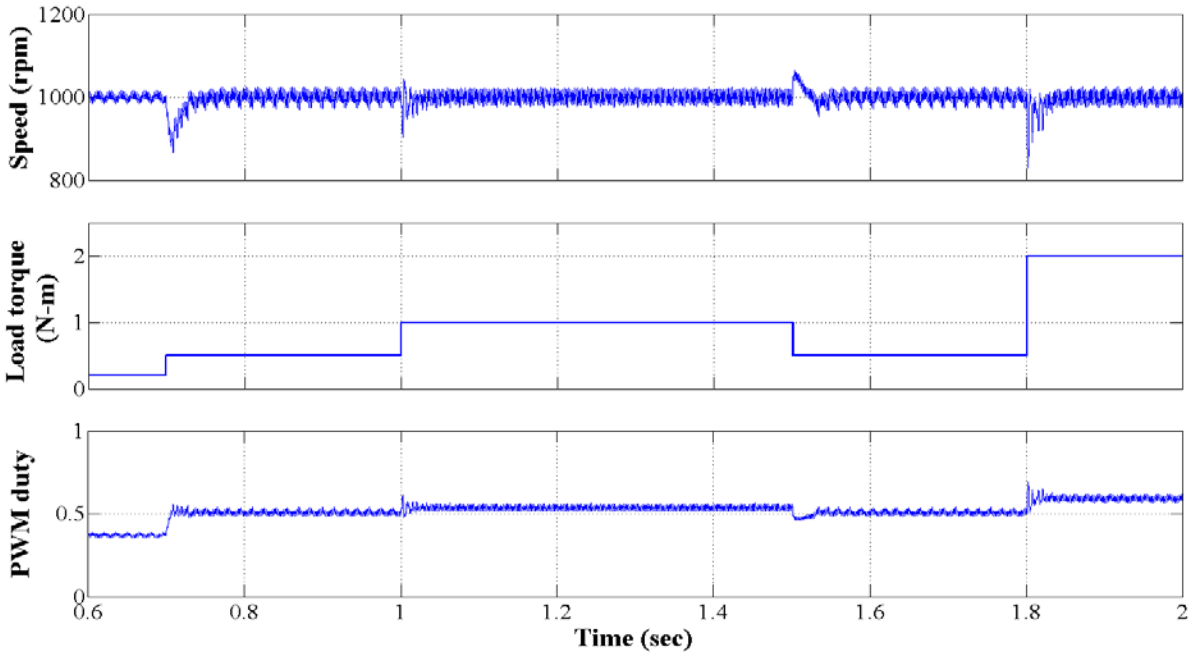

Figure 6.65 Transient response to a load change

Prototype sensorless drive is developed and implemented for 500 W, 8/6 pole, four phase SRM. Detailed block diagram of MCGSM implementation is shown in Figure 6.66. The RT-Lab is used as a real time HIL (hardware-in-loop) controller to implement the open-loop as well closed-loop speed controller and modified current gradient sensorless method. Figure 6.67 shows the two subsystems named *SM_speed_control* and *SC_speed_control* built in MATLAB simulink environment. A subsystem *SM_speed_control* includes the process blocks to configure the input/output card. It produces the desired analog output by

processing on the input signals, with the time step of 10µs. Figure 6.68 shows the detailed model inside this subsystem which includes blocks to configure and control input/outputs, PWM control, speed measurement, PI speed controller and modified sensorless scheme. A subsystem *SC_speed_control* provides a user interface for the real time monitoring and controlling the parameter of the main subsystem. It is made possible to control the motor speed, to changeover from initial startup to the sensorless control and to adjust the delay factor in the real time, via user interface as shown in Figure 6.69.

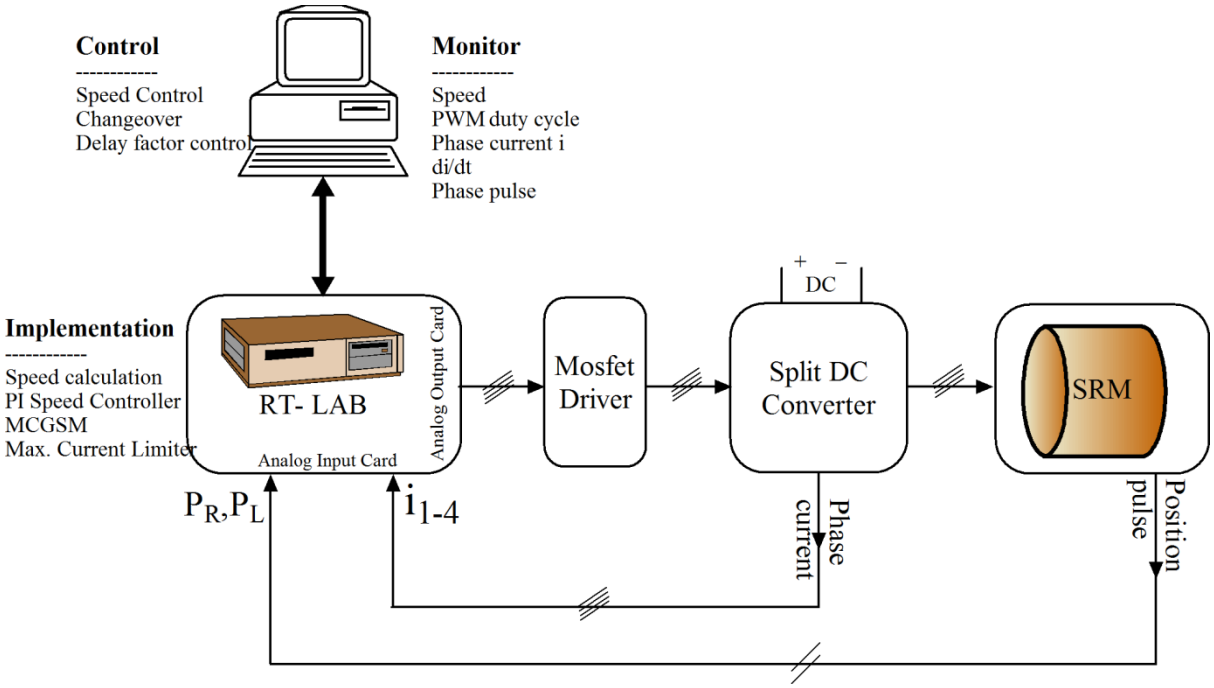

Figure 6.66 Block diagram of MCGSM implementation with RT-Lab

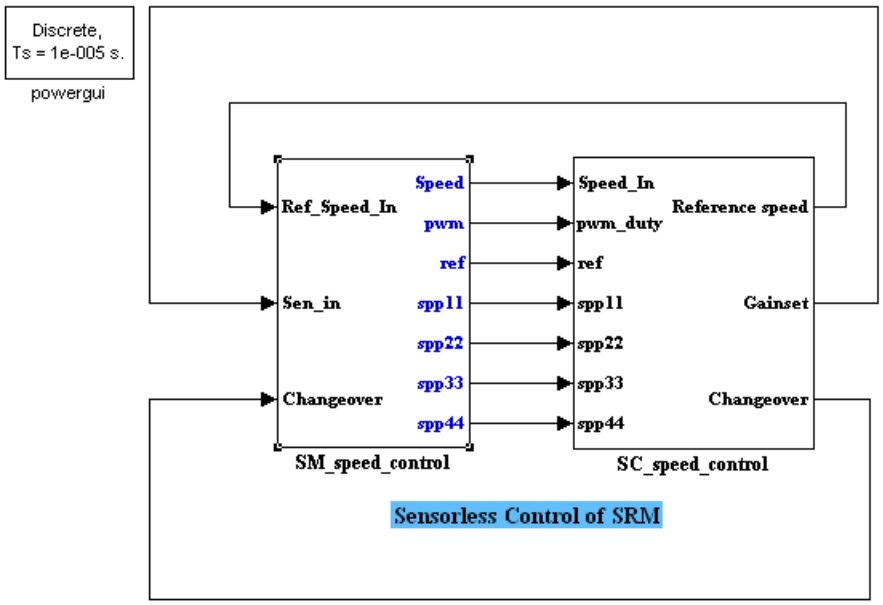

Figure 6.67 MATLAB subsystem diagram of MCGSM implementation

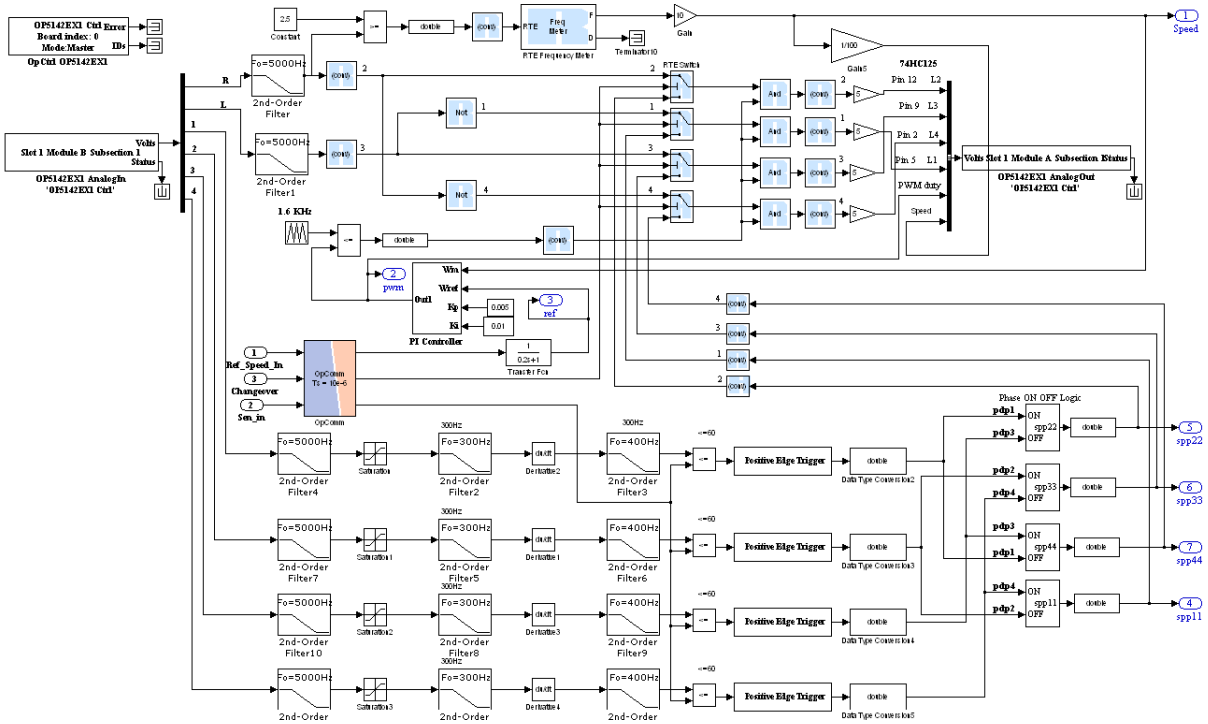

Figure 6.68 Subsystem SM_speed_control

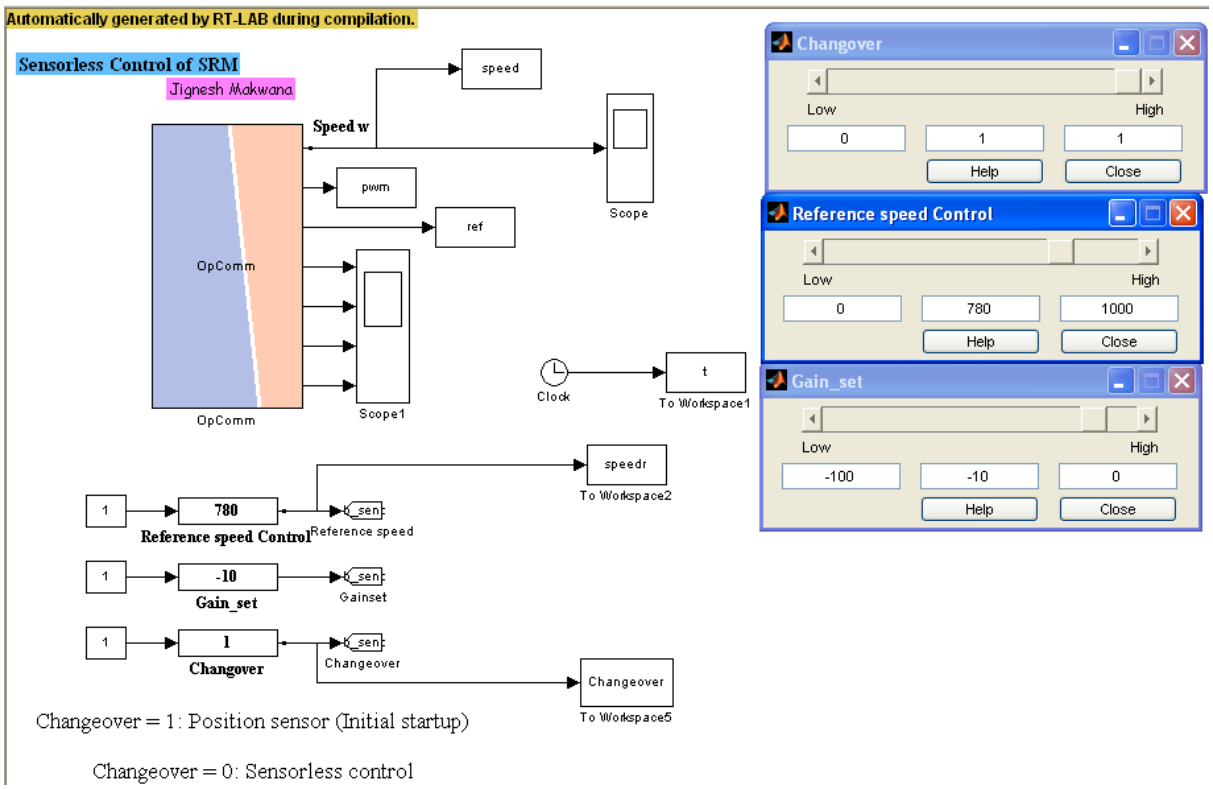

Figure 6.69 Real-time user interface panel

The waveform for the current peak detection pulse at the speed of 1300 rpm and 3500 rpm are shown in Figure 6.37 and Figure 6.38, respectively. The changeover response of the MCGSM with the open-loop speed control system and the closed-loop speed control system are shown in Figure 6.70 and Figure 6.72, respectively. The transient response of

the MCGSM to a PWM duty change is shown in Figure 6.71. The transient response of the MCGSM, with the closed-loop speed control system, for the speed change and torque change is shown in Figure 6.73 and Figure 6.74, respectively. Experimental result ensures the feasibility of proposed MCGSM and supports simulation results as well.

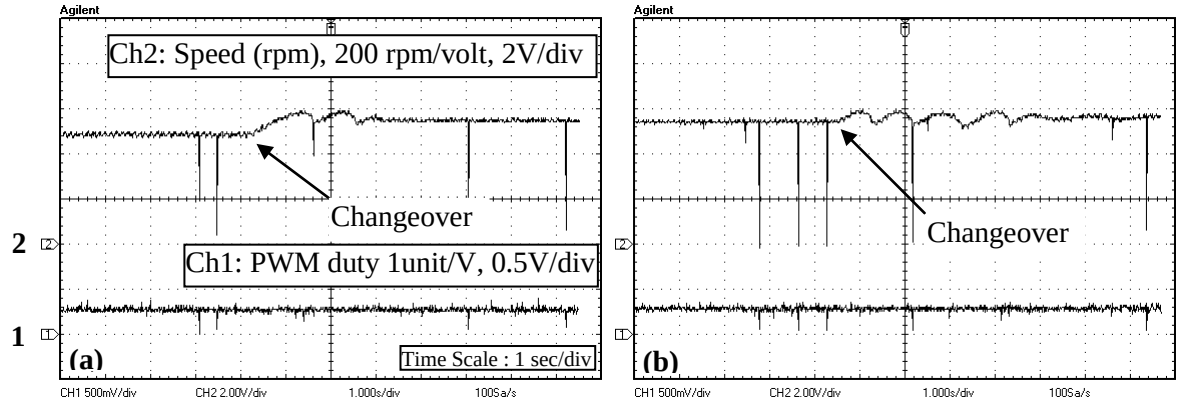

Figure 6.70 Changeover to MCGSM with open-loop speed control at no-load for (a) PWM duty cycle = 24% (950 rpm) (b) PWM duty cycle = 25% (1080 rpm)

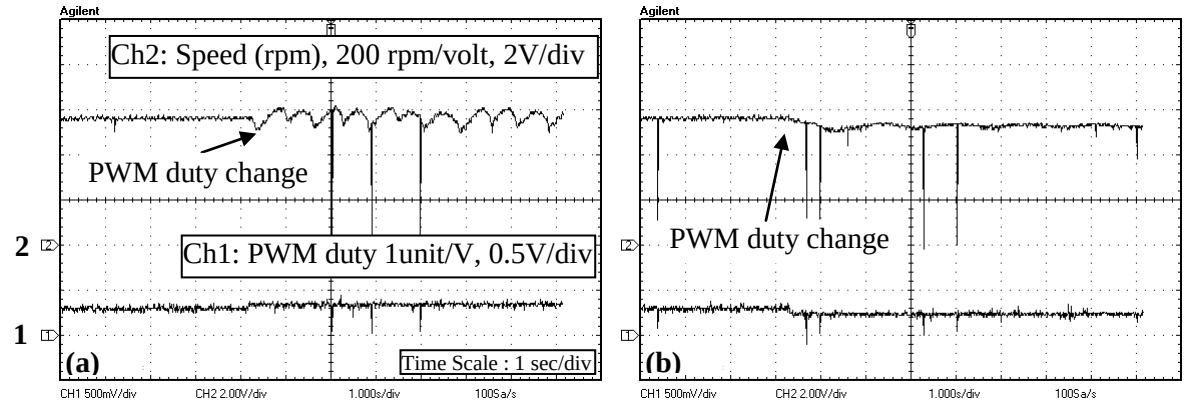

Figure 6.71 Transient response to a PWM duty change at no-load with open-loop speed control (a) from 26% to 30% (b) from 26% to 20%

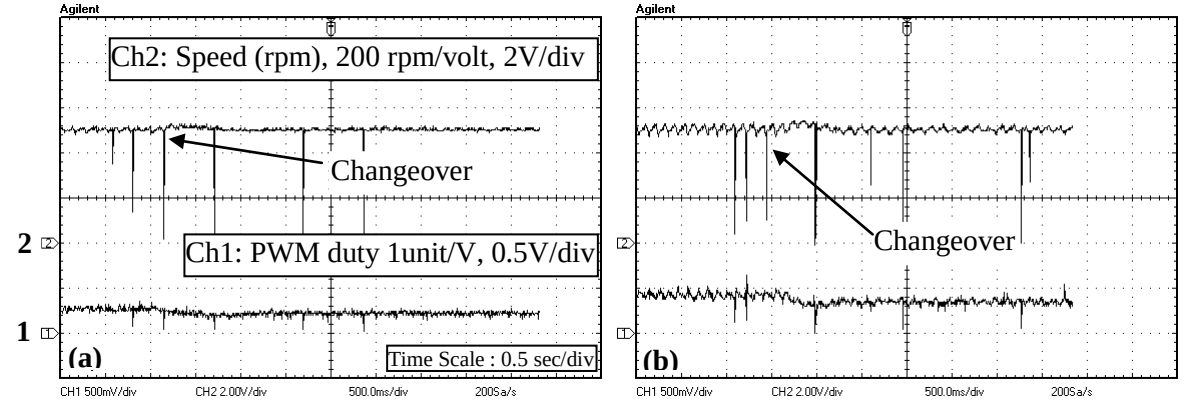

Figure 6.72 Changeover to MCGSM with closed-loop speed control at the speed of 1000 rpm with (a) no-load and (b) load torque of 0.1N-m

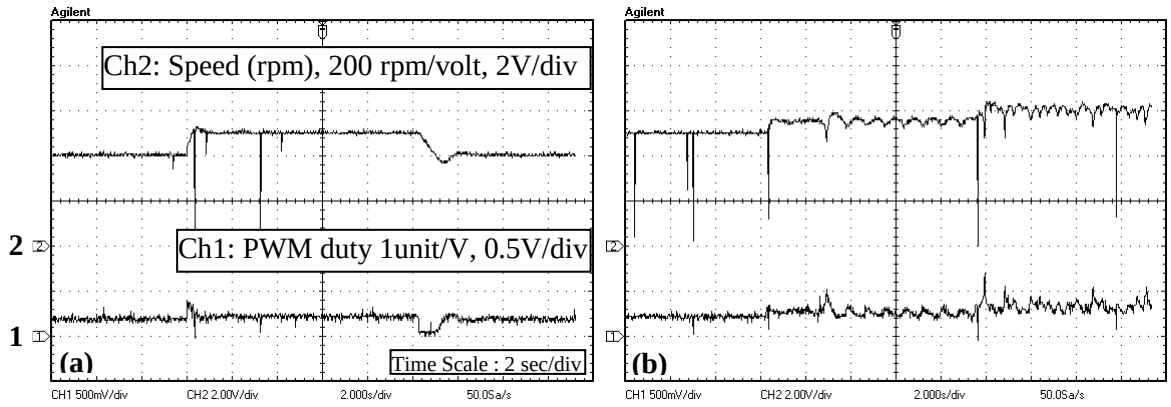

Figure 6.73 Transient response to a speed change with closed-loop speed control (a) from 800 rpm to 1000 rpm and 1000 rpm to 800 rpm (b) form 1000 rpm to 1200 rpm in the step of 100 rpm

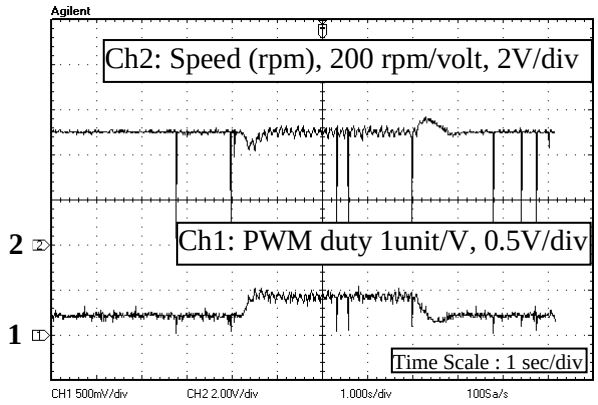

Figure 6.74 Transient response to a load torque step of 0.2 N-m with closed-loop speed control

6.5 CONCLUSION

Simulation and experimental studies validate the practical feasibility of the MCGSM for the low cost SRM drive. Advantages of the MCGSM over conventional CGSM can be summarized as-

- ✓ PLL is not required, which reduces design constrain, and cost and saving in time
- ✓ Ease of implementation
- ✓ Improve stability over speed and torque transient
- ✓ Allow large torque transient
- ✓ Wider speed range
- ✓ Higher efficiency with the commutation angle compensation

Other aspect of the MCGSM regarding practical issues and applications are as-

- The MCGSM gives practical solution for the sensorless control of the low cost SRM drive, which enhances the industrial as well domestic applications of the efficient SRM drive.

- If the motor parameters are available, then it is also possible to optimize a performance of sensorless drive for a particular application.

It is required to carry out the further research work for the performance improvement of the MCGSM in the following area.

- Speed limit imposed by the MCGSM is due to variation in the commutation angle with the speed. However, the commutation angle is not only a function of motor speed, but there is a non-linear relation exists amongst commutation angle, motor speed, and rate of change of phase current. It makes complex the task to design a delay factor which compensate the commutation angle for all speed and load condition. One solution is to store the non-linear relation as lookup table which is required and are available from the pre measurements or accurate modeling of the SRM drive. But, this is not a viable solution for the low cost SRM drive. On the other hand, peak value of the rate of change of current limits maximum delay factor. It depends on the load torque, motor speed as well as rotor angle which increase complexity of the design.
- It is also required to concentrate in the research and development of the initial starting methods for the sensorless control. Most of the sensorless methods available today are unable to start without initial starting method, which reduces the effectiveness of sensorless methods in practical applications.

The MCGSM is applicable to the low cost PWM controlled SRM drive to eliminate the mechanical position sensing arrangement for the limited speed range.

Chapter 7: IN-WHEEL SRM DRIVE FOR AN ELECTRIC VEHICLE

In this chapter, performance of the in-wheel SRM drive is investigated for the battery operated low-power electrical vehicle system. The model of 8/6 pole, four phase SRM is used with asymmetric bridge converter and low-frequency PWM controller. Passive loading scheme is proposed to simulate the complete system model of the in-wheel SRM drive. Also, the performance of the electric braking is investigated with the fixed-angle control scheme.

7.1 INTRODUCTION

The comparison of the SRM drive over other drives has been well documented in the literature [8, 29, 42, 55, 56, 59, 71, 80, 150]. It is proven that the SRM drive offers superior performance over others in varying applications; however its application is still limited to the few industrial and domestic applications.

General advantages of the SRM are low cost (motor and converter), small size and higher efficiency (above 90%), which makes it suitable candidates for the industrial and domestic fan, blowers, compressor and pumps. Capability of high speed range makes it suitable for the textile spinning and vacuum cleaner. The possibility of the wide-speed range operation is beneficial for the washing machines wherein single motor can used in spin, dry and wash cycles. Special features of the SRM like shape adoptability, countable cycle (number of revolution) and fast stop makes it advantageous to the food processor applications. Gear-less operation or reduction of the gear ratio is also favourable for some applications. High low-speed torque and integrated management capability makes it suitable for the automotive application like power steering and wiper. Features like high starting torque, wide constant power region and higher efficiency at varying load make the SRM as most suitable candidates for the electric vehicle propulsion system. The investigation is carried out to analyse the performance of SRM for low-power two-wheeler vehicles.

7.2 CASE STUDY: SRM FOR AN IN-WHEEL ELECTRIC VEHICLE

Performance of the 500W, 8/6 pole, four phase SRM is investigated for an in-wheel electric vehicle system. The SRM drive consists of asymmetric bridge converter and PWM current controller. A 48V battery is used to supply the power to the drive. Passive loading scheme is proposed which makes it possible to develop a simulation model of the in-wheel electric vehicle system from the separate model of the SRM and vehicle system.

7.2.1 Modeling of SRM drive

Simulation model of conventional bridge converter is used with the model of four phase SRM developed earlier. The model of the MOSFET IRFP450 is used as a power switch. The fixed frequency (1.67 KHz) PWM control is incorporated to control the speed while hysteresis current control is used to limit the maximum current. The turn-ON and turn-OFF angles are fixed to the 27° and 57°, respectively. The generic battery model from the 'Electrical source' library is used to supply the power to the converter. The parameters of the equivalent circuit of the battery can be modified to represent a particular battery type, based on its discharge characteristics. The Li-Ion type battery model is used in this application having parameters as under -

Nominal voltage (V) = 48

Internal resistance (ohm) = 0.02

Full charged voltage (V) = 55

Nominal discharge current (A) = 10.5

Rated capacity (Ah) =24

The discharge curve of the 48V Li-Ion battery is shown in Figure 7.1.

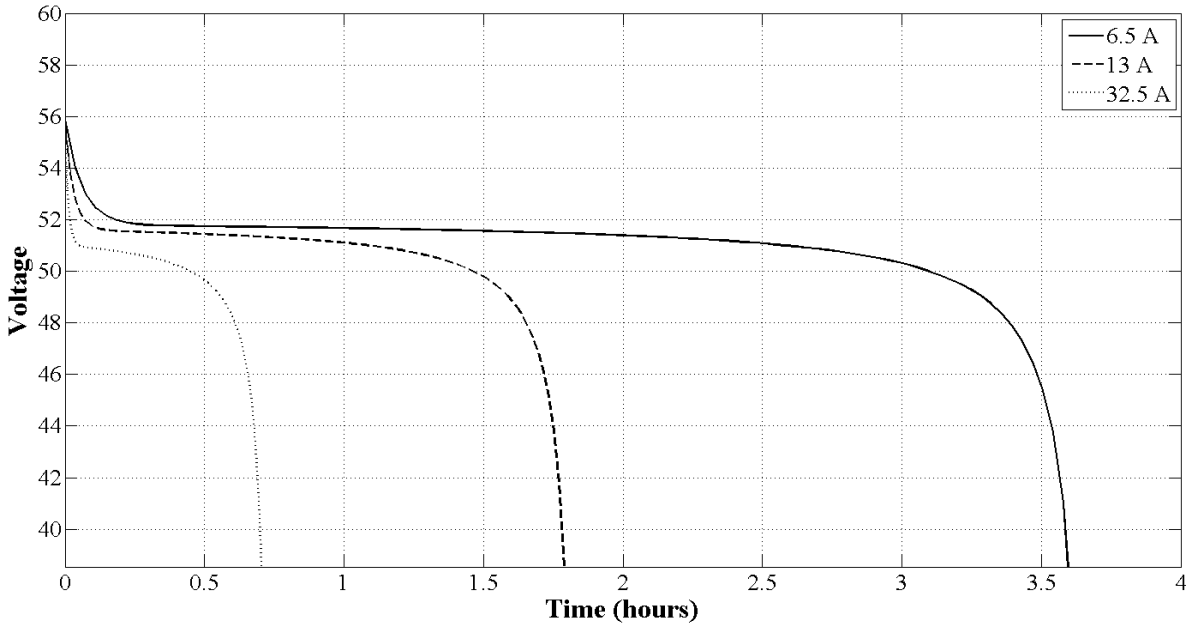

Figure 7.1 Discharge characteristics of the battery

7.2.2 Modeling of electrical vehicle

The mathematical model of the electrical vehicle with two equally sized wheels, moving forward or backward along its longitudinal axis is developed. The geometry of the vehicle is shown in Figure 7.2. It is assumed that vehicle is in vertically balanced condition and thus wheels are always perpendicular to the horizontal plane.

The vehicle parameters are as follows:

'm' is a mass of the vehicle in (kg) = 150

'a' is a horizontal distance of CG from front axis in (m) = 1.4

'b' is a horizontal distance of CG from rear axis in (m) = 1.6

'h' is a height of CG from the ground in (m) = 0.5

'A' is a front area in (m^2) = 0.8

'C_d' is a drag co-efficient = 0.1

'V_x' is a longitudinal velocity of the vehicle in (m/s)

'ρ' is a mass density of air in (Kg/m^3) = 1.2

'F_d' is an aerodynamic drag force in (N)

'F_{xF}' is a longitudinal force applied at the front wheel in (N)

'F_{xR}' is a longitudinal force applied at the rear wheel in (N)

'r' is a radius of the wheel in (m) = 0.21

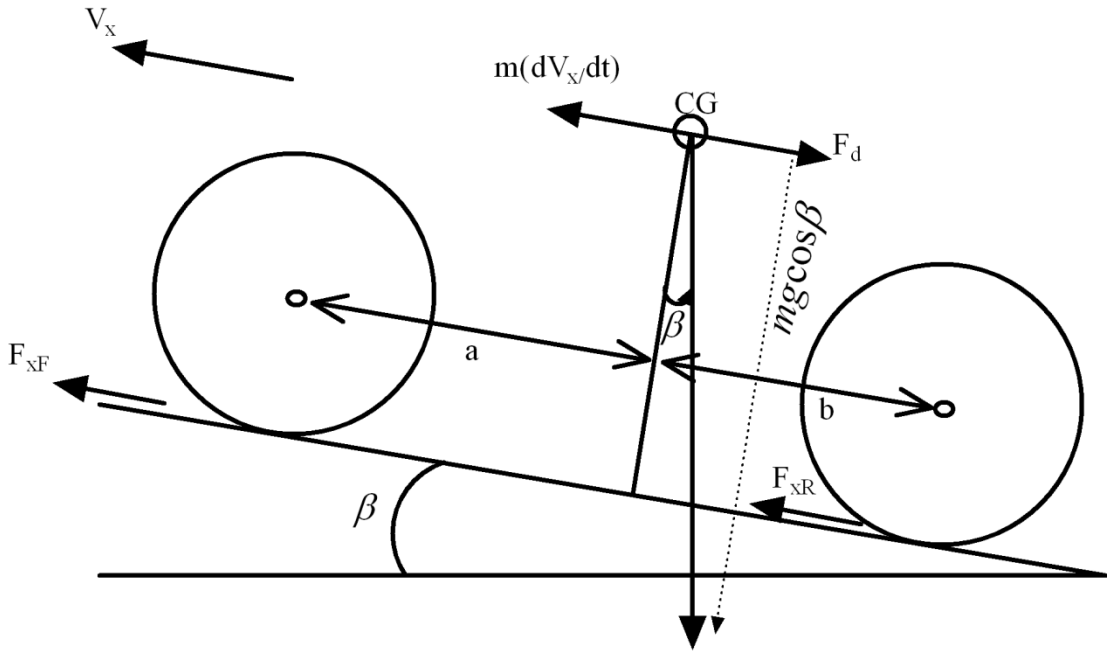

Figure 7.2 Geometry of the vehicle

Output of the model of the vehicle is the longitudinal velocity for the longitudinal force applied to the front and rear wheels. Assuming the rear wheel drive requires longitudinal force at the rear wheel to accelerate the vehicle with the velocity V_x is -

$$F_x = F_{xR} = m\frac{dv_x}{dt} - F_d + mg\sin(\beta) \tag{7.1}$$

Simply,

$$m\frac{dv_x}{dt} = F_{xR} + F_d - mg\sin(\beta) \tag{7.2}$$

Where, aerodynamic drag force,

$$Fd = -\frac{1}{2}C_d \cdot \rho \cdot A \cdot V_x^2 \cdot \mathrm{sgn}(V_x) \tag{7.3}$$

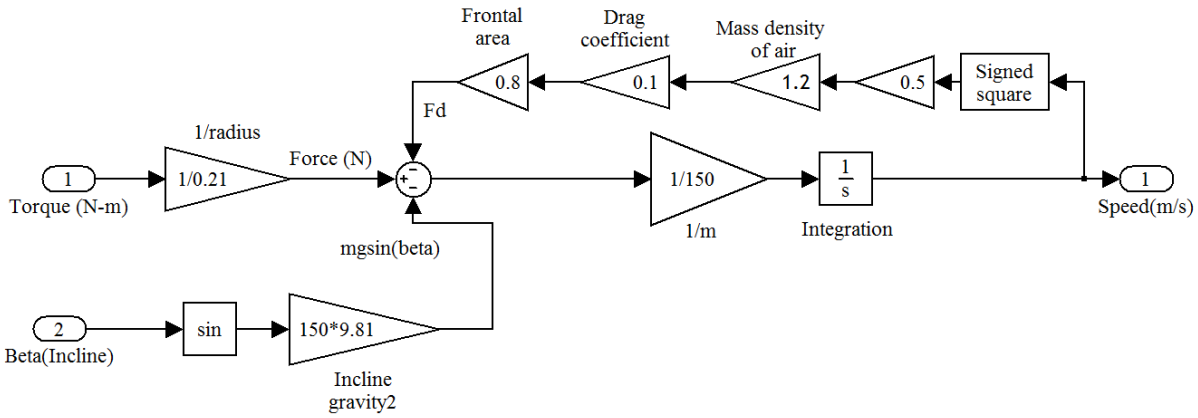

Figure 7.3 Simulation diagram of the vehicle model

Dynamic model of the vehicle system is simulated in the MATLAB simulink environment from the (7.2) and (7.3) as shown in Figure 7.3.

7.2.3 Simulation of in-wheel electric vehicle

To study the exact behaviour of the in-wheel SRM drive, a complete mathematical model of the SRM loaded with the exact model of the vehicle is required. However, two separate models are used for the SRM and electric vehicle. In the vehicle system model torque is an input and instantaneous velocity is an output. The load torque is an input signal to the SRM model which can be used to apply the load torque as constant or function of motor speed. While, SRM model provides an electromagnetic torque for the measurement purpose only, the passive loading scheme is used to load the SRM model with the vehicle model to complete the in-wheel electric vehicle system.

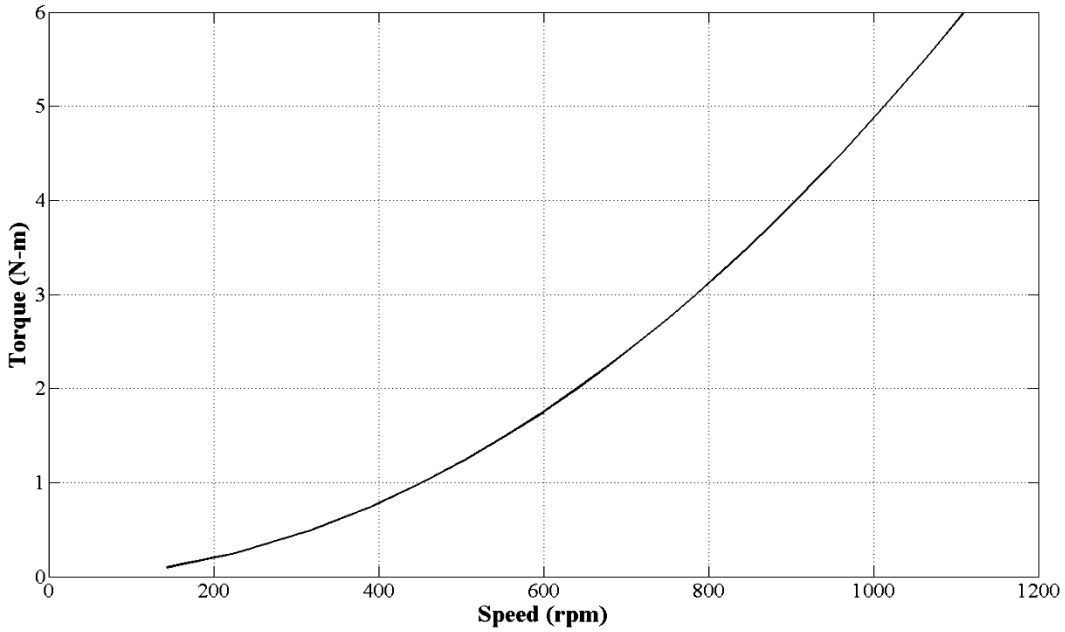

Figure 7.4 Speed-torque curve of the vehicle

Passive loading scheme is divided in two parts. In first part vehicle system model is used. Constant torque is applied as an input to the vehicle model to find the steady state speed of the vehicle. Table 7.1 shows the steady state speed achieved by the vehicle for an applied constant torque. The speed-torque curve of the vehicle is shown in Figure 7.4 which is stored as a look-up table, where measured speed of the SRM is used as an index to obtain the required torque. This torque is applied as a load torque to the SRM model. Thus load torque imposed on the SRM is a function of speed.

Table 7.1 Speed-torque characteristic of vehicle

Sr. No	Torque (N-m)	Steady state speed of wheel of the vehicle (rpm)	Steady state speed of vehicle (Km/h)
1	0.10	143	11
2	0.25	226	18
3	0.50	320	25
4	0.75	393	31
5	1.00	453	36
6	1.25	507	40
7	1.50	555	44
8	1.75	600	47
9	2.00	641	51
10	2.25	680	53.8
11	2.50	716	56
12	2.75	752	60
13	3.00	785	62
14	3.25	817	64.5
15	3.50	848	67
16	3.75	877.5	69.44
17	4.00	906.3	71.71
18	4.25	934.2	73.92
19	4.5	961.3	76.06
20	4.75	987.6	78.15
21	5.00	1013	80.18
22	5.25	1038	82.16
23	5.50	1063	84.09
24	5.75	1087	85.98
25	6.00	1110	87.83

In the second part, combined body of the SRM and vehicle is considerd as the lumped cylindrical shape body having weight same as weight of the vehicle and radius same as the radius of the wheel. The inertia of SRM model is considered as same as the inertia of lumped cylinder as-

$$J = mr^2 = 6.615 \tag{7.4}$$

where 'm' is mass of the vehicle and 'r ' is radius of the wheel and 'J' is the inertia in $K_g m^2$. Thus, the SRM model which is loaded with the vehicle speed-torque characteristics, and has inertia of the lumped cylinder, acts as the model of the in-wheel vehicle system.

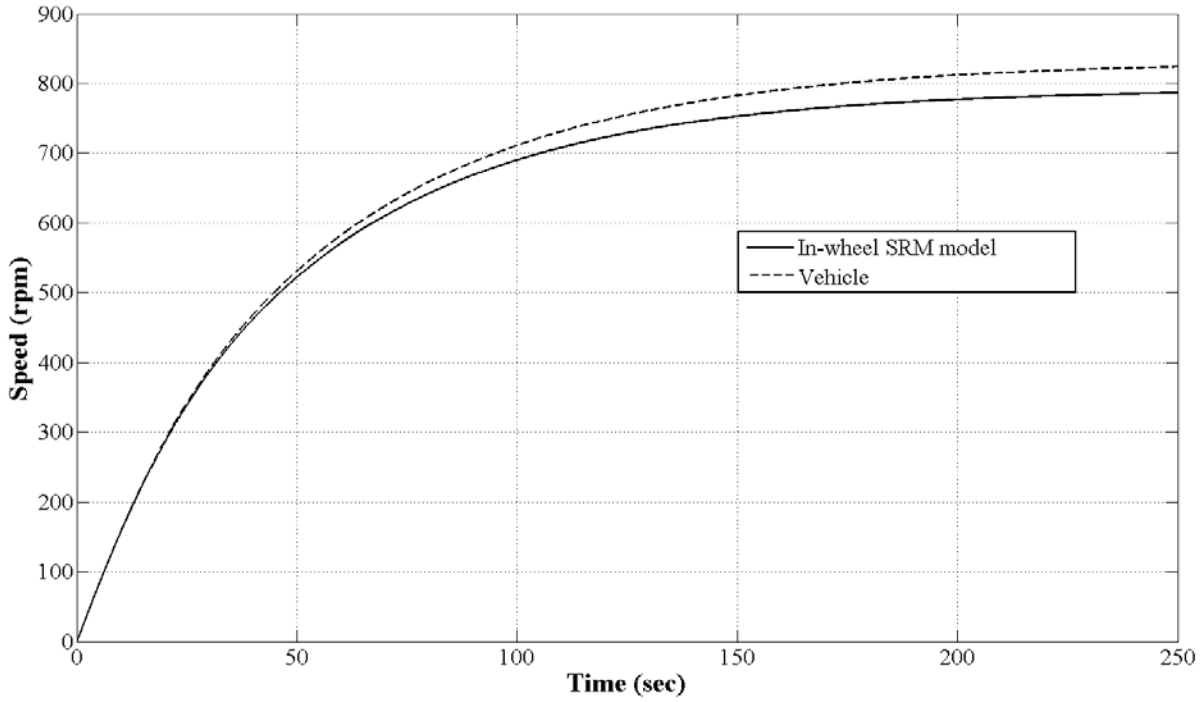

Figure 7.5 Speed response of the in-wheel vehicle

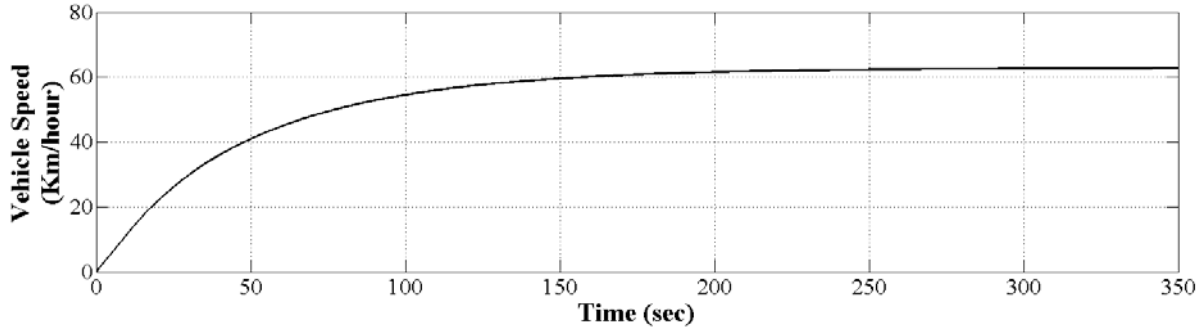

Figure 7.6 Plot of vehicle speed

To validate the proposed scheme, measured torque of the SRM is supplied to the vehicle model, and the speed response of the designed in-wheel SRM model and actual vehicle model are compared. The in-wheel SRM is supplied with the full voltage. The speed response curves shown in Figure 7.5 confirms that the speed response of both the cases are very close which validates that the designed SRM model representing the in-wheel electric vehicle system.

Figure 7.6 show the speed response of the vehicle in Km/hour. It shows that the maximum possible speed of the vehicle is 63 Km/hour, while it takes 150sec to accelerate form 0 to 60 km/hour.

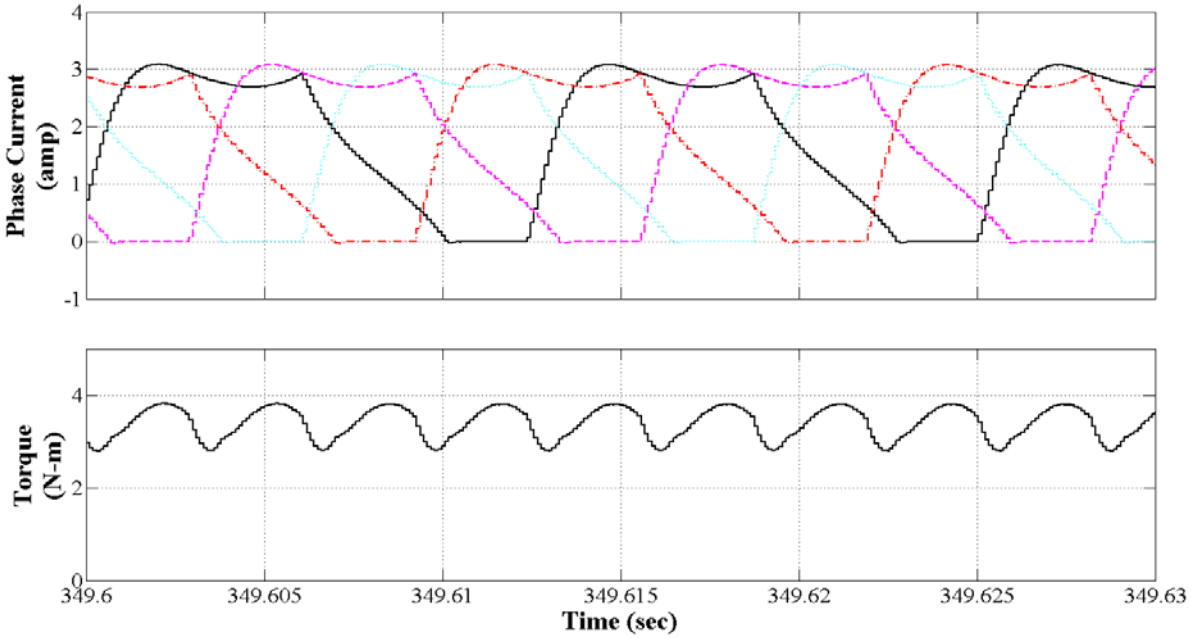

Figure 7.7 Waveform of phase current and motor torque at full speed

Waveform of phase current and torque are shown in Figure 7.7. It shows that the peak current is less than 3.5 Ampere and ripple in torque is very low (0.3 unit) to produce significant effect on the performance of the electric vehicle.

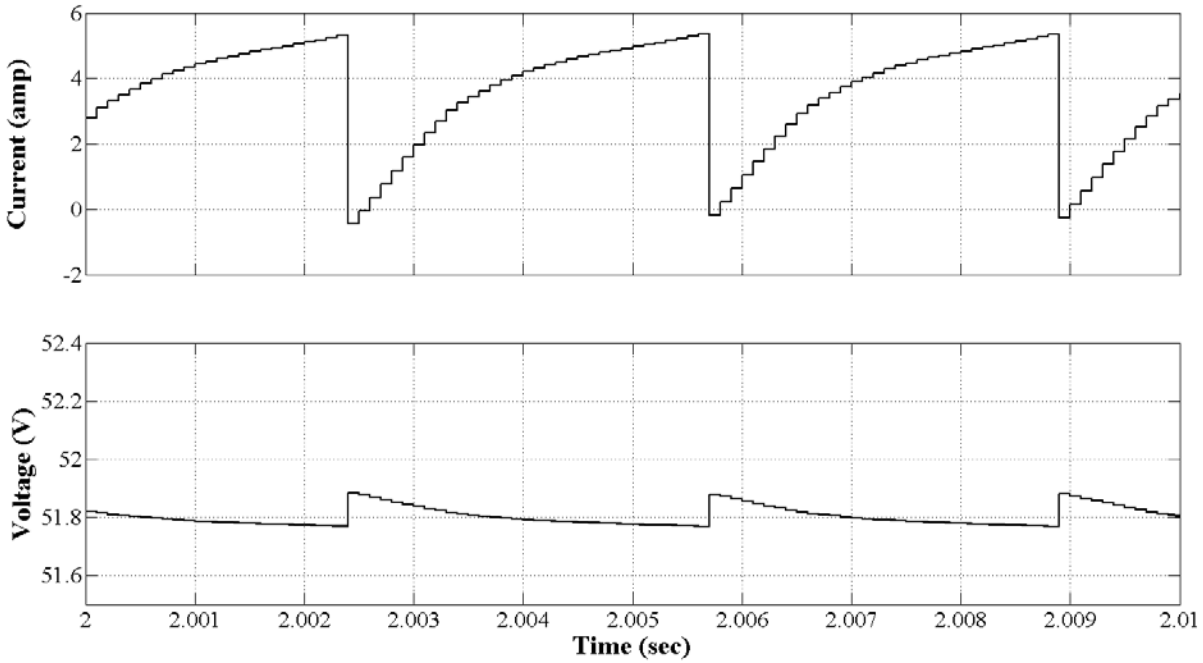

Figure 7.8 Battery voltage and current at full speed

Figure 7.8 shows the battery voltage and current which dictates that the peak current of the battery is less than 6 Ampere. However, the battery current during starting was around 18 Ampere. Assuming average battery current of 10 Ampere, the fully charged battery will serve approximately for the next 2.5 hour. Considering constant speed of 40 Km/h, the vehicle will run for 75 Km with one charge.

Figure 7.9 shows the mechanical output power of the motor at full speed. The average output power is 282W while the peak value is 317W.

The results confirms that the SRM is the suitable alternative to replace the costly BLDC motors for the low-power in-wheel electric vehicles.

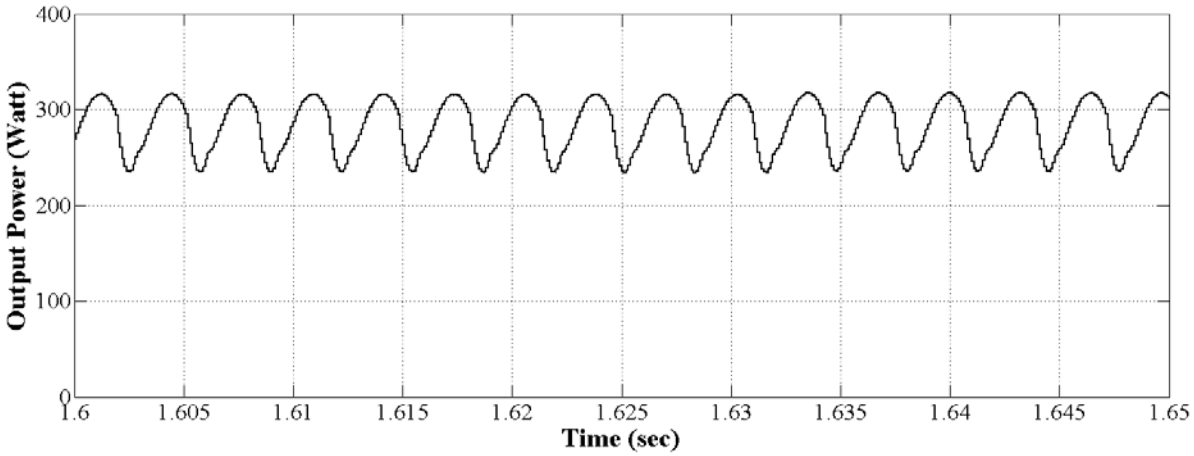

Figure 7.9 Power output at full speed

7.2.4 Performance of regeneration braking

It is convenient to incorporate an electrical regeneration braking with the SRM as compared to conventional motors. The effectiveness of the regeneration breaking is investigated.

The SRM offers easiest way to change the operation mode from motoring to generator. It is required to change the commutation angles (turn ON and turn OFF) such that the phase energizes during the falling inductance profile instead of rising. The scheme is proposed to implement the braking with the low cost fixed angle controller. It uses a simple mechanical switch which interchanges the commutation pulse of each phase as-

Phase-1 to Phase-3

Phase-2 to Phase-4

Phase-3 to Phase-1

Phase-4 to Phase-2

The simple mechanism changes the turn-ON angle to the 57° and turn-OFF angle to the 87°. It produces the negative torque as the falling inductance region of the 8/6 pole, four phase SRM is from 60° to 90°. The simulation results of the electrical braking applied to an in-wheel vehicle system are as follow.

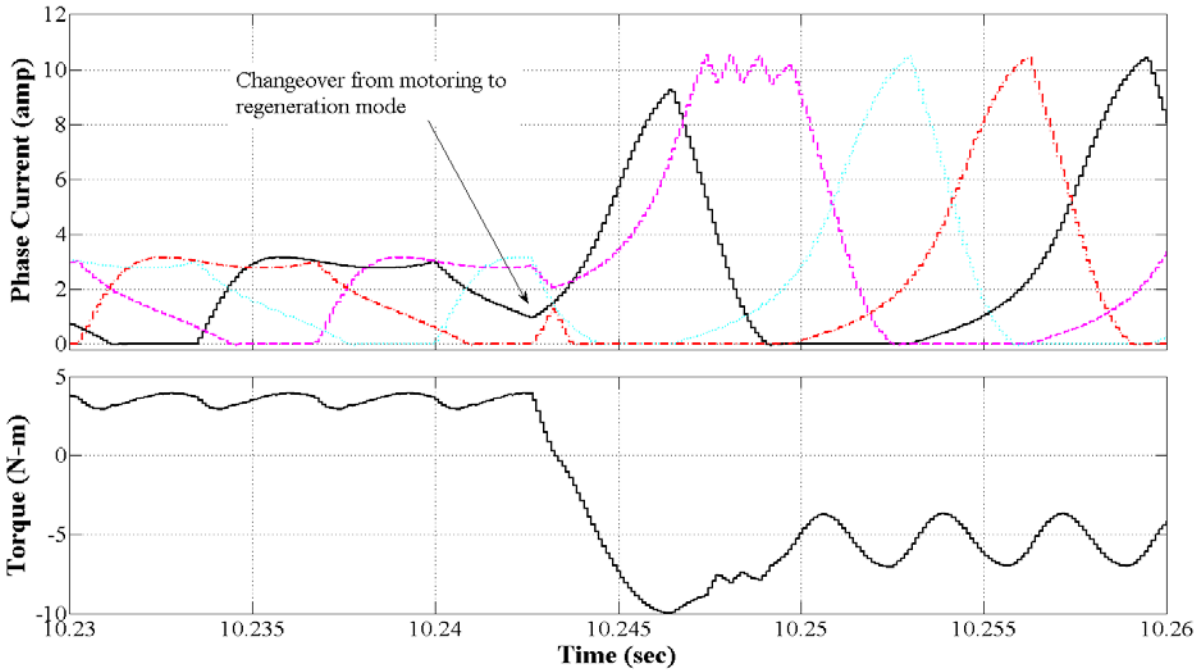

Figure 7.10 Waveform of phase current and torque during regenerative breaking

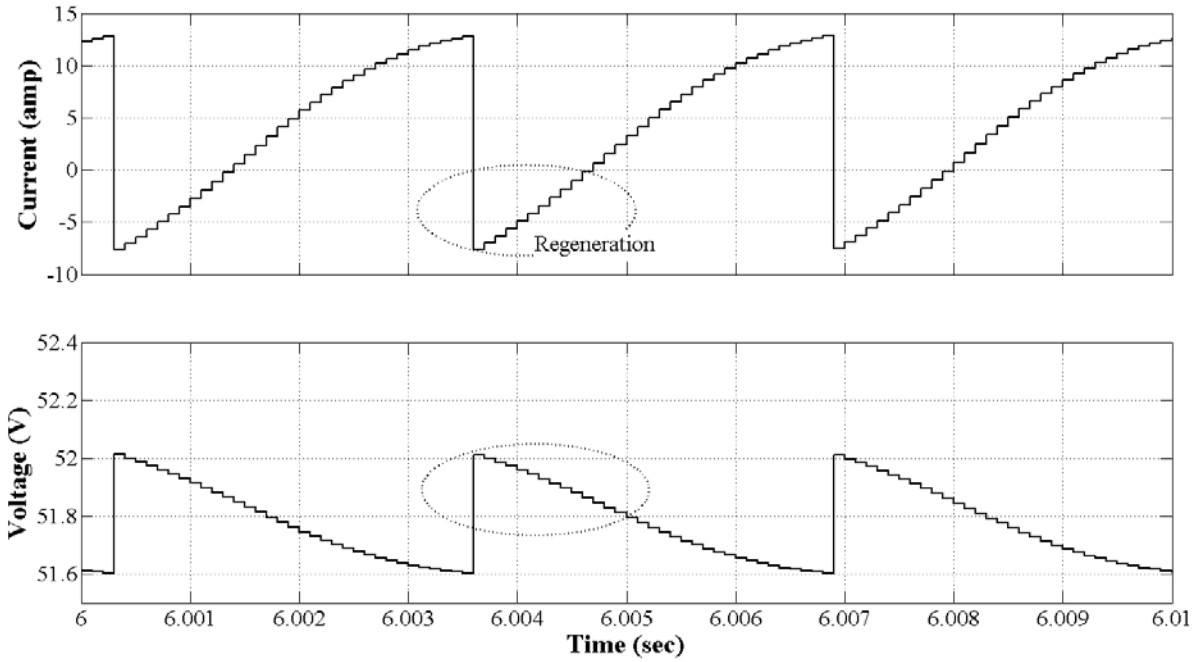

Figure 7.11 Battery voltage and current during regeneration operation

Figure 7.10 shows the waveform of phase current and torque while braking is applied with the full voltage, to the in-wheel vehicle model. Figure 7.11 shows the battery voltage and current for the regeneration operation. However, kinetic energy of the vehicle is not fully utilized because even with regeneration, it consumes the energy in braking. An angle control scheme can offer a more efficient regeneration by ensuring the prevention of phase excitation during rising inductance period. Efficiency of the regeneration can also be increased by reducing the dwell angle to allow the more regeneration time. But, at the same

time it reduces the amount of braking torque. The phenomena is comparable with the motoring operation, where torque can be increased by increasing the dwell angle but at the cost of efficiency. Figure 7.12 shows the battery current and voltage with reduced dwell angle (15°). The regeneration allows recharging of battery during braking and improves the range.

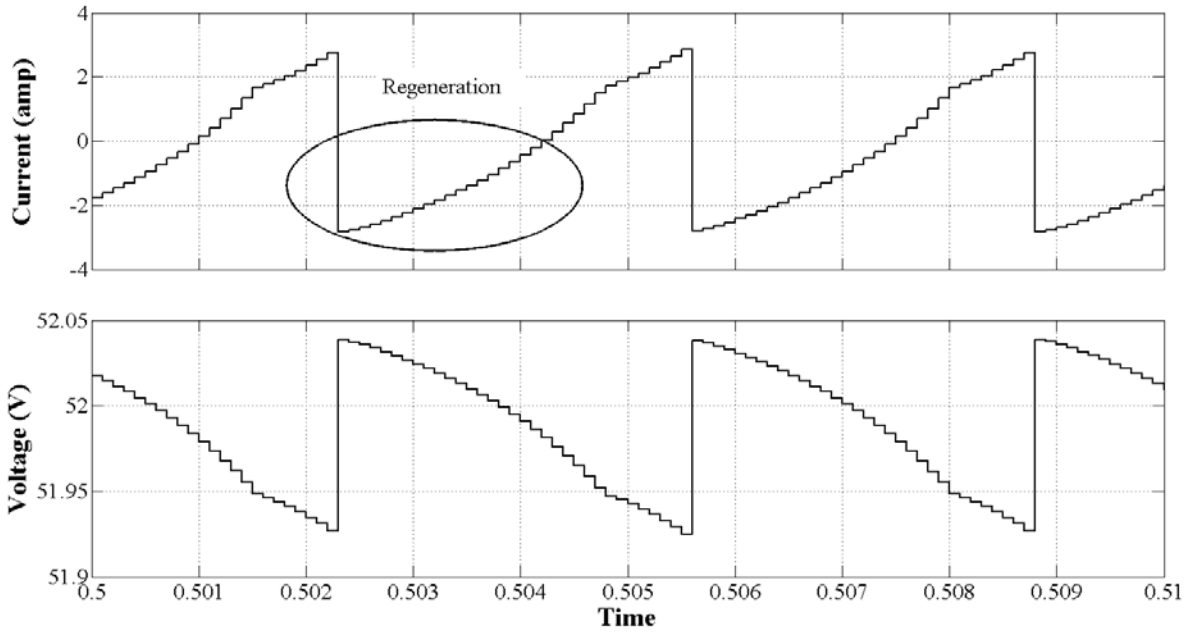

Figure 7.12 Battery voltage and current with reduced dwell angle

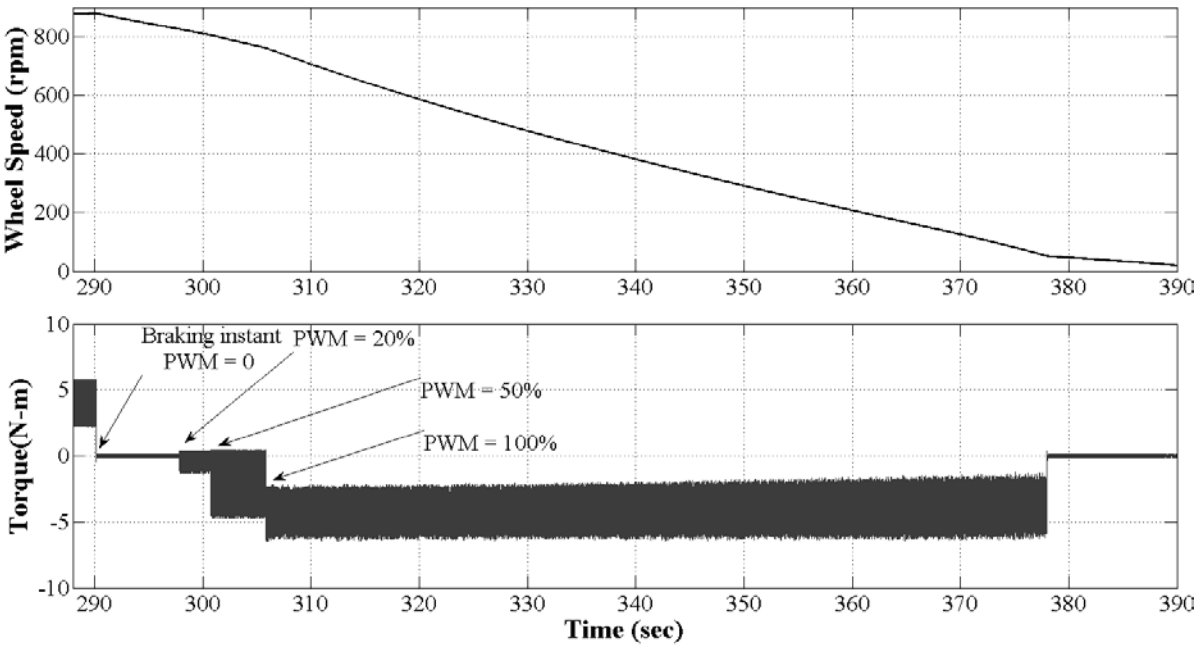

Figure 7.13 Braking torque control

The braking torque can also be controlled by the PWM duty cycle. Figure 7.13 shows the control of braking torque by the PWM duty cycle. It seems that electric braking system

can be used along with the mechanical braking system. The motor that develops more acceleration can also provide fast braking operation.

7.3 CONCLUSION

The SRM offers numbers of advantages compared to conventional BLDC motor for the in-wheel vehicle system. It includes low-cost, smaller size, less weight, higher starting torque and higher efficiency drives. The SRM fits the best for the vehicle propulsion application without having an issue of torque ripple.

Chapter 8: CONCLUSION AND FUTURE SCOPE

8.1 CONCLUSION

This work has been carried out to investigate the performance of the SRM drive and to explore the potential of the same. It has the capability to replace the conventional motors for the variable speed drive application.

The SRM offers many advantages over conventional dc and ac motors as well as over other electronically commutated (EC) motors. The doubly salient structure with no winding on the rotor makes the SRM smaller in size, less in weight, and cheaper in cost compared to dc and ac motors of the same power rating. The repair and maintenance of the motor becomes more convenient as there is winding on the stator only. Besides, the rotor of the SRM is made up of laminated iron or steel unlike other EC motors which use permanent magnet. It reduces the material cost of the motor compared to other EC motors. It has advantage of higher permissible temperature and easy to cool. However, the selection of the stator/rotor pole configuration is an important factor for the efficient operation of the SRM drive as different topologies of the motor are possible. The most adopted SRM topology is the 6/4 pole three phase, as lower phase leads to higher torque ripples and higher phase adds an extra cost and components.

Advancement in technology and simulation software makes the design and development of the SRM drive more convenient. The modeling and simulation study shows that the accurate model of the SRM can be derived with the MATLAB based simulation tool. Several vital schemes to model a SRM are also explored and compared, from which an appropriate modeling technique is selected to meet the application demand. The look-up table based modeling technique offers high accuracy and minimum computation time for the simulation. However, the development cost is higher and it also takes more time. This method is useful where the performance of the existing SRM is to be investigated for the specific drive application. The inductance based modeling method gives reasonable accuracy as well as reduces time and cost of implementation. The analytical modeling method uses geometrical parameters and information about numbers of turns per phase to model a motor. Thus, this method is more economical and convenient to develop compared to others. However, it requires large calculation to obtain the co-efficient of the analytical expression. This method would be a better choice to investigate the performance of power electronics converters and control techniques of the SRM drive. The physical modeling technique is proposed and developed in the present work which allows variation of the physical parameters of the model. This method is useful to obtain the optimized performance of the drive. This method is easy to implement and offers good accuracy. The 3D

visualization model of the motor is developed which added a new dimension to the modeling of the motor. Furthermore, the real-time simulation model of the complete SRM drive is derived in the present work with the RT-Lab based simulator. Also, the effect of variation in advance angle and dwell angle on the torque-speed characteristics of motor is investigated. The desired torque-speed response of the motor can be obtained by adjusting the dwell angle and advance angle. Higher advancement in the turn-ON angle results in higher speed while average torque of the motor can be increased by increasing the dwell angle. It was observed that the minimum dwell angle reflects maximum efficiency of the motor.

The low-cost 8/6 pole four phase SRM drive is designed and developed in this work and performance is investigated. The investigation shows that the proposed four phases SRM with two phase excitation scheme reduces the torque ripple significantly without increase in component cost as the one switched per phase converter is used. The amount of torque ripple is 3.05 at the speed of 1000 rpm and load of 1 N-m, while it is 4.2 for single phase excitation with the same condition. Further, the proposed low-frequency PWM controlled scheme reduces the converter losses, motor noise and electromagnetic interference to the system as compared to the conventional hysteresis current control scheme. The AC small signal model of the SRM is designed in the present work and accordingly PI speed controller is developed. The performance of the SRM drive is investigated for the open-loop and closed-loop condition. The result shows that the efficiency of the proposed SRM drive is higher even at partial loading condition. It is observed that maximum efficiency of the SRM drive is 92% at the full load and 91.2% at the half load (Table C.3). This SRM drive offers higher performance to cost ratio. The investigation shows that the amount of the ripple in the torque is not constant but it varies with the speed, load torque and PWM frequency. It was found that the problem of torque ripple is not predominant for the high speed application and for the application involving heavy inertia load. This investigation shows that, the SRM provides an energy efficient solution to the electric motor driven system for the wide range of applications.

In the present work an investigation is carried out to eliminate the need of mechanical position sensors. Different sensorless control techniques of the SRM drive are analyzed and then performances are compared. The flux-linkage based method is found more accurate than others as they utilize motor magnetic characteristics to estimate a rotor position. In the present work, this method is investigated in detail. The downside of this method is that it requires large amount of data of the motor magnetic characteristics which must be derived experimentally. Thus, it increases the cost and time of implementation. The accuracy of the method also depends upon the accuracy of the measurement and experimental setup used. Efforts have been made to reduce the requirement of the storage space and complexity of the implementation. The fixed-turn off angle method of rotor position estimation is proposed

and developed in the present work which requires lesser amount of data to store. This method is also cost effective, easy to implement and offers high accuracy. Downside of this method is that it does not allow multiphase excitation to reduce the torque ripple. It also deteriorates the peak torque capability of the motor in the high speed operation. This method gives coarse position information rather than estimating continuous rotor position. The method is suitable for the applications where the mechanical position sensor seems to be unreliable due to harsh environment condition. The ANN based rotor position technique is proposed and developed in the present work which is able to estimate the continuous rotor position where the neural network is used to map the non-linear relation of flux-current-angle. This method offers high accuracy of rotor position estimation and allows both the advance angle control and dwell angle control. However, this method is computation intensive which increases the cost and the complexity of implementation. An analytical method of rotor position estimation is also proposed and developed in the present work which reduces computation burden as well requires less storage data to estimate continuous rotor position estimation.

The implementation of the flux-linkage based sensorless technique is limited to the particular motor because it utilizes the magnetic characteristics of that motor. Even the magnetic characteristics of the two motors from the same manufacturing lot may not have exact match. This problem is investigated by the sensorless method that does not require prior knowledge about the motor magnetic characteristics. These methods monitor the phase current waveform and accordingly derive the pulses per electric cycle to represent a rotor angle. The current gradient sensorless method (CGSM) found accurate and easy to implement compared to others. This method is applicable to the SRM drive which incorporates PWM current controller. In the present work, the performance of the CGSM is investigated in detail to be incorporated with low-cost low frequency PWM drive. It was found that the issue of the stability arises during the transient in speed and load variation, which is mainly due to use of PLL. A modified CGSM proposed in the present work which does not require the use of PLL, shows the improvement in the transient stability of the system. This method is found economical and simple to design and implement. Furthermore, the CGSM can be incorporated with any motor having same numbers of stator/rotor poles, without any change in hardware.

A case study is conducted in the present work to investigate the performance of SRM drive as an In-wheel electric vehicle. This investigation shows the superior performance of the SRM drive in many aspects. The SRM drive provides high starting torque without excessive current and also provides larger battery range per one charge. The SRM offers numbers of advantages compared to conventional BLDC motor for the in-wheel vehicle system. It includes low-cost, smaller size, less weight, higher starting torque and higher

efficiency. The investigation concludes that the SRM fits the best for the vehicle propulsion application without having an issue of torque ripple.

The SRM technology is gaining acceptance from the industries mainly on account of its efficiency, speed-torque characteristics, size, weight and cost. The suitability of the SRM covers a wide operating range from few watts to MW and large numbers of application. Although, the complete success of the SRM drive needs proper choice of application, converter, control scheme and position sensing arrangement.

To summarize, in this dissertation, consolidated efforts are made to investigate the performance of the SRM drive. A non-linear modelling and simulation technique of the SRM is developed and examined in this dissertation. The low-cost SRM drive is designed and developed in this work where its performance is investigated with the simulation and experimental analysis. This thesis covers extensive investigation of sensorless techniques to eliminate the need of mechanical position sensors. Also, the applicability and advantages of SRM drive for the low power in-wheel electric vehicle are analysed.

8.2 FUTURE SCOPE

Research is a never ending process. In fact, an end of a research project is a beginning of a lot of other avenues for future work. Following aspects are identified for future research work in this area –

- The ANN based rotor position estimation technique developed in this work can be extended to reduce the phase transient error by incorporating ANN or fuzzy based flux estimator with the same. In case of ANN based implementation, numbers of hidden layers and numbers of neuron can be optimized using genetic algorithm.
- Furthermore, an effect of mutual inductance can be considered to obtain the precise simulation model of the motor.
- The analytical sensorless technique developed in this work provides accurate rotor position information with the requirement of minimum magnetic data to store. The algorithm for the compensation of the error in rotor position is derived for the operating speed range. The error in rotor position estimation is increase at other operating speed. Thus, further work can be carried out to extend the analytical sensorless method to produce the higher accuracy of rotor position estimation for the wide speed range without losing its simplicity.
- The modified CGSM offers accuracy with simplicity in implementation for the low frequency PWM controlled drive. However, to handle the large transient in load and speed, gain of the peak detection stage must be compensated for the speed and current.

It increases the complexity of the implementation as the relation amongst gain, speed and current is non-linear.

- Further investigation must be carried out to design the application specific SRM drive which not includes only selection and designing of speed controller, but also includes the selection of motor geometry, converter topology and position sensing scheme.

PUBLICATIONS FROM THE WORK

Journals

1. Design and Development of openloop CGSM for SR motor
   Journal of Scientific and Industrial Research, Vol-72(05), pp316-322, May 2013.

2. Implementation of Low Cost Switched Reluctance Motor Drive using RT Lab
   International Journal of Engineering Science & Advanced Technology, Vol-02 ISS-04,pp- 772-780, Jul-Aug 2012

3. Real Time Speed Control of Switched Reluctance Motor Drive using RT-Lab
   Accepted for publication in International Review of Automatic Control (IREACO).

4. Rotor Position Estimation Technique for the SR Motor
   Under Review in Sadhana Academy Proceedings in Engineering Sciences, Springer, Aug.2012.

International Conferences

1. Sensorless Control of Switched Reluctance Motor Drive: An analytical method
   IEEE International Conference on Advances in Engineering, Science and Management (ICAESM), 2012**, pp.571-576, March 2012**

2. ANN based Sensorless Rotor Position Estimation for the Switched Reluctance Motor
   IEEE International Conference on Engineering, NUiCONE-2011, Nirma University**, pp.1-6, Dec. 2011**

3. Novel Simulation Approach to Analyses the Performance of In-wheel SRM for an Electrical Vehicle
   IEEE International Conference on Energy Automation and Signal, ICEAS**2011, pp.187–191, Dec.2011.**

BIBLIOGRAPHY

1. **AbdulKadir M. N. and Yatim A. H. M.**, "Maximum efficiency operation of switched reluctance motor by controlling switching angles," *International Conference on Power Electronics and Drive Systems*, pp. 199-204, 1997.
2. **Abera A. G., Bandyopadhyay B., and Agarwal V.**, "Robust multirate output feedback sliding mode controller for sensorless induction motor," Systems Science-Wroclaw, vol. 32, no. 1, pp. 57, 2006.
3. **Abourida S., Balanger J., and Dufour C.**, "Real-Time HIL Simulation of a Complete PMSM Drive at 10 µs Time Step," *11th European Conference on Power Electronics and Applications*,pp 1-9, 2005.
4. **Acarnley P. P., Hill R. J., and Hooper C. W.**, "Detection of rotor position in stepping and switched motors by monitoring of current waveforms," IEEE Transactions on Industrial Electronics, vol. 32, no. 3, pp. 215-222, 1985.
5. **Akhter H. E., Sharma V. K., Chandra A., and Al-Haddad K.**, "Modeling simulation and performance analysis of switched reluctance motor operating with optimum value of fixed turn-on and turn-off switching angles," *IEEE 34th Annual Power Electronics Specialist Conference, PESC'03,* pp. 397-402, 2003.
6. **Akhter H. E., Sharma V. K., Chandra A., and Al-Haddad K.**, "Starting performance of switched reluctance motor with fixed turn-off angle control scheme," *IEEE 28th Annual Conference of the Industrial Electronics Society, IECON 02*, pp. 1020-1025, 2002.
7. **Aljaism W. and Rizk M. N. J.**, "Torque optimization for SRM by changing stator and yoke geometry," *International Conference on Communication, Computer & Power* Muscat, pp. 126-130, 2007.
8. **Andrada P., Blanque B., Martinez E., Perat J. I., Sanchez J. A., and Torrent M.**, "Environmental and life cycle cost analysis of one switched reluctance motor drive and two inverter-fed induction motor drives," IET electric power applications, vol. 6, no. 7, pp. 390-398.
9. **Andrada P., Blanque B., Perat J. I., Torrent M., Martinez E., and Sanchez J.A.**, "Comparative efficiency of switched reluctance and induction motor drives for slowly varying loads," Renewable Energy and Power Quality Journal, vol. 4, pp. 445--450, 2006.

10. **Arkadan A. A. and Kielgas B. W.**, "Switched reluctance motor drive systems dynamic performance prediction and experimental verification," IEEE Transactions on Energy Conversion, , vol. 9, no. 1, pp. 36-44, 1994.
11. **Barnes M. and Pollock C.**, "Power electronic converters for switched reluctance drives," IEEE Transactions on Power Electronics, , vol. 13, no. 6, pp. 1100-1111, 1998.
12. **Barrass P. G. and Mecrow B. C.**, "Flux and torque control of switched reluctance machines," IEE Proceeding Electric Power Applications, pp. 519-527, 1998.
13. **Bartos F. J.**," 'Forward to the past' with SR Technology," Control Engineering International, Nov, 1999.
14. **Bartos F. J.**," Resurgence for SR Motors, Drive?," Control Engineering, March, 2010.
15. **Bhiwapurkar N., Brekken T. K. A., and Mohan N.**, "Torque ripple optimization of switched reluctance motor using two-phase model and optimization search techniques," *37th IEEE Power Electronics Specialists Conference, 2006. PESC'06.*, pp. 1-6, 2006.
16. **Bhiwapurkar N., Jain A. K., and Mohan N.**, "Study of new stator pole geometry for improvement of SRM torque profile," *IEEE International Conference on Electric Machines and Drives,* pp. 516-520, 2005.
17. **Bhuvaneswari G., Rao P. S., Thakurta S. G., and Murthy S. S.**, "Impact of Dwell Angle on the Electromagnetic Torque Ripplesof the Switched Reluctance Motor," Defence Science Journal, vol. 58, no. 3, pp. 363-371, 2008.
18. **Blaabjerg F., Kjaer P. C., Rasmussen P. O. and Cossar C.**, "Improved digital current control methods in switched reluctance motor drives," IEEE Transactions on Power Electronics, vol. 14, no. 3, pp. 563-572, 1999.
19. **Bortoff S. A., Kohan R. R., and Milman R.**, "Adaptive control of variable reluctance motors: a spline function approach," IEEE Transactions on Industrial Electronics, vol. 45, no. 3, pp. 433-444, 1998.
20. **Bose B. K., Miller T. J. E., Szczesny P. M., and Bicknell W. H.**, "Microcomputer control of switched reluctance motor," IEEE Transactions on Industry Applications, vol. 22, no. 4, pp. 708-715, 1986.
21. **Bu J. and Xu L.**, "Eliminating starting hesitation for reliable sensorless control of switched reluctance motors," IEEE Transactions on Industry Applications, vol. 37, no. 1, pp. 59-66, 2001.
22. **Butler K. L., Ehsani M., and Kamath P.**, "A Matlab-based modeling and simulation package for electric and hybrid electric vehicle design," IEEE Transactions on Vehicular Technology, , vol. 48, no. 6, pp. 1770-1778, 1999.

23. **Cajander D. and Le-Huy H.**, "Design and optimization of a torque controller for a switched reluctance motor drive for electric vehicles by simulation," Mathematics and Computers in Simulation, vol. 71, no. 4, pp. 333-344, 2006.
24. **Cameron D. E., Lang J. H., and Umans S. D.**, "The origin and reduction of acoustic noise in doubly salient variable-reluctance motors," IEEE Transactions on Industry Applications, vol. 28, no. 6, pp. 1250-1255, 1992.
25. **Chaitanya B. V. K. and Agarwal V.**, "Fuzzy Logic based Sensorless Control of a BLDC motor," *International Conference on Electrical Energy Systems and Power Electronics in Emerging Economics*, pp 1-6, 2009
26. **Chakraborty C. and Hori Y.**, "Fast efficiency optimization techniques for the indirect vector-controlled induction motor drives," IEEE Transactions on Industry Applications, vol. 39, no. 4, pp. 1070-1076, 2003.
27. **Chancharoensook P. and Rahman M. F.**, "Dynamic modeling of a four-phase 8/6 switched reluctance motor using current and torque look-up tables," *IEEE 2002 28th Annual Conference of the Industrial Electronics Society, IECON 02*, pp. 491-496, 2002.
28. **Chancharoensook P., Rahman M. F. and Kensington S.**, "Determination of magnetisation and static torque characteristics of a four-phase switched reluctance motor: experimental investigations," *Australasian Universities Power Engineering Conference (AUPEC)*, pp. 613-618, 2001.
29. **Chang L.**, "Comparison of AC drives for electric vehicles-a report on experts' opinion survey," IEEE Aerospace and Electronic Systems Magazine, vol. 9, no. 8, pp. 7-11, 1994.
30. **Chapman P. L. and Sudhoff S. D.**, "Design and precise realization of optimized current waveforms for an 8/6 switched reluctance drive," IEEE Transactions on Power Electronics, vol. 17, no. 1, pp. 76-83, 2002.
31. **Chen H.**, "The switched reluctance motor drive for application in electric bicycle," *IEEE International Symposium on Industrial Electronics,* pp. 1152-1156, 2001.
32. **Cheng K. W. E., Yeung Y. P. B, Tang C. Y., Xue X. D., and Sutanto D.**, "Topology analysis of switched reluctance drives for electric vehicles," *IEE Eighth International Conference on Power Electronics and Variable Speed Drives,* pp. 512-517, 2000.
33. **Cheok A. D. and Fukuda Y.**, "A new torque and flux control method for switched reluctance motor drives," IEEE Transactions on Power Electronics, vol. 17, no. 4, pp. 543-557, 2002.
34. **Choi C., Kim S., Kim Y., and Park K.**, "A new torque control method of a switched reluctance motor using a torque-sharing function," IEEE Transactions on Magnetics, vol. 38, no. 5, pp. 3288-3290, 2002.

35. **Davis R. M., Ray W. F., and Blake R. J.**, "Inverter drive for switched reluctance motor: circuits and component ratings," IEE Proceedings B Electric Power Applications, pp. 126-136, 1981.
36. **Dawson G. E., Eastham A. R., and Mizia J.**, "Switched-reluctance motor torque characteristics: finite-element analysis and test results," IEEE Transactions on Industry Applications, no. 3, pp. 532-537, 1987.
37. **Dufour C., Balanger J., Abourida S., and Lapointe V.**, "FPGA-based real-time simulation of finite-element analysis permanent magnet synchronous machine drives," *IEEE Power Electronics Specialists Conference, 2007, PESC 2007,* pp. 909-915, 2007.
38. **Dufour C., Balanger J., and Lapointe V.**, "Fpga-based ultra-low latency hil fault testing of a permanent magnet motor drive using rt-lab-xsg," Simulation, vol. 84, no. 2-3, pp. 161-171, 2008.
39. **Ehsani M. and Fahimi B.**, "Elimination of position sensors in switched reluctance motor drives: state of the art and future trends," IEEE Transactions on Industrial Electronics, vol. 49, no. 1, pp. 40-47, 2002.
40. **Ehsani M., Husain I., and Kulkarni A. B.**, "Elimination of discrete position sensor and current sensor in switched reluctance motor drives," IEEE Transactions on Industry Applications, vol. 28, no. 1, pp. 128-135, 1992.
41. **Ehsani M., Husain I., Mahajan S., and Ramani K. R.**, "New modulation encoding techniques for indirect rotor position sensing in switched reluctance motors," IEEE Transactions on Industry Applications, vol. 30, no. 1, pp. 85-91, 1994.
42. **Elbuluk M. E. and Kankam M.**, "Potential starter/generator technology for future aerospace application," IEEE Aerospace and Electronic Systems Magazine, vol. 11, no. 10, pp. 17-24, 1996.
43. **Elmas C.**, "Position sensorless operation of a switched reluctance drive based on observer," *Fifth European Conference on Power Electronics and Applications*, pp. 82-87, 1993.
44. **Emadi A.**, "Feasibility of power electronic converters for low-voltage (42 V) SRM drives in mildly hybrid electric traction systems," *IEEE International Electric Machines and Drives Conference, IEMDC 2001*, pp. 585-587, 2001.
45. **Fahimi B., Suresh G., Mahdavi J. and Ehsami M.**, "A new approach to model switched reluctance motor drive application to dynamic performance prediction, control and design," *29th Annual IEEE Power Electronics Specialists Conference, PESC 98,* pp. 2097-2102, 1998.
46. **Fahimi B., Suresh G., Rahman K. M. and Ehsani M.**, "Mitigation of acoustic noise and vibration in switched reluctance motor drive using neural network based current

profiling," *IEEE Thirty-Third IAS Annual Meeting Industry Applications Conference,* pp. 715-722, 1998.

47. **Fitzgerald A. E., Kingsley C. and Umans S. D.**, *Electric machinery*: Tata McGraw-Hill Education, 2002.
48. **Franceschini G., Pirani S., Rinaldi M., and Tassoni C.**, "SPICE-assisted simulation of controlled electric drives: an application to switched reluctance drives," IEEE Transactions on Industry Applications*,* vol. 27, no. 6, pp. 1103-1110, 1991.
49. **Fulton N. N.**, "SR Drives for battery electric traction-a comparative assessment," *IEE Colloquium on Motors and Drives for Battery Powered Propulsion,* pp. 4/1-4/7, 1993.
50. **Gallegos-Lopez G., Kjaer P. C., and Miller T. J. E.**, "A new sensorless method for switched reluctance motor drives," IEEE Transactions on Industry Applications*,* vol. 34, no. 4, pp. 832-840, 1998.
51. **Gallegos-Lopez G., Kjaer P. C., and Miller T. J. E.**, "High-grade position estimation for SRM drives using flux linkage/current correction model," IEEE Transactions on Industry Applications*,* vol. 35, no. 4, pp. 859-869, 1999.
52. **Gao H., Salmasi F. R., and Ehsani M.**, "Inductance model-based sensorless control of the switched reluctance motor drive at low speed," IEEE Transactions on Power Electronics*,* vol. 19, no. 6, pp. 1568-1573, 2004.
53. **Ha T. K., Kim C. H., Kim J. H., Pyo S. Y. and Lim S. K.**, "Simple and high-performance drive of switched reluctance motors for low-cost applications," *IEEE International Symposium on Industrial Electronics, ISIE'97,* pp. 631-636, 1997.
54. **Hajatipour M. and Farrokhi M.**, "Adaptive intelligent speed control of switched reluctance motors with torque ripple reduction," Energy Conversion and Management*,* vol. 49, no. 5, pp. 1028-1038, 2008.
55. **Harris M. R., Finch J. W., Mallick J. A., and Miller T. J. E.**, "A review of the integral-horsepower switched reluctance drive," IEEE Transactions on Industry Applications, no. 4, pp. 716-721, 1986.
56. **Harris M. R. and Miller T. J. E.**, "Comparison of design and performance parameters in switched reluctance and induction motors," *Fourth International Conference on Electrical Machines and Drives,* pp. 303-307, 1989.
57. **Harakawa M., Yamasaki H., Nagano T., Abourida S., Dufour C. and Belanger J.**, “Real-Time Simulation of a Complete PMSM Drive at 10 us Time Step,” *International Power Electronics Conference, IPEC 2005, pp. 1-5*, 2005.
58. **Harris W. D. and Lang J. H.**, "A simple motion estimator for variable-reluctance motors," IEEE Transactions on Industry Applications*,* vol. 26, no. 2, pp. 237-243, 1990.

59. **Hashemnia N. and Asaei B.**, "Comparative study of using different electric motors in the electric vehicles," *18th International Conference on Electrical Machines, ICEM 2008*, pp. 1-5, 2008.

60. **Haykin S. S.**, *Neural networks: a comprehensive foundation*: Prentice Hall Englewood Cliffs, NJ, 2007.

61. **Henriques L. O. A. P., Rolim L. G. B., Suemitsu W. I., Branco P. J. C., and Dente J. A.**, "Torque ripple minimization in a switched reluctance drive by neuro-fuzzy compensation," IEEE Transactions on Magnetics, , vol. 36, no. 5, pp. 3592-3594, 2000.

62. **Howard D., Mark B., Martin H.,** *Neural Network Toolbox 6.0 User's Guide*, by The MathWorks, Inc, 2008.

63. **Husain I.**, "Minimization of torque ripple in SRM drives," IEEE Transactions on Industrial Electronics, vol. 49, no. 1, pp. 28-39, 2002.

64. **Husain I. and Ehsani M.**, "Torque ripple minimization in switched reluctance motor drives by PWM current control," IEEE Transactions on Power Electronics, vol. 11, no. 1, pp. 83-88, 1996.

65. **Husain I., Sodhi S., and Ehsani M.**, "A sliding mode observer based controller for switched reluctance motor drives," *IEEE Industry Applications Society Annual Meeting,* pp. 635-643, 1994.

66. **Ichinokura O., Onda T., Kimura M., Watanabe T., Yanada T., and Guo H. J.**, "Analysis of dynamic characteristics of switched reluctance motor based on SPICE," IEEE Transactions on Magnetics, vol. 34, no. 4, pp. 2147-2149, 1998.

67. **Ilic'-Spong M., Marino R., Peresada S., and Taylor D.**, "Feedback linearizing control of switched reluctance motors," IEEE Transactions on Automatic Control, vol. 32, no. 5, pp. 371-379, 1987.

68. **Jain A. K. and Mohan N.**, "Modeling and experimental characterization of SRMs for simultaneous two phase excitation," *29th Annual Conference of the IEEE Industrial Electronics Society, IECON'03,* pp. 1027-1032, 2003.

69. **Jain A. K. and Mohan N.**, "SRM power converter for operation with high demagnetization voltage," IEEE Transactions on Industry Applications, vol. 41, no. 5, pp. 1224-1231, 2005.

70. **Jain A. K. and Mohan N.**, "Dynamic modeling, experimental characterization, and verification for SRM operation with simultaneous two-phase excitation," IEEE Transactions on Industrial Electronics, vol. 53, no. 4, pp. 1238-1249, 2006.

71. **Jeong K. I., Lee J. H., and Ahn J. W.**, "Comparative analysis of SRMs for automotive cooling fan application," *IEEE Vehicle Power and Propulsion Conference VPPC 2012*, pp. 598-602, 2012.

72. **Jones S. R. and Drager B. T.**, "Performance of a high-speed switched reluctance starter/generator system using electronic position sensing," *IEEE Thirtieth IAS Annual Meeting Industry Applications Conference,* pp. 249-253, 1995.
73. **Kalaivani L., Marimuthu N. S. and Subburaj P.**, "Intelligent control for torque-ripple minimization in switched reluctance motor," *International Conference on Electrical Energy Systems, ICEES 2011*, pp. 182-186, 2011.
74. **Kalan B. A., Lovatt H. C., and Prout G.**, "Voltage control of switched reluctance machines for hybrid electric vehicles," *IEEE 33rd Annual Power Electronics Specialists Conference, pesc 02,* pp. 1656-1660, 2002.
75. **Kamalakannan C., Kamaraj V., Paramasivam S. and Paranjothi S. R.**, "Switched reluctance machine in automotive applications: A technology status review," *International Conference on Electrical Energy Systems, ICEES 2011*, pp. 187-197, 2011.
76. **Kim C. C., Hur J. and Hyun D.-S.**, "Simulation of a switched reluctance motors using Matlab/M-file," *IEEE 28th Annual Conference of the Industrial Electronics Society, IECON 02*, pp. 1066-1071, 2002.
77. **Klode H., Omekanda A. M., Lequesne B., Gopalakrishnan S., Khalil A., Underwood S., and Husain I.**, "The potential of switched reluctance motor technology for electro-mechanical brake applications," *Proceedings of the SAE world congress, Detroit, MI*, pp. 01-0296, 2006.
78. **Krishnamurthy M., Edrington C. S. and Fahimi B.**, "Prediction of rotor position at standstill and rotating shaft conditions in switched reluctance machines," IEEE Transactions on Power Electronics, vol. 21, no. 1, pp. 225-233, 2006.
79. **Krishnan R.**, *Switched reluctance motor drives: modeling, simulation, analysis, design, and applications*: CRC Press LLC, 2001.
80. **Krishnan R. and Bharadwaj A. S.**, "A comparative study of various motor drive systems for aircraft applications," *IEEE Annual Meeting of Industry Applications Society,* pp. 252-258, 1991.
81. **Krishnan R. and Materu P. N.**, "Design of a single-switch-per-phase converter for switched reluctance motor drives," IEEE Transactions on Industrial Electronics, vol. 37, no. 6, pp. 469-476, 1990.
82. **Lang J. H. and Vallese F. J.**, "Variable-reluctance motor drives for electric vehicle propulsion," United States Department of Energy Report, DOE/CS-54209-26, 1985.
83. **Laudensack C., Yu Q. and Gerling D.**, "Investigation of different parameters on the performance of switched reluctance machines," *XIX International Conference on Electrical Machines, ICEM 2010*, pp. 1-6, 2010.

84. **Lawrenson P. J., Stephenson J. M., Fulton N. N., Blenkinsop P. T. and Corda J.**, "Variable-speed switched reluctance motors," IEE Proceedings B Electric Power Applications, vol. 127, no. 4, pp. 253-265, Jul. 1980.

85. **Le-Huy H. and Brunelle P.**, "A versatile nonlinear switched reluctance motor model in Simulink using realistic and analytical magnetization characteristics," *31st Annual Conference of IEEE Industrial Electronics Society, IECON 2005*, 2005, pp1-6, 2005.

86. **Le-Huy H., Viarouge P. and Slimani K.**, "A current-controlled quasi-resonant converter for switched reluctance motor," *16th Annual Conference of IEEE Industrial Electronics Society, IECON '90,* vol.2, pp. 1022-1028, 1990.

87. **Li J. and Sun H.**, "Modeling and simulation of four-phase 8/6 switched reluctance motor with an improved winding configuration," *International Conference on Computer Science and Software Engineering,* pp. 1045-1048, 2008.

88. **Liptak M.**, "Principle of Design of Four-phase Low-power Switched Reluctance Machine Aimed: to the Maximum Torque Production," Journal of Electrical Engineering-Bratislava, vol. 55, pp. 138-143, 2004.

89. **Lovatt H. C., McClelland M. L. and Stephenson J. M.**, "Comparative performance of singly salient reluctance, switched reluctance, and induction motors," *IEE Conference Publication, EMD97*, No. 444, 1997.

90. **Lu W., Keyhani A., Klode H. and Proca A. B.**, "Modeling and parameter identification of switched reluctance motors from operating data using neural networks," *IEEE International Electric Machines and Drives Conference, IEMDC'03*, 2003, pp. 1709-1713, 2003.

91. **Lumsdaine A. and Lang J. H.**, "State observers for variable-reluctance motors," IEEE Transactions on Industrial Electronics, vol. 37, no. 2, pp. 133-142, 1990.

92. **Lyons J. P, MacMinn S. R., and Preston M. A.**, "Flux-current methods for SRM rotor position estimation," in *IEEE Annual Meeting of Industry Applications Society,* pp. 482-487, 1991.

93. **Mademlis C. and Kioskeridis I.**, "Performance optimization in switched reluctance motor drives with online commutation angle control," IEEE Transactions on Energy Conversion, vol. 18, no. 3, pp. 448-457, 2003.

94. **Mahdavi J., Suresh G., Fahimi B., and Ehsani M.**, "Dynamic modeling of nonlinear SRM drive with Pspice," *IEEE Thirty-Second IAS Annual Meeting Industry Applications Conference, IAS'97,* pp. 661-667, 1997.

95. **Manzer D. G., Varghese M., and Thorp J. S.**, "Variable reluctance motor characterization," IEEE Transactions on Industrial Electronics, vol. 36, no. 1, pp. 56-63, 1989.

96. **McCann R. A., Islam M. S., and Husain I.**, "Application of a sliding-mode observer for position and speed estimation in switched reluctance motor drives," IEEE Transactions on Industry Applications, vol. 37, no. 1, pp. 51-58, 2001.

97. **Mese E. and Torrey D. A.**, "An approach for sensorless position estimation for switched reluctance motors using artifical neural networks," IEEE Transactions on Power Electronics, vol. 17, no. 1, pp. 66-75, 2002.

98. **Miller T. J. E.**, *Brushless permanent-magnet and reluctance motor drives*: Oxford Science Publications, 1989.

99. **Miller T. J. E.**, "Converter volt-ampere requirements of the switched reluctance motor drive," IEEE Transactions on Industry Applications, no. 5, pp. 1136-1144, 1985.

100. **Miller T. J. E.**, *Electronic control of switched reluctance machines*: Newnes, 2001.

101. **Miller T. J. E.**, *PC-SRD Version 8.5 User Manual*: SPEED Laboratory, University of Glasgow, 2004.

102. **Miller T. J. E., Bower P. G., Becerra R., and Ehsani M.**, "Four-quadrant brushless reluctance motor drive," *Third International Conference on Power Electronics and Variable-Speed Drives,* pp. 273-276, 1988.

103. **Miller T. J. E., Cossar C., and Anderson D.**, "A new control IC for switched reluctance motor drives," *Fourth International Conference on Power Electronics and Variable-Speed Drives,* pp. 331-335, 1991.

104. **Miller T. J. E., Glinka M., McGilp M., Cossar C., Gallegos-Lopez G., Ionel D., and Olaru M.**, "Ultra-fast model of the switched reluctance motor," *IEEE Thirty-Third IAS Annual Meeting Industry Applications Conference,* pp. 319-326, 1998.

105. **Miller T. J. E. and McGilp M.**, "Nonlinear theory of the switched reluctance motor for rapid computer-aided design," *IEE Proceedings B Electric Power Applications*, pp. 337-347, 1990.

106. **Mir S., Elbuluk M. E., and Husain I.**, "Torque-ripple minimization in switched reluctance motors using adaptive fuzzy control," IEEE Transactions on Industry Applications, vol. 35, no. 2, pp. 461-468, 1999.

107. **Murthy S. S.**, "Modeling of a Switched Reluctance Motor in Sensorless and With Sensor Modes," Journal of Power Electronics, vol. 6, no. 4, pp. 315-321, 2006.

108. **Murthy S. S., Singh B., and Kumar Sharma V.**, "A frequency response method to estimate inductance profile of switched reluctance motor," *International Conference on Power Electronics and Drive Systems,* pp. 181-187, 1997.

109. **Nagel N. J. and Lorenz R. D.**, "Modeling of a saturated switched reluctance motor using an operating point analysis and the unsaturated torque equation," IEEE Transactions on Industry Applications, vol. 36, no. 3, pp. 714-722, 2000.

110. **Parreira B., Rafael S., Pires A. J. and Branco P. J. C.**, "Obtaining the magnetic characteristics of an 8/6 switched reluctance machine: from FEM analysis to the experimental tests," IEEE Transactions on Industrial Electronics, vol. 52, no. 6, pp. 1635-1643, 2005.

111. **Panda S. K. and Amaratunga G. A. J.**, "Waveform detection technique for indirect rotor-position sensing of switched-reluctance motor drives. I. Analysis," IEE Proceedings B Electric Power Applications, vol. 140, no. 1, pp. 80-88, 1993.

112. **Panda S. K. and Amaratunga G. A. J.**, "Waveform detection technique for indirect rotor-position sensing of switched-reluctance motor drives. II. Experimental results," IEE Proceedings B Electric Power Applications, vol. 140, no. 1, pp. 89-96, 1993.

113. **Panda S. K. and Dash P. K.**, "Application of nonlinear control to switched reluctance motors: a feedback linearisation approach," *IEE Proceedings Electric Power Applications,* pp. 371-379, 1996.

114. **Panda S. K., Zhu X. M., and Dash P. K.**, "Fuzzy gain scheduled PI speed controller for switched reluctance motor drive," *23rd International Conference on Industrial Electronics, Control and Instrumentation, IECON 97*, pp. 989-994, 1997.

115. **Pekarek S. D., Wasynczuk O., and Hegner H. J.**, "An efficient and accurate model for the simulation and analysis of synchronous machine/converter systems," IEEE Transactions on Energy Conversion, vol. 13, no. 1, pp. 42-48, 1998.

116. **Pollock C. and Wu C. Y.**, "Acoustic noise cancellation techniques for switched reluctance drives," IEEE Transactions on Industry Applications, vol. 33, no. 2, pp. 477-484, 1997.

117. **Rafajdus P., Zrak I. and Hrabovcova V. R.**, "Analysis of the Switched Reluctance Motor (SRM) Parameters," Journal of Electrical Engineering-Bratislava, vol. 55, no. 7/8, pp. 195-200, 2004.

118. **Rahman K. M., Fahimi B., Suresh G., Rajarathnam A. V., and Ehsani M.**, "Advantages of switched reluctance motor applications to EV and HEV: design and control issues," IEEE Transactions on Industry Applications, vol. 36, no. 1, pp. 111-121, 2000.

119. **Rahman K. M., Gopalakrishnan S., Fahimi B., Velayutham Rajarathnam A., and Ehsani M.**, "Optimized torque control of switched reluctance motor at all operational regimes using neural network," IEEE Transactions on Industry Applications, vol. 37, no. 3, pp. 904-913, 2001.

120. **Rahman K. M. and Schulz S. E.**, "High performance fully digital switched reluctance motor controller for vehicle propulsion," *IEEE Thirty-Sixth IAS Annual Meeting Industry Applications Conference,* pp. 18-25, 2001.

121. **Rain X., Hilairet M. I. and Bethoux O.**, "Comparative study of various current controllers for the switched reluctance machine," *IEEE Vehicle Power and Propulsion Conference, VPPC 2010*, pp. 1-6, 2010.

122. **Ramamurthy S. S. and Balda J. C.**, "Sizing a switched reluctance motor for electric vehicles," IEEE Transactions on Industry Applications, vol. 37, no. 5, pp. 1256-1264, 2001.

123. **Ray W. F., Lawrenson P. J., Davis R. M., Stephenson J. M., Fulton N. N., and Blake R. J.**, "High-performance switched reluctance brushless drives," IEEE Transactions on Industry Applications, no. 4, pp. 722-730, 1986.

124. **Russa K., Husain I., and Elbuluk M. E.**, "Torque-ripple minimization in switched reluctance machines over a wide speed range," IEEE Transactions on Industry Applications, vol. 34, no. 5, pp. 1105-1112, 1998.

125. **Sahoo N. C., Xu J. X., and Panda S. K.**, "Low torque ripple control of switched reluctance motors using iterative learning," IEEE Transactions on Energy Conversion, vol. 16, no. 4, pp. 318-326, 2001.

126. **Saint-Eve F., Sauvey C., and Abba G.**, "A 100kHz-2kW converter for switched reluctance rnotor used in high speed machining applications," in *IEEE 32nd Annual Conference on Industrial Electronics, IECON 2006*, pp. 2274-2279, 2006.

127. **Shang C., Reay D., and Williams B.**, "Adapting CMAC neural networks with constrained LMS algorithm for efficient torque ripple reduction in switched reluctance motors," IEEE Transactions on Control Systems Technology, vol. 7, no. 4, pp. 401-413, 1999.

128. **Sharma V. K., Murthy S. S., and Singh B.**, "Analysis of switched reluctance motor drive under fault conditions," *IEEE Thirty-Third IAS Annual Meeting Industry Applications Conference,* pp. 553-562, 1998.

129. **Sharma V. K., Murthy S. S., and Singh B.**, "An improved method for the determination of saturation characteristics of switched reluctance motors," IEEE Transactions on Instrumentation and Measurement, vol. 48, no. 5, pp. 995-1000, 1999.

130. **Sharma V. K., Singh B., and Murthy S. S.**, "Performance analysis of unity power factor converter-inverter fed switched reluctance motor drive," *IEEE International Electric Machines and Drives Conference*, pp. WA1/5.1-WA1/5.3, 1997.

131. **Shen L., Wu J. and Yang S.**, "Initial position estimation in SRM using bootstrap circuit without predefined inductance parameters," IEEE Transactions on Power Electronics, vol. 26, no. 9, pp. 2449-2456, 2011.

132. **Shukla J. and Fernandes B. G.**, "Three-phase soft-switched PWM inverter for motor drive application," IET Electric Power Applications, vol. 1, no. 1, pp. 93-104, 2007.

133. **Singh B., Jain P., Mittal A. P., and Gupta J. R. P.**, "Direct torque control: a practical approach to electric vehicle," *IEEE Power India Conference,* p. 4, 2006.

134. **Singh B., Sharma V. K., and Murthy S. S.**, "Performance analysis of adaptive fuzzy logic controller for switched reluctance motor drive system," *IEEE Thirty-Third IAS Annual Meeting Industry Applications Conference,* pp. 571-579, 1998.

135. **Singh B., Sharma V. K., and Murthy S. S.**, "Comparative study of PID, sliding mode and fuzzy logic controllers for four quadrant operation of switched reluctance motor," *International Conference on Power Electronic Drives and Energy Systems for Industrial Growth,* pp. 99-105, 1998.

136. **Soares F. and Costa Branco P. J.**, "Simulation of a 6/4 switched reluctance motor based on Matlab/Simulink environment," IEEE Transactions on Aerospace and Electronic Systems, vol. 37, no. 3, pp. 989-1009, 2001.

137. **Somesan L. E., Padurariu E., Viorel I. A,, Martis C., and Cornea O.**, "Simple analytical models of the switched reluctance motors, case study," *XIX International Conference on Electrical Machines, ICEM 2010*, pp. 1-6, 2010.

138. **Stankovic A. M., Tadmor G., Coric Z. J., and Agirman I.**, "On torque ripple reduction in current-fed switched reluctance motors," IEEE Transactions on Industrial Electronics*,* vol. 46, no. 1, pp. 177-183, 1999.

139. **Stephenson J. M., Hughes A., and Mann R.**, "Torque ripple minimisation in a switched reluctance motor by optimum harmonic current injection," *IEE Proceedings Electric Power Applications*, pp. 322-328, 2001.

140. **Tandon P., Velayutham Rajarathnam A., and Ehsani M.**, "Self-tuning control of a switched reluctance motor drive with shaft position sensor," *IEEE Thirty-First IAS Annual Meeting Industry Applications Conference, IAS'96,* pp. 101-108, 1996.

141. **Torrey D. A.**, "Switched reluctance generators and their control," *IEEE* Industrial Electronics*,* vol. 49, no. 1, pp. 3-14, 2002.

142. **Torrey D. A.**, "Variable-reluctance generators in wind-energy systems," *24th Annual IEEE Power Electronics Specialists Conference, PESC'93*, pp. 561-567, 1993.

143. **Torrey D. A. and Hassanin M.**, "The design of low-speed variable-reluctance generators," *IEEE Thirtieth IAS Annual Meeting Industry Applications Conference, IAS'95,* pp. 427-433, 1995.

144. **Torrey D. A. and Lang J. H.**, "Modelling a nonlinear variable-reluctance motor drive," IEE Proceedings B Electric Power Applications*,* vol. 137, no. 5, pp. 314-326, 1990.

145. **Torrey D. A. and Lang J. H.**, "Optimal-efficiency excitation of variable-reluctance motor drives," *IEE Proceedings B Electric Power Applications*, pp. 1-14, 1991.

146. **Torrey D. A., Niu X. M., and Unkauf E. J.**, "Analytical modelling of variable-reluctance machine magnetisation characteristics," *IEE Proceedings Electric Power Applications*, pp. 14-22, 1995.

147. **Torrey D. A.**, *Constant-speed optimal-eficiency control of nonlinear variable reluctance motor drives*, PhD Thesis, Department of Electrical Engineering and Computer Science, Massachusetts Institute of Technology, USA, January 1988.

148. **Uematsu T. and Hoft R. G.**, "Resonant power electronic control of switched reluctance motor for electric vehicle propulsion," *26th Annual IEEE Power Electronics Specialists Conference, PESC'95*, pp. 264-269, 1995.

149. **Vamsidhar S. and Fernandes B. G.**, "Hardware-in-the-loop simulation based design and experimental evaluation of DTC strategies," *35th Annual IEEE Power Electronics Specialists Conference, PESC 04,* pp. 3615-3621, 2004.

150. **Van der Broeck H., Gerling D., and Bolte E.**, "Switched reluctance drive and PWM induction motor drive compared for low cost applications," *Fifth European Conference on Power Electronics and Applications,* pp. 71-76, 1993.

151. **Vandana R. and Fernandes B. G.**, "Optimal sizing of motorâ€"Battery system for in wheel electric vehicles," *36th Annual Conference on IEEE Industrial Electronics Society*, *IECON 2010,* pp. 2510-2515, 2010.

152. **Vattikuti N., Rallabandi V., and Fernandes B, G.**, "A novel high torque and low weight segmented switched reluctance motor," *IEEE Power Electronics Specialists Conference, PESC 2008*, pp. 1223-1228, 2008.

153. **Vijayakumar K., Karthikeyan R., Paramasivam S., Arumugam R. and Srinivas K. N.**, "Switched reluctance motor modeling, design, simulation, and analysis: a comprehensive review," IEEE Transactions on Magnetics*,* vol. 44, no. 12, pp. 4605-4617, 2008.

154. **Vijayraghavan P.**, "Design of Switched Reluctance Motors and Development of a Universal Controller for Switched Reluctance and Permanent Magnet Brushless DC Motor Drives," Phd Thesis, Virginia Polytechnic Institute and State University, 2011.

155. **Vukosavic S. and Stefanovic V. R.**, "SRM inverter topologies: a comparative evaluation," IEEE Transactions on Industry Applications*,* vol. 27, no. 6, pp. 1034-1047, 1991.

156. **Wang X. and Lai J.-S.**, "Small-signal modeling and control for PWM control of switched reluctance motor drives," *33rd Annual IEEE Power Electronics Specialists Conference, pesc 02,* pp. 546-551, 2002.

157. **Wichert T. and Hans K.**, "Innovative compact drives with switched reluctance motor (SRM) for industrial applications," Prace Naukowe Instytutu Maszyn, Napedow i Pomiarow Elektrycznych Politechniki Wroclawskiej, University of Applied Sciences Dresden, Germany, vol. 62, no. 28, pp. 3-11, 2008.

158. **Wu C. Y. and Pollock C.**, "Analysis and reduction of vibration and acoustic noise in the switched reluctance drive," IEEE Transactions on Industry Applications, vol. 31, no. 1, pp. 91-98, 1995.

159. **Xu J.-X., Panda S. K. and Zheng Q.**, "Multiobjective optimization of current waveforms for switched reluctance motors by genetic algorithm," *Proceedings of the 2002 Congress on Evolutionary Computation, CEC'02*, pp. 1860-1865, 2002.

160. **Xue X. D., Cheng K., and Cheung N. C.**, "Selection of electric motor drives for electric vehicles," *Australasian Universities Power Engineering Conference, AUPEC'08*, pp. 1-6, 2008.

161. **Zaim M. E., Dakhouche K., and Bounekhla M.**, "Design for torque ripple reduction of a three-phase switched-reluctance machine," IEEE Transactions on Magnetics, vol. 38, no. 2, pp. 1189-1192, 2002.

162. **Zhu X. M., Panda S. K., Dash P. K., and Tan S. H.**, "Experimental investigation of variable structural PID control for switched reluctance motor drives," *International Conference on Power Electronics and Drive Systems,* pp. 205-210, 1997.

163. **Zurada J. M.**, *Introduction to artificial neural systems* vol. 408: West St. Paul, 1992.

PHOTOGRAPHS OF THE EXPERIMENTAL SETUP

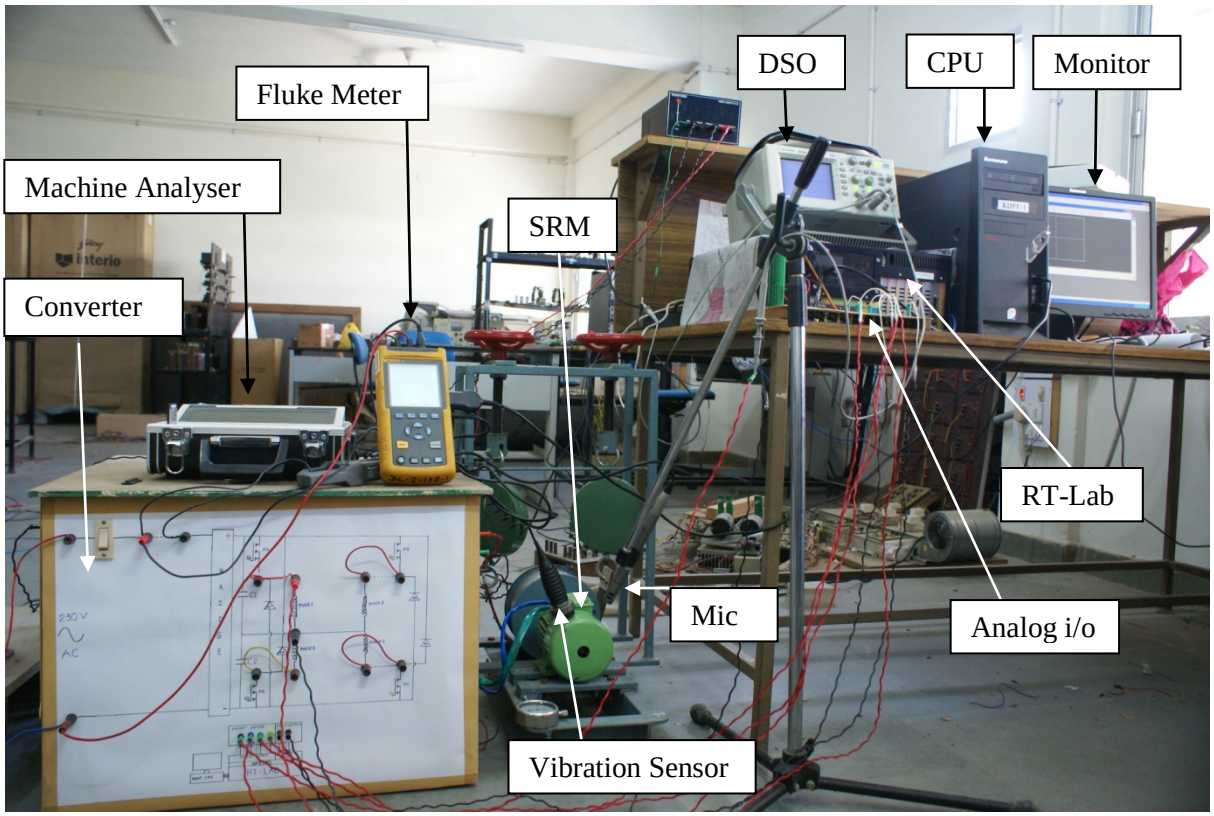

Figure A.1 Complete hardware setup of SRM drive with RT-Lab

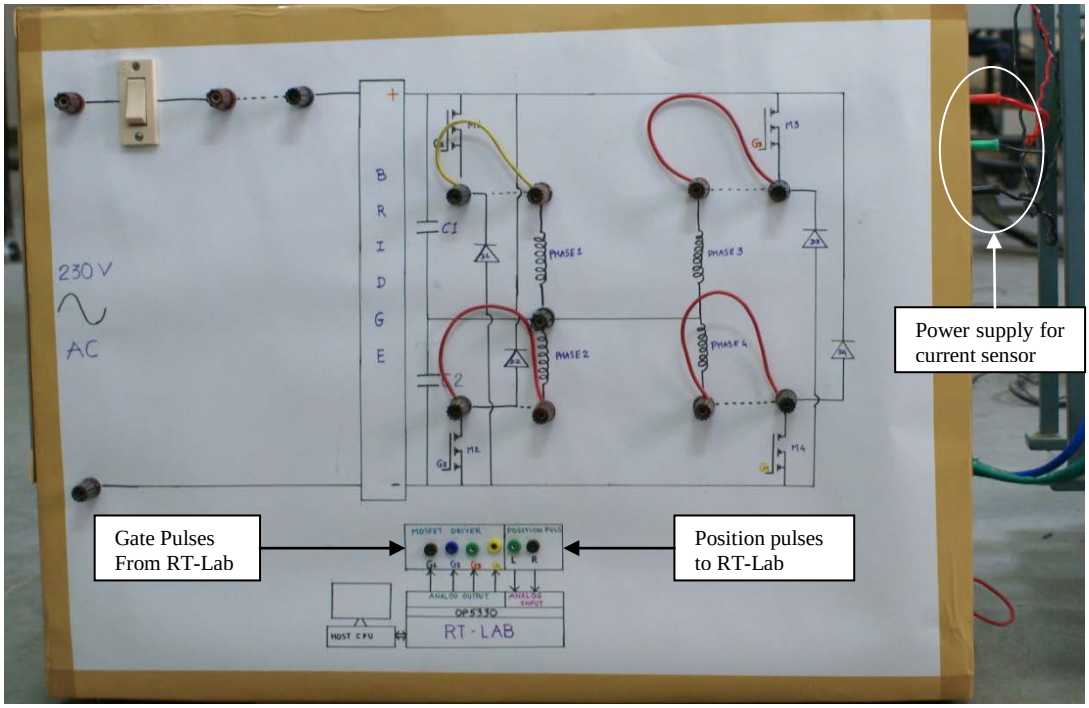

Figure A.2 Split DC converter and MOSFET drivers unit

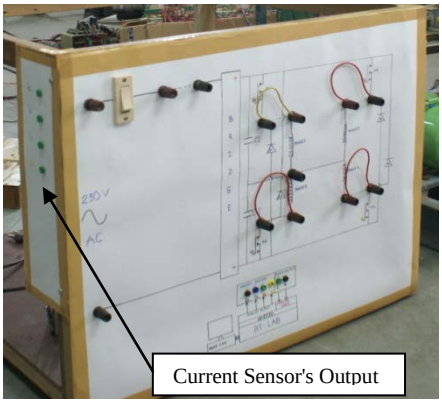

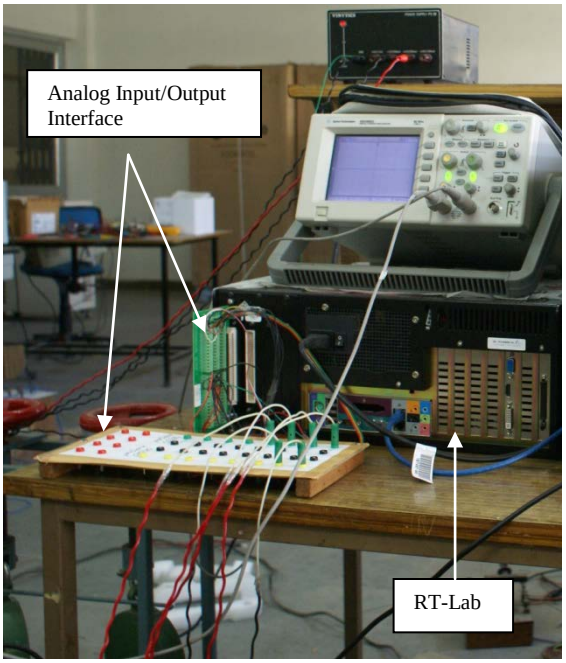

Figure A.3 Analog input-output interface of RT-Lab

APPENDIX-B

RT-LAB CONFIGURATION

Table B.1 RT-Lab Simulator Characteristics

Hardware	PC with dual quad-core Intel processor (2.3 GHz)
Real-time operating system	QNX or RedHawk Linux
RT-Lab Version	10.3
Digital I/O	16 Di_n - 16 D_{out} (Time Stamped)
Analog I/O	16 Inputs and 16 Outputs
User Programmable FPGA	Xilinx Spartan 3

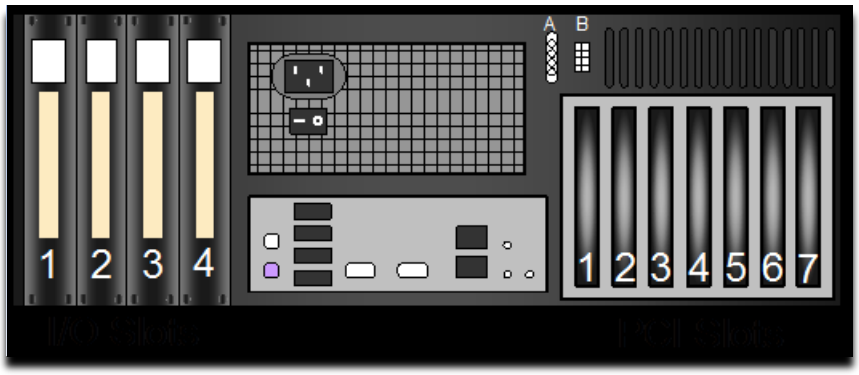

Figure B.1 Rear view of the RT-Lab simulator

Table B.2 Power slots

Power Slot	Power source
A	+5 VDC, +12 VDC
B	+/- 18 VDC

Table B.3 Input output slots

I/O Slot	Carrier Type	Section A	Section B
1	OP5220	OP5330 Analog Out	OP5340 Analog In
2	OP5210-S3	OP5311 Digital In	OP5312 Digital Out
3	Empty	Empty	Empty
4	Empty	Empty	Empty

RECONFIGURABLE FPGA BOARD

Table B.4 FPGA Configuration

Model Name	FPGA	Bus Type	FPGA Clock	Gate	Logic Cells	Slices	CLB Flip Flop	I/O Lines
OP5142	Xilinx Spartan 3 XC3S500	PCI-Express 1x	100 MHz	5M	74,880 (74K)	33K	66K	296

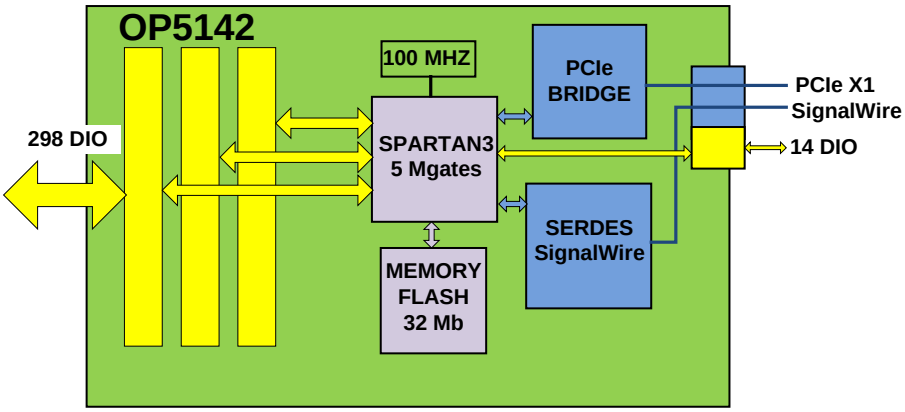

Figure B.2 Block diagram of OP5142

SignalWire : 625 Mb/sec

PCIe X1: 2.5 Gb/sec

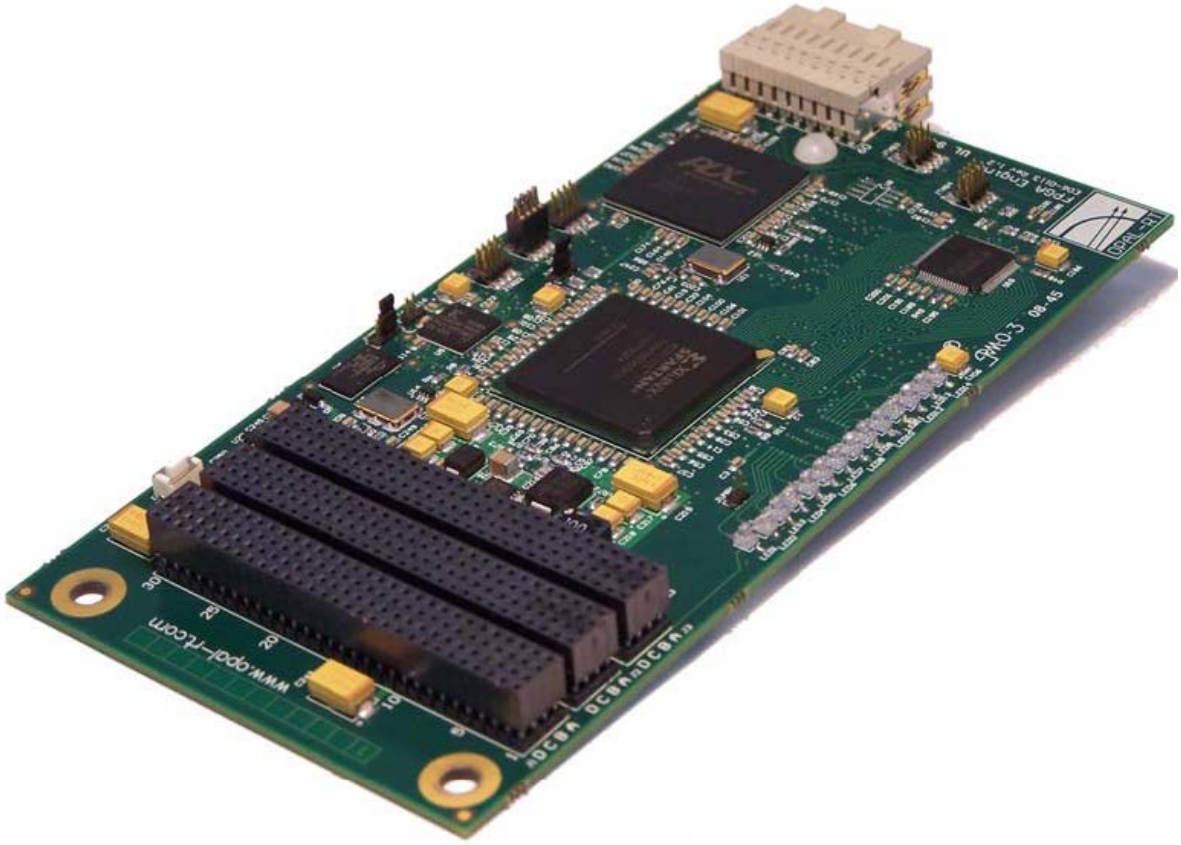

Figure B.3 The OP5142 reconfigurable board

Table B.5 Configuring FPGA board through 'OP5142EX1 Ctrl'

I/O BitStream	Index
OP5142_1-EX-0000-1_3_4-S_160_C3_C1_EB_EA_EB_EA-01-01.bin	0

ANALOG CONVERSION INTERFACE

Two types of analog conversion modules are available: the OP5340 is a bank of analog-to-digital converters and the OP5330 is a bank of digital-to-analog converters. It features follows

OP5330 Analog Output Module

Feature/Overview

- Up to 16 analog output channels
- One 16-bit DAC per channel
- Simultaneous output on all channels: eliminates skew errors inherent in multiplexed channels
- 1 MS/s max. update rate per channel
- Total throughput of 16 MS/s for 16 channels
- Voltage ranges of +/- 16 Volts
- On-board signal conditioning
- Maximum current +/- 15 mA
- Outputs short-circuit protected at 30 mA
- Minimum conversion/acquisition time is 1 µs per channel
- Library of drag-and-drop blocks for Simulink

The OP5330 features 16 channels with individual 16-bit Digital-to-Analog Converters (DAC) that ensures simultaneous signal generation from multiple channels, thus eliminating the skew errors associated with multiplexed channels. Each DAC can update up to 1 MS/s, giving a total throughput of 16 Ms/s. On-board signal conditioning provides voltage ranges of +/- 16 V.

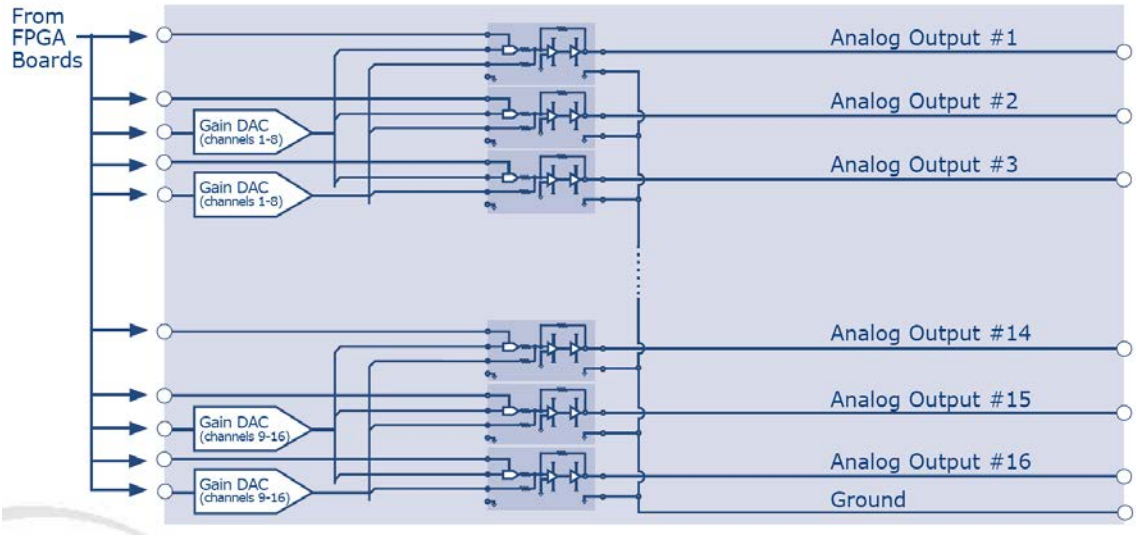

Figure B.4 Schematic of 0P5330 analog output module

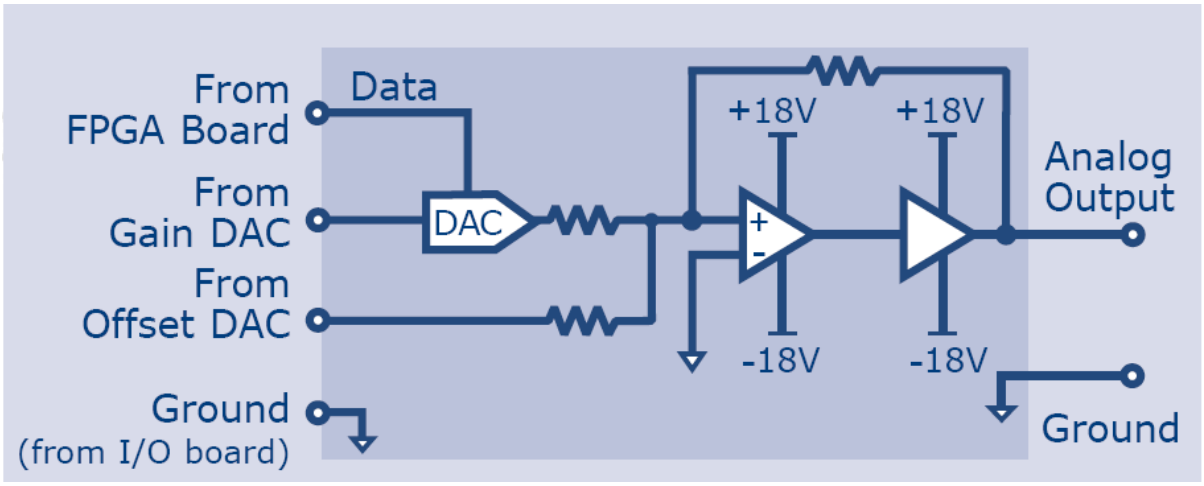

Figure B.5 Schematic of one channel of OP5330

Figure A.6 represents a simplified schematic of one channel of the OP5330 module. It is composed of three stages: the first stage consists of one gain DAC and one offset DAC; the second stage consists of a signal DAC with an operational amplifier that allows for gain adjustments; the third stage consists of an operational amplifier that receives final signal value and integrates the offset.

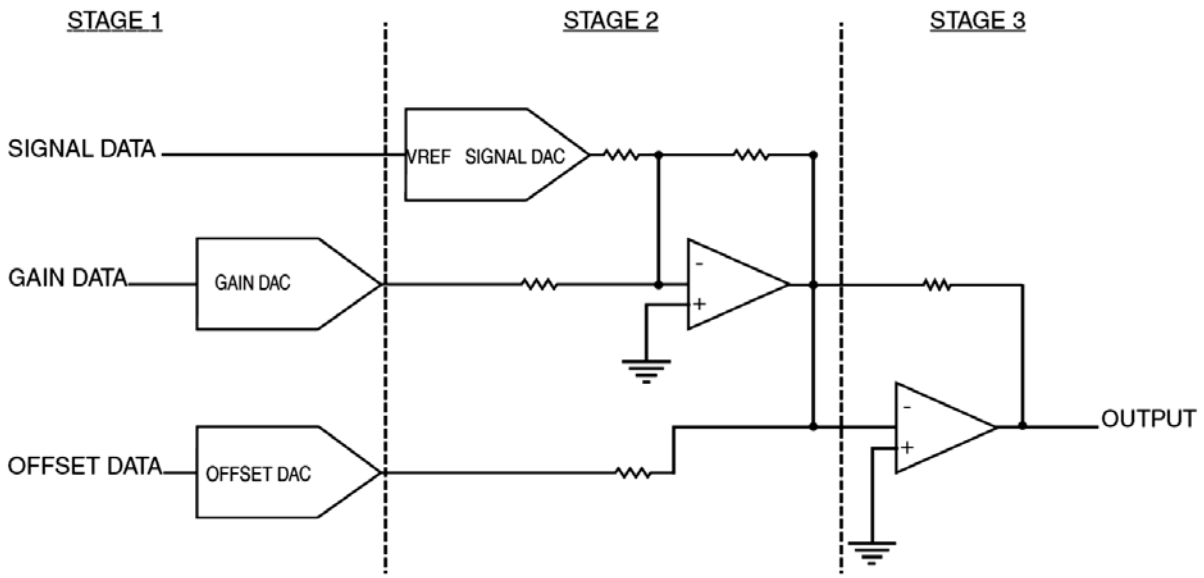

Figure B.6 simplified schematic of one channel of the OP5330 module

OP5340 Analog Input Module

- Up to 16 differential analog Input channels, one 16-bit ADC per channel
- Simultaneous sampling on all channels: Eliminates skew errors inherent in multiplexed channels
- Up to 500 kS/s update rate per channel. Total throughput of 8 MS/s.

- Independent programmable ranges from +/- 100 mVolt to +/- 16 Volt, with software calibration (gain and offset)
- Minimum conversion/acquisition time is 2 µs per channel
- On-board signal conditioning
- Library of drag-and-drop RT-LAB blocks for Simulink

The OP5340 features 16 differential channels with individual 16-bit Analog-to- Digital Converters (ADC), which ensures simultaneous signal capture from multiple channels, thus eliminating the skew errors associated with multiplexed channels. Each ADC can sample up to 500 kS/s, giving a total throughput of 8 Ms/s. Onboard signal conditioning provides offsets and gains from +/- 100 mV to +/- 16 V as well as over-voltage protection.

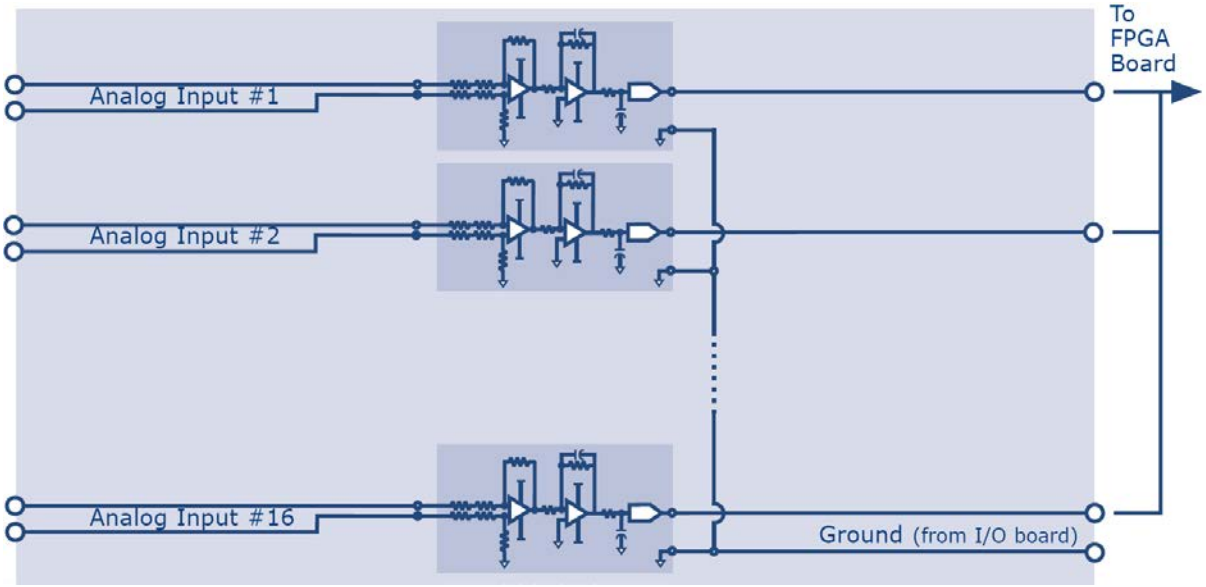

Figure B.7 Schematic of 0P5340 analog input module

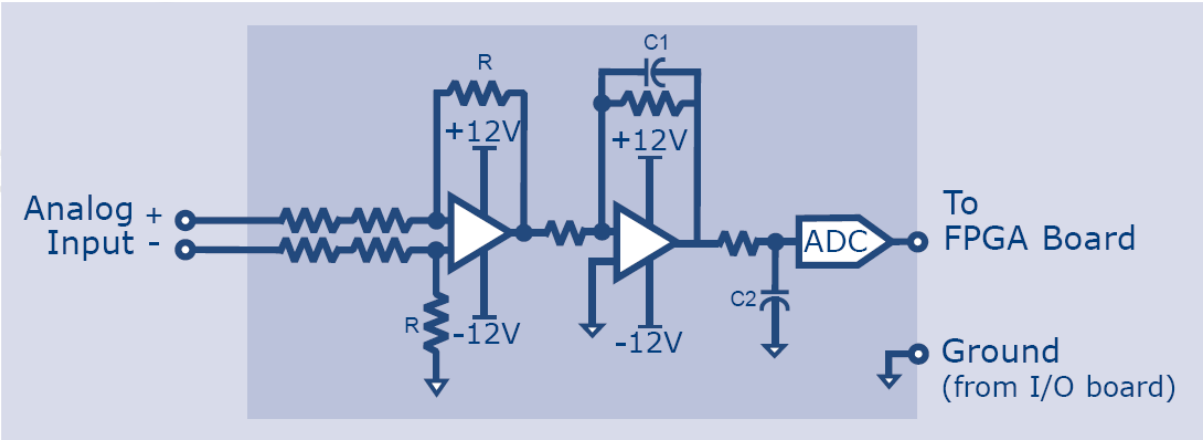

Figure B.8 Schematic of one channel of OP5330

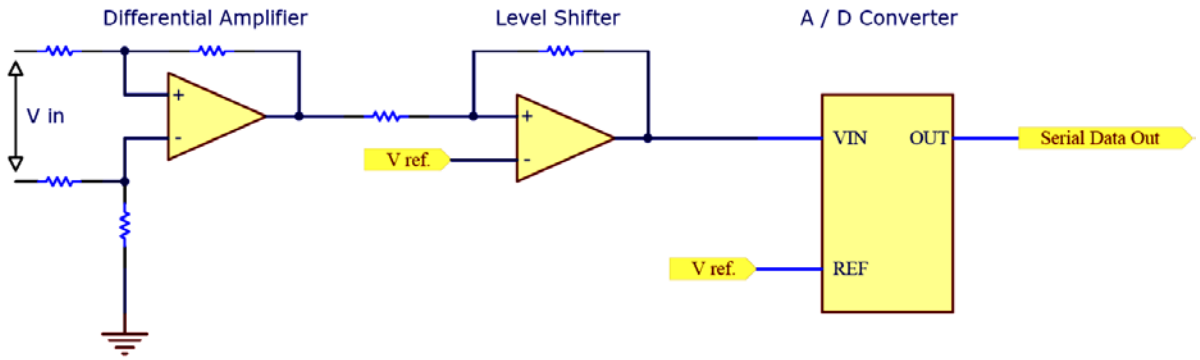

Figure B.9 Simplified schematic of one channel of the OP5330 module

Figure A.9 represents a simplified schematic of one channel of the OP5340 module. It is composed of three stages. First stage consists of one operational amplifier that works in differential input mode and permits the gain adjustment. Second stage, the level shifter, forms the signal for the A/D converter input. Then, after the conversion to the digital type, the signal is sent to the FPGA.

- Up to 16 analog Input (OP5340) or Output (OP5330) channels
- One 16-bit ADC (OP5340) or DAC (OP5330) per channel
- Simultaneous sampling on all channels eliminates skew errors inherent in multiplexed channels
- Up to 500 kS/s update rate for every channel. Total throughput of up to 8 MS/s
- Dynamic range of ± 16V
- Accuracy of +/- 5mV
- Current/Load of ± 15mA
- Hardware configurable on-board signal conditioning and antialiasing filter
- On-board EEPROM memory for calibration parameters
- Library of drag-and-drop Opal-RT RT-XSG blocks for Simulink

Pin assignement

All inputs/outputs are accessible via a 96 pin, 3 x 32, DIN96 connector which shown in **Figure A.10**. Model OP5941 shown in **Figure** A.11 is a dual 38-screw terminal used to connect field I/O signals to the OP5330 and OP5340 module. Table shows the Pin assigned to the each terminals of OP5330 and OP5340 board.

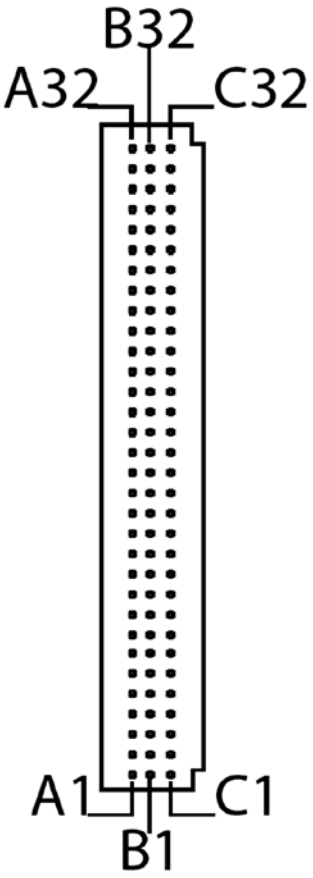

Figure B.10 Carrier front view of male connector

Figure B.11 Model OP5941 Terminal connection board

Table B.6 Terminal description of analog inputs/outputs

Section A: Analog Output			Section B: Analog Input		
Channels	**Pin Number**	**Output**	**Channels**	**Pin Number**	**Input**
0	A32	+ CH 00	16	A16	+ CH 00
	B32	GND		B16	- CH 00
1	C32	+ CH 01	17	C16	+ CH 01
	A31	GND		A15	- CH 01
2	B31	+ CH 02	18	B15	+ CH 02
	C31	GND		C15	- CH 02
3	A30	+ CH 03	19	A14	+ CH 03
	B30	GND		B14	- CH 03
4	C30	+ CH 04	20	C14	+ CH 04
	A29	GND		A13	- CH 04
5	B29	+ CH 05	21	B13	+ CH 05
	C29	GND		C13	- CH 05
6	A28	+ CH 06	22	A12	+ CH 06
	B28	GND		B12	- CH 06
7	C28	+ CH 07	23	C12	+ CH 07
	A27	GND		A11	- CH 07
8	B27	+ CH 08	24	B11	+ CH 08
	C27	GND		C11	- CH 08
9	A26	+ CH 09	25	A10	+ CH 09
	B26	GND		B10	- CH 09
10	C26	+ CH 10	26	C10	+ CH 10
	A25	GND		A09	- CH 10
11	B25	+ CH 11	27	B09	+ CH 11
	C25	GND		C09	- CH 11
12	A24	+ CH 12	28	A08	+ CH 12
	B24	GND		B08	- CH 12
13	C24	+ CH 13	29	C08	+ CH 13
	A23	GND		A07	- CH 13
14	B23	+ CH 14	30	B07	+ CH 14
	C23	GND		C07	- CH 14
15	A22	+ CH 15	31	A06	+ CH 15
	B22	GND		B06	- CH 15

MAPPING I/O BLOCKS TO SIGNAL CONDITIONING

Slot 1 Section A: 16 Analog Out

Relation between Simulink blocks and OP5330

Description: Icon Name: OP5142EX1 AnalogOut

OpFcnOP5142EX1AnalogOut Parameters

Controller Name	'OP5142EX1 Ctrl'
Data-In port number	1
Number of AOut channels	8

Slot 1 Section B: 16 Analog In

Relation between Simulink blocks and OP5340:

Description: Icon Name: OpOP5142EX1 AnalogIn

OpFcnOP5142EX1AnalogIn Parameters:

Controller Name	'OP5142EX1 Ctrl'
DataIn port number	1
Number of AOut channels	8